Low-Temperature Surface Passivation of Crystalline Silicon and its Application to the Rear Side of Solar Cells

von

Dipl.-Phys. Stefan Dauwe

geboren am 7. Juli 1968 in Harderberg

2004

Kurzzusammenfassung

Zentrales Thema der Arbeit ist die Untersuchung von passivierenden Filmen zur Minimierung der Ladungsträgerrekombination an kristallinen Silicium-Oberflächen. Neben der Erweiterung der Standardtheorie zur Oberflächenrekombination wird erstmals die Anwendung von amorphen hydrogenisierten Siliciumnitrid (SiN_x) Filmen und amorphen Silicium (a-Si:H) Filmen zur Rückseitenpassivierung von Solarzellen eingehend untersucht.

Das Standardverfahren zur Verringerung der Rekombination an der Oberfläche ist die thermische Oxidation des Siliciums bei hohen Temperaturen ($\geq 1000\,°C$). Die hohen Herstellungstemperaturen sind aus prozesstechnischen und energetischen Gründen ungünstig. Als vielversprechende Alternative werden SiN_x und a-Si:H Filme untersucht, die plasmagestützt aus der Gasphase abgeschieden werden (engl. plasma-enhanced chemical vapour deposition (PECVD)).

Im theoretischen Teil wird das Modell zur Beschreibung der Oberflächenrekombination bei Vorliegen einer Bandverbiegung erweitert. Für den Fall einer starken Oberflächenbandverbiegung wird eine Näherungslösung für die Berechnung der Bandverbiegung und der Oberflächenrekombinationsgeschwindigkeit (ORG) abgeleitet.

Die SiN_x Filme werden in einem remote PECVD Reaktor bei $400\,°C$ abgeschieden wobei die Filmzusammensetzung (Si/N Verhältnis) variiert wird. Kapazitäts-Spannungs (C-V)-Messungen zeigen, dass N-reiche SiN_x Filme wegen einer höheren Grenzflächenzustandsdichte eine schlechtere Passivierqualität aufweisen. Die feste positive Ladung Q_f in den SiN_x Filmen wird erstmals unter Beleuchtung bestimmt. Dazu wird die Bandverbiegung an der Silicium-Oberfläche mittels zusätzlich aufgebrachter Koronaladungen gezielt variiert. Anhand des Zusammenhangs zwischen gemessener ORG und Koronaladungsdichte ergibt sich $Q_f \approx 2 \times 10^{12}\,cm^{-2}$ in Übereinstimmung mit C-V-Messungen im Dunkeln. Bei Si-reichen SiN_x Filmen, die wegen hoher Leckströme weder mit der C-V noch mit der Korona-Lebensdauermethode untersucht werden können, werden die bislang unbekannten Grenzflächenparameter anhand von Schichtwiderstandsmessungen der Inversionsschicht an der Silicium-Oberfläche abgeschätzt. Damit wird gezeigt, dass sehr stark Si-reiche SiN_x Filme trotz ihres hervorragenden Passiviervermögens ein geringeres Q_f haben.

Des weiteren wird die Passivierqualität von a-Si:H Filmen optimiert. Mit den Filmen werden erstmals die exzellenten Werte für die Oberflächenpassivierung, die derzeit mit SiN_x und SiO_2 Filmen erzielt werden, erreicht und übertroffen. ORGs unter $10\,cm/s$ werden sowohl auf p ($1{,}5\,\Omega cm$) als auch auf n ($3{,}8\,\Omega cm$) dotiertem Silicium erreicht.

Um die Passivierqualität auch am Bauelement zu verifizieren, werden SiN_x und a-Si:H Filme als Rückseitenpassivierung in hocheffiziente Solarzellen implementiert. Aufgrund der hohen positiven Ladung in den SiN_x Filmen wird eine Inversionsschicht an der Silicium-Oberfläche influenziert. Es konnte erstmals unzweifelhaft gezeigt werden, dass Elektronen, die aus der Inversionsschicht in den Rückseitenkontakt einfließen, den Wirkungsgrad bei den SiN_x passivierten Zellen verringern. Im Vergleich zu Referenzzellen, die eine SiO_2 passivierte Rückseite haben, werden statt $20{,}9\,\%$ nur $19{,}5\,\%$ erreicht. Der Einbau eines lokalen Back Surface Fields (LBSF) oder die Passivierung mit stark Si-reichen SiN_x Filmen verringert diese Einbußen. Mit den LBSF Zellen wird ein unabhängig bestätigter Wirkungsgrad von $20{,}6\,\%$ erreicht. Mit a-Si:H Filmen als Rückseitenpassivierung werden $19{,}2\,\%$ erzielt.

Abstract

The main focus of this work is the investigation of passivating films that minimise charge carrier recombination at crystalline silicon surfaces. Besides the extension of the standard surface recombination theory, amorphous hydrogenated silicon nitride (SiN_x) and amorphous hydrogenated silicon (a-Si:H) films are used for the first time as rear surface passivation schemes for solar cells.

The standard method to reduce surface recombination is thermal oxidation at high temperatures ($\geq 1000\,°C$). These high fabrication temperatures are unfavourable for both process risks and energy consumption. This work focuses on promising alternatives: films fabricated using plasma-enhanced chemical vapour deposition (PECVD).

The theoretical part of this work extends the model for surface recombination in the presence of surface band bending. In the case of strong band bending, an approximate solution for the calculation of the band bending and the surface recombination velocity (SRV) is derived.

The passivation mechanisms of SiN_x films are examined, building on the results of earlier research studies. The films are deposited in a remote PECVD reactor at $400\,°C$. The film composition (Si/N ratio) is varied by changing the silane gas flow while maintaining the gas flow of the remaining process gases (ammonia and nitrogen). Capacitance-voltage (C-V) measurements reveal that the poorer surface passivation provided by N-rich SiN_x films is due to a higher interface state density. Using a novel method developed in this work, the fixed positive charge density Q_f within the SiN_x films is determined for the first time under illumination. The method is based on adjusting the surface band bending by depositing corona charges and determining the SRV from contactless lifetime measurements. A value of $Q_f \approx 2 \times 10^{12}\,cm^{-2}$ is unambiguously determined under illumination in correspondence with dark C-V measurements. Si-rich SiN_x films that are neither accessible with C-V nor with corona-lifetime measurements due to high leakage currents are investigated by measuring the sheet resistance of the underlying inversion layer. Despite an excellent surface passivation of SiN_x films with a very high Si content, a lower Q_f is determined.

Furthermore, the passivation quality of a-Si:H films is optimised. At deposition temperatures in the range of $200 - 250\,°C$, outstanding surface passivation with SRVs well below $10\,cm/s$ are achieved both on p- ($1.5\,\Omega cm$) and n- ($3.8\,\Omega cm$) type silicon. These low SRVs obtained for the first time can easily compete with the record low SRVs reported for SiO_2 and SiN_x films.

In order to verify the demonstrated passivation quality on real devices, high-efficiency solar cells have been fabricated incorporating SiN_x and a-Si:H films for rear surface passivation. Owing to the high positive charge density within the SiN_x films, an inversion layer is induced at the silicon surface. Electrons flowing from the inversion layer into the rear contact reduce the energy conversion efficiency of the SiN_x passivated cells. Compared with $20.9\,\%$ efficient reference cells with high-temperature SiO_2 rear surface passivation, only $19.5\,\%$ are obtained with SiN_x passivation. An incorporation of a local back surface field (LBSF) or the usage of SiN_x films with a very high Si content reduce the losses considerably. In case of the LBSF cells, an independently confirmed cell efficiency of $20.6\,\%$ is achieved. Using a-Si:H films for rear surface passivation, $19.2\,\%$ efficient solar cells are obtained.

Contents

Chapter 1

Introduction

Sunlight can be converted directly into electricity by means of solar cells utilising the photo-voltaic (PV) effect. Generally speaking, the photovoltaic effect is the generation of electron-hole pairs in a material by light and their separation by an internal electric field. Becquerel discovered the photovoltaic effect in 1839 while experimenting with a solid electrode in an electrolyte solution [1]. A similar effect was observed in a solid (selenium) several decades later by Hertz. A comprehensive understanding of these phenomena, however, had to wait until the introduction of quantum theory in the early decades of the 20th century. The development of the first solid-state devices in the late forties then paved the way to the first silicon solar cell in 1954 having an energy conversion efficiency of 6 % [2].

Solar cells did not have to wait long to find an application. The year 1958 witnessed the launch of the first satellite to use electricity from the sun. The technology has been developing ever since. Interest in terrestrial photovoltaics developed rapidly, particularly in the wake of the oil crisis in the early 1970s. The shipment of PV modules started in the late 1970s at a very low level, but has seen an average annual growth rate of 12 % in the 1980s and the early 1990s. In the last 7 years, the PV market has undergone a tremendous growth at an average annual rate of 34 %. Today, 99.7 % of the PV production is used for terrestrial applications and photovoltaics is becoming accepted as an increasingly important form of power generation. Today's solar cell market is about 381 MW per year corresponding to more than 1 billion Euros (2001) [3].[1] Assuming that the annual growth rate of today $(20 - 30 \%)$ will continue in the nearer future, about half of the world's electricity demand could be supplied by PV power by the middle of this century [4, 5, 6].[2] Both, supporting programmes to stimulate the market and scientific progress in increasing the efficiency and cost effectiveness of the technology will be necessary to sustain growth in the use of solar electricity.

Silicon solar cells have an overwhelming share of 99 % of the PV market (37 % single

---

[1]The power output specified for a solar cell or PV module refers to the maximum power that can be extracted if the cell or module is illuminated at standard test conditions (25 °C, spectrum AM1.5G, intensity $1 \, \text{kW/m}^2$). Note that a PV module specified as 100 W yields about 100 kWh per year assuming a solar power generator located in mid-Europe.

[2]Note that the average consumption of electrical power in Germany is about 5800 kWh per head per annum (2000) amounting to 19 % of the total end energy consumption [6].

crystalline Si, 48 % block-cast polycrystalline Si, 4 % ribbon-sheet Si, 10 % amorphous Si) [7]. With polycrystalline silicon solar cells - which are generally referred to as multicrystalline solar cells to underline the relatively large grains of the material - conversion efficiencies up to 15 % are achieved with industrial mass production while with monocrystalline cells efficiencies up to 17 % are obtained. In contrast, efficiencies well above 20 %, with top efficiencies of nearly 25 %, are obtained for laboratory type cells and on very small production scales [8, 9, 10, 11]. The difference between industrially and laboratory fabricated solar cells arise from less sophisticated and, hence, significantly cheaper production sequences. In this respect, surface passivation, i.e., the reduction of surface carrier recombination, is omitted in most industrially manufactured solar cells.

The state-of-the-art surface passivation for laboratory crystalline silicon solar cells is thermal oxidation at temperatures around $1000\,^{\circ}$C. However, for a number of reasons, the high-temperature processing has some problems, including:

- the need for a very clean production equipment and a thorough cleaning of the samples due to the risk of contamination and diffusion of unwanted impurities into the bulk;

- long fabrication times (several hours at $1000\,^{\circ}$C);

- thermal degradation of lower quality silicon material (e.g. multicrystalline silicon);

- potentially higher costs due to a high thermal budget and long processing times.

For industrial solar cells, surface passivation is either completely omitted or a so-called back surface field is applied providing only moderate surface passivation. Since nowadays, the electronic quality of silicon substrate material is of relatively high quality the incorporation of an excellent surface passivation into industrial solar cells would lead to a direct increase of their efficiency, thereby decreasing the area-related costs for PV-generated electricity. Promising candidates which avoid the above mentioned problems while at the same time provide an outstanding surface passivation are amorphous hydrogenated silicon nitride (referred to as SiN_x) and amorphous hydrogenated silicon films (referred to as a-Si:H) deposited by plasma-enhanced chemical vapour deposition (PECVD). While SiN_x films have been used in laboratories and industry for some years, a-Si:H passivation is a relatively new concept. Despite some efforts in optimising and characterising Si/SiN_x interfaces for photovoltaic applications, some of the underlying concepts including the exact value for the fixed positive charge density within the SiN_x films are still under discussion. In order to gain an comprehensive understanding, this work deals with a thorough characterisation of well-passivating SiN_x films deposited using plasma-enhanced chemical vapour deposition (PECVD). Before doing so, the theoretical background of surface passivation is discussed in detail including a new concept of recombination in the surface space-charge region. In order to verify the applicability of SiN_x and a-Si:H films to high-efficiency solar cells, the films are applied to the rear of crystalline silicon solar cells.

Chapter 2 discusses the basics of surface passivation including the recombination via surface states and via defect levels in a surface space-charge region. A quasi-exact calculation, the so-called 'extended Shockley-Read-Hall formalism', is used to include the presence

of a band-bending towards the surface. Analytical expressions for the surface band-bending and the recombination via surface states are derived for limiting cases. The formalism is further extended to calculate the shape of the band-bending which is a prerequisite for the subsequent calculation of the recombination in the surface space-charge region. The inclusion of this recombination path is relatively new and is discussed in great detail for the first time.

Chapter 3 introduces the experimental techniques that have been used in this work for sample fabrication and measurement. First, the methods used to deposit the SiN_x and a-Si:H films are described. Second, the different carrier lifetime measurement techniques are introduced. Special attention is paid to what extent surface space-charge regions modify the measured carrier lifetimes. Finally, the solar cell process as well as the various solar cell characterisation techniques used to test the applicability of the passivating films are introduced.

Chapter 4 examines Si/SiN_x interfaces. The SiN_x films have been deposited at $400\,°C$ using PECVD. The interface state density and the fixed charge density within the SiN_x films are investigated using the capacitance-voltage technique. The fixed charge density is also determined for the first time by a novel technique based on corona-charging of the surface and the measurement of the effective carrier lifetime of the wafer. Furthermore, the inversion layer sheet resistance underneath the SiN_x films and the way in which the surface passivation quality of the SiN_x films relates to the film composition are investigated.

Chapter 5 reports on measurement results of the crystalline silicon surface passivation using a-Si:H films. The surface passivation relating to the deposition temperature is investigated and the thermal stability of the passivation is examined. Although the films were deposited at an even lower temperature $(200 - 250\,°C)$ than the SiN_x films, outstanding surface passivation both on n and p-type silicon material has been achieved.

In Chapter 6, the SiN_x and a-Si:H films examined in the foregoing chapters are applied to the rear surface of silicon solar cells. If SiN_x films are used, an unexpected loss in efficiency occurs. The loss mechanism is examined in detail and means for its reduction are suggested and applied. An extensive characterisation of the solar cells is presented including illuminated and dark I-V characteristics and (spatially resolved) spectral response measurements. The analysis of the cells is further extended by means of solar cell simulation based on experimentally determined device parameters.

Chapter 2

Carrier Recombination in Crystalline Silicon

Recombination mechanisms are physical processes that are responsible for the recovery of the thermal equilibrium after excess carriers have been introduced into a semiconductor. The objective of this chapter is to discuss the basic recombination mechanisms for electrons and holes in a semiconductor. Recombination in a semiconductor can occur in the bulk and at the surfaces. Bulk recombination has been addressed extensively in previous works [12, 13]. In this work, only the basic equations are presented, illustrated by plots of the fundamental recombination processes in bulk silicon material. For surface recombination, the theoretical foundations, including a new concept of recombination in a surface space-charge region, are discussed in detail. We are concerned with semiconductor-insulator interfaces and, strictly speaking, the recombination occurs at an interface. However, since the generation of excess carriers within the insulating film and the injection of carriers into the film can be neglected, in this work the term 'surface recombination' rather than 'interface recombination' is used. In this work, surface recombination includes recombination at the actual surface and in a surface layer which consists of a possible space-charge region. Simply speaking, all recombination paths that do not occur in the bulk are lumped into the surface recombination. In the past, recombination in the surface space-charge region has been neglected. However, as will be shown in Chapter 4, recombination in the surface space-charge region can contribute significantly to the total surface recombination.

Following a few basic definitions in Section 2.1, the differentiation between bulk and surface recombination is made in Section 2.2. The next Section (2.3) deals with bulk recombination. The various recombination mechanisms that may be important in crystalline silicon are discussed from a physical point of view, including radiative and Auger recombination and recombination through defects. Since an accurate knowledge of the bulk recombination is necessary to extract the surface recombination, a general parameterisation is given to determine the total bulk recombination as a function of carrier injection and doping concentration. Section 2.4 examines the surface recombination. The general concept of recombination at the actual surface is a recombination through surface defects. However, due to a surface band-bending at the surface the calculation of the surface recombination is far more complicated. Thus, the following subsections deal with the calculation of the

band-bending and the surface potential (2.4.2 - 2.4.2.3) that serve as prerequisites for the calculation of the recombination at the actual surface (2.4.2.4). In the following section (2.4.3) the calculation of the recombination in a surface space-charge region is addressed. For the calculation, the position-dependent potential needs to be known. This is calculated in subsection 2.4.3.1. The sum over the different contributions to the surface recombination is denoted the effective surface recombination velocity that is addressed in Section 2.4.4. The concept of the effective carrier lifetime being a characteristic quantity for all recombination processes within a semiconductor is introduced in Section 2.5. This chapter concludes with a discussion of possible means to reduce surface recombination in Section 2.6.

Many of the concepts described in this chapter are valid for all semiconductor materials. However, for the exemplary calculations, we use the properties of crystalline silicon.

2.1 Definitions

In a semiconductor, a transition of an electron in the conduction band into the valence band is called recombination. During this process an electron-hole pair recombines and vanishes. The excess energy of the electron is carried away by photons, phonons or other electrons. In thermal equilibrium, the concentration of electrons in the conduction band n_0 and that of holes in the valence band p_0 is constant as is the product: $n_0 p_0 = n_\mathrm{i}^2$, with n_i being the intrinsic carrier density in the semiconductor. The equation reflects a dynamic equilibrium (also called detailed balance) between the rates of thermal generation and recombination of electron-hole pairs. The considerations in this work are done exclusively for room temperature. Hence, assuming the doping atoms are fully ionised, the following relations hold:

$$
\begin{aligned}
n_0 &= N_\mathrm{D}, \quad p_0 = \frac{n_\mathrm{i}^2}{n_0} \quad \text{for } n\text{-type semiconductors and} \\
p_0 &= N_\mathrm{A}, \quad n_0 = \frac{n_\mathrm{i}^2}{p_0} \quad \text{for } p\text{-type semiconductors,}
\end{aligned}
\tag{2.1}
$$

where N_D denotes the concentration of donor atoms and N_A that of acceptor atoms.

Additional energy, for instance light shining on the semiconductor, can lift electrons from the valence band into the conductance band. The additional electron-hole pairs are called excess carriers with $\Delta n = n - n_0$ and $\Delta p = p - p_0$ being the excess concentrations of electrons and holes, respectively. After the perturbation has been switched off, recombination processes restore the thermal equilibrium. With the net recombination rate U, that is the total recombination rate less the thermal generation rate, only the recombination of excess carriers is considered (U in $\mathrm{cm^{-3}s^{-1}}$). The time evolution of the excess carriers follows the rate equation

$$
\frac{\partial \Delta n(t)}{\partial t} = -U(\Delta n(t), n_0, p_0).
\tag{2.2}
$$

Different recombination mechanisms contribute to the net recombination rate. Assuming independent recombination paths, the total net recombination rate equals the sum of the

individual recombination rates

$$U(\Delta n(t), n_0, p_0) = U_1(\Delta n(t), n_0, p_0) + U_2(\Delta n(t), n_0, p_0) + ... \tag{2.3}$$

In the simple case, U is proportional to Δn, a mono-exponential decay is obtained for Δn with a time constant τ of

$$\tau \equiv \frac{\Delta n(t)}{U(n_0, p_0)}. \tag{2.4}$$

The time constant, generally referred to as *carrier lifetime*, is a very powerful quantity and the definition 2.4 is used for multi-exponential decays as well. In this case, the carrier lifetime is also a function of the excess carrier density ($\tau = \tau(\Delta n, n_0, p_0)$). Historically, the term 'minority carrier lifetime' has been used frequently. The term arose from the importance of the minority carrier lifetime in controlling the recombination rate in low-injection conditions that prevail in many devices. This term obviously applies only to minority carriers, and as such has no meaning in conditions other than low injection. However, silicon solar cells, often operate under mid-injection, particular under open-circuit conditions. Hence, in this work the general term 'carrier lifetime' is used[1]. Since the net recombination rate is the sum of the rates of individual processes, the reciprocal carrier lifetimes of the processes add up to a reciprocal carrier lifetime. The inverse of this quantity is referred to as *effective carrier lifetime* τ_{eff} (Section 2.5).

   The reduction of recombination is called *passivation*. As for the recombination, passivation of the bulk and of the surface is distinguished. The main focus of this thesis is the examination of passivation of crystalline silicon surfaces. In this context, it is experimentally challenging to resolve the different recombination paths. In particular, if some of the recombination processes contribute to a similar extent it is difficult to determine the individual recombination rates. Hence, for the examination of the surface recombination it is of paramount importance to minimise the bulk recombination and to be able to quantify the recombination rate. Therefore, before considering the surface recombination in detail we will first give a parameterisation of the bulk lifetime.

2.2   Distinction between Bulk and Surface Recombination

The measurement of the carrier lifetime in a semiconductor sample results in an effective carrier lifetime τ_{eff} that is generally determined by contributions of the different individual recombination processes. For the investigation of the recombination mechanisms in the bulk and at the surface it is essential to resolve the individual processes, requiring a method for separating the bulk and the surface contributions to the total recombination rate. The samples examined in this work are homogeneously doped and free of carrier traps. Hence, charge neutrality applies:

$$p - n + N_{\mathrm{D}} - N_{\mathrm{A}} = 0 \tag{2.5}$$

[1]If recombination through deep defects dominates and low-injection prevails, the SRH carrier lifetime is equal to the capture time constant of the minority carriers (p. 15). The identification of the SRH carrier lifetime with the minority carrier lifetime is appropriate in this case only.

or, using Eq. 2.1, $\Delta n = \Delta p$. In thermal equilibrium the potential gradient vanishes or, equivalently, the band edges are flat. At the surface a band-bending can prevail, for instance due to a diffusion of doping atoms to form an emitter, or due to fixed charges present at the semiconductor surface. This leads to the following distinction between the bulk and the surface region: recombination occurring in regions with flat band edges is defined as bulk recombination, whereas recombination outside this region as surface recombination. The definition assumes a region with flat band edges, i.e., besides a homogeneous doping, a sample thickness a lot greater than the Debye length is a prerequisite (Eq. 2.47). Hence, the following theory is not applicable for thin or very weakly doped samples. Note that for a doping density of $10^{16}\,\mathrm{cm}^{-3}$, the Debye length is $40\,\mathrm{nm}$ at $300\,\mathrm{K}$.

The quality of the surface passivation is characterised by the surface recombination velocity (SRV). For uniform energy bands up to the surface it is defined as:

$$S \equiv \frac{U_\mathrm{s}}{\Delta n_\mathrm{s}}, \tag{2.6}$$

where U_s denotes the surface recombination rate and Δn_s the excess carrier density at the surface (2.32). If a band-bending towards the surface exists, the evaluation of Δn_s is difficult since measurement systems generally determine the carrier density in the bulk. This problem is avoided by considering the excess carrier density Δn_{d_sc} at the edge d_sc of the space-charge region and by defining the SRV as

$$S_\mathrm{it} = \frac{U_\mathrm{s}}{\Delta n_{d_\mathrm{sc}}}. \tag{2.7}$$

It is obvious from Eq. 2.7 that recombination in the space-charge region is neglected. S_it can be calculated using the extended Shockley-Read-Hall formalism developed by Girisch *et al.* [14]. In the past, S_it has been identified with the *effective SRV* S_eff [15, 14, 16]. However, in this work S_eff is defined more generally as

$$S_\mathrm{eff} \equiv \frac{U_{z<d_\mathrm{sc}}}{\Delta n_{d_\mathrm{sc}}}. \tag{2.8}$$

where z is the coordinate perpendicular to the semiconductor surface having its origin at the surface, d_sc is the width of the space-charge region and $U_{z<d_\mathrm{sc}}$ denotes the recombination rate beyond the edge of the space-charge region. This quantity includes recombination at the actual surface as well as recombination in the space-charge region (Fig. 2.11). In order to determine the recombination in the space-charge region, the recombination rate per unit volume is integrated along the z-axis, resulting in a recombination rate per unit area. Hence, the SRV in the space-charge region (SCR) S_sc is given by

$$S_\mathrm{sc} = \frac{1}{\Delta n_{d_\mathrm{sc}}} \int_0^{d_\mathrm{sc}} U(z)dz. \tag{2.9}$$

Considering the contribution of the actual interface and that of the space-charge region to the effective SRV, we obtain

$$S_\mathrm{eff} = S_\mathrm{it} + S_\mathrm{sc}. \tag{2.10}$$

The question wether further recombination processes contribute to the effective SRV is discussed in Section 2.4.4.

$J_{\mathrm{s}} = qU_{z<d_{\mathrm{sc}}}$ is the electron (or hole) recombination current density flowing from the bulk towards the surface. Thus, the boundary condition for the solution of the carrier transport equation in the bulk reads as [17]

$$J_{\mathrm{s}} = qU_{z<d_{\mathrm{sc}}} = q\Delta n_{\mathrm{dsc}}S_{\mathrm{eff}}. \tag{2.11}$$

Since we consider flatband conditions in the bulk, Δn_{dsc} equals Δn_{b} where Δn_{b} denotes the excess carrier density in the bulk. Wherever it is clear from the context, we abbreviate Δn_{dsc} and Δn_{b} to Δn.

2.3   Bulk Recombination

The total recombination in the bulk of a semiconductor is composed of two *intrinsic* and one *extrinsic* processes. Intrinsic recombination processes are found even in ideal semiconductor crystals, while extrinsic processes are related to impurities embedded in the crystal as well as crystallographic defects. One of the intrinsic recombination processes, the radiative recombination, is assigned a recombination lifetime τ_{rad}. The other intrinsic process is the Auger recombination (assigned lifetime τ_{A}). The recombination through defects is an extrinsic process. The corresponding rate is described by the lifetime τ_{SRH}. The total bulk carrier lifetime τ_{b} is given by the reciprocal sum of the individual processes:

$$\frac{1}{\tau_{\mathrm{b}}} = \frac{1}{\tau_{\mathrm{rad}}} + \frac{1}{\tau_{\mathrm{A}}} + \frac{1}{\tau_{\mathrm{SRH}}}. \tag{2.12}$$

The individual recombination processes are discussed in the following sections.

2.3.1   Radiative Band-to-Band Recombination

Radiative recombination is the annihilation of an electron in the conduction band, and a hole in the valence band releasing the excess energy by a photon. It is the inverse process of optical absorption. The process is of minor importance for indirect semiconductors like silicon since energy and momentum conservation necessitate the additional participation of a phonon. Since an electron and hole is required for the recombination, the recombination rate is proportional to the product of their densities. The net recombination rate is thus given as

$$U_{\mathrm{rad}} = B(np - n_{\mathrm{i}}^2), \tag{2.13}$$

resulting in a radiative carrier lifetime of

$$\tau_{\mathrm{rad}} = \frac{1}{B(n_0 + p_0) + B\Delta n}. \tag{2.14}$$

For the case of silicon, the coefficient B has been determined by Schlangenotto *et al.* as a function of the temperature [18]. For $T = 300\,\mathrm{K}$ a value of $B = 0.95 \times 10^{-14}\,\mathrm{cm^3 s^{-1}}$ has been found.

2.3.2   Band-to-Band Auger Recombination

The second intrinsic recombination process is Auger recombination. The excess energy set free during the annihilation of the electron-hole pair is transferred to another electron in the conduction band (eeh-process) or to another hole in the valence band (ehh-process). As for the radiative recombination, the Auger net recombination rate is proportional to the product of the densities of the involved carriers:

$$U_{\mathrm{A}} = C_n(n^2 p - n_{\mathrm{i}}^2 n_0) + C_p(np^2 - n_{\mathrm{i}}^2 p_0), \tag{2.15}$$

where C_n und C_p are the Auger coefficients. Providing charge neutrality holds, Eq. 2.15 can be written as a polynomial in Δn. Using Eq. 2.4 the Auger lifetime in low injection is given by the expression

$$
\begin{aligned}
\tau_{\mathrm{A}} &= \frac{1}{C_n n_0^2} \quad \text{for } n\text{-type semiconductors and} \\
\tau_{\mathrm{A}} &= \frac{1}{C_p p_0^2} \quad \text{for } p\text{-type semiconductors.}
\end{aligned}
\tag{2.16}
$$

Dziewior and Schmid determined the Auger coefficients C_n and C_p under low-injection conditions [19]. A fit for doping concentrations $N_{\mathrm{dop}} > 10^{18}\,\mathrm{cm}^{-3}$ resulted in $C_n = 2.8 \times 10^{-31}\,\mathrm{cm}^6\mathrm{s}^{-1}$ and $C_p = 9.9 \times 10^{-32}\,\mathrm{cm}^6\mathrm{s}^{-1}$. Experimentally, a higher Auger recombination rate has been measured for low doping concentrations and low-injection conditions. An explanation and quantitative calculation by Hangleiter and Häcker is now generally accepted [21]. They proposed that this finding is due to Coulomb interaction of the carriers. They included the Coulomb interaction by multiplying the Auger coefficients C_n and C_p in Eq. 2.16 by so-called 'enhancement' factors g_{eeh} and g_{ehh}. The Auger coefficients including Coulombic interactions are therefore given as:

$$
\begin{aligned}
C_n^* &= g_{\mathrm{eeh}} C_n \quad \text{and} \\
C_p^* &= g_{\mathrm{ehh}} C_p.
\end{aligned}
\tag{2.17}
$$

The enhancement factors calculated by Hangleitner and Häger using a quantum mechanical approach matched their experimental results only for n-Si. Altermatt *et al.* could experimentally verify that also for p-Si an excellent agreement with the theory by Hangleiter and Häcker could be achieved [22]. Fitting newly determined experimental data they determined a parameterisation for the low-injection Auger lifetime in the temperature range between 70 and 400 K for n- and p-Si with arbitrary doping concentrations and published the following empirical equations for the enhancement factors

$$
\begin{aligned}
g_{\mathrm{eeh}} &= 1 + (g_{\mathrm{max},n} - 1) \times \left(1 - \tanh\left[\left\{ \frac{n}{5 \times 10^{16}\mathrm{cm}^{-3}} \right\}^{0.34} \right] \right) \quad \text{and} \\
g_{\mathrm{ehh}} &= 1 + (g_{\mathrm{max},p} - 1) \times \left(1 - \tanh\left[\left\{ \frac{p}{5 \times 10^{16}\mathrm{cm}^{-3}} \right\}^{0.29} \right] \right),
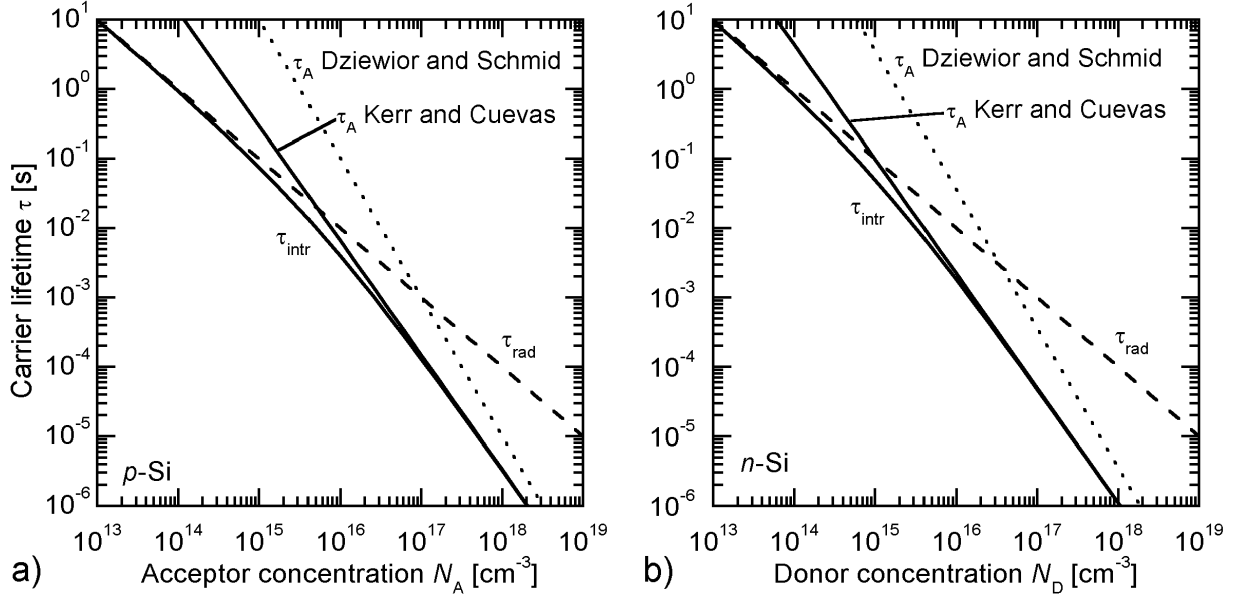\end{aligned}
\tag{2.18}
$$

Figure 2.1: Calculated dependence of the intrinsic bulk lifetime $\frac{1}{\tau_{\mathrm{intr}}} = \frac{1}{\tau_{\mathrm{rad}}} + \frac{1}{\tau_A}$ on the doping concentration for p-Si (a) and n-Si (b) under low-injection conditions (lowest solid line). The radiative lifetime τ_{rad} is calculated using $B = 0.95 \times 10^{-14}\,\mathrm{cm^3 s^{-1}}$ [18]. For the calculation of the Auger lifetime τ_A, the parameterisation of Kerr and Cuevas is used that includes Coulomb interaction (Eq. 2.20) [20]. Shown as well is the Auger lifetime calculated using the parameters determined by Dziewior and Schmid using $C_p = 9.9 \times 10^{-32}\,\mathrm{cm^6 s^{-1}}$ [19].

with

$$g_{\mathrm{max},n} = 235548 \cdot T^{-1.5013} \quad \text{and} \quad g_{\mathrm{max},p} = 564812 \cdot T^{-1.6546}. \tag{2.19}$$

The most recent parameterisation of the low-injection Auger lifetime was published by Kerr and Cuevas [20]. This parameterisation also was determined by empirically fitting an extensive data set. Following a parameterisation by Schmidt [12], they found for the Auger lifetime in low-injection conditions:

$$\begin{aligned}
\tau_A &= \frac{1}{1.8 \times 10^{-24} N_{\mathrm{D}}^{1.65}} \quad \text{for } n\text{-Si and} \\
\tau_A &= \frac{1}{6 \times 10^{-25} N_{\mathrm{A}}^{1.65}} \quad \text{for } p\text{-Si.}
\end{aligned} \tag{2.20}$$

Figs. 2.1 (a) and (b) show the radiative, the Auger and the corresponding total intrinsic low-injection lifetime as a function of the doping concentration for n- and p-Si, respectively. The Auger lifetime was calculated using the parameters published by Dziewior and Schmid and the parameterisation of Kerr and Cuevas. The difference of the respective Auger lifetime curves arises from the Coulombic interaction. The intrinsic carrier lifetime τ_{intr} is calculated using the radiative carrier lifetime and the Auger lifetime published by Kerr and Cuevas [20]. The intrinsic lifetime is dominated by radiative recombination under low-injection conditions and doping concentrations below $10^{15}\,\mathrm{cm^{-3}}$, however, on a very high lifetime level.

For doping concentrations above $10^{16}\,\mathrm{cm}^{-3}$, the Auger recombination limits the intrinsic lifetime.

Let us now consider the Auger lifetime as a function of the injection level. Schmidt *et al.* [23] extended the enhancement factors proposed by Altermatt *et al.* [22] to include mid- and high-injection regimes. They generalized the enhancement factors in Eq. 2.18 by replacing n and p, respectively, by $n + p$ resulting in $g_{\mathrm{eeh}} = g_{\mathrm{ehh}}$ for $T = 300\,\mathrm{K}$. They found a good agreement between calculated and measured data without the necessity to adjust any parameter. The most recent parameterisation of the Auger recombination for varying doping and excess carrier density has been proposed by Kerr and Cuevas in the already mentioned paper [20]. Their starting point is the total Auger recombination rate

$$
\begin{aligned}
R_{\mathrm{A}} &= C_n n^2 p + C_p n p^2 \\
&= np(C_n n_0 + C_p p_0 + C_{\mathrm{a}} \Delta n),
\end{aligned}
\tag{2.21}
$$

with $C_{\mathrm{a}} = C_n + C_p$ being the ambipolar Auger coefficient. By fitting Auger lifetime data collected by different authors, they determined the Auger coefficients, including the Coulombic interaction, for n- and p-Si in low-injection conditions (C_n^* und C_p^*) and in high-injection conditions (C_{a}^*). The Auger coefficients in Eq. 2.21 were then replaced by the newly determined ones to include Coulombic interactions:

$$
\begin{aligned}
C_n &\rightarrow g_{\mathrm{eeh}} C_n = C_n^*(n_0), \\
C_p &\rightarrow g_{\mathrm{ehh}} C_p = C_p^*(p_0), \\
C_{\mathrm{a}} &\rightarrow C_{\mathrm{a}}^*(\Delta n).
\end{aligned}
\tag{2.22}
$$

For the Auger recombination rate, they obtained the following parameterisation:

$$
R_{\mathrm{A}} = np(1.8 \times 10^{-24} n_0^{0.65} + 6 \times 10^{-25} p_0^{0.65} + 3 \times 10^{-27} \Delta n^{0.8}).
\tag{2.23}
$$

The carrier concentrations n, p, n_0, p_0 and Δn have to be inserted in cm^{-3} in Eq. 2.23 resulting in a recombination rate in $\mathrm{cm}^{-3}\mathrm{s}^{-1}$. Note that for the calculation of the *net* Auger recombination rate U_{A}, strictly speaking, the thermal generation rate has to be subtracted from R_{A}. However, since thermal generation rate includes a term proportional to $n_0^2 p_0$ and another one proportional to $n_0 p_0^2$, it dominates the net recombination rate only for very low injection levels (for $N_{\mathrm{dop}} = 10^{16}\,\mathrm{cm}^{-3}$ and $\Delta n > 10^6\,\mathrm{cm}^{-3}$ the thermal generation rate can be safely neglected). Keeping this assumption in mind, the Auger lifetime is calculated using Eq. 2.4:

$$
\tau_{\mathrm{A}} = \frac{\Delta n}{U_{\mathrm{A}}} \approx \frac{\Delta n}{R_{\mathrm{A}}} = \frac{\Delta n}{np(1.8 \times 10^{-24} n_0^{0.65} + 6 \times 10^{-25} p_0^{0.65} + 3 \times 10^{-27} \Delta n^{0.8})}.
\tag{2.24}
$$

Fig. 2.2 shows the calculated Auger lifetime according to Schmidt *et al.* [23] and Kerr and Cuevas [20] in comparison for three doping concentrations . The low-injection limits are approached towards low excess carrier densities (cf. Eq. 2.16, 2.17, 2.18 and 2.20). While the Auger lifetime calculated by Schmidt *et al.* is lower for mid-injection conditions, it is higher for high-injection conditions. Table 2.1 shows exemplarily some calculated values for certain doping and excess carrier concentrations.
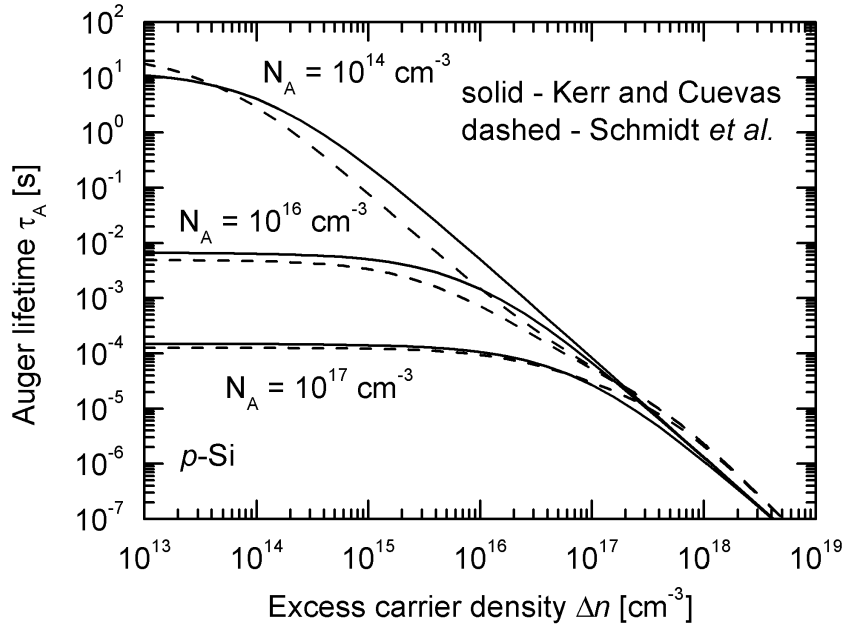
Figure 2.2: Calculated Auger lifetime τ_A as a function of the excess carrier density for p-Si for three different doping concentrations. For the calculation of τ_A, the parameterisation of Schmidt *et al.* [23] and that of Kerr and Cuevas [20] were used (Eq. 2.24). The low-level injection lifetimes, being independent of the excess carrier density, are approached towards low Δn values.

N_A	10^{14}		10^{15}		10^{16}		10^{17}	
Δn	Schmidt	Kerr	Schmidt	Kerr	Schmidt	Kerr	Schmidt	Kerr
10^{13}	17600	10900	307	287	4.9	6.6	0.126	0.148
10^{14}	2870	4060	214	236	4.71	6.37	0.125	0.147
10^{15}	78.1	242	37.3	78.4	3.35	5.03	0.122	0.141
10^{16}	1.51	5.03	1.38	4.08	0.716	1.47	0.0938	0.105

Table 2.1: Calculated Auger lifetime in ms. Authors: Schmidt *et al.* [23], Kerr and Cuevas [20].

For the sake of simplicity, we use the parameterisation of the intrinsic bulk lifetime proposed by Kerr and Cuevas throughout this work, unless otherwise stated. Including radiative and Auger recombination processes, it is given by the expression

$$\tau_{\text{intr}} = \frac{\Delta n}{U_A} \approx \frac{\Delta n}{R_A} = \frac{\Delta n}{np(1.8 \times 10^{-24} n_0^{0.65} + 6 \times 10^{-25} p_0^{0.65} + 3 \times 10^{-27} \Delta n^{0.8} + 9.5 \times 10^{-15})}.$$

$$(2.25)$$

The carrier densities have to be inserted in cm^{-3}, resulting in carrier lifetimes in s.

Figure 2.3: Calculated dependence of the intrinsic bulk lifetime $\frac{1}{\tau_{\text{intr}}} = \frac{1}{\tau_{\text{rad}}} + \frac{1}{\tau_{\text{A}}}$ on the injection level for p-Si (lowest solid line). The radiative lifetime is calculated using Eq. 2.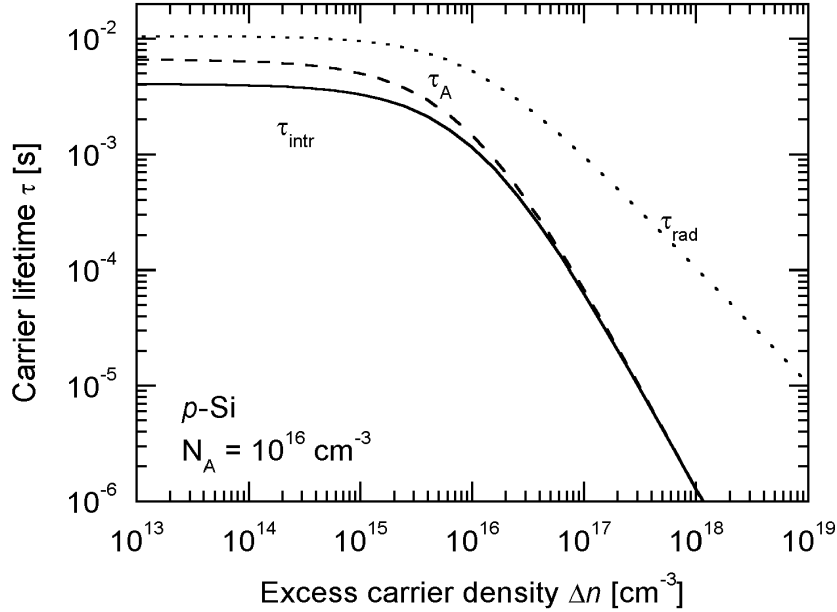14 using $B = 0.95 \times 10^{-14}\,\text{cm}^3\text{s}^{-1}$ [18]. The parameterisation of Kerr and Cuevas is used for the Auger lifetime (Eq. 2.24) [20]. The low-level injection lifetime, being independent of the excess carrier density, is approached towards low excess carrier densities.

2.3.3 Recombination through Defects

Crystallographic imperfection, like dislocations, as well as impurity atoms or complexes in the semiconductor crystal may cause energy levels in the otherwise forbidden bandgap. These defects can be effective recombination centres for excess carriers. The recombination rate was first calculated by Shockley and Read [24] as well as Hall [25] and the recombination is therefore often referred to as Shockley-Read-Hall (SRH) recombination. They developed a statistical model that uses the recombination centre density N_{t}, the capture cross sections for electrons σ_n and holes σ_p and the energy level of the recombination centre E_{t} and found the following expression for the net SRH recombination rate

$$U_{\text{SRH}} = \frac{(np - n_{\text{i}}^2)}{\tau_{p0}(n + n_1) + \tau_{n0}(p + p_1)}. \tag{2.26}$$

with the capture time constant for electrons $\tau_{n0} = (\sigma_n v_{\text{th}} N_{\text{t}})^{-1}$ and for holes $\tau_{p0} = (\sigma_p v_{\text{th}} N_{\text{t}})^{-1}$. Since one electron and one hole is involved in each individual recombination act, the recombination rate is proportional to $(np - n_{\text{i}}^2)$ as for the radiative recombination. $v_{\text{th}} = \sqrt{8kT/\pi m_{\text{th}}^*}$ is the mean thermal carrier velocity where m_{th}^* is the thermal velocity effective mass [26]. At $T = 300\,\text{K}$ it's value is $m_{\text{th}}^* = 0.28\,m_0$ $(m_{\text{th}}^* = 0.41\,m_0)$

for the conductance (valence) band with the electron rest mass $m_0 = 0.91095 \times 10^{-30}$ [26]. Hence $v_{\text{th}} = 2.0 \times 10^7$ cm/s and 1.7×10^7 cm/s for the thermal electron and hole velocity, respectively. The statistical factors n_1 and p_1 are a function of the energy level of the recombination centre:

$$n_1 \equiv n_{\text{i}} \exp\left(\frac{E_{\text{t}} - E_{\text{i}}}{kT}\right), \quad p_1 \equiv n_{\text{i}} \exp\left(\frac{-(E_{\text{t}} - E_{\text{i}})}{kT}\right). \tag{2.27}$$

Using Eq. 2.4 and the charge neutrality condition, the SRH carrier lifetime reads as

$$\tau_{\text{SRH}} = \frac{\tau_{p0}(n_0 + n_1 + \Delta n) + \tau_{n0}(p_0 + p_1 + \Delta n)}{p_0 + n_0 + \Delta n}. \tag{2.28}$$

Under low-injection conditions τ_{SRH} becomes independent of the injection level:

$$\begin{aligned} \tau_{\text{SRH}} &= \tau_{n0}\left(\frac{p_1}{n_0}\right) + \tau_{p0}\left(1 + \frac{n_1}{n_0}\right) \quad \text{for } n\text{-type semiconductors} \\ \tau_{\text{SRH}} &= \tau_{p0}\left(\frac{n_1}{p_0}\right) + \tau_{n0}\left(1 + \frac{p_1}{p_0}\right) \quad \text{for } p\text{-type semiconductors.} \end{aligned} \tag{2.29}$$

A further simplification of Eq. 2.29 is obtained if only deep recombination centres (with energy levels being close to mid-gap) are considered. In this case, n_1 and p_1 are small in comparison with the doping concentration, leading to $\tau_{\text{SRH}} = \tau_{n0}$ for p-type and $\tau_{\text{SRH}} = \tau_{p0}$ for n-type semiconductors. Hence, in the limiting case of low-injection conditions and recombination through deep defects, the SRH carrier lifetime equals the capture time constant of the respective minority carriers (cf. footnote 1 on page 7). For shallow recombination centres, the capture time constant is a lower limit of the SRH lifetime as can be seen from Eq. 2.29. Defects close to mid-gap are therefore effective recombination centres. (Fig. 2.4).

For the limiting case of high-injection, Eq. 2.28 simplifies to

$$\tau_{\text{SRH}} = \tau_{n0} + \tau_{p0}, \tag{2.30}$$

i.e., the SRH carrier lifetime is independent of the energy level of the recombination centre, of the doping concentration and of the injection level. Deep centres exhibit a higher lifetime in high- than in low-injection as is additionally illustrated in Fig. 2.5, whereas shallow defects are effective recombination centres under high-injection conditions only.

2.4   Surface Recombination

The surface terminates the lattice continuity that is the prerequisite for delocalised electrons in energy bands. Hence, localized states may appear at the surface. The concept of surface states was introduced by Tamm [27] and extended by Shockley [28] using fundamental quantum-mechanical considerations. From a chemical point of view, the concept of dangling bonds at the surface that can capture or release carriers may be more illustrative [29]. Since these states exist even at an ideal surface they are called intrinsic surface states. The density
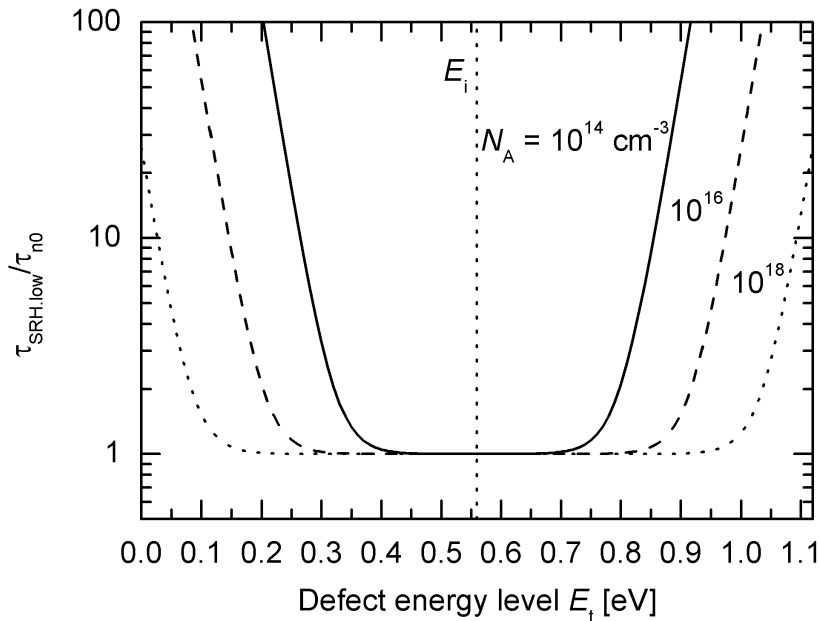
Figure 2.4: Calculated normalized low-injection SRH lifetime as a function of the recombination centre energy level E_t according to Eq. 2.29 for p-Si of different doping concentrations. As can be seen, defects close to midgap are effective recombination centres. The energy range exhibiting a low carrier lifetime increases with doping concentration. Assumptions: $T = 300\,\mathrm{K}$, $n_i = 10^{10}\,\mathrm{cm}^{-3}$, $\tau_{n0} = \tau_{p0}$.

of the dangling bonds and hence, the density of recombination centres can be reduced if chemical bonds are formed with atoms of a film on top of the semiconductor surface. On the other hand, the surface is prone to be contaminated unless a cleaved surface is fabricated in an ultra-high vacuum chamber. This may lead to adatom-induced surface states if the adatoms are sparsely distributed [29] or to interface states if a dense layer is built [29]. Surface or interface states may lead to effective recombination centres as defects do in the bulk. The treatment of surface recombination is analogous to that of recombination through defects in the bulk. For detailed reviews on surface and interface states please refer also to the monographs of Many *et al.* [15], Mönch [29] and Nicollian and Brews [30].

If a clean silicon surface is exposed to an atmospheric ambient, air molecules react with the dangling bonds to minimise the total energy of the surface. The silicon surface atoms react mainly with oxygen atoms and a thin SiO_2 film forms that saturates at a thickness of $1 - 1.5\,\mathrm{nm}$. This film provides virtually no passivation. The requirements for films that permanently reduce the surface recombination are therefore twofold. Firstly, a chemical inert silicon surface is to be produced and secondly, the density of surface states should be reduced by the film. The latter is of particular importance for devices with a high surface-to-volume ratio as are solar cells. Both requirements are for instance provided by SiO_2 films grown at high temperature. These films can effectively passivate the silicon surface and represent the state-of-art in silicon microelectronics and photovoltaics. Surface
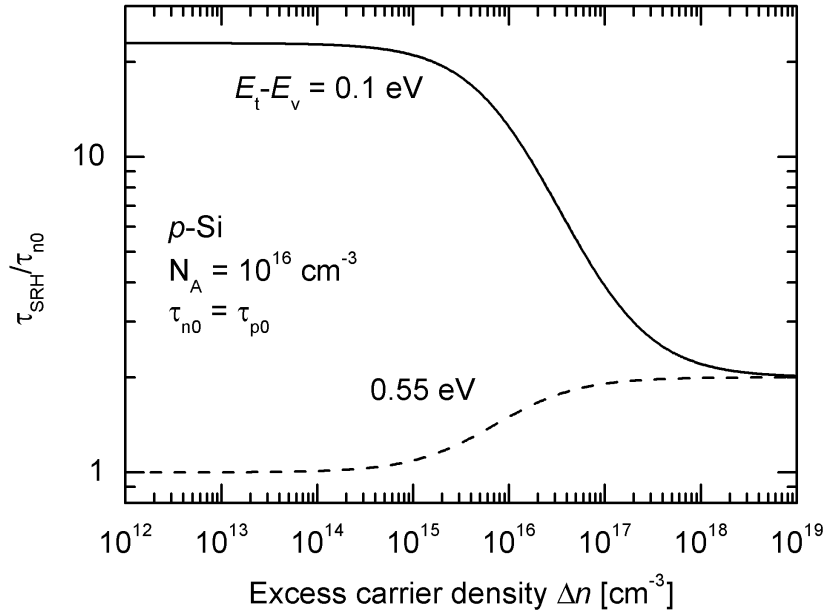
Figure 2.5: Calculated SRH carrier lifetime τ_{SRH} as a function of the injection level Δn for p-Si for a shallow ($E_{\mathrm{t}} - E_{\mathrm{V}} = 0.1\,\mathrm{eV}$) and a deep ($E_{\mathrm{t}} - E_{\mathrm{V}} = 0.55\,\mathrm{eV}$) recombination centre. Assumptions: $T = 300\,\mathrm{K}$, $n_{\mathrm{i}} = 10^{10}\,\mathrm{cm}^{-3}$, $\tau_{n0} = \tau_{p0}$.

state densities as low as $10^9\,\mathrm{cm^2 eV^{-1}}$ can be achieved routinely using this technique. For comparison, note that $6.8 \times 10^{14}\,\mathrm{atoms/cm^2}$ exist at <100> orientated silicon surfaces [31]. At an abrupt Si/SiO$_2$ interface, local deformations of the binding angles exist, which produce a high density of states at the band edges ([32, 33, 34]). However, the recombination activity of these shallow defects (tail states) is usually negligible (Fig. 2.4). The silicon dangling bonds at the interface generate different types of recombination centres, depending on the number of oxygen atoms involved in the remaining three bonds.

For many passivating films, hydrogen plays an essential role, since hydrogen atoms are small and can saturate dangling bonds at the surface without much distortion of the lattice. Also, the hydrogen diffusivity in silicon is high. A very different way to passivate a semiconductor surface apart from the reduction of the density of recombination centres, is the reduction of charge carriers at the surface. This can be achieved by electric fields (field-effect passivation) at the surface and will be discussed in detail in the following sections.

2.4.1   Recombination at the Actual Surface

Since the main focus of this work is on semiconductor-insulator interfaces, we neglect any generation or recombination of carriers outside the semiconductor. Recombination at the interface deals exclusively with the annihilation of excess carriers in the semiconductor at the semiconductor-insulator interface. The calculation of the surface recombination rate

is analogous to that of the SRH recombination discussed in Section 2.3.3. The essential difference is the fact that surface states are continuously distributed within the energy bandgap. For the calculation of the net recombination rate, it is therefore necessary to integrate Eq. 2.26 over the entire bandgap. Carrier transitions from one to another energy level are neglected, i.e, we assume that the defects only interact with the energy bands and not among each other. The surface recombination rate U_s is thus given as

$$U_\text{s} = (n_\text{s}p_\text{s} - n_\text{i}^2) \int_{E_\text{V}}^{E_\text{C}} \frac{v_\text{th}D_\text{it}(E)dE}{\sigma_p^{-1}(E)\left(n_\text{s} + n_1(E)\right) + \sigma_n^{-1}(E)\left(p_\text{s} + p_1(E)\right)}, \qquad (2.31)$$

with n_s and p_s being the electron or hole concentration at the surface, respectively. D_it is the density of interface states at the surface per energy interval ($\text{cm}^{-2}\text{eV}^{-1}$). It should be noted that in Eq. 2.31, D_it, the capture cross sections σ_n, σ_p as well as the statistical factors n_1, p_1 are *energy dependent* quantities. Since U_s is a recombination rate per unit area, the definition of a 'surface carrier lifetime' using Eq. 2.4 is obviously not possible. Instead, a *surface recombination velocity* (SRV) is defined via

$$S(\Delta n_\text{s}, n_0, p_0) \equiv \frac{U_\text{s}(\Delta n_\text{s}, n_0, p_0)}{\Delta n_\text{s}}, \qquad (2.32)$$

where $\Delta n_\text{s} = n_\text{s} - n_\text{s0} = p_\text{s} - p_\text{s0}$ denotes the excess carrier density at the surface. By insertion of Eq. 2.31 into Eq. 2.32

$$S(\Delta n_\text{s}, n_0, p_0) = (n_0 + p_0 + \Delta n_\text{s}) \int_{E_\text{V}}^{E_\text{C}} \frac{v_\text{th}D_\text{it}dE}{\sigma_p^{-1}(n_0 + n_1 + \Delta n_\text{s}) + \sigma_n^{-1}(p_0 + p_1 + \Delta n_\text{s})} \qquad (2.33)$$

is obtained.

We will now discuss Eq. 2.33 using exemplary calculations. Fig. 2.6 shows the SRV as a function of the excess carrier density for different ratios of σ_n/σ_p and a constant D_it throughout the bandgap. In analogy to the SRH carrier lifetime, the low-injection SRV is determined by the capture cross section of the minority carriers. Despite very different values of σ_p, the set of curves in Fig. 2.6 lies close together in the low-injection range. Under high-injection conditions, where $\Delta n_\text{s} = \Delta p_\text{s} \gg p_0$, the capture of carriers of both types of polarity are significant. Hence, the curve calculated with the lowest σ_p exhibits the lowest SRV under high-injection condition. The asymmetry in the σ_n/σ_p ratio results in a strongly injection-level dependent surface recombination velocity.

The small increase in S towards high injection in Fig. 2.6 is examined further in the following figure. The curve with $\sigma_n/\sigma_p = 1$ is shown again in Fig. 2.7, where it is denoted with ΣS. Additionally, Fig. 2.7 shows $S(\Delta n)$ curves that were calculated with either only deep or shallow interface states, respectively, the sum of which is ΣS. As can be seen, the deep states are responsible for the main share of the SRV under low-injection conditions. The increase towards high injection levels is due to the increasing impact of the shallow states. This result is analogous to the dependence of the carrier lifetime on the energy level for bulk defects, as is illustrated in Fig. 2.5. Considering the inverse relationship between the carrier lifetime and the surface recombination velocity, the decrease (increase)
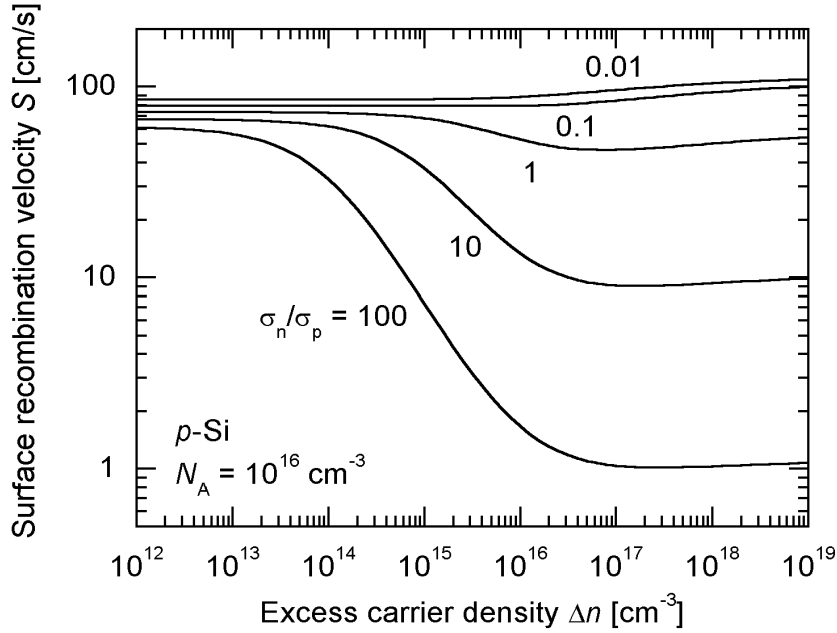
Figure 2.6: Calculated surface recombination velocity S as a function of the excess carrier density Δn and the ratio of the capture cross sections for p-Si. Assumptions: $N_{\mathrm{A}} = 10^{16}\,\mathrm{cm}^{-3}$, $T = 300\,\mathrm{K}$ and energy independent recombination parameters $D_{\mathrm{it}} = 10^{10}\,\mathrm{eV}^{-1}\mathrm{cm}^{-2}$ and $\sigma_n = 10^{-15}\,\mathrm{cm}^2$.

towards higher injection levels in Fig. 2.5 corresponds to the increase (decrease) of the SRV in Fig. 2.7. Shallow states only contribute under high-injection conditions to the total recombination rate.

Fig. 2.8 shows a plot of the SRV vs the injection level for different doping concentrations. Under low-injection conditions, the SRV is higher for higher doping concentration, whereas the same value is approached for all doping level towards high-injection conditions. Consequently it is generally more difficult to passivate highly doped silicon wafers. This can also be seen from Fig. 2.4: The energy range being responsible for a lower carrier lifetime is broader for material with higher doping concentrations. Since for the calculation of the SRV an integration over the whole bandgap is carried out, a higher SRV is obtained for the highly doped material.

A simple relationship can be given only for the maximum of the SRV under low-injection condition $S_{\mathrm{li.max}}$. According to Eq. 2.33

$$
\begin{aligned}
S_{\mathrm{li.max}} &= v_{\mathrm{th}} D_{\mathrm{it}} E_{\mathrm{g}} \sigma_n \quad \text{for } n\text{-type semiconductors and} \\[2mm]
S_{\mathrm{li.max}} &= v_{\mathrm{th}} D_{\mathrm{it}} E_{\mathrm{g}} \sigma_p \quad \text{for } p\text{-type semiconductors,}
\end{aligned}
\tag{2.34}
$$

where $E_{\mathrm{g}} = E_{\mathrm{C}} - E_{\mathrm{V}}$ is the bandgap.

If only one energetically localised recombination centre with a density of N_{it} (in cm^{-2}) is considered at the surface, the integral in Eq. 2.33 can be omitted. With $S_{n0} = v_{\mathrm{th}} \sigma_n N_{\mathrm{it}}$
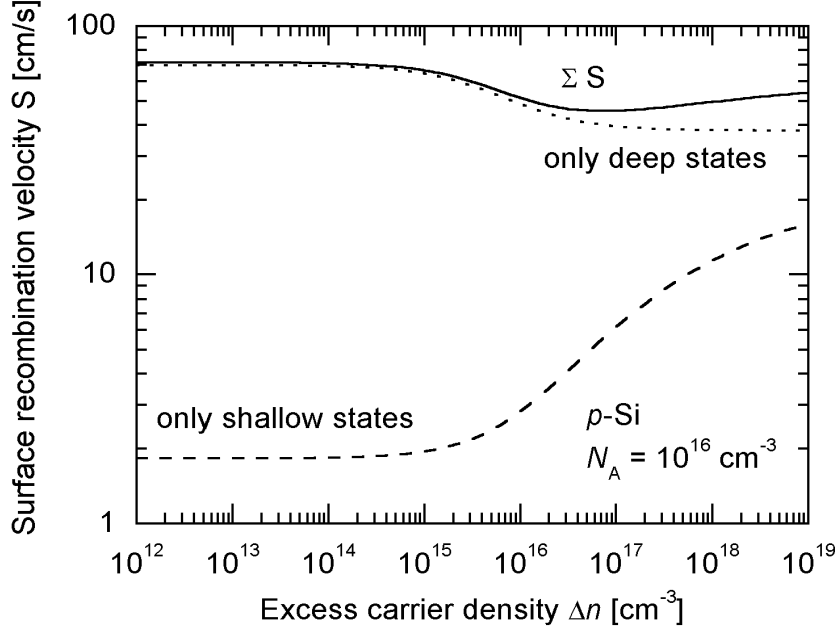
Figure 2.7: Calculated SRV as a function of the excess carrier density for p-Si. The interface state density D_{it} is assumed to be a step function with $D_{\mathrm{it}} = 10^{10}\,\mathrm{eV^{-1}cm^{-2}}$ and $D_{\mathrm{it}} = 0$, respectively. For the curve denoted with 'only deep states', interface states are in the energy range $0.18 < E_{\mathrm{t}} - E_{\mathrm{V}} \leq 0.94$ ($D_{\mathrm{it}} = 0$ elsewhere), while for the other curve ('only shallow states') the interface states distribution is the opposite ($D_{\mathrm{it}} = 0$ in the energy range $0.18 < E_{\mathrm{t}} - E_{\mathrm{V}} \leq 0.94$ and $10^{10}\,\mathrm{eV^{-1}cm^{-2}}$ elsewhere). The curve denoted with ΣS is the sum of both curves and is therefore equal to that shown in Fig. 2.6 with $\sigma_n/\sigma_p = 1$. The increase or decrease of S with increasing injection level is in analogy to the decrease and increase shown in Fig. 2.5 considering the reciprocal relationship between the carrier lifetime and the SRV. Assumptions: $N_{\mathrm{A}} = 10^{16}\,\mathrm{cm^{-3}}$, $n_{\mathrm{i}} = 10^{10}\,\mathrm{cm^{-3}}$, $T = 300\,\mathrm{K}$ and energy independent capture cross sections $\sigma_n = \sigma_p = 10^{-15}\,\mathrm{cm^2}$.

and $S_{p0} = v_{\mathrm{th}}\sigma_p N_{\mathrm{it}}$ the SRV becomes:

$$S(\Delta n_{\mathrm{s}}, n_0, p_0) = \frac{n_0 + p_0 + \Delta n_s}{S_{p0}^{-1}(n_0 + n_1 + \Delta n_s) + S_{n0}^{-1}(p_0 + p_1 + \Delta n_s)}. \qquad (2.35)$$

Eq. 2.35 is formally identical to Eq. 2.28 if the reciprocal relation between τ and S is considered. Hence, the limiting cases for deep defect levels and high- and low-injection condition are in complete analogy if only S, S_{n0} and S_{p0} are substituted by $1/\tau_{\mathrm{SRH}}$, $1/\tau_{n0}$ and $1/\tau_{p0}$, respectively.

2.4.2 Band-Bending towards the Surface

The case of flat bands towards the surface, as it was discussed in the previous section, is an idealised exception. Usually, a bending of the energy bands towards the surface of the
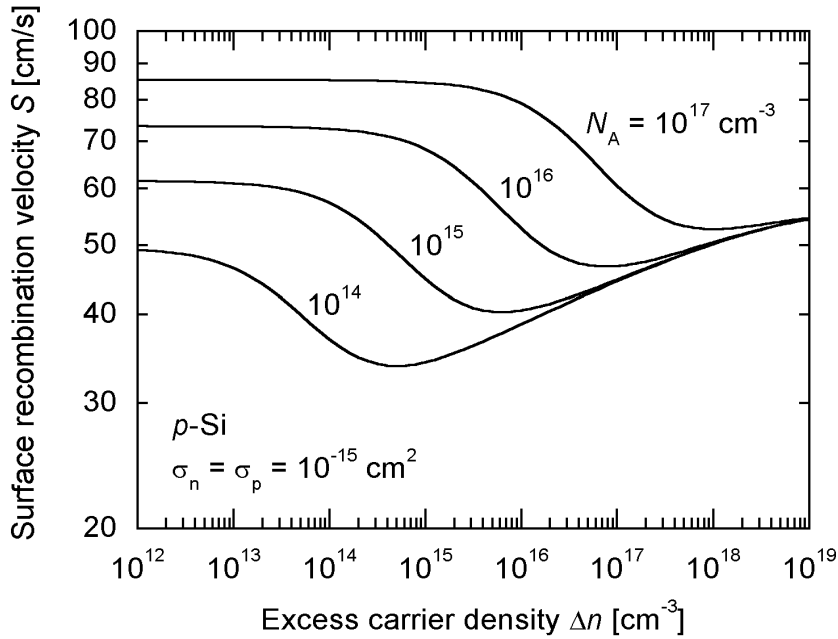
Figure 2.8: Calculated impact of the doping concentration N_A on the $S(\Delta n_s)$ dependence for p-Si. The maximum low-injection SRV according to Eq. 2.34, would be $S_{li.max} = 112$ cm/s. Assumptions: $T = 300$ K and energy independent recombination parameters $D_{it} = 10^{10}$ eV^{-1}cm^{-2}, $\sigma_n = \sigma_p = 10^{-15}$ cm^2.

semiconductor exists. This can be due to external potentials as a result of (i) a work function difference between the semiconductor and a metal capping layer, (ii) charged states at the surface or within an insulating film on top of the surface, (iii) surface states interacting with the semiconductor. Additionally, an applied bias at a gate electrode may bend the energy bands. Semiconductor heterojunctions that may cause a band-bending are not considered in this work. Unlike metals that contain a high density of mobile carriers and compensate potential differences in infinitesimal thin layers, the band-bending within semiconductors extends usually hundreds of nanometres into the bulk[2].

In order to calculate the SRV under band-bending conditions using Eq. 2.7, Eq. 2.31 has to be evaluated. Hence, the carrier densities at the surface n_s, p_s or, equivalently, the surface potential Ψ_s has to be known. The following three subsections deal with the calculation of Ψ_s. S_{it} is then calculated in subsection 2.4.2.4. An exact calculation of the surface potential requires the simultaneous solution of the Poisson equation and the continuity equations with the corresponding boundary conditions. The Poisson equation can be solved analytically which will be shown below. However, for the numerical evaluation, the surface potential has to be known. This can be done with strong simplifications only ([15], Chapter 4). Computer simulation packages like PC1D [35] or DESSIS [36] use the method of finite elements to solve

---

[2]The so-called *Debye length* characterises the width of a band-bending in a semiconductor. It is defined in Eq. 2.47.

the differential equations numerically. A result of such a calculation using PC1D is shown in Fig. 2.9. In this example, a fixed positive charge is assumed on top of the silicon surface. The positive charge attracts electrons in the semiconductor conduction band and repels holes in the valence band. The increased electron density at the surface causes a band-bending downwards. The fixed charge density of $Q_\mathrm{f} = 2 \times 10^{11}\,\mathrm{cm^{-2}}$ causes depletion conditions at the surface for the considered case. If photons are absorbed in the semiconductor, the surface potential decreases as can be seen from the $E_\mathrm{C.lgt}$ and $E_\mathrm{V.lgt}$ curves. However, the silicon surface changes from depletion conditions in thermal equilibrium ($p_\mathrm{s.drk} > n_\mathrm{s.drk}$) to inversion conditions under illumination ($p_\mathrm{s.lgt} < n_\mathrm{s.lgt}$) as can be seen in the bottom graph of Fig. 2.9. This example illustrates the interesting effects that can occur at the surface. For a deeper understanding, the dependence of the band-bending and the SRV on different parameters is now examined in detail. In order to analyse some general relations, we do not use PC1D but rather a quasi-exact approximation developed by Girisch *et al.* [14] (Section 2.4.2.3). They introduced the so-called *extended Shockley-Read-Hall formalism*, which was applied by Aberle *et al.* [16] to the Si/SiO$_2$ and by Schmidt *et al.* to the Si/SiN$_\mathrm{x}$ interface [12, 37]. An extensive discussion can be found in [38] as well. The formalism uses the charge neutrality within the sample as the starting point:

$$Q_\mathrm{sc} + Q_\mathrm{it} + Q_\mathrm{f} + Q_\mathrm{G} = 0, \tag{2.36}$$

where Q_it is the charge density located in the interface states, Q_f that of fixed charges within the insulating film and Q_G that in an optional gate electrode (unit elementary charges per cm^2). Q_sc will be calculated in the next section, following an excellent derivation by Many ([15], Chapter 4). The derivation is based on earlier works by Schrieffer [39] as well as Garrett and Brattain [40]. A further revision can be found in the book of Mönch ([29], Chapters 2 and 5) and partly in that of Sze ([31], Chapter 7). Subsequently, in Section 2.4.2.2, the quasi-Fermi levels in the bulk are calculated. The surface potential Ψ_s as well as the quasi-Fermi levels in the bulk uniquely determine both the shape of the potential in the space-charge region $\Psi(z)$ and the space-charge density Q_sc. With the help of the surface potential Ψ_s and the charge densities Q_it and Q_G that are calculated in Section 2.4.2.3 we have the prerequisites to calculate the recombination at a semiconductor surface, which will be done in Section 2.4.2.4.

2.4.2.1   Calculation of the Space-Charge Density

The space-charge density Q_sc is defined as the total net charge in the space-charge region per unit surface area. As such, it can be calculated using Gauß's law:

$$q Q_\mathrm{sc} = -\epsilon_\mathrm{s} \mathcal{E}_\mathrm{s} = \epsilon_\mathrm{s} \left. \frac{\partial \Psi}{\partial z} \right|_{z=0}, \tag{2.37}$$

with ϵ_s being the semiconductor permittivity, $\mathcal{E}_\mathrm{s}$ the electric field at the surface and Ψ the potential. Ψ is defined as

$$\Psi \equiv \frac{1}{q}(E_\mathrm{Vb} - E_\mathrm{V}(z)), \tag{2.38}$$
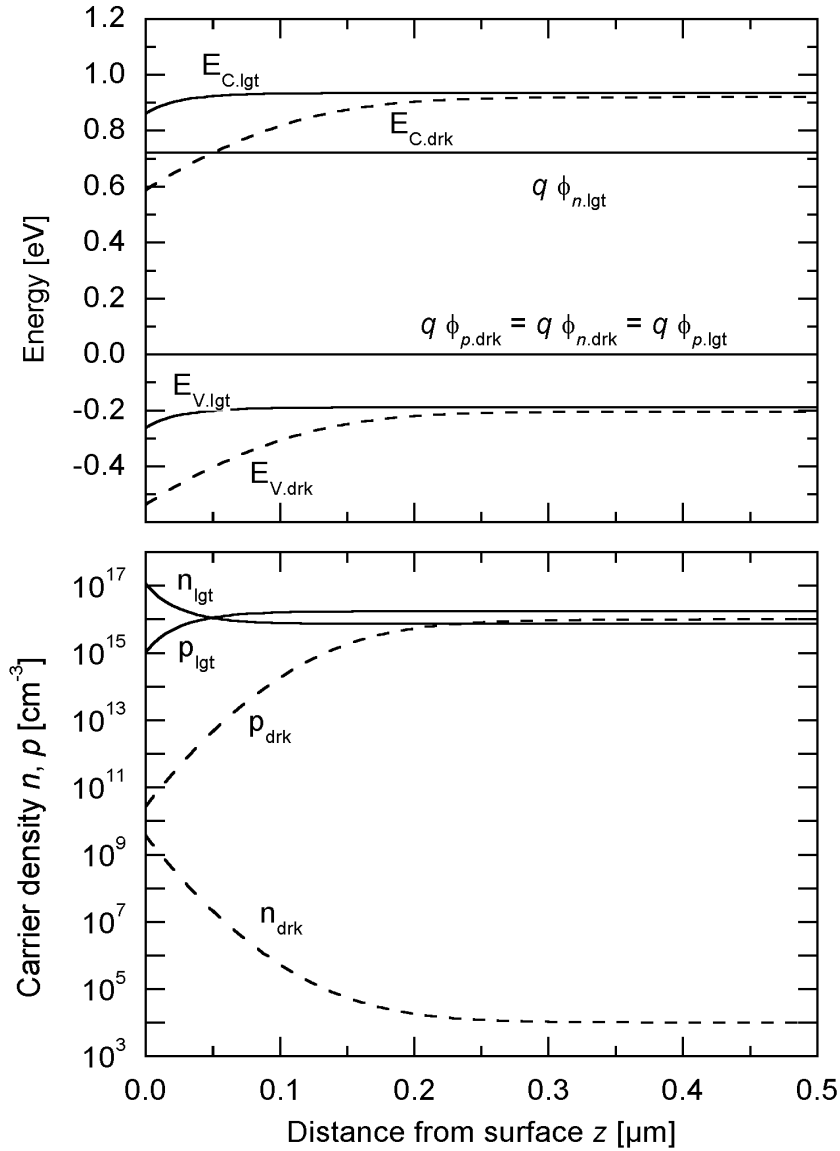
Figure 2.9: Top: Calculated band-bending using PC1D for a p-Si wafer with a fixed positive charge density of $Q_f = 2 \times 10^{11}\,\mathrm{cm}^{-2}$ on top of the wafer. The energy bands in thermal equilibrium (dark case) and under illumination of 1 sun (AM1.5G spectrum) are shown in the top graph. The bottom graph shows the corresponding carrier densities. Assumptions: $N_A = 10^{16}\,\mathrm{cm}^{-3}$, 300 μm thick sample, $\tau_b = 1\,\mathrm{ms}$, zero front and rear SRV, sample covered with anti reflection coating to increase optical absorption.

where E_{Vb} and $E_V(z)$ denote the edge of the valence band in the bulk and throughout the semiconductor, respectively. The definitions of the energies, potentials and charge densities are given in Fig. 2.10 showing a schematic sketch of a metal-semiconductor structure in thermal equilibrium and in Fig. 2.11 showing a sketch of a metal-insulator-semiconductor

Figure 2.10: Energy-level diagram for a metal/p-semiconductor structure in thermal equilibrium.

(MIS) structure. Ψ is now obtained by solving the Poisson equation:

$$\frac{\partial^2 \Psi}{\partial z^2} = -\frac{\rho(z)}{\epsilon_{\mathrm{s}}}.$$
(2.39)

The space charge density $\rho(z)$ is composed of positive and negative charges due to static impurities as well as mobile electrons and holes:

$$\rho(z) = q(N_{\mathrm{D}} - N_{\mathrm{A}} - n(z) + p(z)).$$
(2.40)

It is assumed that the shallow donors and acceptors are homogeneously distributed and the semiconductor is in the saturation range, i.e., all donor or acceptor atoms are ionized. Furthermore, non-degenerately doped silicon is assumed so that Maxwell-Boltzmann statistics can be applied. The density of mobile carriers in the neutral bulk of the semiconductor is given via

$$\begin{aligned} n_{\mathrm{b}} &= n_{\mathrm{i}} e^{-\beta \phi_n} \quad \text{and} \\ p_{\mathrm{b}} &= n_{\mathrm{i}} e^{\beta \phi_p}, \end{aligned}$$
(2.41)

where ϕ_n, ϕ_p and n_{i} denote the quasi-Fermi levels for electrons and holes and the intrinsic carrier density of the semiconductor, respectively. β is defined as $\beta \equiv q/kT$. Including the
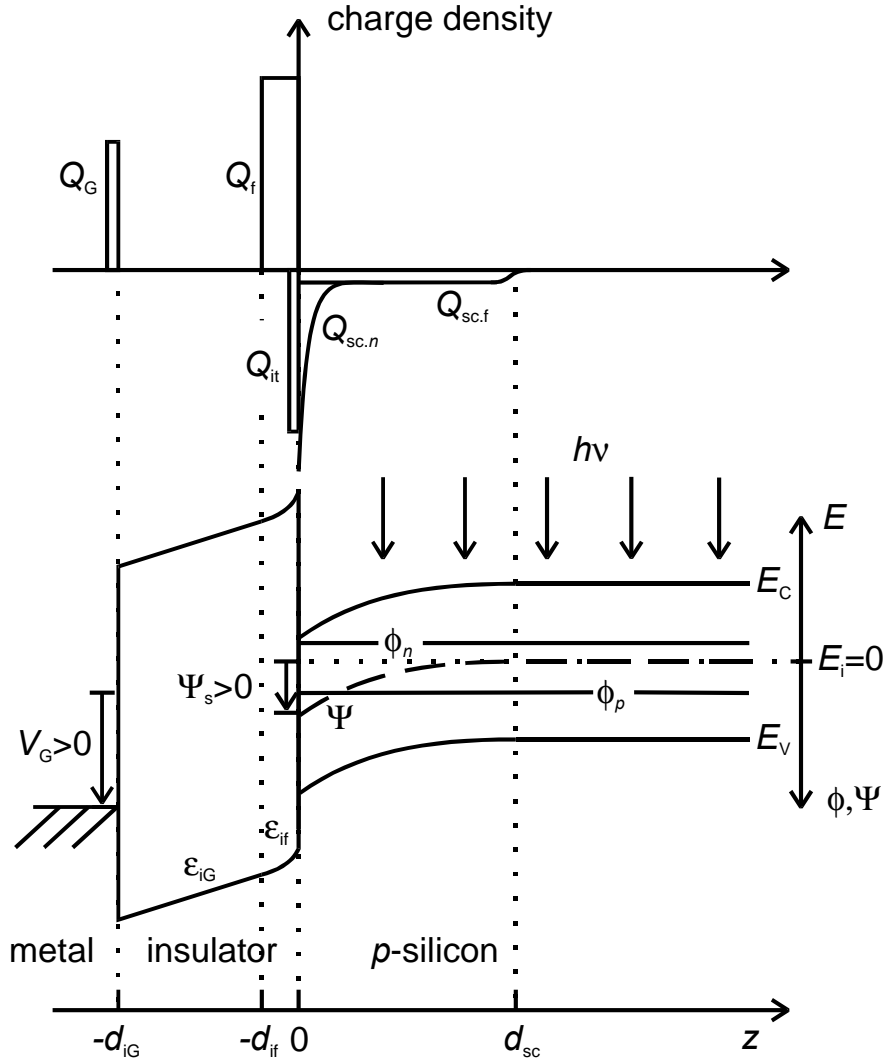
Figure 2.11: Charge density distribution and band diagram of an MIS structure with a p-type semiconductor under illumination. A positive fixed charge density Q_f and a stack of two different insulators having different dielectric constants are assumed.

space-charge region, the carrier densities are

$$
\begin{aligned}
n(z) &= n_b e^{\beta\Psi} \quad \text{and} \\
p(z) &= p_b e^{-\beta\Psi}.
\end{aligned} \tag{2.42}
$$

Due to charge neutrality in the bulk (2.5), $N_D - N_A$ can be replaced by $n_b - p_b$ such that the Poisson equation is given as

$$
\frac{\partial^2 \Psi}{\partial z^2} = -\frac{q}{\epsilon_s}\{n_b - p_b + p_b e^{-\beta\Psi} - n_b e^{\beta\Psi}\} = -\frac{q n_i}{\epsilon_s}\{e^{-\beta\phi_n}(1 - e^{\beta\Psi}) - e^{\beta\phi_p}(1 - e^{-\beta\Psi})\}. \tag{2.43}
$$

The space charge on the right side of Eq. 2.43 does not explicitly depend on the positon z. By multiplying the equation with $2\partial\Psi/\partial z$ and using the identity

$$2\frac{\partial\Psi}{\partial z}\frac{\partial^2\Psi}{\partial z^2} = \frac{\partial}{\partial z}\left[\frac{\partial\Psi}{\partial z}\right]^2 \tag{2.44}$$

it can be brought into an integrable expression [31]:

$$\int_0^{(\partial\Psi/\partial z)^2} d\widetilde{\left[\frac{\partial\Psi}{\partial z}\right]}^2 = -\frac{2qn_i}{\epsilon_s}\int_0^\Psi d\tilde{\Psi}\{e^{-\beta\phi_n}(1-e^{\beta\tilde{\Psi}}) - e^{\beta\phi_p}(1-e^{-\beta\tilde{\Psi}})\}. \tag{2.45}$$

Since $\partial\Psi/\partial z = 0$ for $\Psi = 0$, the electric field $\mathcal{E}$ is given via the expression [14]

$$-\mathcal{E} = \frac{\partial\Psi}{\partial z} = \mp\sqrt{\frac{2q}{\beta\epsilon_s}\left\{p_b\left(e^{-\beta\Psi}+\beta\Psi-1\right)+n_b\left(e^{\beta\Psi}-\beta\Psi-1\right)\right\}}. \tag{2.46}$$

The upper sign in Eq. 2.46 refers to $\Psi_s > 0$ and the lower one to $\Psi_s < 0$. Please note that $\Psi_s > 0$ indicates a downward bend-bending in the band diagram. With the *steady-state extrinsic* Debye length [15], [29]

$$\lambda_D = \sqrt{\frac{\epsilon_s}{\beta q(n_b + p_b)}} \tag{2.47}$$

and the function [15]

$$F(\Psi, \phi_p, \phi_n) = \sqrt{\frac{2}{p_b+n_b}\left\{p_b\left(e^{-\beta\Psi}+\beta\Psi-1\right)+n_b\left(e^{\beta\Psi}-\beta\Psi-1\right)\right\}}, \tag{2.48}$$

Eq. 2.46 can be abbreviated to

$$-\mathcal{E} = \frac{\partial\Psi}{\partial z} = \mp\frac{1}{\beta\lambda_D}F(\Psi, \phi_p, \phi_n). \tag{2.49}$$

It is noticeable that the steady-state extrinsic Debye length characterises the width of the space-charge region. Since the density of mobile charge carriers is higher under illumination than in the dark, the Debye length under illumination is shorter than in the dark. Using Eq. 2.46 we obtain

$$qQ_{sc} = \mp\epsilon_s\frac{F(\Psi_s, \phi_p, \phi_n)}{\beta\lambda_D}, \tag{2.50}$$

with the same sign conventions as in Eq. 2.46. For completeness, the individual contributions to Q_{sc}, namely the density of free electrons $Q_{sc.n}$, of free holes $Q_{sc.p}$ and that of fixed ions $Q_{sc.f}$ are given as:

$$Q_{sc.n} = -\int_0^{d_{sc}} n(z)dz = -\beta\lambda_D\int_{\Psi_s}^0 \frac{n(\Psi)}{F}d\Psi, \tag{2.51}$$

$$Q_{sc.p} = \int_0^{d_{sc}} p(z)dz = \beta\lambda_D\int_{\Psi_s}^0 \frac{p(\Psi)}{F}d\Psi, \tag{2.52}$$

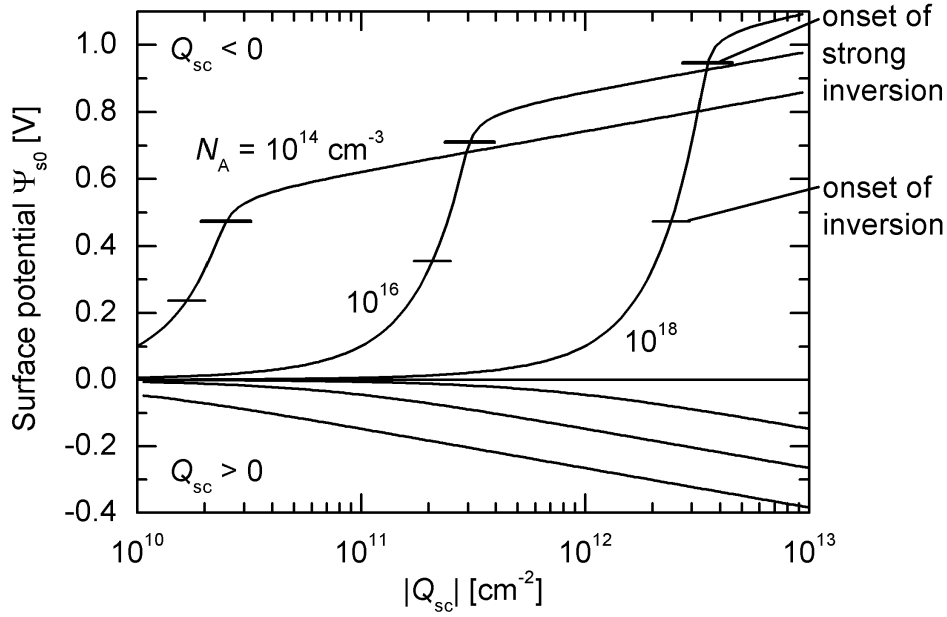$$Q_{sc.f} = (N_D - N_A)d_{sc}. \tag{2.53}$$

Figure 2.12: Calculated surface potential as a function of Q_{sc} for p-type silicon with different doping concentrations. Assumptions: no interface states, $T = 300$ K, thermal equilibrium.

Fig. 2.12 illustrates Eq. 2.50 for the case of thermal equilibrium and three different doping densities [31]. For the following let us consider a sample without a gate electrode and, let us neglect the charges stored in the interface traps($Q_{sc} = -Q_f$). In this case, Fig. 2.12 can be regarded as the surface band-bending as a function of the fixed charge density. The surface potential under accumulation conditions varies only weakly with Q_f owing to the relatively high density of holes in the valence band. In contrast, under depletion conditions, the surface potential varies strongly. Once strong inversion occurs, the variation of the surface potential is similar to that in the accumulation region. Inversion starts at a surface potential of $\Psi_s = \Psi_B$ and strong inversion begins at twice this value ($\Psi_s = 2\Psi_B$). Using these expressions, the onset of (strong) inversion is shown as a function of doping concentration in Fig. 2.13. Typical values for Q_f in SiO_2 (SiN_x) films are 10^{11} cm^{-2} (2×10^{12} cm^{-2}). Hence, for doping concentrations below 3×10^{15} cm^{-3} (8×10^{17} cm^{-3}), the surface of the silicon wafer is inverted for SiO_2 (SiN_x) films in thermal equilibrium.

Due to charge neutrality, Q_{sc} remains constant under illumination if the interface charge is neglected. Considering Eq. 2.37 and Eq. 2.46, it can be seen that $|\Psi_s|$ decreases as the injection level increases (increasing illumination intensity). In the limit of very strong illumination, Ψ_s approaches zero. In other words, the effect of illumination is always such as to decrease the absolute magnitude of the barrier height. This has already been demonstrated for the particular example in Fig. 2.9. It should be noted that Q_{sc} depends only on the surface potential and quasi-Fermi levels in the bulk. The quasi-Fermi levels are calculated in the next section, while Ψ_s is calculated in the Section 2.4.2.3.
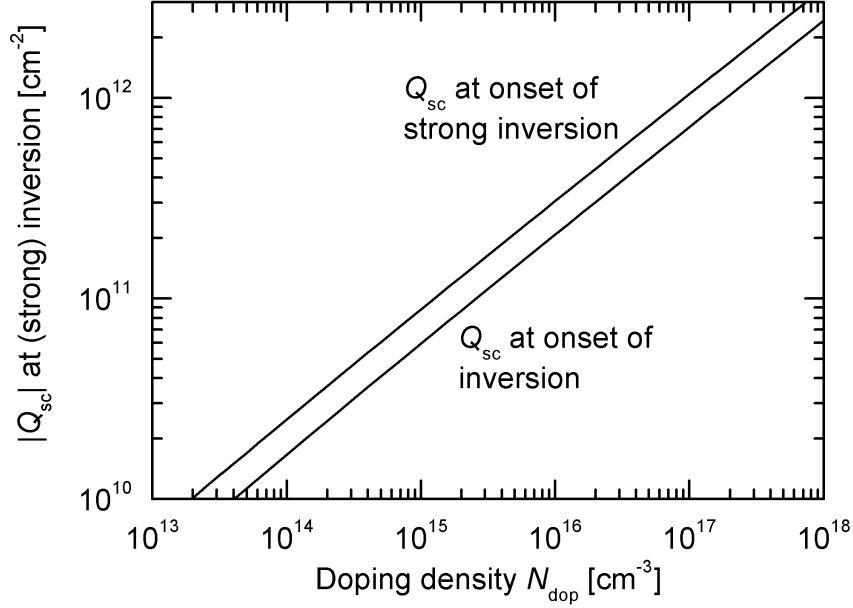
Figure 2.13: Calculated space-charge density Q_{sc} in thermal equilibrium as a function of the doping concentration N_{dop} for the onset of inversion or strong inversion, respectively. The onset of inversion occurs at $\Psi_s = \Psi_B$ while that of strong inversion is at $\Psi_s = 2\Psi_B$. Ψ_B is the potential difference between the Fermi level and the intrinsic level. For p-Si the space charge is negative while for n-Si it is positive. Assumptions: $T = 300$ K, $n_i = 10^{10}$ cm^{-3}.

2.4.2.2   Calculation of the Quasi-Fermi Levels

In the preceding section it was assumed that the quasi-Fermi levels are flat throughout the sample. This assumption holds if the carrier diffusion length is large compared with the width of the space-charge region and if no recombination takes place at the surface, i.e., if there is no significant carrier flow towards the surface. Actually, to a good approximation, the quasi-Fermi levels are constant throughout the space-charge region, even in the presence of a weak surface recombination as will be investigated in Section 2.4.5 [41, 40]. The quasi-Fermi levels (ϕ_n for electrons and ϕ_p for holes) can be calculated using the condition of charge neutrality in the bulk (Eq. 2.5) and the definitions of the quasi-Fermi level in Eq. 2.41. Using $V_{oc} \equiv \phi_p - \phi_n$ we obtain

$$\phi_n = \phi_p - V_{oc} \quad \text{and} \tag{2.54}$$

$$\phi_p = \frac{1}{\beta} \ln \left[\frac{(p_0 - n_0) + \sqrt{(p_0 - n_0)^2 + 4n_i^2 e^{\beta V_{oc}}}}{2n_i} \right]. \tag{2.55}$$

With

$$pn = n_i^2 e^{\beta V_{oc}}, \tag{2.56}$$

$n = n_0 + \Delta n$ and $p = p_0 + \Delta n$, the following expression is obtained for Δn as a function of V_{oc}:

$$\Delta n = \sqrt{n_{\mathrm{i}}^2(e^{\beta V_{\mathrm{oc}}} - 1) + \left(\frac{p_0 + n_0}{2}\right)^2} - \frac{p_0 + n_0}{2}. \tag{2.57}$$

This function is plotted in Fig. 2.14. Under low-injection conditions, i.e., $p_0 + n_0 \approx N_{\mathrm{dop}}$, $p \approx N_{\mathrm{dop}}$ and $n = n_0 + \Delta n_{\mathrm{li}}$ for p-type semiconductors (or $n \approx N_{\mathrm{dop}}$ and $p = p_0 + \Delta n_{\mathrm{li}}$ for n-type semiconductors) Eq. 2.56 or, equivalently, Eq. 2.57 simplifies to

$$\Delta n_{\mathrm{li}} = \frac{n_{\mathrm{i}}^2}{N_{\mathrm{dop}}}\left(e^{\beta V_{\mathrm{oc}}} - 1\right). \tag{2.58}$$
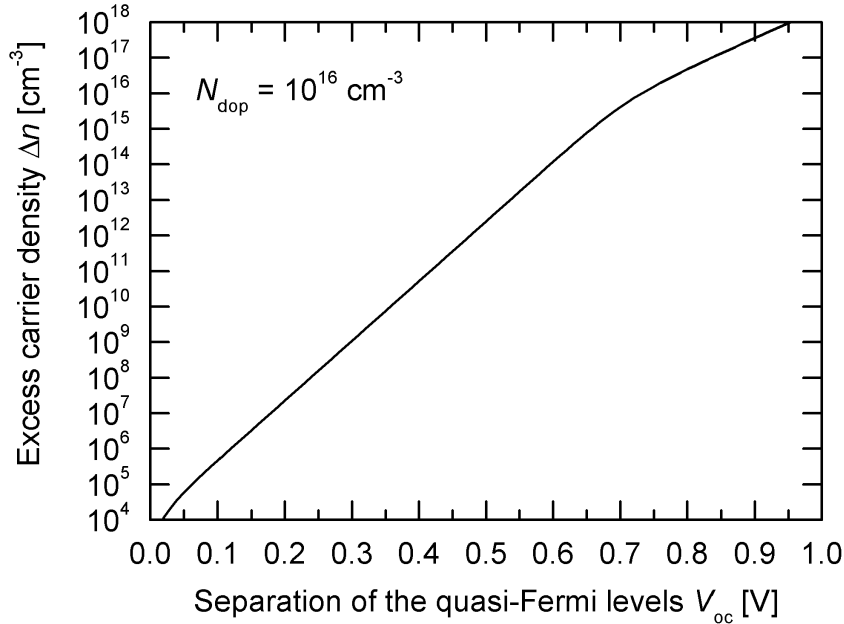

Figure 2.14: Calculated dependence of the excess carrier density Δn on the separation of quasi-Fermi levels V_{oc} using Eq. 2.57. Assumptions: $N_{\mathrm{dop}} = 10^{16}\,\mathrm{cm}^{-3}$, $n_{\mathrm{i}} = 10^{10}\,\mathrm{cm}^{-3}$, $T = 300\,\mathrm{K}$ and Boltzmann statistics.

2.4.2.3   Calculation of the Surface Potential

As has been mentioned in Section 2.4.2.1, the surface potential Ψ_{s} is an essential parameter for the calculation of Q_{sc} using Eq. 2.50. For metal-semiconductor contacts, Ψ_{s} is given in the simplest approximation by the work function difference $q\Delta\phi_{\mathrm{ms}}$ between the work function of the metal $W_{\mathrm{m}} = q\phi_{\mathrm{m}}$ and that of the semiconductor $W_{\mathrm{s}} = q\phi_{\mathrm{s}}$:

$$-\Psi_{\mathrm{s}} = \Delta\phi_{\mathrm{ms}} \equiv \phi_{\mathrm{m}} - \phi_{\mathrm{s}} \tag{2.59}$$
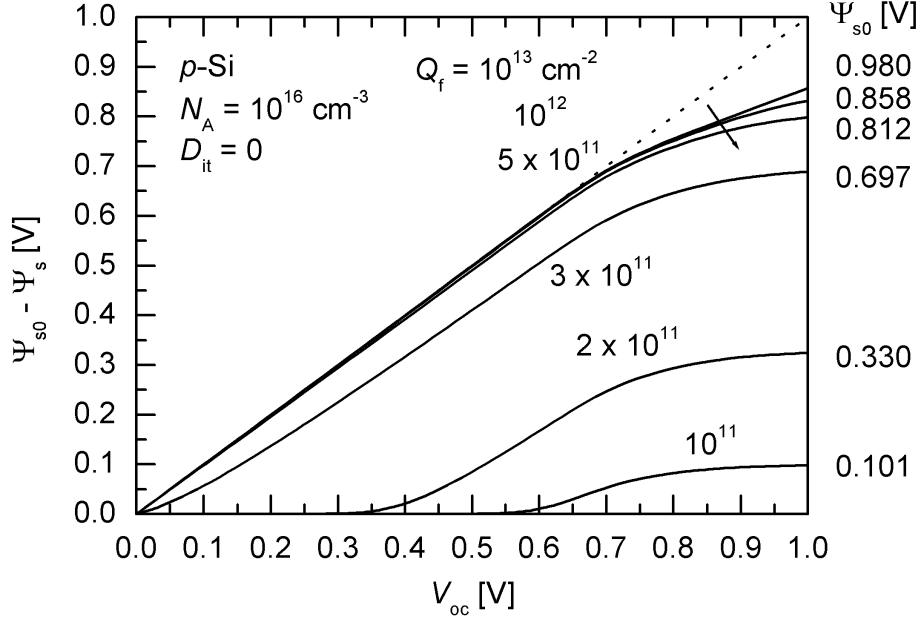
Figure 2.15: Calculated dependence of $\Psi_{s0} - \Psi_s$ as a function of the separation of the quasi-Fermi levels V_{oc} and the fixed charge density Q_f. The dotted line shows the bisector of an angle. Assumptions: p-Si with $N_A = 10^{16}\,\text{cm}^{-3}$, $D_{it} = 0$, $T = 300\,\text{K}$.

as is illustrated in Fig. 2.10. In semiconductors it is useful to define a second quantity, the electron affinity $q\chi$. $q\chi$ is the work required to remove an electron from the bottom edge of the conduction band to the vacuum level [31]. Hence, the work function of a semiconductor is

$$\phi_s = \chi + \frac{(E_C - E_F)}{q}, \tag{2.60}$$

where E_C and E_F denote the edge of the conduction band and the Fermi energy level, respectively. Realistically, at the metal-semiconductor interface, the large number of interface states determines the surface potential. Experimental evidence has shown that Ψ_s is virtually independent of the metal and the conductivity of the semiconductor. This fact complicates the determination of the surface potential. An analytical calculation can only be done for simplified distributions of surface states and limiting cases [31]. Additionally, the shape of the potential barrier is influenced by mirror charges in the metal [31].

If the semiconductor surface is strongly inverted and surface states are neglected, an approximate expression for Ψ_s in thermal equilibrium and low-injection can be derived analytically. Assuming a p-type semiconductor, strong inversion at the surface and low-injection conditions, the total fixed charge is compensated by mobile electrons in the inversion layer of the semiconductor. Considering this, $\rho(z)$ can be approximated by $-qn(z)$ and, hence,
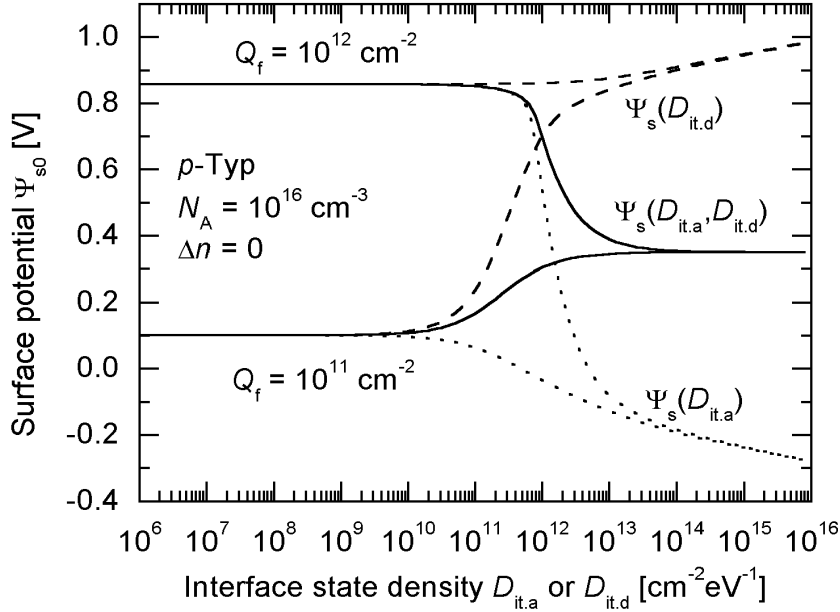
Figure 2.16: Calculated surface potential for p-type silicon with a doping concentration of $N_A = 10^{16}\,\text{cm}^2$ and different Q_f values as a function of the interface state density D_{it}. $\Psi_s(D_{it.d})$ ($\Psi_s(D_{it.a})$) denotes the curves that have been calculated assuming only donor-like (acceptor-like) interface states (dashed and dotted lines, respectively). $\Psi_s(D_{it.a}, D_{it.d})$ denotes those curves calculated with both types of interface states present (solid lines). Assumptions: $T = 300$ K, thermal equilibrium.

Q_{sc} in Eq. 2.50 by

$$-qQ_f \approx qQ_{sc} \approx qQ_{sc.n} \approx -\frac{\epsilon_s}{\beta\lambda_D}\sqrt{\frac{2n_b e^{\beta\Psi_s}}{p_b}} = -\sqrt{\frac{2\epsilon_s q n_b e^{\beta\Psi_s}}{\beta}}. \tag{2.61}$$

Solving Eq. 2.61 for Ψ_s using Eq. 2.58 we get

$$\Psi_s = \Psi_{s0} - V_{oc}. \tag{2.62}$$

where Ψ_{s0} denotes the surface potential in thermal equilibrium and is given by

$$\Psi_{s0} = \frac{1}{\beta}\ln\frac{\beta q Q_f^2 p_0}{2\epsilon_s n_i^2} = \frac{1}{\beta}\ln\frac{Q_f^2}{2n_i^2\lambda_{D0}^2}. \tag{2.63}$$

λ_{D0} is the extrinsic Debye length in thermal equilibrium (Eq. 2.47). Eq. 2.62 can be compared with the potential difference between the conduction bands on either side of a p-n junction. In thermal equilibrium this potential difference is known as the diffusion potential V_{bi}. It is reduced by carrier injection to the potential difference V by an applied forward bias V_a or by illumination such that the following relation holds

$$V = V_{bi} - V_a. \tag{2.64}$$

Neglecting any recombination in the space-charge region, V_a equals the separation of the quasi-Fermi levels at the edge of the SCR. For induced junctions, the SCR extends to the surface. Hence, the corresponding quantities for induced junctions are $\Psi_{s0} = V_{bi}$, $\Psi_s = V$ and $V_{oc} = V_a$. The important conclusion from these consideration is that the equations derived for diffused junctions are equally valid for induced junctions if strong inversion and low-injection conditions prevail. Hence, by replacing the quantities relevant for an induced junction by their corresponding quantities for diffused junctions, the well-known equations can be used. The excess carrier density at the surface is thus given by

$$\Delta p_s = p_{s0} \left(e^{\beta V_{oc}} - 1 \right), \tag{2.65}$$

with $p_{s0} = p_{b0} e^{-\beta \Psi_{s0}}$. In complete analogy to diffused junctions, the current flowing towards the surface is

$$J_s = J_{0E}(e^{\beta V_{oc}} - 1). \tag{2.66}$$

Apart from the two limiting cases, for which the surface potential could be calculated analytically (Eq. 2.59 and Eq. 2.62), in general, a numerical calculation has to be carried out to determine Ψ_s. In particular, for silicon surfaces passivated using SiO_2 or SiN_x films, numerical calculations are necessary in order to include the specific distributions of interface states and the characteristic fixed charge density within the films.

A numerical calculation of Ψ_s without any simplifying assumptions regarding the distribution of interface states is possible using the so-called extended SRH formalism. The formalism developed by Grove and Fitzgerald [42, 43] has been improved by Girisch *et al.* [14]. The Girisch formalism includes work-function differences, surfaces charges and external potentials. Still, it is a quasi-exact solution with the assumption of flat quasi-Fermi levels extending to the surface, which is equivalent to moderate SRVs. Fig. 2.11 shows a schematic of the bend-bending problem to be solved for the case of an MIS structure with a p-type silicon wafer. The upper sketch illustrates the charges involved while the lower one shows the energy diagram. The charge density in the space-charge region at the silicon surface Q_{sc} is divided into that of ionised acceptors in the SCR $Q_{sc.f}$ and that of mobile electrons in the conduction band $Q_{sc.n}$. $Q_{sc.p}$ being relevant for accumulation and depletion conditions, is not shown in the figure. Q_{it} is the charge density located in interface states, Q_f that of fixed charges within the insulating film and Q_G that in an optional gate electrode (each measured in elementary charges per cm^2). The starting point is the charge neutrality given in Eq. 2.36 that holds for any operating conditions. Q_{sc} is given by Eq. 2.50 while Q_f is assumed to be constant. Q_{it} depends on the energetic distribution of the donor- and acceptor-like interface states ($D_{it.d}$ and $D_{it.a}$ in $cm^{-2}eV^{-1}$). The interface states are neutral if they are not occupied. An acceptor-like (donor-like) state carries a negative (positive) elementary charge if it is occupied by an electron (hole). The electron-occupancy function f_a and the hole-occupancy function f_d determine the occupancy state of the traps. Hence, the charge density located in interface states is:

$$Q_{it} = \int_{E_V}^{E_C} \left\{ -D_{it.a}(E) f_a(E) + D_{it.d}(E) f_d(E) \right\} dE. \tag{2.67}$$

In case of steady-state, the net rate of capture (i.e. capture minus emisson) has to be zero for any interface trap. This leads to the following expressions for the functions f_a and f_d [24]:

$$
\begin{aligned}
f_a(E) &= \frac{\sigma_n n + \sigma_p p_1}{\sigma_n(n + n_1) + \sigma_p(p + p_1)} \quad \text{and} \\
f_d(E) &= \frac{\sigma_n n_1 + \sigma_p p}{\sigma_n(n + n_1) + \sigma_p(p + p_1)}.
\end{aligned} \tag{2.68}
$$

Using Faraday's law of induction, the remaining image charge in the gate electrode Q_G can be derived [14, 38, 44]. According to Faraday's law, the sum of the potentials is zero along a closed path, i.e., in the present case:

$$
\int_{-\infty}^{0} \mathcal{E} dz + \Psi_s - V_G + \Delta\phi_{ms} = 0, \tag{2.69}
$$

with V_G being the applied gate voltage. Note the Eq. 2.69 simplifies to Eq. 2.59 if the insulating layer is omitted and $V_G = 0$. Using Gauß's law the electric field is

$$
\mathcal{E}(z) = \int_{-\infty}^{z} \frac{\rho(\tilde{z})}{\epsilon(\tilde{z})} d\tilde{z}, \tag{2.70}
$$

where $\rho(z)$ denotes the charge per unit volume in the gate electrode and the insulator. Assuming the following distribution for $\rho(z)$:

$$
\rho(z) = qQ_G\,\delta(z + d_{iG}) + \frac{qQ_f}{d_{if}}\,\theta(z + d_{if}) \quad \text{for } z < 0, \tag{2.71}
$$

where δ denotes Dirac's delta distribution, θ the Heaviside function and d_{iG}, d_{if} are defined in Fig. 2.11, we find for $\mathcal{E}$

$$
\begin{aligned}
\mathcal{E} &= \frac{qQ_G}{\epsilon_{iG}} & \text{for } -d_{iG} < z < -d_{if} \\
\mathcal{E} &= \frac{qQ_G}{\epsilon_{if}} + \frac{qQ_f}{d_{if}\epsilon_{if}}(z + d_{if}) & \text{for } -d_{if} < z < 0.
\end{aligned} \tag{2.72}
$$

Note that we have generalised the consideration to include the case of two different insulating films having different dielectric constants. The first insulating film extends from $z = -d_{iG}$ to $-d_{if}$ having a dielectric constant of ϵ_{iG}, while the second film extends from $z = -d_{if}$ to 0, having a dielectric constant of ϵ_{if}. Integrating $\mathcal{E}$ we find for the potential difference across the insulating film:

$$
\begin{aligned}
\int_{-d_{iG}}^{0} \mathcal{E}(z)\,dz &= \int_{-d_{iG}}^{-d_{if}} \frac{qQ_G}{\epsilon_{iG}}\,dz + \int_{-d_{if}}^{0} \left\{ \frac{qQ_G}{\epsilon_{if}} + \frac{qQ_f}{d_{if}\epsilon_{if}}(z + d_{if}) \right\} dz \\
&= \frac{qQ_G}{\epsilon_{iG}}(d_{iG} - d_{if}) + \frac{qQ_G}{\epsilon_{if}}d_{if} + \frac{qQ_f}{\epsilon_{if}}\frac{d_{if}}{2} \\
&= \frac{qQ_G}{C_i} + \frac{qQ_f}{\epsilon_{if}}\frac{d_{if}}{2},
\end{aligned} \tag{2.73}
$$

with the insulator capacitance

$$C_\text{i} = \frac{\epsilon_\text{if}\epsilon_\text{iG}}{d_\text{if}\epsilon_\text{iG} + (d_\text{iG} - d_\text{if})\epsilon_\text{if}}. \tag{2.74}$$

Inserting Eq. 2.73 into Eq. 2.69 yields

$$Q_\text{G} = C_\text{i}\left\{-\frac{Q_\text{f}d_\text{if}}{2\epsilon_\text{iG}} + \frac{1}{q}(V_\text{G} - \Psi_\text{s} - \Delta\phi_\text{ms})\right\}. \tag{2.75}$$

Note that the factor of 2 is omitted in Eq. 2.73 and Eq. 2.75 if a δ-distribution at $z = -d_\text{if}$ is assumed instead of a constant distribution.

Although we have derived expressions for the charges involved, the surface potential as a function of Δn (or V_oc) is still unknown. Note that we can easily switch between V_oc and Δn using Eq. 2.57. However, depending on the context, the usage of one of these two quantities may be more common. The calculation of Ψ_s is now determined via a method proposed by Girisch *et al.* [14]. First, the quasi-Fermi levels are calculated using Eq. 2.54 and Eq. 2.55. The next step is an iterative procedure to determine Ψ_s. Assuming a starting value for Ψ_s and using Eq. 2.50, 2.67, 2.75, 2.68, the charge densities Q_sc, Q_it and Q_G are calculated. Subsequently, Ψ_s is varied until the sum of the charges $Q_\text{f} + Q_\text{sc} + Q_\text{it} + Q_\text{G}$ is below a certain limit. The limit determines the accuracy for the determination of Ψ_s. We use the algorithm *Golden* from the Numerical Recipes book by Press *et al.* to accomplish the iteration [45].

The results of a quantitative investigation of the relation between Ψ_s and V_oc are plotted in Fig. 2.15. For small fixed charge densities, causing only depletion or weak inversion conditions at the surface, and small values of V_oc, the band-bending is independent of the injection level. In contrast, for strong inversion conditions, the relation given in Eq. 2.62 is found.

Next, we consider the surface potential as a function of the interface state density in thermal equilibrium. For high interface state densities, the charge that may be stored in the interface states can contribute considerably to the total charge. Depending on the type of interface states (acceptor- or donor-like), the charge density in the occupied states is either negative or positive. Fig. 2.16 shows the calculated surface potential as a function of interface state density for the presence of one of the interface state types alone and for both types. It is obvious that for low interface state densities, the surface potential is independent of D_it, whereas for high densities, Ψ_s is independent of Q_f. The transition region from the first to the latter condition occurs very roughly at $D_\text{it} \times E_\text{g} \approx Q_\text{f}$. Acceptor-like interface states either carry a negative elementary charge or they are neutral, depending on their occupancy. For increasing interface state density, the negative interface charge compensates or overcompensates Q_f that is assumed to be positive in the given example. Hence, the bands bend upwards, i.e., Ψ_s decreases, as can be seen from the $\Psi_\text{s}(D_\text{it.a})$ curve in Fig. 2.16. The bands bend to the opposite direction if only donor-like interface states are assumed ($\Psi_\text{s}(D_\text{it.d})$ curve in Fig. 2.16). If both types of interface states with the same density are assumed, the band-bending at the surface approximates the intrinsic case, i.e., $q(\Psi_\text{s} + \Psi_\text{B}) = E_\text{i} - E_\text{V}$.

2.4.2.4   Surface Recombination Including Band-Bending

With the help of Ψ_s, the electron and hole densities at the surface, n_s and p_s, respectively, can be calculated using Eq. 2.42. Then, the surface recombination rate and the surface recombination velocity at the actual surface S_{it} are obtained using Eq. 2.31 and Eq. 2.7, respectively. Note that S_{it} has been identified with S_{eff} in the past, thereby implicitly neglecting any recombination in the space-charge region (Section 2.2).

S_{it} as a function of Q_f is shown in Fig. 2.17 for different interface parameters. For the calculations, p-type material with a doping concentration of 10^{16} cm^{-3}, an injection level of $\Delta n = 10^{14}$ cm^{-3} and energy-independent interface parameters (interface state density D_{it}, electron (hole) capture cross section σ_n (σ_p)) were assumed. The pronounced peak in the SRV occurs where the electron equals the hole concentration at the surface, each multiplied by its capture cross section:

$$n_s \sigma_n = p_s \sigma_p. \tag{2.76}$$

For equal capture cross sections, this peak appears at a small positive charge density of $Q_f = 8 \times 10^{10}$ cm^{-2} since p-type material is assumed. Under accumulation and inversion conditions, the SRV is limited by the capture cross section of the less available carrier type. An increase in D_{it} increases the SRV. If the electron capture cross section exceeds the hole capture cross section (dotted curve) the peak is shifted to lower or even negative charge densities. It should be emphasised that even a difference in the capture cross sections by three orders of magnitude results in a position of the peak not below $Q_f = -7 \times 10^{10}$ cm^{-2}.

Fig. 2.18 shows the calculated impact of fixed positive charges on the $S_{it}(\Delta n)$ dependence of a p-type silicon wafer with $N_A = 10^{16}$ cm^{-3}. The behaviour of the $Q_f = 0$ curve has already been discussed in Section 2.4.1. In this case (flatband conditions) and under low-injection conditions, the SRV is limited by the minority carrier density (i.e., the electrons). Under depletion conditions at the surface (curves for $Q_f = 0.5 - 1 \times 10^{11}$ cm^{-2}), the recombination under low-injection conditions is enhanced due to the higher availability of electrons. If the assumed fixed charge density is further increased, the hole density at the surface is further reduced, while that of the electrons is increased, resulting in an inversion layer at the surface. The stronger the inversion condition, the more is the recombination rate reduced under low-injection conditions since it is limited by the availability of holes. All curves approach the same value towards high-injection conditions. This can be explained by the decreasing band-bending with higher injection level regardless of the fixed charge density. Hence, the influence of Q_f decreases and all curves approach the value calculated for $Q_f = 0$.

As can be seen from Fig. 2.18, the curves calculated for fixed charge densities causing strong inversion at the surface approach a constant value towards low injection. Again, this can be derived with using Eq. 2.61 [44, 46]. If recombination in the space-charge region is completely neglected, the current density flowing towards the surface is given by the expression

$$J_s = q \Delta n_b S_{it} = q \Delta p_s S. \tag{2.77}$$

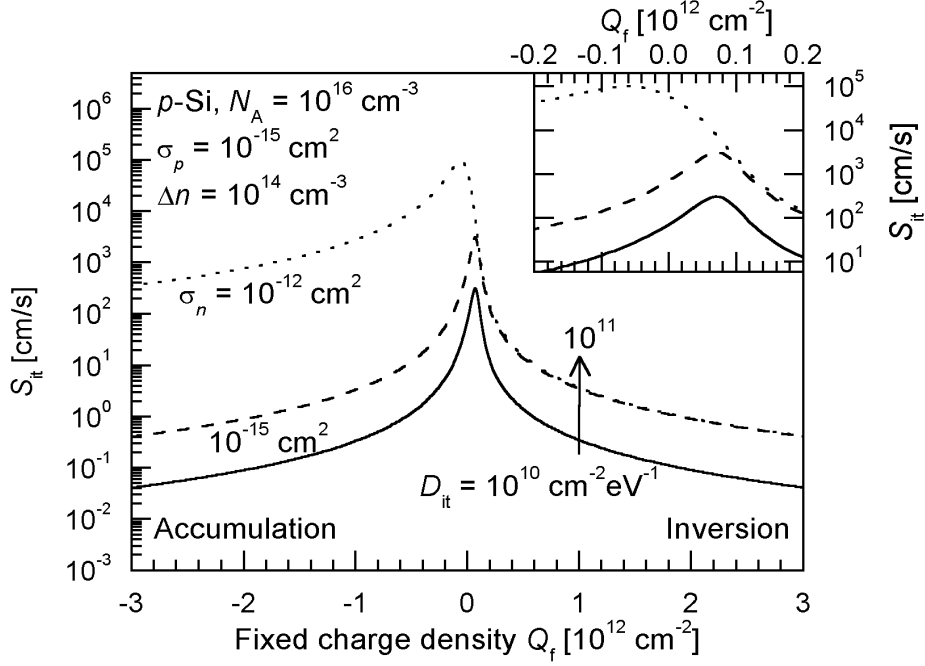The hole density at the surface is given by Eq. 2.65. Using Eq. 2.62 and inserting Eq. 2.61

Figure 2.17: Calculated SRV S_{it} as a function of Q_f for p-Si. Assumptions: $N_A = 10^{16}\,\mathrm{cm}^{-3}$, $\Delta n = 10^{14}\,\mathrm{cm}^{-3}$, $T = 300\,\mathrm{K}$ and energy-independent recombination parameters: $\sigma_p = 10^{-15}\,\mathrm{cm}^2$, $D_{it} = 10^{10}\,\mathrm{cm}^{-2}\mathrm{eV}^{-1}$ (solid line) and $10^{11}\,\mathrm{cm}^{-2}\mathrm{eV}^{-1}$ (dashed and dotted line), $\sigma_n = 10^{-15}\,\mathrm{cm}^2$ (solid and dashed line) and $10^{-12}\,\mathrm{cm}^2$ (dotted line). The inset shows a magnification for small Q_f values.

into Eq. 2.77, S_{it} is obtained as

$$S_{it} = \frac{2\epsilon_s}{q\beta Q_f^2} p_0 S \frac{n_b}{\Delta n_b} \approx \frac{2\epsilon_s}{q\beta Q_f^2} p_0 S. \tag{2.78}$$

Hence, in the case of strong inversion, the SRV calculated using the extended SRH formalism is independent of the injection level and depends only on the base doping concentration, the interface recombination parameters, the fixed charge density and the temperature. It should be emphasised that the condition $\Psi_s = \Psi_{s0} - V_{oc}$ and, hence, Eq. 2.78 holds only for low-injection conditions (Fig 2.18). However, it can be extended to intermediate injection regimes using Eq. 2.66. Inserting the condition $np = n_i^2 e^{\beta V_{oc}}$ and Eq. 2.77 into Eq. 2.66 we obtain

$$S_{it} = J_{0E} \frac{(N_A + \Delta n_b)}{q n_i^2}. \tag{2.79}$$

The injection range for which the approximate solution of Eq. 2.79 is valid will be examined in the following. Using Eq. 2.34, the maximum SRV can be calculated. The result is used to calculate the constant low-injection value of S_{it} according to Eq. 2.78. Using Eq. 2.79 and $\Delta n_b \ll N_A$, J_{0E} can be calculated and then, again using Eq. 2.79, S_{it} in dependence on the injection level is determined. Assuming the same parameter values as for the calculated curves shown in Fig. 2.18 ($Q_f = 10^{12}\,\mathrm{cm}^{-2}$), we obtain $S_{li.max} = 112\,\mathrm{cm/s}$, $S_{it} = 0.38\,\mathrm{cm/s}$
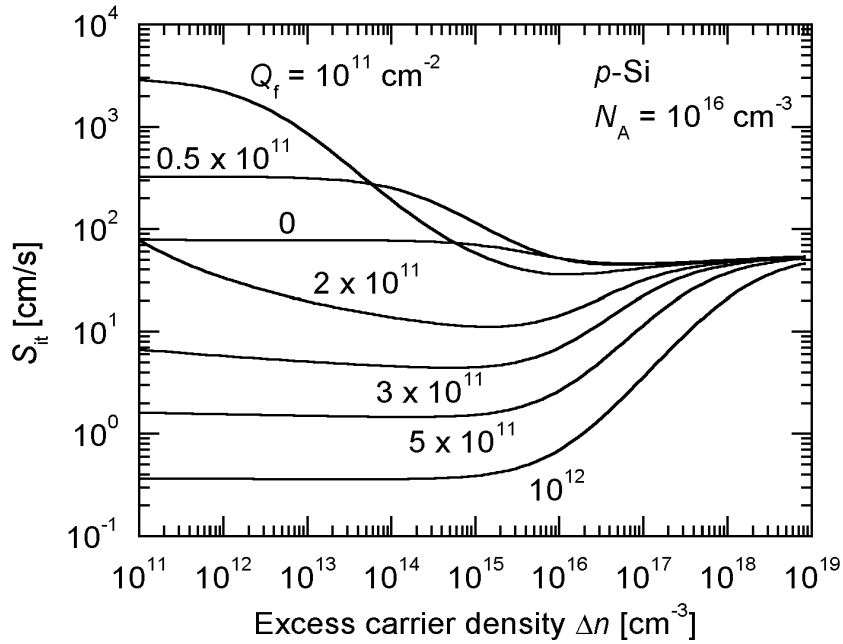
Figure 2.18: Calculated SRV S_{it} as a function of the excess carrier density Δn for p-Si for different values of the fixed positive charge density Q_{f}. Assumptions: $N_{\text{A}} = 10^{16}\,\text{cm}^{-3}$, $T = 300\,\text{K}$ and energy-independent recombination parameters $D_{\text{it}} = 10^{10}\,\text{eV}^{-1}\text{cm}^{-2}$ and $\sigma_n = \sigma_p = 10^{-15}\,\text{cm}^2$.

and $J_{0\text{E}} = 0.61\,\text{fA}$. Fig. 2.19 shows the SRV S_{it} as a function of the injection level, calculated using the extended SRH formalism and the approximate solution given above. Both curves match perfectly in the low and intermediate injection regime. This is particular noteworthy, as $S_{\text{li.max}}$ was used for the approximate solution. Unlike the curve calculated with the extended SRH formalism, the approximate curve does not saturate towards high injection. This is due to the fact that the band-bending decreases with increasing injection level, i.e., the 'emitter' behaviour vanishes. This is accounted for by the extended SRH formalism but not by the simplified approximation.

The same equation as Eq. 2.79 is obtained if recombination in a diffused emitter is investigated [47, 48]. However, it should be emphasised that in the case of induced emitters the applicability range of Eq. 2.79 is more restricted. As has been mentioned above, Eq. 2.79 does not hold for highly injected samples. Furthermore, in the case of diffused emitters, the equation holds also for the transient case since the quasi-static emitter approximation holds for diffused samples [49]. This approximation holds if the lifetime in the emitter is low compared with that in the bulk, which is generally true for diffused emitters due to the high Auger-recombination rate within highly doped emitters. In this case, the injection level varies a lot faster in the emitter than in the base and, hence, the transport equations in the base can be solved using steady-state boundary conditions. In the case of induced emitters, the lifetime in the emitter region can be comparable to that in the bulk and, hence, the
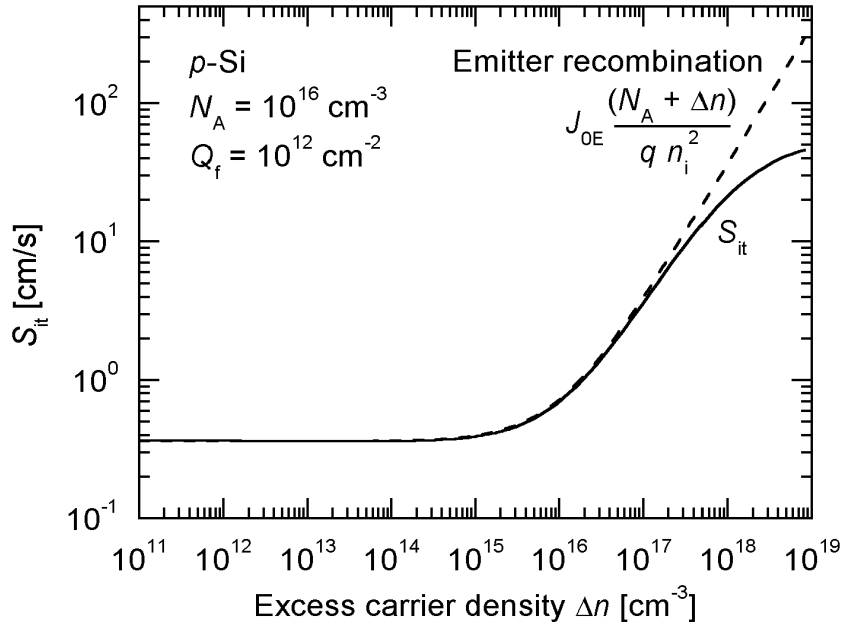
Figure 2.19: Calculated SRV S_{it} as a function of the excess carrier density Δn for a p-Si sample. The solid curve was calculated using the extended SRH-Formalism (Fig. 2.18), while the dashed curve was calculated using Eq. 2.79. The low-level injection values of both curves were adjusted resulting in $J_{0\mathrm{E}} = 5.768 \times 10^{-16}\,\mathrm{A/cm^2}$. Assumptions: $N_\mathrm{A} = 10^{16}\,\mathrm{cm^{-3}}$, $T = 300\,\mathrm{K}$ and energy-independent recombination parameters $D_{\mathrm{it}} = 10^{10}\,\mathrm{eV^{-1}cm^{-2}}$, $\sigma_n = \sigma_p = 10^{-15}\,\mathrm{cm^2}$.

quasi-static emitter approximation may not hold in general.

2.4.3   Recombination in the Space-Charge Region

As will be shown in Chapter 4, the recombination in the depletion region at the surface may have a significant influence on the effective SRV [50]. This section deals with the theoretical foundations to quantify this influence. For p-n junction diodes, the recombination rate in the space charge region is often taken to be proportional to $e^{\beta V/m}$, where m is the ideality factor of the depletion region recombination. Using some simplifying assumptions $m = 2$ is often used [31]. However, McIntosh has pointed out that m is generally less than 2 if the dependence of the recombination rate with position is taken into account [51]. Hence, we will calculate the recombination in the SCR considering the dependence of the recombination rate U on the position and will discuss whether the approximation using a single ideality factor is appropriate.

In order to calculate the depletion region recombination, it is assumed that the dominant source of recombination is due to SRH recombination. The recombination rate is given by Eq. 2.26 with the extension of position-dependent quantities $n(z)$, $p(z)$, $\tau_{n0}(z)$, $\tau_{p0}(z)$, $n_1(z)$
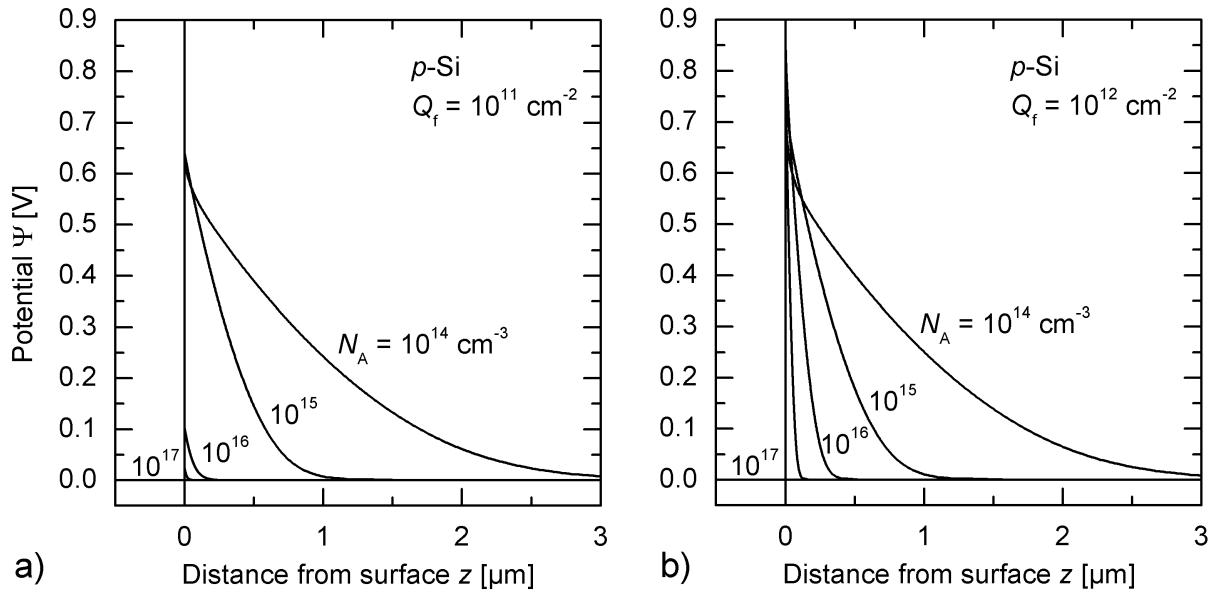
Figure 2.20: Calculated spatial dependence of the potential $\Psi(z)$ at the surface of a p-type silicon wafer for different base doping concentrations N_A assuming a fixed positive charge density of a) $Q_f = 10^{11}\,\text{cm}^{-2}$ and b) $Q_f = 10^{12}\,\text{cm}^{-2}$. Assumptions: thermal equilibrium (i.e., $\Delta n = 0$) and no interface states ($D_{it} = 0$).

and $p_1(z)$. For the sake of simplicity, we assume that the capture time constants as well as the factors n_1 and p_1 are constant throughout the SCR. Hence, for the calculation of the recombination rate, the carrier concentrations (or alternatively, the band-bending, cf. Eq. 2.42) as a function of the position need to be known. The densities of mobile electrons and holes vary across a junction and change such that the carriers are the majority on one side of the junction and the minority on the other side. Hence, the electron equals the hole density at some point within the SCR. The recombination rate will peak at this point, assuming equal capture time constants.

The band-bending will be calculated in the next section, while the recombination rate will be calculated thereafter.

2.4.3.1   Position-dependent potential

In Section 2.4.2.1 an expression for the spatial derivative of the potential was given (Eq. 2.49). Integrating this expression using $z = 0$ for $\Psi = \Psi_s$, we obtain the functional relationship between the potential and the position [15, 42, 29]

$$z = \beta \lambda_D \int_{\Psi_s}^{\Psi} \mp \frac{1}{F} d\tilde{\Psi}. \qquad (2.80)$$

The integration in Eq. 2.80 has to be done numerically. In doing so, one has to take care that no change in sign of the variable $\tilde{\Psi}$ occurs, since $\Psi = 0$ represents either an upper
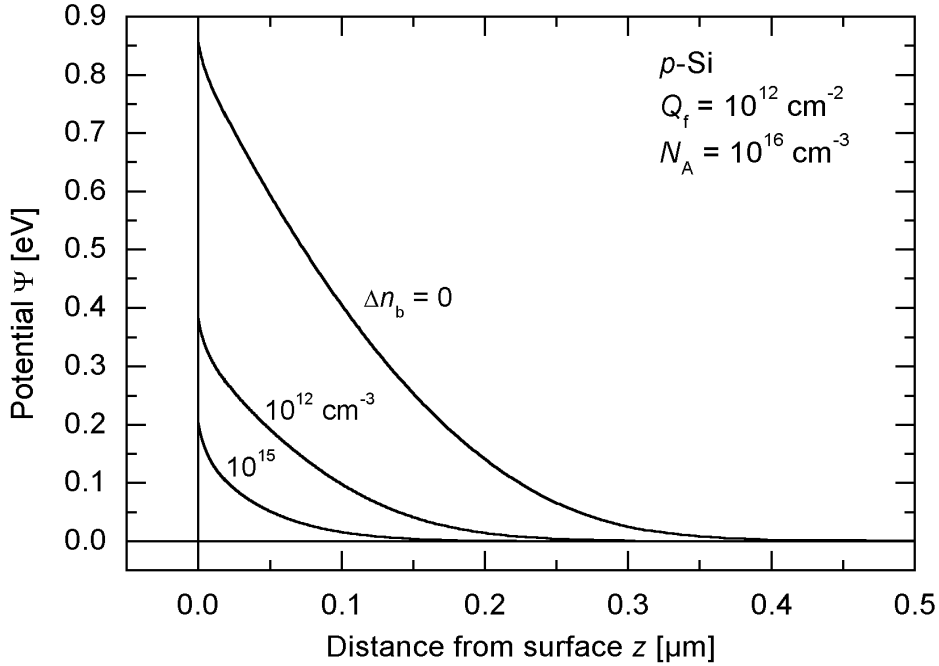
Figure 2.21: Calculated band-bending as a function of the position for different injection levels in the bulk Δn_b or, equivalently, for different illumination intensities. Assumptions: p-type silicon, $N_A = 10^{16}\,\mathrm{cm}^{-3}$ and $Q_f = 10^{12}\,\mathrm{cm}^{-2}$.

or a lower limit. With the knowledge of the surface potential, we will discuss the exact relationship given in Eq. 2.80 (Fig. 2.20 and 2.21). Please refer to the books of Many *et al.* [15] or Mönch [29] for analytical expressions of Eq. 2.80 that can be obtained in certain limiting cases. If the calculation of the integral is done across the whole SCR, i.e., from Ψ_s to 0, we obtain the width of the space-charge region. It should be noted that the shape of the potential barrier $\Psi(z)$ depends only on the surface potential and the quasi-Fermi levels in the bulk.

Fig. 2.20 (a) and (b) illustrate the shape of the potential for different bulk doping densities and fixed charge densities. As can be seen, the width of the SCR d_{sc} depends only weakly on Q_f but strongly on N_A. In contrast, the surface band-bending is a strong function of Q_f as long as no inversion is induced by the fixed charge (cf. Fig. 2.12). This is additionally demonstrated in Fig. 2.22, showing Ψ_s and d_{sc} as a function of N_A in the case of thermal equilibrium[3]. If the surface is inverted, Ψ_s is only a weak function of Q_f (Fig. 2.20). This is due to the high amount of charges that can be stored in inversion regions, i.e., the impact of Q_f on the potential shape of inverted surfaces extents only over a very small region at the surface.

The band-bending as a function of z and the injection level is shown in Fig. 2.21. As has

---

[3]For numerical reasons, the calculation of d_{sc} using the integral in Eq. 2.80 was performed only from Ψ_s to 0.001 V.
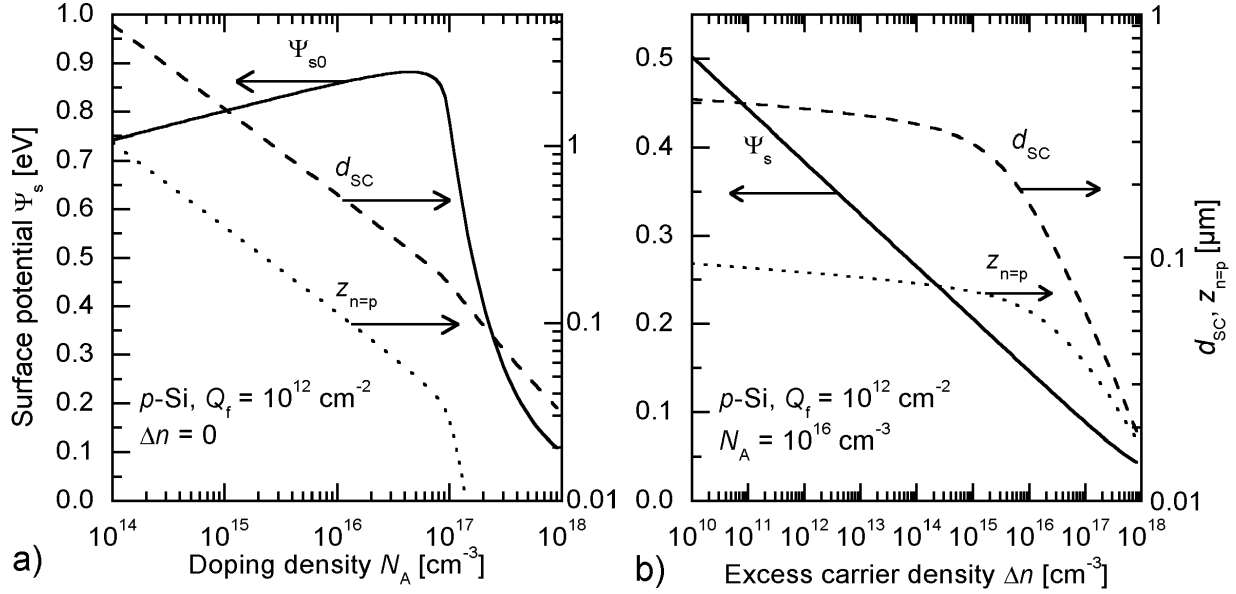
Figure 2.22: a) Calculated surface potential Ψ_s as a function of the doping density N_A for p-type Si in thermal equilibrium (left axis, solid line). Also shown are the calculated width of the space-charge region d_{sc} (right axis, dashed line) and the position where the electron and hole concentrations are equal $z_{n=p}$ (right axis, dotted line). b) Calculated Ψ_s (left axis, solid line), d_{sc} and $z_{n=p}$ (right axis, dashed and dotted line, respectively) as a function of the excess carrier density Δn for p-type Si. Assumption: $Q_f = 10^{12}\,\text{cm}^{-2}$. For numerical reasons, the calculation of d_{sc} using the integral in Eq. 2.80 was performed only from Ψ_s to $0.001\,\text{V}$.

been illustrated by the example shown in Fig. 2.9, the band-bending decreases for increasing injection levels. This is also demonstrated in Fig. 2.22 (b). d_{sc} varies only weakly with Δn under low-injection conditions. However, since the band-bending vanishes at very high injection levels, d_{sc} decreases strongly if Δn increases from intermediate to high injection conditions.

2.4.3.2   Calculation of the Recombination Rate within the Space-Charge Region

Fig. 2.23 shows the carrier densities $n(z)$ and $p(z)$ as a function of the position z for a p-type silicon wafer with an assumed fixed charge density of $Q_f = 10^{12}\,\text{cm}^{-2}$ on top of the surface. An injection level of $\Delta n_b = 10^{13}\,\text{cm}^{-3}$ is assumed in the bulk. Using Eq. 2.26 with capture time constants of $\tau_{n0} = \tau_{p0} = 1\,\text{ms}$ and a midgap defect state, $U_{SRH}(z)$ was calculated. $U_{SRH}(z)$ peaks at the position of equal electron and hole concentrations ($n(z) = p(z)$). In the bulk or at the surface, respectively, the recombination rate is limited by the availability of minority carriers. U_{SRH} is much smaller at the surface than in the bulk since $p_s \ll n_b$. Also shown in Fig. 2.23 is the net Auger recombination rate $U_A(z)$ which was calculated using the parameterisation of Altermatt *et al.* (Eq. 2.15, Eq. 2.17, Eq. 2.18, [22]). As can be seen, $U_A(z)$ peaks at the surface which can be attributed to the high electron density.
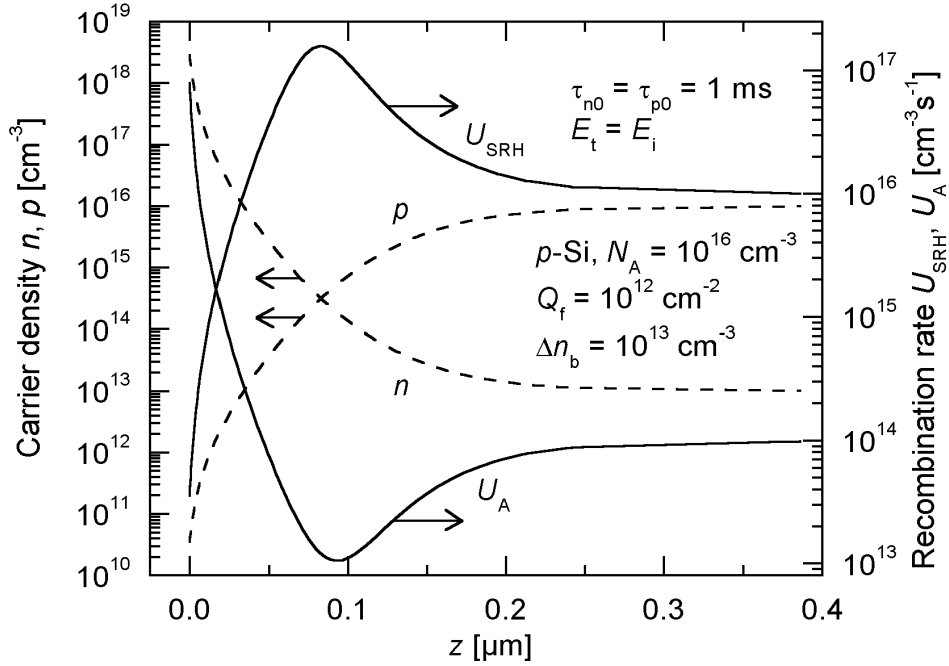
Figure 2.23: Calculated dependencies of the carrier densities n and p on the position z within the space charge region using the Eq. 2.80 and Eq. 2.42. Also shown are the net SRH recombination rate $U_{\mathrm{SRH}}(z)$ and the net Auger recombination rate $U_{\mathrm{A}}(z)$. Assumptions: p-type silicon, $N_{\mathrm{A}} = 10^{16}\,\mathrm{cm}^{-3}$, $Q_{\mathrm{f}} = 10^{12}\,\mathrm{cm}^{-2}$, $\Delta n_{\mathrm{b}} = 10^{13}\,\mathrm{cm}^{-3}$. U_{SRH} was calculated using Eq. 2.26 and the following parameters: $\tau_{n0} = \tau_{p0} = 1\,\mathrm{ms}$, $E_{\mathrm{t}} = E_{\mathrm{i}}$. For the calculation of U_{A}, the parameterisation of Altermatt *et al.* was used (Eq. 2.15, Eq. 2.17, Eq. 2.18, [22]).

The net Auger recombination rate is rather low besides the high recombination rate at the surface.

The SRV in the SCR S_{sc} is calculated using Eq. 2.9. Recombination centres located close to the position of the peak contribute most to S_{sc}. As long as the surface is inverted, this contribution is relatively independent of the surface potential, i.e., Q_{f}. Hence, it is expected that S_{sc} is only a weak function of Q_{f}. This is confirmed by calculated curves plotted in Fig. 2.24. As long as the surface is depleted, the carrier densities will not be equal at any position within the SCR, i.e., no peak in the recombination rate will occur and the SRV will be lower than that found for inverted surfaces. However, as soon as inversion conditions occur, either because of a higher Q_{f} value or because of a higher injection level, all curves in Fig. 2.24 follow the same trend. Assuming equal capture times, $\tau_{n0} = \tau_{p0}$, they can be factored out in Eq. 2.26 and the integration in Eq. 2.9 can be performed without considering the actual value of the capture time constants. Hence, the product $S_{\mathrm{sc}}\tau_{n0}$ is independent of τ_{n0}. This quantity is shown at the left axis in Fig. 2.24 while S_{sc} assuming $\tau_{n0} = 1\,\mathrm{ms}$ is shown at the right axis. Additionally shown in Fig. 2.24 is the SRV that is due to Auger recombination in the SCR $S_{\mathrm{sc.A}}$ (dashed line, right axis). $S_{\mathrm{sc.A}}$ was calculated by integration of $U_{\mathrm{A}}(z)$ shown in Fig. 2.23. For the assumed parameters, S_{sc} is a lot greater than $S_{\mathrm{sc.A}}$ in

the low injection regime justifying the above assumption that only recombination via defects is considered in the SCR. In the intermediate injection regime, both S_{sc} and $S_{sc.A}$ are very low and can be neglected in comparison with recombination at the actual surface. $S_{sc.A}$ is virtually constant in the low injection regime in contrast to the experimental finding, that the SRV decreases with increasing injection level in that regime (Section 4.5). Hence, $S_{sc.A}$ will be neglected throughout this work.

Also, the doping concentration has only a weak impact on S_{sc}, as can be seen from Fig. 2.25. Note that the capture times are assumed to be equal for this calculation which may be a severe simplification.
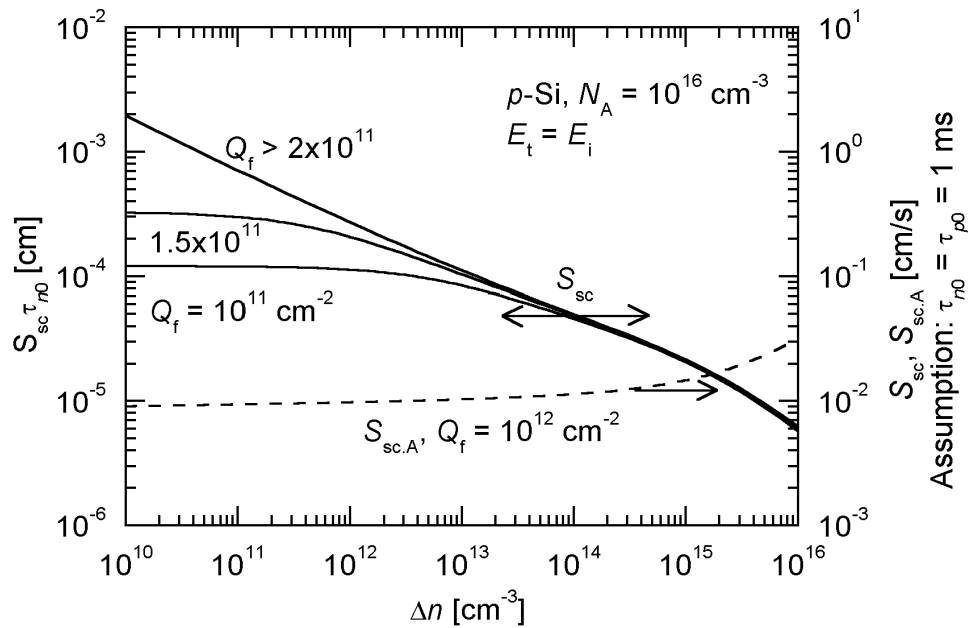

Figure 2.24: Calculated product $S_{sc}\tau_{n0}$ as a function of excess carrier density Δn and fixed charge density Q_f (solid lines, left axis). The right axis shows S_{sc} with assumed capture time constants $\tau_{n0} = \tau_{p0} = 1\,\text{ms}$ (same solid lines). Also shown is the SRV arising from Auger recombination in the space-charge region $S_{sc.A}$ (dashed line, right axis). Assumptions: p-type silicon, $N_A = 10^{16}\,\text{cm}^{-3}$, $E_t = E_i$ and $\tau_{n0} = \tau_{p0}$. For the calculation of $S_{sc.A}$, the parameterisation of Altermatt et $al.$ was used (Eq. 2.15, Eq. 2.17, Eq. 2.18, [22]).

A further difference of samples with different doping concentrations may arise from the position where the electron and hole densities are equal $z_{n=p}$. The lower the doping concentration the greater is $z_{n=p}$, as can be seen from Fig. 2.22 (a). If a region with additional damage at the surface is present, the position of the peak may fall into this region for highly but not for lightly doped material. Since the capture time constants will be lower in the damaged region, it will adversely affect only the recombination of highly doped material, assuming only in this case $z_{n=p}$ falls into the damaged region.

Fig. 2.26 shows the product $S_{sc}\tau_{n0}$ as a function of injection level for different defect
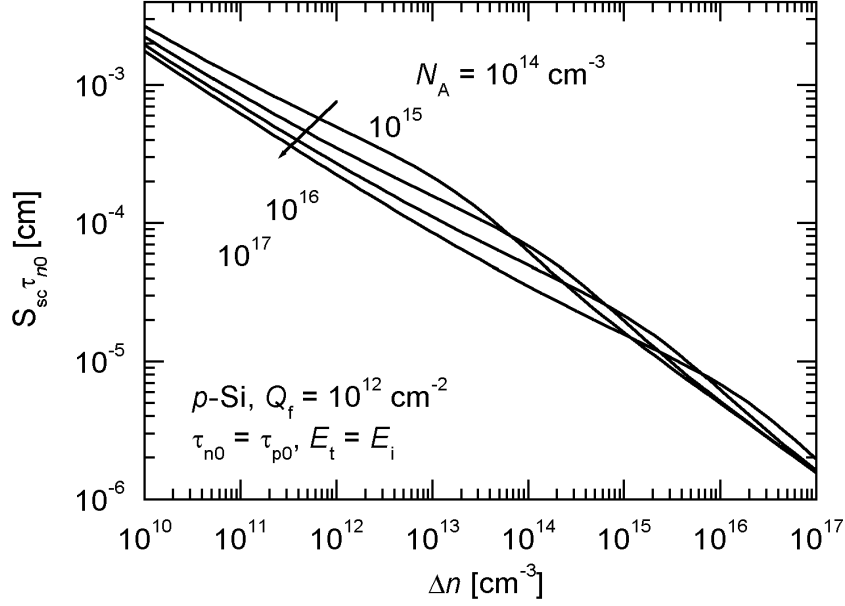
Figure 2.25: Calculated product $S_{sc}\tau_{n0}$ as a function of excess carrier density Δn and doping concentration N_A. Assumptions: p-type silicon, $Q_f = 10^{12}\,\mathrm{cm}^{-2}$, $\tau_{n0} = \tau_{p0}$.

energy levels in the SCR. As can be seen from Fig. 2.26, the slope of the $S_{sc}(\Delta n)$ curve under low-injection condition decreases for shallower defect levels.

The recombination in the SCR is often accounted for by a recombination current defined as

$$J_2 \equiv J_{02}\left(e^{\beta V_{oc}/m} - 1\right) = J_{02}\left[\left(\frac{\Delta n}{n_0} + 1\right)^{1/m} - 1\right], \tag{2.81}$$

where Eq. 2.58 was used for the transformation from the second to the third term. m is the so-called ideality factor and J_{02} the saturation current density. Using an analogous equation to Eq. 2.11, the corresponding SRV associated with the recombination in the SCR can be written as

$$S_{sc} = \frac{J_2}{q\Delta n} = \frac{J_{02}}{q\Delta n}\left[\left(\frac{\Delta n}{n_0} + 1\right)^{1/m} - 1\right]. \tag{2.82}$$

The $S_{sc}(\Delta n)$ data shown in Fig. 2.24 - 2.26 can now be used to calculate m and J_{02}. Neglecting the '+1' and '-1' in Eq. 2.82, the ideality factor is:

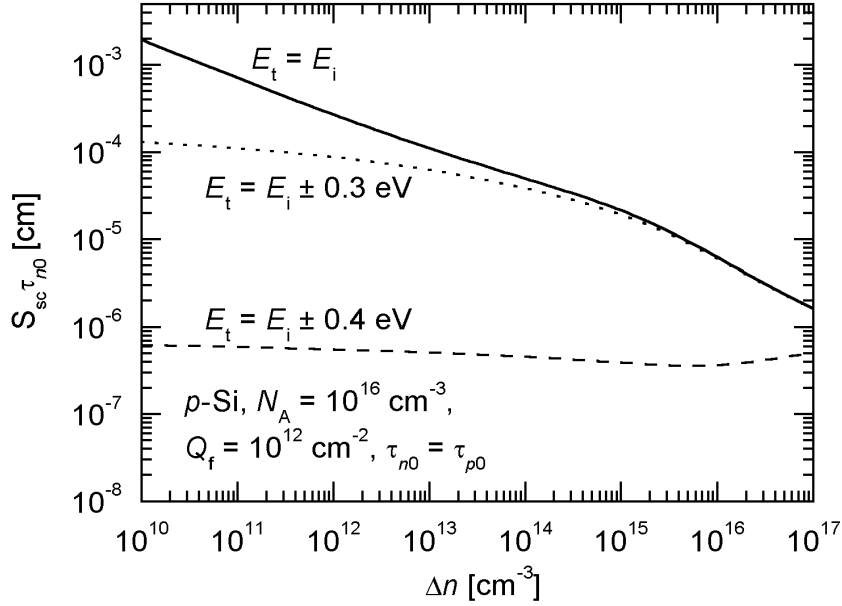$$m = \left(\frac{\partial \ln S_{sc}}{\partial \ln \Delta n} + 1\right)^{-1}. \tag{2.83}$$

Figure 2.26: Calculated product $S_{sc}\tau_{n0}$ as a function of the excess carrier density Δn and the energy level of the defects in the space-charge region. The solid lines show the results for midgap states. Also shown are the results for an intermediate state (dashed line) and a shallow state (dotted line). The intermediate or the shallow states, respectively, lie either in the upper or in the lower bandgap which is marked by the sign '$\pm$'. Assumptions: p-type silicon, $N_A = 10^{16}$ cm^{-3}, $Q_f = 10^{12}$ cm^{-2} and $\tau_{n0} = \tau_{p0}$.

The saturation current density J_{02} can be calculated using the expression

$$J_{02} = \frac{q\Delta n S_{sc}}{\left(\frac{\Delta n}{n_{0b}} - 1\right)^{1/m}}.$$

(2.84)

For equal capture time constants, the product $J_{02}\tau_{n0}$ like the product $S_{sc}\tau_{n0}$ is constant. Fig. 2.27 shows the calculated dependencies of m and the product $J_{02}\tau_{n0}$ on Δn as obtained from the $S_{sc}(\Delta n)$ curve shown in Fig. 2.25 ($N_A = 10^{16}$ cm^{-3}). As can be seen, the ideality factor varies between 1.5 and 1.8 in the examined injection range, i.e., the $m = 2$ approximation is a clear oversimplification. An extensive discussion of the ideality factor for diffused p-n junctions can be found in Ref. [51].

It can be concluded from the above considerations that the $S_{sc}(\Delta n)$ curve and, hence, the J_{02} value, can only be shifted by different capture time constants. The slope of the $S_{sc}(\Delta n)$ curve and, hence, the ideality factor, is determined by the energy level of the recombination centre (Fig. 2.26) and at very low injection levels by the fixed positive charge density (Fig. 2.24). However, for low Q_f values inducing only depletion or weak inversion, S_{it} rather than S_{sc} may contribute to a higher extent to S_{eff} (Fig. 2.18).
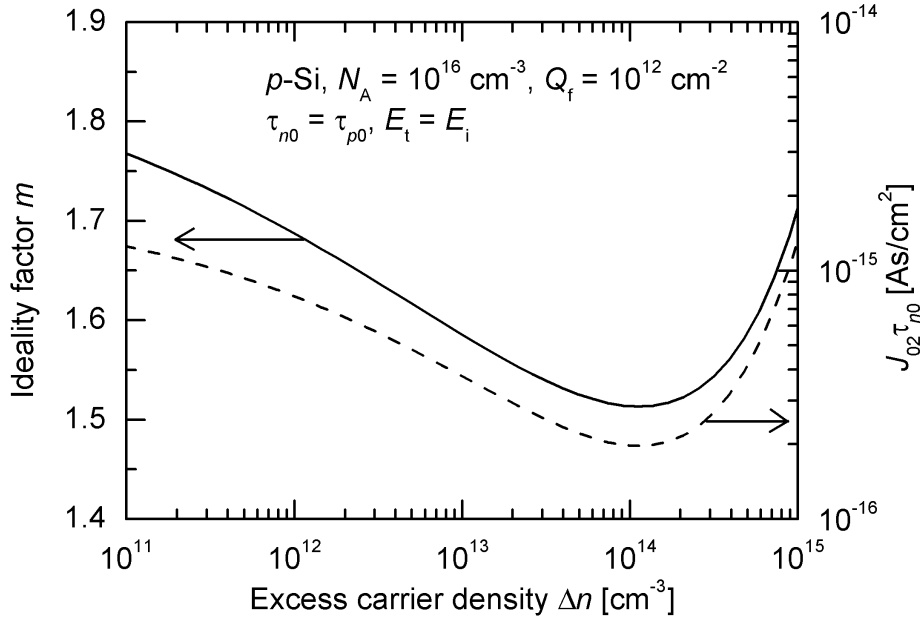
Figure 2.27: Calculated ideality factor m and product of the dark saturation current J_{02} times the capture time constant τ_{n0} as a function of the excess carrier density Δn. The curves are obtained from the data shown in Fig. 2.25 using Eq. 2.83 and Eq. 2.84. Assumptions: p-type silicon with $N_A = 10^{16}\,\mathrm{cm}^{-3}$, $Q_f = 10^{12}\,\mathrm{cm}^{-2}$ and $\tau_{n0} = \tau_{p0}$.

2.4.4   Effective Surface Recombination Velocity

Two different contributions to the effective surface recombination velocity defined in Eq. 2.8 had been discussed in the previous sections. The first contribution is due to recombination at the surface of the semiconductor, while the second one is due to the recombination in the SCR. Girisch *et al.* could not observe any discrepancy between the measured effective SRV and the calculated S_{it} and, hence, justified the negligibility of recombination in the SCR on the basis of their experimental results. However, today, outstanding silicon surface passivation can be achieved and, as will be shown in Section 4, recombination in the space-charge region cannot be neglected in general.

An third contribution to the effective SRV was proposed by Glunz *et al.* [50]. They included a term that accounted for shunt currents through the space charge region. The shunt currents were proposed to be due to tunneling of minority carriers through the potential barrier and recombination at highly recombinative 'bad spots' at the surface. They included this term in order to be able to fit their experimental data. They assumed the ideality factor for the recombination current J_2 to be $m = 2$ but found a $S_{eff}(\Delta n)$ dependence exhibiting a shallower slope. However, as was shown in the previous section, the ideality factor is actually lower than 2 and, hence, the inclusion of an additional term into the effective SRV is not necessary to fit $S_{eff}(\Delta n)$ data with a shallower slope. In the present work, it will

be shown that this additional recombination mechanism is either completely negligible in comparison to the other components or is at least so small that our experimental data can be excellently fitted including S_{it} and S_{sc} only. Considering only the terms discussed in the previous sections, the effective SRV is given by

$$S_{eff} = S_{it} + S_{sc}. \tag{2.85}$$

For the sake of simplicity, the subscript of S_{eff} is often omitted, in particular when measured values of the SRV (S-values) are considered.

2.4.5   Constant Quasi-Fermi Levels

In this section, the validity of the assumption of constant quasi-Fermi levels is investigated. This assumption was used to determine the SRV according to the extended SRH formalism and in the derivation of the recombination in the surface space-charge region. The questions arising are, (i) which SRV can be tolerated for the assumption to be valid and (ii) how does the violation of the assumption gives rise to an incorrect determination of the effective SRV.

Due to carrier recombination at the surface, the separation of the quasi-Fermi levels at the surface $V_{oc.s}$ is smaller than that in the bulk (V_{oc}). We define the difference as

$$\begin{aligned} \Delta V_{oc} &\equiv V_{oc} - V_{oc.s} \\ &= (\phi_{p_b} - \phi_{n_b}) - (\phi_{p_s} - \phi_{n_s}), \end{aligned} \tag{2.86}$$

where ϕ_{p_b} (ϕ_{n_b}) and ϕ_{p_s} (ϕ_{n_s}) denote the hole (electron) quasi-Fermi level in the bulk and the hole (electron) quasi-Fermi level at the surface, respectively. The electron and hole recombination current densities are given by [31]

$$J_n = -q\mu_n n(z)\nabla\phi_n(z) \approx q\mu_n n_b \frac{\phi_{n_s} - \phi_{n_b}}{d_{sc}} \quad \text{and} \tag{2.87}$$

$$J_p = -q\mu_p p(z)\nabla\phi_p(z) \approx q\mu_p p_b \frac{\phi_{p_s} - \phi_{p_b}}{d_{sc}}. \tag{2.88}$$

Both recombination current densities are equal. However, for p-type material, $p_b \gg n_b$ and, hence, the difference $\phi_{p_s} - \phi_{p_b}$ must be a lot smaller to support the same current. We can therefore approximate ΔV_{oc} by

$$\Delta V_{oc} = \phi_{n_s} - \phi_{n_b}. \tag{2.89}$$

The electron recombination current density towards the surface can also be written as

$$J_n = q\Delta n S_{eff}. \tag{2.90}$$

Using Eq. 2.87, Eq. 2.89 and Eq. 2.90, we obtain

$$\Delta V_{oc} = \frac{d_{sc}}{\mu_n} S_{eff}. \tag{2.91}$$

Assuming $d_{\text{sc}} = 0.1 \,\mu\text{m}$ (Fig. 2.22) and $\mu_n = 1500 \,\text{cm}^2/\text{Vs}$, $\Delta V_{\text{oc}} = 6.7 \times 10^{-9} \frac{\text{Vs}}{\text{cm}} S_{\text{eff}}$ is obtained demonstrating the rather small differences obtained for ΔV_{oc} even for relatively large SRVs.

We will now consider the error for the calculated SRV $S_{\text{eff.calc}}$ if ΔV_{oc} is neglected. S_{it} and S_{J02} contribute to $S_{\text{eff.calc}}$ and are both calculated using the SRH recombination rate. According to Eq. 2.26, the SRH recombination rate is proportional to the product of the electron and hole density np and, hence, to the factor $e^{\beta V_{\text{oc}}}$. Thus, the relative deviation of $S_{\text{eff.calc}}$ from the exact value S_{eff} is

$$\frac{\Delta S_{\text{eff.calc}}}{S_{\text{eff.calc}}} = \beta \Delta V_{\text{oc}}. \tag{2.92}$$

Using Eq. 2.91 we obtain

$$\frac{\Delta S_{\text{eff.calc}}}{S_{\text{eff.calc}}} = \frac{\beta d_{\text{sc}}}{\mu_n} S_{\text{eff.real}}. \tag{2.93}$$

Using the same values as above for μ_n and d_{sc}, it is seen from Eq. 2.93 that $S_{\text{eff.real}}$ can be as high as $6 \times 10^5 \,\text{cm/s}$ for a deviation of $S_{\text{eff.calc}}$ from the exact value of $1\,\%$. Thus, the approximation of flat quasi-Fermi levels across the surface space-charge region holds up to rather high recombination rates within the SCR and at the actual surface.

2.5 Effective Carrier Lifetime

The different recombination path in the bulk and at the surface may occur simultaneously within a semiconductor. The recombination rate of some of the processes might be negligible, while others may contribute to a higher extent. It is obvious, that those processes resulting in the highest recombination rates will determine the overall recombination. In order to analyse a particular recombination process in detail, it is necessary to minimise the recombination rates of the other processes. In particular, if the surface recombination is of interest, the samples should exhibit a negligible or at least well-known bulk recombination rate. Hence, we will use high-quality float-zone (FZ) material throughout this work. The FZ samples are homogeneously doped and possess a high diameter-to-thickness ratio. The bulk recombination rate per unit sample area is then given as the sum of the radiative, Auger and SRH recombination rate integrated over the thickness W:

$$U_{\text{b}} \times W = (U_{\text{rad}} + U_{\text{A}} + U_{\text{SRH}}) \times W. \tag{2.94}$$

For planar samples, having a large diameter-to-thickness ratio, the surface recombination occurs at two surfaces, each contributing with a recombination rate per unit sample area of

$$U_{\text{z}<\text{d}_{\text{sc}}} = U_{\text{it}} + \int_0^{d_{\text{sc}}} U(z)\,dz, \tag{2.95}$$

where U_{it} and $\int_0^{d_{\text{sc}}} U(z)\,dz$ are the recombination rates per unit area at the actual surface and in the space charge region, respectively. The total recombination rate can be expressed as

$$U_{\text{eff}} = U_{\text{b}} + 2U_{\text{z}<\text{d}_{\text{sc}}}/W. \tag{2.96}$$
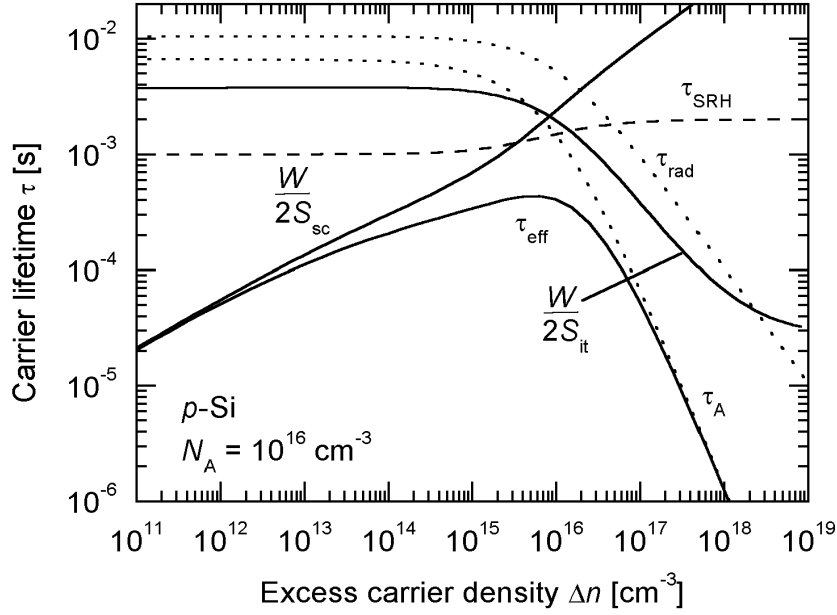
Figure 2.28: Calculated effective carrier lifetime as a function of the injection level for a p-type silicon wafer ($N_A = 10^{16}\,\text{cm}^{-3}$). τ_{eff} was calculated according to $\frac{1}{\tau_{\text{eff}}} = \frac{1}{\tau_{\text{rad}}} + \frac{1}{\tau_A} + \frac{1}{\tau_{\text{SRH}}} + \frac{2S_{\text{it}}}{W} + \frac{2S_{\text{sc}}}{W}$. The intrinsic lifetimes τ_{rad} and τ_A (dotted lines) were calculated using the published parameters of Ref. [18] and Ref. [20], respectively. All other curves were calculated using exemplary parameters. The SRH lifetime (dashed line, Eq. 2.28) was calculated assuming $\tau_{n0} = \tau_{p0} = 1\,\text{ms}$ and $E_t = E_i$. To calculate the impact of the surface, a $300\,\mu\text{m}$ thick wafer was assumed. The recombination at the actual surface was calculated using the extended SRH formalism, assuming $Q_f = 10^{12}\,\text{cm}^{-2}$, $D_{\text{it}} = 10^{11}\,\text{cm}^{-2}\text{eV}^{-1}$, $\sigma_n = \sigma_p = 10^{-15}\,\text{cm}^2$ and the recombination in the SCR assuming $\tau_{n0} = \tau_{p0} = 1\,\mu\text{s}$, $E_t = E_i$. It should be noted that the carrier capture time constants in the SCR region are assumed to be 3 orders of magnitude lower than those in the bulk.

From the definitions for the bulk lifetime (Eq. 2.4 and Eq. 2.12) and the surface recombination velocity (Eq. 2.8), respectively, we can define the effective carrier lifetime as

$$\frac{1}{\tau_{\text{eff}}} = \frac{1}{\tau_{\text{b}}} + \frac{2S_{\text{eff}}}{W}. \qquad (2.97)$$

In this equation, a uniform injection profile across the whole bulk of the sample is assumed. This simplification holds only for a homogeneous generation profile and low surface recombination velocities. A comprehensive analysis, taking into account the spatial and time dependence of the excess carrier density, had been carried out by Luke and Cheng [52]. They found that the carrier decay occurs exponentially with different modes, having different time constants. The fundamental mode having the longest lifetime is identified with the effective carrier lifetime and the relation between the SRV and the effective carrier lifetime

is given as

$$S_{\text{eff}} = \sqrt{D_n \left(\frac{1}{\tau_{\text{eff}}} - \frac{1}{\tau_{\text{b}}} \right)} \tan \left(\frac{W}{2} \sqrt{\frac{1}{D_n} \left(\frac{1}{\tau_{\text{eff}}} - \frac{1}{\tau_{\text{b}}} \right)} \right), \qquad (2.98)$$

with the diffusion coefficient for electrons being D_n. As can be easily shown, Eq. 2.97 is an approximation of Eq. 2.98 for small SRVs ($\tan(x) \approx x$). The detailed analysis shows that the relative deviation of the approximate from the exact solution is below $4\,\%$ if $\frac{W}{D_n} S_{\text{eff}} < \frac{1}{4}$ [53]. For a typical wafer thickness of $300\,\mu$m and an electron diffusion constant of $30\,\text{cm}^2/\text{s}$, S_{eff} has to be below $250\,\text{cm/s}$ for the validity of the approximation.

As has been stated before, different recombination processes may contribute to the measured effective carrier lifetime. To investigate the surface recombination, the influence of the bulk recombination has to be subtracted from the effective lifetime. It is obvious that if the bulk recombination rate is overestimated, the surface recombination rate is underestimated, resulting in higher surface recombination velocities and vice versa. Let us consider the following example for illustration: We assume a p-type silicon wafer with $N_A = 10^{16}\,\text{cm}^{-3}$, a thickness of $300\,\mu$m, a diffusion coefficient of $D_n = 30\,\text{cm}^2/\text{s}$ and $\Delta n = 10^{15}\,\text{cm}^{-3}$. Let us further assume that that Auger recombination prevails in the bulk. If a τ_{eff} of $2.5\,$ms would be measured, S is determined to be $1.5\,\text{cm/s}$ ($3.0\,$cm/s) if the Auger lifetime of Schmidt et $al.$ (Kerr and Cuevas) is assumed. However, if $\tau_{\text{eff}} = 0.5\,$ms would be measured, both Auger lifetime values result in a similar S of $26\,\text{cm/s}$ and $27\,\text{cm/s}$, respectively.

2.6   Surface Passivation of Silicon

From the previous discussion, different methods can be derived to reduce the surface recombination, i.e., to passivate the silicon surface:

1. *Variation of the interface parameters.*
   As can be seen from Eq. 2.33, a reduction of the interface state density D_{it} leads to a lower SRV. The reduction of the capture cross sections σ_n and σ_p would have the same effect. However, it is generally believed that the capture cross sections are a property of the specific interface recombination centres and, hence, cannot be varied. Technologically, the reduction of the interface state density is achieved in the case of silicon by growing an oxide film at high temperatures or by depositing silicon nitride or amorphous silicon, respectively, using plasma-enhanced deposition techniques. Further passivation techniques will be discussed in Section 3.1.

2. *Reduction of the carrier density at the surface.*
   A different approach to decrease the surface recombination is the reduction of the electron or hole density at the surface (n_{s} or p_{s}), respectively. Since both an electron and a hole are required for the recombination process, the recombination rate is maximal if $n_{\text{s}} = p_{\text{s}}$ (assuming equal capture cross sections, $n_{\text{s}}\sigma_n = p_{\text{s}}\sigma_p$ in general). The previous sections have shown some examples of this effect. The electron (hole)

density at the surface can be reduced by a fixed positive (negative) charge at the surface, assuming that either accumulation or inversion conditions are obtained (so-called *charge-induced* or *field-effect* passivation). A second possibility to reduce the density of one type of carrier at the surface is the introduction of a doping profile within the semiconductor. If the dopants result in a layer with the same polarity as the bulk, the passivation is referred to as 'back surface field' since it is often used for the rear surface passivation of solar cells. An emitter is formed by the opposite polarity which is called a 'floating junction' if it is not contacted. In order to reduce contributions from the recombination in the SCR, accumulation conditions at the surface rather than inversion conditions are generally preferable.

In many practical cases, the above-mentioned possibilities occur at the same time. For instance, the passivation by thermally-grown silicon dioxide drastically reduces the interface state density and additionally provides a field-effect passivation due to charges present in the SiO_2 films. In general, a low interface state density is a prerequisite for an effective charge- or work-function-induced passivation. Because the interface state density is rather high for metal-semiconductor interfaces, a work function difference between the metal and the semiconductor does not provide any passivation. Hence, in practical applications a thin insulator at the interface may be introduced, resulting in metal-insulator-semiconductor (MIS) structures to reduce the interface state density and enable an improved field-effect passivation. For the realisation of conductive MIS structures, a trade-off between the surface passivation and the conductivity of the structure is necessary.

Chapter 3

Experimental

In this chapter, the experimental techniques for sample fabrication and measurement are introduced. Carrier lifetime test structures were used for investigating the surface passivation quality of different plasma-deposited films on silicon. The samples consisted of silicon wafers identically passivated on both surfaces. The surface passivation techniques will be introduced in Section 3.1. The effective carrier lifetimes were determined using the microwave-detected photoconductance decay (MW-PCD) as well as the quasi-steady state photoconductance (QSSPC) method described in Section 3.2.1 and 3.2.2, respectively. After characterising the quality of the passivation schemes by lifetime measurements, some of them were incorporated at the rear surface of silicon solar cells to investigate their applicability on real devices. The solar cell structure used is described in Section 3.3. The cell characterisation techniques described include: (i) current-voltage characteristics described in Section 3.4.1, (ii) quantum efficiency measurements described in Section 3.4.2 and (iii) spatially resolved light beam induced current measurements described in Section 3.4.3. The capacitance-voltage (C-V) technique used to investigate the interface state density at the Si/SiN_x interfaces and the fixed charge density within the SiN_x films is described in the next chapter (Section 4.2).

3.1   Surface Passivation Techniques

The standard method for the passivation of silicon surfaces, both in microelectronics and photovoltaics, is thermal oxidation of the surfaces at high temperatures ($900 - 1100\,^{\circ}$C) [54]. The oxide film grows into the substrate, consuming the silicon and moving the silicon-silicon dioxide interface into the silicon. This creates a fresh interface region, with surface contamination on the original silicon ending up on the oxide surface. Using thermally grown SiO_2 films, very low SRVs can be achieved for n-type and high-resistivity ($> 10\,\Omega$cm) p-type material [55, 56]. For low-resistivity p-type silicon, very low SRVs can be obtained with an additional anneal by capping with a layer of aluminium. During this so-called 'alneal', atomic hydrogen is believed to be generated by the reaction of aluminium with residual water within the oxide ([57], p. 169). Thermally grown silicon dioxide films are highly reproducible and highest surface passivation quality is ascribed to them as long as care is taken to avoid

contamination of the silicon bulk during the high-temperature treatment. Hence, silicon dioxide passivation can be regarded as a reference for other passivation techniques.

However, high-temperature processing required for thermal oxidation results in a number of possible problems, including:

- higher energy consumption and potentially higher costs in silicon solar cell fabrication,

- the risk of contaminating the bulk material by the diffusion of unwanted impurities,

- thermal degradation of lower quality silicon materials (e.g. multicrystalline silicon).

For these reasons, low-temperature passivation schemes are preferable. Promising candidates like amorphous hydrogenated silicon nitride (SiN_x) and amorphous hydrogenated silicon (a-Si:H) films deposited by plasma-enhanced chemical vapour deposition (PECVD) were investigated in this work (Section 3.1.1 and 3.1.2). The standard method to reduce the SRV at the rear surface of industrially fabricated solar cells is the incorporation of an aluminium back surface field (Al-BSF). The fabrication is described in Section 3.1.3. Surface passivation utilising floating junctions is discussed in Section 3.1.4. In addition to these permanent surface passivation techniques, there are a few techniques that can be used for characterisation purposes only since the obtained surface passivation is not stable on the long term. A prominent one, relying on additionally deposited corona charges is introduced in Section 3.1.5. Further passivation techniques are briefly discussed in Section 3.1.6.

3.1.1 Amorphous Hydrogenated Silicon Nitride

Amorphous hydrogenated silicon nitride (referred to SiN_x throughout this work) films deposited by chemical vapour deposition (CVD) are a promising alternative to thermally grown SiO_2 films and have been introduced to industrial fabrication already. The CVD processes can be subdivided into thermally and plasma-assisted deposition techniques depending on how the decomposition of the precursor gases is obtained. Thermal CVD includes depositions at atmospheric pressure using the reaction of silane (SiH_4) and ammonia (NH_3) at temperatures in the $700 - 1000\,^\circ$C range (APCVD) and at low pressure ($\sim$0.1 mbar) using the reaction of dichlorosilane ($SiCl_2H_2$) and NH_3 at temperatures around $750\,^\circ$C (LPCVD) [58]. LPCVD films serve as good barriers to the diffusion of water, sodium and typical dopants for silicon and are therefore frequently used for encapsulation. LPCVD films have been applied to photovoltaics also, e.g. as antireflection coatings, however, they do not provide a reasonable surface passivation. A probable reason is the relatively low hydrogen content of the films.

A major disadvantage of APCVD and LPCVD arises from the high substrate temperatures. Difficulties occur, for instance, if silicon nitride is to be deposited as antireflection coatings on already metalised solar cell surfaces since the metallisation does not withstand the high temperatures. A solution to this difficulty has been the use of anisothermal low-temperature plasmas, also known as glow discharges. In this so-called plasma-enhanced chemical vapour deposition (PECVD), the injected process gases are dissociated in the plasma so that the reactive species can build up a thin solid film on the substrate. Although it is not necessary to have the substrate at a high temperature in order to achieve

acceptable deposition rates, it may still be desirable to have a moderately high wafer temperature to obtain films of reasonable quality. Electrical energy can be coupled into a plasma by inductively or capacitively coupling of high frequency electromagnetic fields. In general these methods use hydrogen-containing reactants, resulting in non-stoichiometric silicon nitride films with up to 40 atomic % of hydrogen.

Thermo-catalytic CVD is a relatively new method to deposit SiN_x films thermally-assisted. In contrast to the previously mentioned thermal CVD techniques the substrate temperature remains relatively cold (a few hundred degrees Celsius) during the deposition. The decomposition of the reactant gases occurs at heated catalyser filaments with temperatures in the range of $1500 - 2000\,°C$. This so-called Cat-CVD (also known as hot-wire CVD) has found widespread use for the deposition of amorphous silicon, polycrystalline silicon and silicon nitride films [59]. Very promising surface recombination velocities have been reported for SiN_x films fabricated using Cat-CVD [60].

For a detailed overview of the deposition principles, please refer to Ref. [61]. A more detailed introduction to different deposition techniques and equipment, in particular those used at ISFH for SiN_x deposition, is given in the Ph. D. dissertations of Lauinger [62] and Moschner [63]. For SiN_x films deposited using PECVD techniques, excellent surface recombination velocities have been reported in the literature [64, 65]. However, some aspects of the underlying physics are still in discussion. A main focus of this work was the investigation of the recombination processes at Si/SiN_x interfaces as a contribution to an improved understanding of the passivation mechanisms.
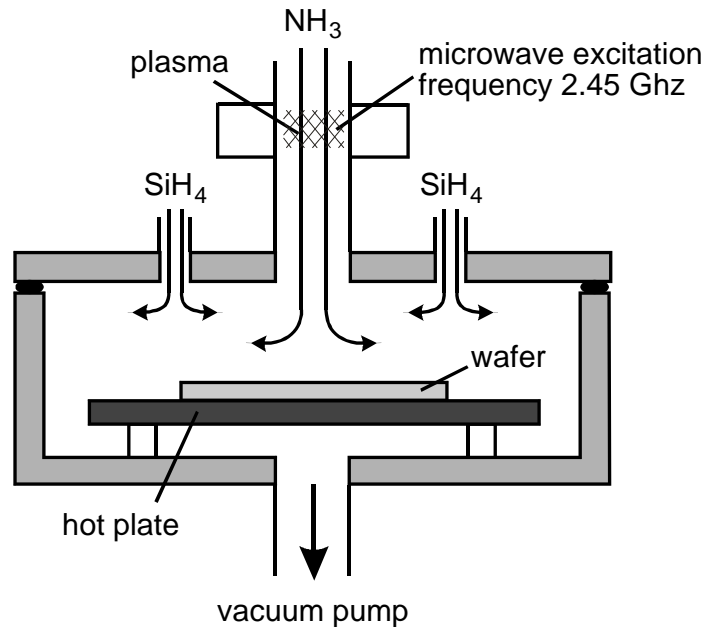

Figure 3.1: Schematic sketch of the remote PECVD reactor used for SiN_x film depositions. NH_3 (and optionally N_2) are excited in the quartz cavity by microwaves while SiH_4 is added downstream. The wafers are located outside the plasma excitation volume.

Film	PECVD	T	Power	Pressure	SiH$_4$ gas flow	NH$_3$ gas flow	N$_2$ gas flow
		°C	W	Torr	sccm	sccm	sccm
SiN$_x$	remote	400	150	150	$2-30$	200	100
a-Si	direct	225	100	450	30	-	-

Table 3.1: Typical process parameters used in this work for the deposition of PECVD SiN$_x$ and a-Si films.

The SiN$_x$ films studied in this work were prepared using a PECVD reactor schematically shown in Fig. 3.1. The Plasmalab 80+ reactor used, fabricated by Oxford Plasma Technology, uses of the so-called *remote* plasma excitation approach. The microwave excitation of the plasma occurs outside the vacuum chamber and the excited species (note that only NH$_3$ and N$_2$ are excited while SiH$_4$ is injected downstream) are directed onto the wafer by means of a narrow quartz tube. The resulting directional SiN$_x$ deposition allows for the deposition of SiN$_x$ films with only minor parasitic film deposition at the reactor walls. For spatially homogeneous depositions over a larger area an additional gas distribution head was installed underneath the quartz tube [66]. The gas flows of the reactant gases injected through the quartz tube (NH$_3$ and N$_2$) has to be adjusted if the gas distribution head is used. However, the typical characteristics of the deposited films do not change if the films are deposited using the extra head. The values for the process parameters used in this study are given in table 3.1.

3.1.2   Amorphous Hydrogenated Silicon

Recently, amorphous hydrogenated silicon (a-Si:H) films have attracted the interest of the PV community since very high efficiencies have been obtained using a-Si:H films as front and rear surface passivation [67]. Both, Cat-CVD as well as PECVD can be used for the deposition of a-Si:H films. In this work, the PECVD reactor used for a-Si:H film preparation is characterised by the use of the direct plasma excitation approach in a so-called direct-plasma reactor (sometimes also called parallel-plate reactor), where the processing gases are excited by an electromagnetic field and the wafers are located within the plasma. The electromagnetic field has a frequency of either 13.56 MHz ('high-frequency' method) or in the 10 - 500 kHz range ('low-frequency' method). Due to a detrimental ion bombardment of the surface in case of the low-frequency method [68, 69], only high-frequency (HF) excitation was used in this work. Fig. 3.2 shows a cross-sectional view of the plasma reactor used having a hot-plate diameter of 16 cm (Oxford Plasma Technology, Plasmalab 80). Typical process variables used in this work are given in Tab. 3.1.

The remote reactor used for SiN$_x$ deposition (Fig. 3.1) has the additional option to be used as a parallel-plate reactor. In order to investigate whether the surface passivation depends on the reactor chamber, a-Si:H films were prepared in this reactor using the parallel-plate option. However, no differences in passivation quality were observed. A remote deposition of a-Si:H films was not possible in the reactor shown in Fig. 3.1 for technical reasons: The SiH$_4$ which was the only precursor gas used could not be injected through the
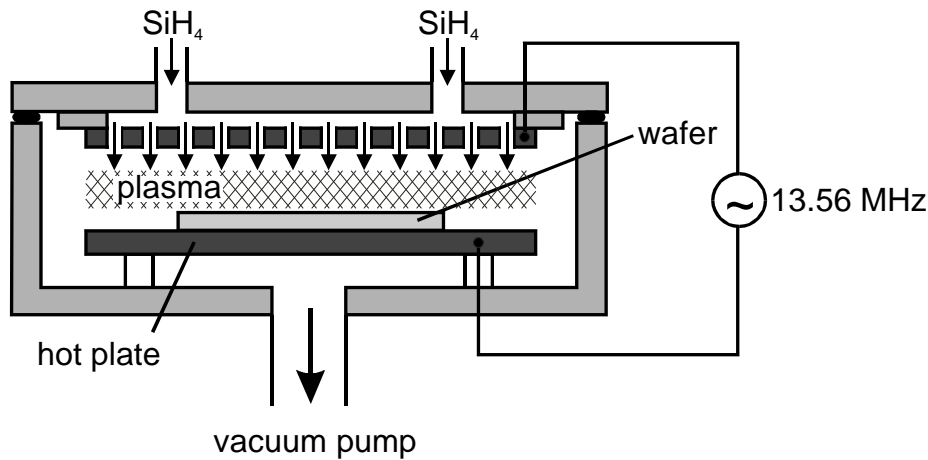
Figure 3.2: Schematic sketch of the parallel-plate PECVD reactor used for a-Si film depositions. SiH_4 is excited by the electromagnetic field and the wafers are located within the plasma excitation volume.

quartz tube where the excitation occurs.

3.1.3   Back Surface Fields

An economic means to reduce surface recombination is the use of a back surface field (BSF) which was first proposed by Mandelkorn in 1972 [70]. The somewhat inappropriate term arose since it is typically used at the rear of solar cells. A heavily doped region is included at the rear surface of the cell reducing the minority carrier concentration and hence the recombination rate (Eq. 2.31 and Section 2.6). In practice, the most effective technique for producing a back surface field has been to evaporate aluminium or to screen-print an aluminium-based paste onto the rear of the cell and alloy the aluminium into the silicon in a subsequent firing step. Not only does this technique improve voltage and current output of the cell, it also facilitates the realisation of low contact resistances. The alloying process is typically been done at $800 - 900\,°C$. During the process the Al melts and alloys with the silicon. At the subsequent cooling cycle a p^+ layer is produced by liquid phase epitaxial growth of primary silicon from the melt. At the eutectic temperature ($577\,°C$) an aluminium rich layer of silicon-aluminium eutectic recrystallises over the p^+ layer.

Besides doping with aluminium, back surface fields are also fabricated using boron diffusion. This has advantages in that boron is more soluble in silicon than aluminium and diffusion yields more uniform junctions than alloying [71]. High-efficiency silicon solar cells having a p-type bulk incorporating a local B-BSF have shown very high conversion efficiencies up to about 25 % [8]. However, the fabrication of a B-BSF requires rather high diffusion temperature of about $1000\,°C$ resulting in similar problems as mentioned in connection with high-temperature oxidation at the beginning of Section 3.1.

3.1.4   Floating Junctions

The principle of a doping profile with a dopant concentration increasing towards the surface can also be applied using dopants generating the opposite polarity than the base material. If the dopant concentration increases towards the surface, as is usually the case for diffused emitters, the resulting electric field forces minority carriers towards the p-n junction, i.e., away from the surface. This drastically reduces the minority carrier concentration - and hence the recombination rate - at the surface. This principle was proposed also for the rear surface of silicon solar cells, keeping the p-n junction floating, i.e., electrically not contacted [72]. The so-called floating junction (FJ) combined with oxide passivation of the n-type surface was proposed to provide a better effective surface recombination velocity at the rear of p-type Si solar cells compared with oxide passivation of the undiffused p-type surface [72]. The reason given is the fact that oxide passivation is more effective when applied to the n-type Si. The excellent surface passivation of a FJ in combination with oxide passivation has been demonstrated by very high open-circuit voltages for p-type Si solar cells well in excess of 700 mV [73].

SiN$_\mathrm{x}$ films contain a high density of fixed positive charges inducing an n inversion layer at the surface of p-type Si. Hence by applying SiN$_\mathrm{x}$ films as a rear surface passivation scheme, conceptually the same approach is used as FJ passivation, except that an inversion layer is used in place of a diffused junction. The advantages and limitations of this concept are discussed in great detail in Chapter 6.

3.1.5   Corona Charges

Schöfthaler introduced a method that employs additional, so-called corona charges on top of a SiO$_2$ film to enhance the surface passivation [74] [75]. The approach again uses the concept of reducing the density of one carrier type at the silicon surface, thereby reducing the recombination rate (charge-induced or field-effect passivation, Section 2.6). They reported very low SRV values below $1\,\mathrm{cm/s}$ for $0.25\,\Omega$cm FZ p-Si material. A difficulty of the method used by Schöfthaler is the necessity of an oxide film grown at high temperature. Schmidt *et al.* simplified the method by using a polymer film deposited using a spinner on the silicon surface [76].

In this work, corona charges were used to characterise the surface passivation and to investigate the underlying mechanisms of SiN$_\mathrm{x}$ passivation. Fig. 3.3 shows a schematic view of the corona chamber used in this work [77]. The wafer prepared with insulating films on both sides is placed on a grounded metal electrode. A metal tip about $10\,\mathrm{cm}$ above the sample forms the counter electrode. A voltage of $5-10\,\mathrm{kV}$ is applied generating a high electric field strength adjacent to the needle thereby ionising air molecules. Ninety percent of the negative charges consist of CO_3^- ions, whereas for positive charging the main part of the charges consist of hydrated H_3O^+ ions [78, 79]. Negative (positive) ions follow the electric field lines to regions of higher (lower) potential. Depending on the polarity of the applied voltage, positive or negative ions can be deposited on the sample surface where they stick due to the induced mirror charges within the silicon. It should be noted that the ions reach the sample surface having thermal energy only since the electric field strength

decreases distinctly from the tip towards the sample and the mean free path length is rather low at atmospheric pressure. Hence, no surface damage is caused by the ions. The corona charges are stable under illumination. Only strong humidity or not well insulating layers can decrease this stability. On the other hand, the charges can be easily removed by rinsing the wafer in water or alcohol. Hence, corona charging is an ideal non-destructive tool for characterisation purposes.
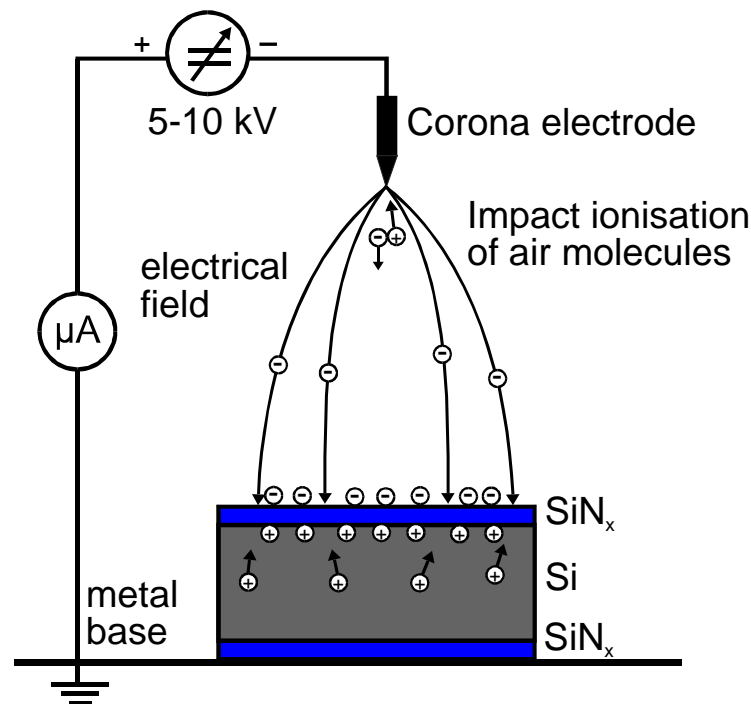

Figure 3.3: Schematic view of the corona chamber used in this work to deposit additional charges on insulating films. Using this apparatus, positive and negative charges can be deposited upon insulating films thereby varying the surface potential of the semiconductor.

The charge density on top of the films was determined using a Trek 344 electrostatic voltmeter. The apparatus uses the vibrating electrode technique based on the experimental approach of Lord Kelvin ([80, 81, 82]). Fig. 3.4 shows a schematic diagram of the apparatus. The sensing electrode (Kelvin probe) is placed in close proximity to the charged surface. It is electromechanically vibrated to produce capacitive modulation between the electrode and the test surface. If the voltage, or equivalently, the charge, on the test surface is different than the voltage on the probe, an AC signal is induced upon the electrode by virtue of this modulation in the presence of the electrostatic field. The probe voltage is driven toward the potential of the test surface until the electrostatic field between the electrode and the test surface is reduced to zero. At this point, the compensation voltage equals the voltage
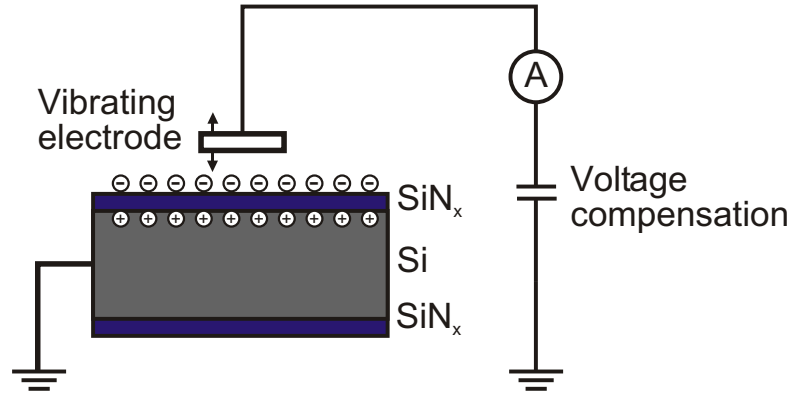
Figure 3.4: Schematic diagram of the electrostatic voltmeter used in this work to measure the deposited corona charges on insulating films. The measurement technique is based on the experimental approach of Lord Kelvin [80].

at the test surface. The voltage can be used to determine the charge density on top of an insulating film. Since the silicon substrate is grounded, the corona charge density Q_c is compensated by an equal charge density in the sample. The correlation between the voltage at the test surface, i.e., the voltage on the SiN_x film surface, V_s and Q_c is therefore given by the expression

$$V_s = \frac{qQ_c}{C_i}, \tag{3.1}$$

where C_i denotes the insulator capacity given in Eq. 2.74. For a typical SiN_x film thickness of $d_{iG} = 100\,nm$ and permittivity of $\epsilon_{SiN} = 7\epsilon_0$, a corona charge density of $Q_c = 10^{12}\,cm^{-2}$ and neglecting d_{if} in comparison with d_{iG}, the measured voltage would be $V_s = 3\,V$. The fixed charge density within the SiN_x films cannot be determined with the method as the following calculation shows. Since $Q_f \approx 10^{12}\,cm^{-2}$ and $d_{if} \approx 10\,nm$, $V_s = 0.3\,V$ which is below the resolution of $1\,V$ of the Kelvin probe used.

3.1.6   Further Surface Passivation Techniques

For the sake of completeness further surface passivation techniques are introduced. The first two methods (silicon carbide and titanium dioxide films) can be applied to achieve permanent surface passivation in devices whereas the remaining methods are suited for characterisation purposes only since the obtained passivation is not long-term stable.

Amorphous silicon carbide films   Martín *et al.* investigated the surface passivation provided by amorphous silicon carbide (SiC_x:H) films [83]. They published S-values as low as $30\,cm/s$ for $3.3\,\Omega cm$ FZ p-Si wafers. The SiC_x:H films were deposited at $400\,°C$ using CH_4 and SiH_4 as precursor gases and a direct PECVD reactor similar to that described in

Section 3.1.2. However, the passivation quality seems to decrease distinctly with increasing doping concentration. In this respect, they reported an S-value of 650 cm/s for 0.4 Ωcm.

Titanium dioxide films   Titanium dioxide (TiO_2) films have been used frequently in the photovoltaic industry as an antireflection coating for silicon solar cells. TiO_2 has a number of advantages for solar cell processing including an industrially feasible low-cost high-throughput deposition and good optical properties [84]. Therefore, it would be desirable if the films provided a surface passivation as well. Stoichiometric TiO_2 films afford very little surface passivation on silicon surfaces, although some degree of surface passivation has been demonstrated with non-stoichiometric TiO_x films. In this respect, Doeswijk *et al.* reported a minimum SRV of 176 cm/s for $5.1 - 6.9\,\Omega$cm FZ p-type Si(100) wafers [85]. A different way to use TiO_2 films as an antireflection coating and provide a surface passivation was proposed by Richards *et al.* [86]. They performed a post-treatment of the TiO_2 coated silicon wafer with a furnace oxidation process thereby oxidising the buried silicon. However, since a Si/SiO_2 interface rather than a Si/TiO_2 interface is obtained with this method, the correspondence to TiO_2 passivation is limited.

Hydrofluoric acid   Hydrofluoric acid (HF) has been successfully used to passivate silicon surfaces ([87, 88, 89]). The wafer is placed in a concentrated or diluted HF solution during the carrier lifetime measurement. SRVs as low as 0.25 cm/s for (111)-orientated high-resistivity 150 Ωcm FZ n-type silicon wafers were reported [88]. For (100)-orientated 1 Ωcm FZ p-type silicon material that is more typical for solar cell fabrication, S-values below 10 cm/s have been reported [89]. The passivation by HF results in potential difficulties including: (i) the passivation provided is not stable with time and depends on the pretreatment of the wafer and (ii) HF is highly toxic and can lead to corrosion of the measurement equipment.

Iodine/ethanol   In order to avoid the problems arising from HF passivation, iodine/ethanol solutions have been used as an alternative. Horányi *et al.* have first investigated iodine/ethanol solutions and reported S-values below 10 cm/s for (111)-orientated 25 Ωcm FZ n-Si wafers [90]. For material more typical for solar cell fabrication ((100)-orientated 1 Ωcm FZ p-Si wafers), Stephens and Green reported SRVs below 50 cm/s [91]. During an international carrier lifetime measurement comparison, S-values below 42 cm/s were obtained for (100)-orientated 1.5 Ωcm FZ p-Si material passivated using iodine/ethanol by the majority of the participants [92].

Quinhydrone/ethanol   Recently, a similar method has been reported based on a quinhydrone/ethanol solution [93]. Using this solution, a surface passivation could be demonstrated both for n- and p-type silicon. A maximum lifetime of 380 μs was reported for 5 Ωcm FZ p-type Si(100) wafers of 400 μm thickness corresponding to an S-value of 50 cm/s. For a lower doped 150 Ωcm Si wafer having a thickness of 380 μm, an effective carrier lifetime of 4.1 ms was reported corresponding to $S = 4.6$ cm/s. On an 0.7 Ωcm CZ n-type Si(100) wafer of 380 μm thickness the measured lifetime was 476 μs ($S_{\text{eff}} = 35$ cm/s).

Polymer films   A novel surface passivation method based on polymer films was introduced by Biro and Warta [94]. The authors claim that it is easy to apply and no special pre-cleaning steps are necessary. S-values as low as $30\,\text{cm/s}$ were found for various doping concentrations, nearly independent of bulk injection level being stable for at least $6\,\text{h}$.

UV radiation   A rather simple method to achieve surface passivation was reported by Katayama *et al.* [95]. They irradiated Si-wafers whose surfaces was only covered by a natural oxide by ultraviolet light and observed an increase of the measured effective carrier lifetime. They reported τ_{eff} values of several hundred microseconds for p- and n-type silicon, however, the material had a relatively high resistivity of $20 - 30\,\Omega\text{cm}$. Furthermore, the passivation observed was rather unstable and already after $4-5\,\text{min}$, the originally measured carrier lifetimes were reached.

3.2   Carrier Lifetime Measurement Techniques

In order to measure the carrier lifetime of a sample a number of contactless measurements techniques have been employed [82]. In general, the carrier lifetime is measured via the photoconductance of the sample since it is easily experimentally accessible. Many techniques have been used to sense the conductance without contacting the wafer, including microwave reflectance ([96, 97, 98]), the transmission of infrared light ([99, 100, 101, 102, 103]) and the use of a coil to couple the wafer conductance inductively to a resonant circuit ([104, 47]).

The microwave-detected photoconductance decay measurement (MW-PCD) technique and the quasi-steady-state photoconductance (QSSPC) technique have found widespread use and were also employed in this study. The techniques are described in Section 3.2.1 and Section 3.2.2, respectively.

3.2.1   Microwave-Detected Photoconductance Decay (MW-PCD)

The time dependence of the excess carrier density after carrier excitation is terminated, is given by the expression (Eq. 2.2 and 2.4)

$$\Delta n = \Delta n_0\, e^{-\frac{t}{\tau_{\text{eff}}}}, \tag{3.2}$$

where Δn_0 denotes the excess carrier concentration at $t = 0$. The transient decay of the excess photoconductance $\Delta\sigma$ corresponds to the decay of the excess carrier density via the expression

$$\Delta\sigma(t) = q(\mu_n\Delta n(t) + \mu_p\Delta p(t))\,W, \tag{3.3}$$

where W is the sample thickness and μ_n and μ_p are the electron and hole mobilities. Assuming charge neutrality ($\Delta n = \Delta p$), the excess photoconductance is proportional to the excess carrier density. In MW-PCD, the photoconductance is sensed by microwave reflection. The measured reflected microwave intensity (P) is a non-linear function of the conductance of the sample ($P = P(\sigma)$). Also, the mobilities μ_n and μ_p are functions of Δn in the high-injection regime ([105, 106, 107]). Hence, sufficiently small changes of $\Delta\sigma$ have to be assured

in order to guarantee a linear relation between ΔP and Δn. Moreover, in general, Eq. 3.2 is valid only over a small injection range, since τ_{eff} itself is a function of the carrier density. Thus, light-biased techniques are preferred where a steady-state background carrier density is generated and the excess photoconductance is created by a comparatively small laser pulse.

In this study, light-biased MW-PCD measurements were performed using a modified Phoenicon MRM system. In this system, the sample is illuminated by 100 ns light pulses from a 904 nm GaAs laser diode (20 pulses/s), increasing the wafer conductance. The decay of the photoconductance after termination of each laser pulse is recorded by time-resolved measurements of the microwave power (microwave frequency 22 GHz) reflected from the silicon wafer under test. Due to spatially inhomogeneous carrier distributions immediately after each laser pulse, a multi-exponential decay occurs at the beginning of each transient. Hence, the effective carrier lifetime is determined by a fit to the mono-exponential part of the asymptotic photoconductance decay. In order to adjust a defined injection level within the wafer, in addition to the laser pulses the sample is illuminated by a constant bias light from a halogen lamp. The bias light intensity is varied by means of a combination of different neutral density filters. At each bias light level the laser pulse energy is adjusted to ensure that the laser-induced excess carrier concentration is small compared with the injection level generated by the steady-state illumination. For technical details of the measurement system, the interested reader is referred to [108, 12].

It should be emphasised that light-biased PCD techniques measure *differential* SRVs as was remarked by Brendel *et al.* [109] as well as *differential* bulk carrier lifetimes as was shown by Aberle *et al.* [110, 111]. The differential SRV is defined as

$$S_{\text{eff.diff}}(n_{\text{b}}) \equiv \left. \frac{\partial U_{z<d_{\text{sc}}}(\Delta n)}{\partial \Delta n} \right|_{n_{\text{b}}} \tag{3.4}$$

while the differential bulk lifetime as

$$\tau_{\text{b.diff}}(n_{\text{b}}) \equiv \left[\frac{\partial U_{\text{b}}(\Delta n)}{\partial \Delta n} \right]_{n_{\text{b}}}^{-1}. \tag{3.5}$$

n_{b} denotes the excess carrier density generated by the bias light. The total excess carrier density can be written as

$$\Delta n(t) = n_{\text{b}} + \delta n(t), \tag{3.6}$$

where $\delta n \ll n_{\text{b}}$ has to be ensured for Eq. 3.4 and Eq. 3.5 to be valid. In order to obtain *actual* quantities, the $S_{\text{eff.diff}}$ and $\tau_{\text{b.diff}}$ have to be integrated [110, 112, 111]:

$$S_{\text{eff}}(n_{\text{b}}) = \frac{1}{n_{\text{b}}} \int_0^{n_{\text{b}}} S_{\text{eff.diff}}(\Delta n) d\Delta n \tag{3.7}$$

and

$$\tau_{\text{b}} = n_{\text{b}} \left(\int_0^{n_{\text{b}}} \tau_{\text{b.diff}}^{-1}(\Delta n) d\Delta n \right)^{-1}. \tag{3.8}$$

A simplified, approximate evaluation was proposed by Schuurmans *et al.* [112]. They took advantage of the fact that for sufficiently small effective SRVs, the approximate expression

given in Eq. 2.97 is valid. In this case, the actual effective lifetime τ_{eff} can be calculated from the measured differential effective lifetime $\tau_{\text{eff.diff}}$ by integration over the incident power density E:

$$\tau_{\text{eff}} = \frac{1}{E} \int_0^E \tau_{\text{eff.diff}}(\tilde{E}) d\tilde{E}. \tag{3.9}$$

After the calculation of τ_{eff}, Eq. 2.97 can be used to calculate the actual quantities S_{eff} or τ_{b}, respectively.

3.2.2   Quasi-Steady-State Photoconductance (QSSPC)

A drawback of the transient measurements is the fact that the measurement of short carrier lifetimes requires fast electronics for recording the photoconductance decay and a light pulse with a very steep cut-off ramp. Sinton and Cuevas introduced a carrier lifetime measurement technique based on the measurement of the photoconductance under quasi-steady-state illumination [113]. Nagel *et al.* generalised their analysis procedure in order to extent the capability of the method to longer carrier lifetimes [114]. Here, we will give a brief outline of the evaluation scheme. The time evolution of the carrier density is governed by the well-known continuity equation:

$$\frac{\partial \Delta n}{\partial t} = G(t) - U(t) + \frac{1}{q}\nabla J. \tag{3.10}$$

In the case of a spatially uniform carrier concentration, i.e., a homogeneous photogeneration and small SRVs, the last term of Eq. 3.10 vanishes. For simplicity, the quantities Δn, G and U are taken as spatially averaged. Upon insertion of the relationship $U_{\text{eff}} = \Delta n/\tau_{\text{eff}}$ (Eq. 2.96 and 2.4) Eq. 3.10 can be rewritten as

$$\tau_{\text{eff}} = \frac{\Delta n(t)}{G(t) - \frac{\partial \Delta n(t)}{\partial t}}. \tag{3.11}$$

In order to determine τ_{eff} from this definition, it is therefore necessary to measure the time dependence of the excess carrier density and the generation rate within the test sample. The experimental apparatus used in the course of this work is shown in Fig. 3.5 [115]. The apparatus measures both, the time dependence of the excess photoconductance of the test sample $\Delta\sigma(t)$ and that of the generation rate $G(t)$ at the same time. The excess carrier density in the test sample Δn can be calculated via

$$\Delta n(t) = \frac{\Delta\sigma(t)}{q(\mu_n + \mu_p)W}. \tag{3.12}$$

The generation rate is determined from the short-circuit current I_{sc} of the reference solar cell:

$$I_{\text{sc}}(t) = qW_{\text{cell}}G(t), \tag{3.13}$$

where W_{cell} is the cell thickness. A factor T_{eff} is introduced to take into account reflection and transmission differences between the reference cell and the test sample. Hence, the

generation rate is given by the expression

$$G(t) = \frac{I_{sc}(t)}{qW} T_{eff}. \tag{3.14}$$

The effective lifetime can then be calculated using Eq. 3.11 where the excess carrier density is determined via Eq. 3.12 and the generation rate via Eq. 3.14.
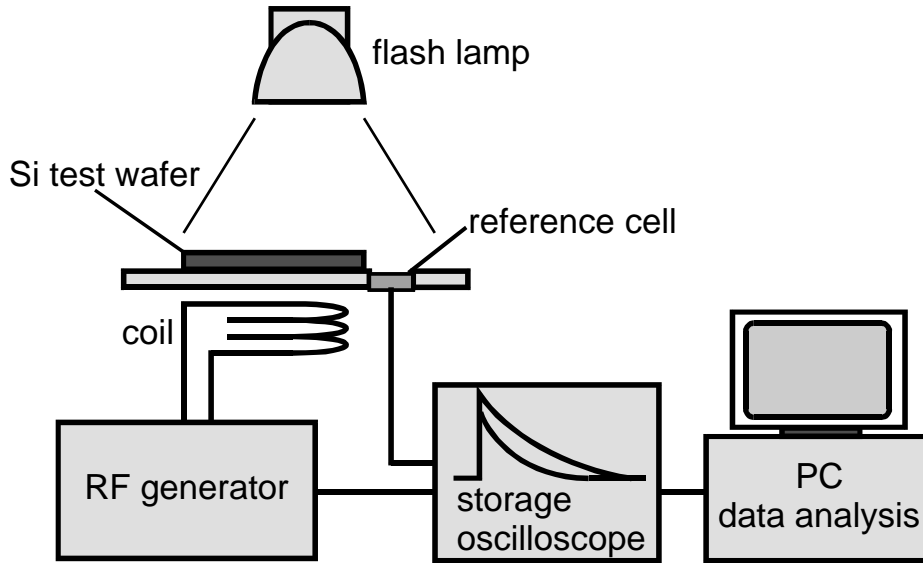

Figure 3.5: Schematic of the inductively-detected photoconductance apparatus used for the QSSPC measurements.

Up to now we have assumed a spatially homogeneous carrier profile. Nagel *et al.* [116] and Cuevas and Sinton [117] have discussed the impact of a high SRV on the spatial distribution of the excess carrier density. Nagel *et al.* found that in the case of a spatially non-uniform photogeneration by illumination with a wavelength of $\lambda = 400$ nm, the measurement error does not exceed 5 % if $S < 310$ cm/s assuming wafer thicknesses below 300 μm. In the case of spatially more uniform photogeneration ($\lambda = 1140$ nm), S-values as high as 5700 cm/s are tolerable. We used a filter that cuts off the flash spectrum at wavelengths below 700 nm. Since we were basically concerned with passivation techniques providing a low surface recombination, the samples comply with the above mentioned assumptions.

A further difficulty arises from inversion layers at the sample surface contributing to the excess photoconductance of the sample. Bail *et al.* discussed the influence of an inversion layer on the measured effective carrier lifetime and derived an expression for the excess photoconductance [118]. In the following, we present a derivation for the influence on the effective carrier lifetime. As a starting point, we consider the excess photoconductance for flat band conditions

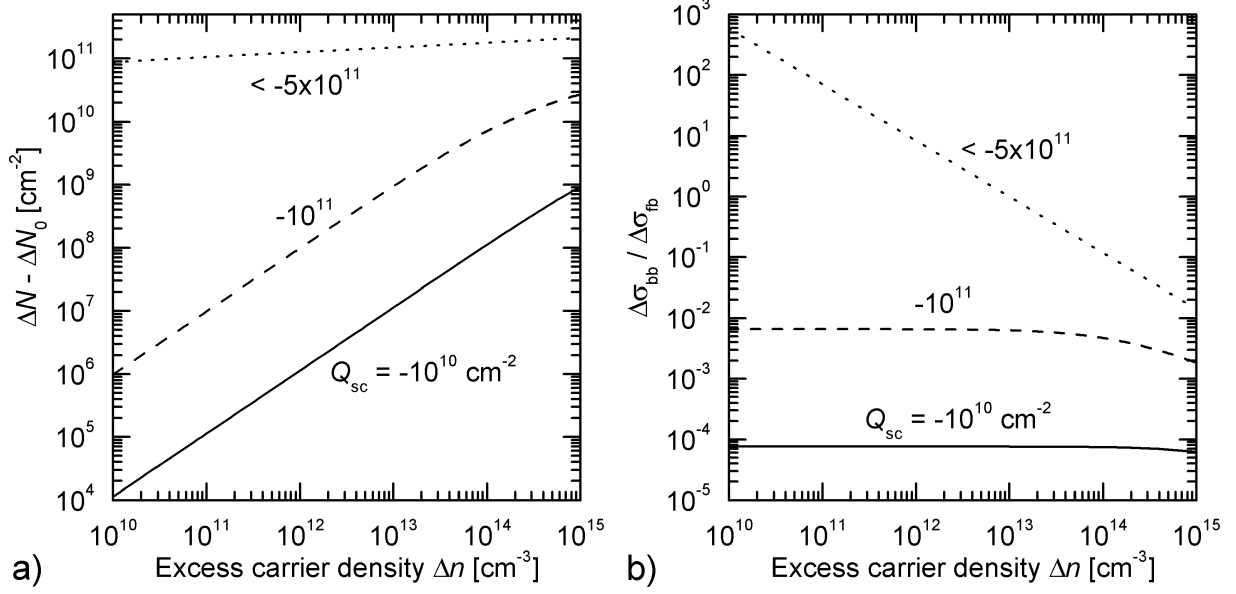$$\Delta\sigma_{fb} = q\Delta n_b W(\mu_n + \mu_p). \tag{3.15}$$

Figure 3.6: a) Difference of the excess surface-carrier density under illumination and in thermal equilibrium $\Delta N - \Delta N_0$ as a function of Δn for different charge densities in the space-charge region Q_{sc}. For $Q_{\mathrm{sc}} < -5 \times 10^{11}\,\mathrm{cm}^{-3}$ strong inversion conditions prevail at the surface. b) Ratio of the band-bending induced excess photoconductance $\Delta\sigma_{\mathrm{bb}}$ and the flat-band excess photoconductance $\Delta\sigma_{\mathrm{fb}}$ ($\frac{\Delta\sigma_{\mathrm{bb}}}{\Delta\sigma_{\mathrm{fb}}} = \frac{2(\Delta N - \Delta N_0)}{\Delta n_{\mathrm{b}} W}$ from Eq. 3.23). Assumptions: $W = 300\,\mu\mathrm{m}$, p-Si, $N_{\mathrm{A}} = 10^{16}\,\mathrm{cm}^{-3}$, $T = 300\,\mathrm{K}$, $D_{\mathrm{it}} = 0$, hence, $Q_{\mathrm{f}} = -Q_{\mathrm{sc}}$.

The effect of a band-bending towards the surface is taken into account by the excess surface-carrier densities defined as the number (per unit surface area) of mobile electrons ΔN and holes ΔP in the space-charge region with respect to their numbers under flat-band conditions. It should be noted that if ΔN is positive then ΔP is negative, and conversely. According to this definition, the densities can be expressed as ([15], [31])

$$
\begin{aligned}
\Delta N &= \int_0^\infty (n(z) - n_{\mathrm{b}})\,dz \quad \text{and} \\
\Delta P &= \int_0^\infty (p(z) - p_{\mathrm{b}})\,dz.
\end{aligned}
\tag{3.16}
$$

In terms of these quantities, the space-charge density Q_{sc} is given by

$$
Q_{\mathrm{sc}} = \Delta P - \Delta N.
\tag{3.17}
$$

By changing the variable of integration to Ψ and using Eq. 2.42 and 2.49, we obtain

$$
\begin{aligned}
\Delta N &= \int_{\Psi_{\mathrm{s}}}^{0} \frac{n(\Psi) - n_{\mathrm{b}}}{d\Psi/dz} d\Psi \\
&= n_{\mathrm{b}} \beta \lambda_{\mathrm{D}} \int_{\Psi_{\mathrm{s}}}^{0} \frac{e^{\beta\Psi} - 1}{\mp F(\Psi, \phi_n, \phi_p)} d\Psi \quad \text{and} \\
\Delta P &= p_{\mathrm{b}} \beta \lambda_{\mathrm{D}} \int_{\Psi_{\mathrm{s}}}^{0} \frac{e^{-\beta\Psi} - 1}{\mp F(\Psi, \phi_n, \phi_p)} d\Psi.
\end{aligned}
$$
(3.18)

Hence, the band-bending induced excess photoconductance is given by the expression

$$
\begin{aligned}
\Delta\sigma_{\mathrm{bb}} &= 2q \left\{ (\Delta N - \Delta N_0)\mu_n + (\Delta P - \Delta P_0)\mu_p \right\} \\
&= 2q(\Delta N - \Delta N_0)(\mu_n + \mu_p),
\end{aligned}
$$
(3.19)

where ΔN_0 (ΔP_0) are the excess surface-carrier densities in thermal equilibrium and Eq. 3.17 was used for the last transformation. The total excess photoconductance is then given by the expression

$$
\Delta\sigma = \Delta\sigma_{\mathrm{fb}} + \Delta\sigma_{\mathrm{bb}}.
$$
(3.20)

For photoconductance-based techniques, $\Delta\sigma$ is measured, but for the determination of τ_{eff}, the flat-band conductance is required only. The error that arises since $\Delta\sigma$ instead of $\Delta\sigma_{\mathrm{fb}}$ is used for the evaluation will now be derived. In the static case, i.e., $\partial\Delta n/\partial t = 0$, the effective lifetime is given by the expression (Eq. 3.11)

$$
\tau_{\mathrm{eff}}(\Delta n_{\mathrm{b}}) = \frac{\Delta n_{\mathrm{b}}}{U_{\mathrm{eff}}} = \frac{\Delta n_{\mathrm{b}}}{G},
$$
(3.21)

with the excess carrier density given by Eq. 3.15. Due to the measurement of the total photoconductance $\Delta\sigma$, an apparent excess carrier density of

$$
\Delta n_{\mathrm{b.app}} = \frac{\Delta\sigma}{qW(\mu_n + \mu_p)}
$$
(3.22)

is determined. Hence, using Eq. 3.21, 3.15 and 3.19, the apparent effective lifetime is calculated to be

$$
\begin{aligned}
\tau_{\mathrm{eff.app}} &= \frac{\Delta n_{\mathrm{b.app}}}{G} \\
&= \frac{\Delta\sigma_{\mathrm{fb}} + \Delta\sigma_{\mathrm{bb}}}{GqW(\mu_n + \mu_p)} \\
&= \tau_{\mathrm{eff}} \left(1 + \frac{\Delta\sigma_{\mathrm{bb}}}{\Delta\sigma_{\mathrm{fb}}} \right) \\
&= \tau_{\mathrm{eff}} \left(1 + \frac{2(\Delta N - \Delta N_0)}{\Delta n_{\mathrm{b}} W} \right).
\end{aligned}
$$
(3.23)

It can be seen from Eq. 3.23 that the difference between $\tau_{\text{eff.app}}$ and τ_{eff} depends only on the thickness of the sample, the injection level and the difference $\Delta N - \Delta N_0$. Fig. 3.6 (a) shows the difference $(\Delta N - \Delta N_0)$ as a function of Δn where a $300\,\mu\text{m}$ thick p-Si wafer with $N_A = 10^{16}\,\text{cm}^{-3}$ was assumed. The difference is relatively constant for strongly negative Q_{sc} values (inversion conditions) while it increases approximately linearly with Δn for lower Q_{sc}. The factor $\Delta\sigma_{\text{bb}}/\Delta\sigma_{\text{fb}}$ that determines the difference between $\tau_{\text{eff.app}}$ and τ_{eff} is shown in Fig. 3.6 (b). For low band-bending conditions a very low value is determined over the entire injection range. Thus, the difference between $\tau_{\text{eff.app}}$ and τ_{eff} is negligible. If strong inversion conditions at the surface prevail, the ratio $\Delta\sigma_{\text{bb}}/\Delta\sigma_{\text{fb}}$ increases with decreasing excess carrier density Δn. From Fig. 3.6 (b), it can be seen that $\tau_{\text{eff.app}}$ is twice the value of τ_{eff} for $\Delta n = 10^{13}\,\text{cm}^{-3}$ (a factor of 10 for $\Delta n = 10^{12}\,\text{cm}^{-3}$). Hence, in the low-injection regime, this is a drastic effect even for thick wafers. Similar results were obtained using PC1D [35] calculations. It should be noted that for strongly negative Q_{sc} values, the approximation given in Eq. 2.61 cannot be used for the determination of $\Delta N - \Delta N_0$. The approximation would result in $\Delta N \approx \Delta N_0 \approx Q_{\text{sc}}$ and, hence, the difference $\Delta N - \Delta N_0$ as well as $\Delta\sigma_{\text{bb}}$ would vanish.

The effect of surface space-charge regions on transient photoconductance decay measurements are discussed in Ref. [119] and [120].

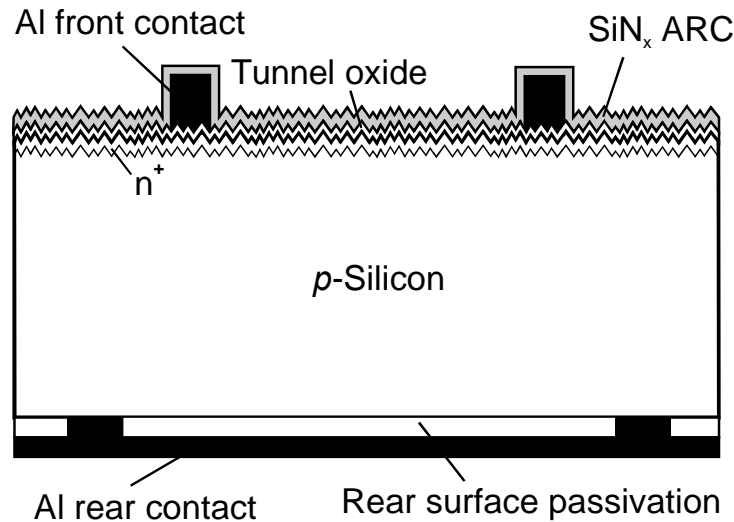## 3.3   Fabrication of Solar Cells

Figure 3.7: Schematic cross section of an MIS-contacted n^+-p-junction silicon solar cell with a passivated rear surface and a front grid deposited by metal evaporation through a shadow mask. The rear surface was passivated by SiO_2 (Process A in Fig. 3.8), SiN_x (Process B) or a-Si:H (Process C).
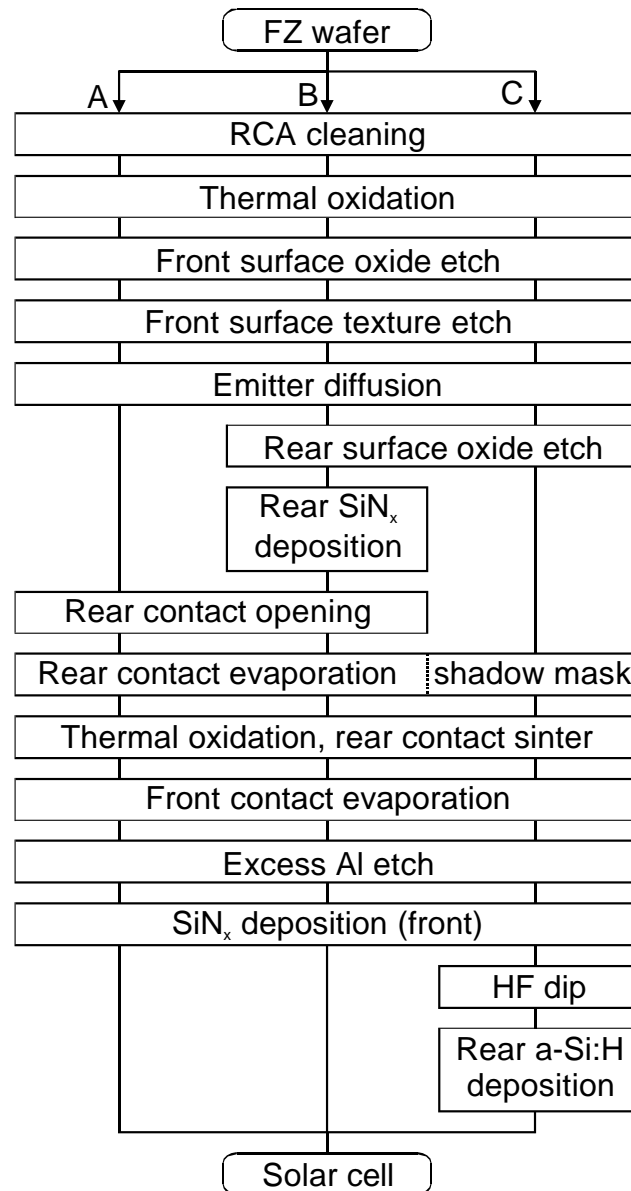
```
                        ┌─────────────┐
                        │   FZ wafer  │
                        └─────────────┘
            A│              B│              C│
        ┌──────────────────────────────────────────┐
        │              RCA cleaning                 │
        ├──────────────────────────────────────────┤
        │            Thermal oxidation              │
        ├──────────────────────────────────────────┤
        │         Front surface oxide etch          │
        ├──────────────────────────────────────────┤
        │        Front surface texture etch         │
        ├──────────────────────────────────────────┤
        │            Emitter diffusion              │
        └──────────────────────────────────────────┘
                  ┌──────────────────────────────────┐
                  │      Rear surface oxide etch      │
                  ├───────────────────┐
                  │     Rear SiNₓ     │
                  │    deposition     │
        ┌─────────┴───────────────────┘
        │      Rear contact opening    │
        ├──────────────────────────────┬───────────┐
        │   Rear contact evaporation   │shadow mask│
        ├──────────────────────────────────────────┤
        │   Thermal oxidation, rear contact sinter  │
        ├──────────────────────────────────────────┤
        │        Front contact evaporation          │
        ├──────────────────────────────────────────┤
        │              Excess Al etch               │
        ├──────────────────────────────────────────┤
        │           SiNₓ deposition (front)         │
        └──────────────────────────────────────────┘
                                  ┌───────────────┐
                                  │    HF dip     │
                                  ├───────────────┤
                                  │  Rear a-Si:H  │
                                  │   deposition  │
                                  └───────────────┘
                        ┌─────────────┐
                        │  Solar cell │
                        └─────────────┘
```

Figure 3.8: Processing sequence for MIS-contacted n^+-p-junction silicon solar cells. Reference solar cells with a SiO_2 film as rear surface passivation were processed according to process A. SiN_x and a-Si:H passivated solar cells were fabricated according to process B and process C, respectively.

MIS-contacted diffused n^+p junction (MIS-n^+p) solar cells were fabricated in the course of this work following a cell structure that is regularly employed at ISFH [9]. Starting material were $0.5\,\Omega\mathrm{cm}$ and $1.5\,\Omega\mathrm{cm}$ FZ p-silicon wafers with shiny etched surfaces and a thickness of $300\,\mu\mathrm{m}$. The samples were given an RCA clean [121] and, subsequently, a $250\,\mathrm{nm}$ thick thermal oxide was grown at $1050\,^\circ\mathrm{C}$, serving as diffusion mask and rear surface passivation for the cells passivated using SiO_2 films at the rear surface. Subsequently, a diffusion

window was opened and the wafers were immersed in a solution of KOH and isopropanol at 75 °C, resulting in a front surface texture consisting of upright random pyramids. The phosphorous diffusion was performed at 830 °C using a POCl$_3$ source, leading to an emitter with a sheet resistance of around 100 Ω/sq. For the cells passivated at the rear surface using SiN$_x$ films (Process B in Fig. 3.8) and a-Si:H films (Process C), respectively, the rear oxide film was etched off. Subsequently, a PECVD SiN$_x$ film was deposited at 400 °C using the deposition chamber described in Section 3.1.1 on the rear surface of the SiN$_x$ passivated cells. After the definition of contact holes through the rear passivating oxide or nitride film, respectively, and the removal of the P$_2$O$_5$ layer from the front surface, the rear electrode was formed by evaporation of Al onto the entire rear surface (Process A and B). For the a-Si:H passivated cells (Process C), the rear contact grid was evaporated through a shadow mask. A thin tunnel oxide was grown in a 15-min thermal oxidation step at 500 °C, which also provides the sintering of the back contact. Subsequently, the front grid was deposited by vacuum evaporation of Al through a shadow mask. The front electrode consists of 20 μm wide fingers and covers about 4 % of the front surface (including the busbar). An antireflection coating (ARC) consisting of SiN$_x$ was deposited onto the front surface of the cell by means of PECVD. The front SiN$_x$ films were deposited at 300 °C since the front contacts do not withstand higher temperatures, in contrast to the deposition temperature of 400 °C used for the preparation of the carrier lifetime test structures and the rear surface. In order to minimise optical losses, a second antireflection coating consisting of SiO$_2$ deposited using PECVD was prepared for some of the cells. Finally, for the a-Si:H passivated solar cells, an HF dip was performed and the a-Si:H films were deposited as described in Section 3.1.2.

3.4   Solar Cell Characterisation Techniques

3.4.1   *I-V* curves

The solar cells fabricated in this work were characterised using *I-V* curves measured in the dark and under illumination. The illumination was provided by halogen lamps supplied by a highly stabilised DC power system. During each measurement, the sample was mounted on a temperature controlled holder. *I-V* curves were measured under standard test conditions (STC), i.e., an illumination intensity of 1 sun (100 mW/cm^2) and a temperature of 25 °C, but with a spectrum determined by the halogen lamps instead of the required AM1.5G spectrum. The measurement deviations due to the spectral mismatch are rather small as was additionally proven by solar cells whose parameters were independently confirmed by the Fraunhofer ISE CalLab. A measurement of the light *I-V* curve resulted in the following solar cell parameters: short-circuit current density J_{sc}, open-circuit voltage V_{oc}, fill factor FF and output power P_{out}. For an illumination intensity of 1 sun, the standard conversion efficiency η was obtained. The series resistances were evaluated using the method proposed by Aberle *et al.* [122] and the shunt resistance was obtained from the slope of the dark *I-V* curve at low forward bias voltage (40 mV). The measurement set-up is further described in Ref. [122]. The dark and illuminated *I-V* curves can locally be described by a one-diode

model:

$$J_{\text{drk}} = J_{0.\text{drk}} \left(e^{\beta V / m_{\text{drk}}} - 1 \right) \quad \text{and} \tag{3.24}$$

$$J_{\text{lgt}} = J_{0.\text{lgt}} \left(e^{\beta V / m_{\text{lgt}}} - 1 \right) - J_{\text{sc}}. \tag{3.25}$$

Knowledge of the ideality factors m_{drk} and m_{lgt} and the saturation current density $J_{0.\text{drk}}$ and $J_{0.\text{lgt}}$ as a function of the cell voltage is helpful for the understanding of the dominant recombination mechanisms in solar cells. The ideality factors are determined via

$$m = \beta \left(\frac{\partial \ln J}{\partial V} \right)^{-1}, \tag{3.26}$$

where m and J have to be replaced by m_{drk} and J_{drk} or m_{lgt} and J_{lgt}, respectively. In Chapter 6 the ideality factor is used to determine the loss mechanisms in solar cells passivated at the rear surface using SiN_x films.

3.4.2   Spectral Response

The optical absorption coefficient of silicon varies strongly with the wavelength. This fact can be exploited to investigate the depth dependencies of recombination properties within the silicon solar cell. The spectral response SR of a solar cell is defined as the output current under short-circuit $J_{\text{sc}}(\lambda)$ per unit incident power in monochromatic light $E(\lambda)$ as a function of wavelength λ:

$$\text{SR}(\lambda) \equiv \frac{J_{\text{sc}}(\lambda)}{E(\lambda)}. \tag{3.27}$$

Since the response of cells to light of increasing intensity may not be linear, a preferred method is to use a white light bias source and measure the incremental response to a small superimposed alternating component of monochromatic light. As for the light-biased MW-PCD technique (Section 3.2.1), a *differential* quantity - the differential spectral response - is measured when using a bias light [123, 124]:

$$\text{SR}_{\text{diff}}(\lambda, E_{\text{b}}) \equiv \left. \frac{\partial J_{\text{sc}}(\lambda, E_{\text{b}})}{\partial E(\lambda)} \right|_{E_{\text{b}}}, \tag{3.28}$$

where E_{b} is the bias light intensity. In order to determine the actual spectral response SR_{diff} has to be integrated over the bias light intensity:

$$\text{SR}(\lambda, E_{\text{b}}) = \frac{1}{E_{\text{b}}} \int_0^{E_{\text{b}}} \text{SR}_{\text{diff}} \, dE. \tag{3.29}$$

By a simple transformation, the external quantum efficiency EQE defined as the number of electron-hole pairs collected under short-circuit conditions to the number of incident photons, is obtained

$$\text{EQE}(\lambda, E_{\text{b}}) \equiv \text{SR}(\lambda, E_{\text{b}}) \frac{hc}{q\lambda}, \tag{3.30}$$

where h is Planck's constant and c is the speed of light. Considering only photons that are absorbed by the solar cell, the internal quantum efficiency IQE is defined as

$$\text{IQE}(\lambda, E_\text{b}) \equiv \frac{\text{EQE}(\lambda, E_\text{b})}{1 - R^*(\lambda)}, \tag{3.31}$$

where R^* accounts for reflection and transmission losses and absorption losses other than in the active cell volume. The IQE at infrared wavelengths ($\lambda = 800 - 1000\,\text{nm}$) can be used to extract information about the effective carrier diffusion length L_eff in the bulk of the cell that is composed by the bulk carrier lifetime and the rear surface recombination velocity. By plotting the inverse IQE as a function of inverse absorption coefficient α, L_eff can be determined via the expression [125]:[1]

$$\frac{1}{\text{IQE}} = 1 + \frac{1}{\alpha L_\text{eff}}. \tag{3.32}$$

For p-type material and low-injection conditions, L_eff is defined as

$$L_\text{eff} \equiv L_n \frac{S_\text{r}\frac{L_n}{D_n}\sinh(\frac{W}{L_n}) + \cosh(\frac{W}{L_n})}{S_\text{r}\frac{L_n}{D_n}\cosh(\frac{W}{L_n}) + \sinh(\frac{W}{L_n})}, \tag{3.33}$$

where $L_n = \sqrt{D_n \tau_\text{b}}$ is the electron diffusion length in the bulk, S_r is the SRV at the rear surface, D_n is the electron diffusion length and W is the width of the cell. If the bulk lifetime is known, Eq. 3.32 and 3.33 can be used to determine the SRV at the rear surface. This will be done in Chapter 6 for cells with SiN$_\text{x}$ rear surface passivation and compared with data obtained from lifetime measurements. Keller *et al.* critically discussed the assumptions that led to Eq. 3.32 [126].

3.4.3   Light Beam Induced Current (LBIC)

The light beam induced current (LBIC) method is used for a spatially resolved measurement of the short-circuit current of a cell. It is often applied to multi-crystalline solar cells to obtain a mapping of the inhomogeneous diffusion length distribution in these cells. In this work, the response of cells to an infrared light beam (980 nm) is measured. This yields spatially resolved diffusion lengths and, hence, rear surface recombination velocities.

---

[1]In the regime $\lambda = 800 - 1000\,\text{nm}$, the light penetration depth is $1/\alpha = 12 - 156\,\mu\text{m}$, hence, the absorption occurs predominantly in the bulk assuming a cell thickness of about $300\,\mu\text{m}$.

Chapter 4

Characterisation of Silicon Nitride Films

Silicon nitride has been used since the 1960s in silicon semiconductor components. Today, the applications of silicon nitride films include (1) masking layers for diffusion, oxidation and etch processes, (2) insulating films, (3) circuit encapsulation, (4) MNOS memory structures, (5) thin-film transistors, and (6) CCD structures. For a number of reasons, including the adjustable refractive index, SiN_x films have been introduced in photovoltaic applications as well. First reports were published by Wang *et al.* in 1973 [127] and by Hovel in 1975 [128]. Starting in 1980, Hezel and coworkers have consequently introduced SiN_x films in photovoltaics [129, 130]. First, they used SiN_x films to fabricate silicon inversion layer solar cells. Due to the high amount of fixed positive charges within the films that can be increased in conjunction with a thin silicon dioxide film and cesium ions, an inversion layer is induced on the surface of a p-type silicon wafer. During their research the additional surface passivation properties that SiN_x films provide became obvious. Nowadays, SiN_x films have found widespread use in photovoltaics including their use as antireflection coatings [131, 132], as surface passivation films [130, 64] and as a hydrogen source for bulk passivation [133, 134, 135].

SiN_x surface passivation has attracted increasing attention and has been investigated by several research groups [136, 69, 137, 37, 138, 139]. A detailed investigation of the properties of PECVD SiN_x films that are typically used for silicon solar cells was carried out by Lauinger *et al.* [62, 69] and by Schuurmans [140]. The film composition, binding conditions and hydrogen content in dependence on the deposition parameters were investigated. Furthermore, the conductance, the temperature stability and the stability against UV radiation were examined. Nagel *et al.* investigated the optical properties of the films [141]. Schmidt *et al.* [37] as well as Schuurmans [140] investigated the interface parameters of Si/SiN_x interfaces. However, since the analysed films were deposited by direct PECVD at *low frequency*, the interface state density was rather high due to plasma damage during deposition and may be different from the SiN_x films that provide a superior surface passivation.

In this chapter, the properties of well-passivating SiN_x films are examined as a function of the film composition. The fixed charge density within the SiN_x films is examined in the dark using traditional capacitance-voltage (C-V) measurements (Section 4.2) and under

illumination using a novel technique based on lifetime measurements and corona charging (Section 4.3). Furthermore, the sheet resistance of the inversion layer that is induced at the Si surface if passivated using SiN_x films is investigated in Section 4.4. The effective SRV as a figure of merit for surface passivation quality is examined as a function of injection level for SiN_x films of different compositions (Section 4.5). Using the novel theoretical model developed in Section 2.4.4 and the parameters determined in this chapter, the $S_{eff}(\Delta n)$ curves are calculated.

4.1   Previous Work
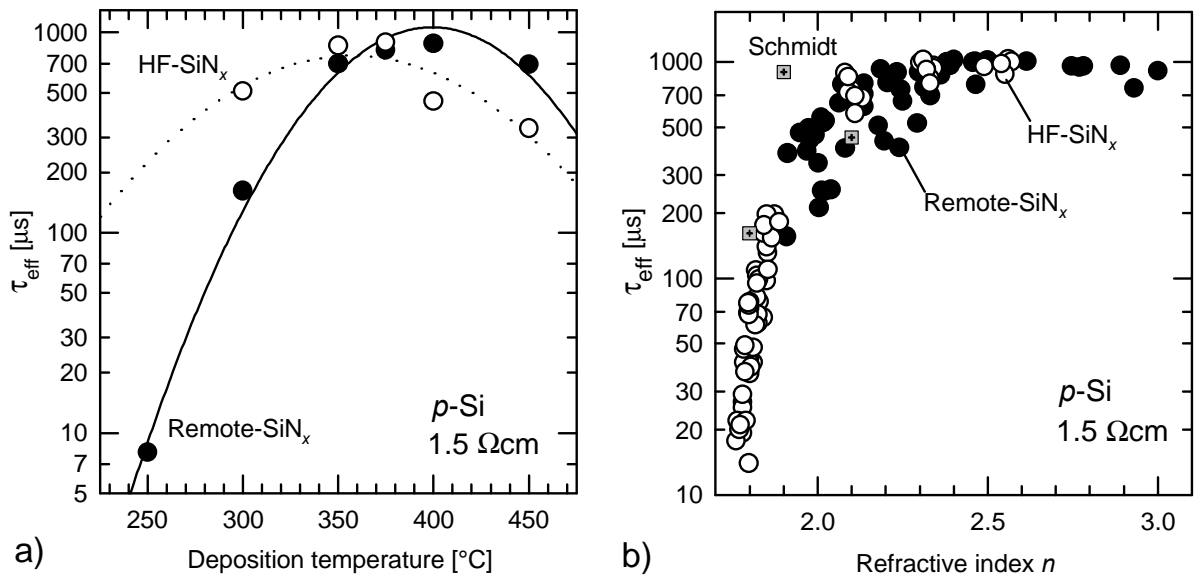
Figure 4.1: a) Measured effective carrier lifetime τ_{eff} of SiN_x passivated planar $1.5\,\Omega$cm FZ p-Si wafers as a function of the SiN_x deposition temperature for SiN_x films prepared by HF direct PECVD and remote PECVD [142]. b) Measured effective carrier lifetime τ_{eff} of SiN_x passivated planar $1.5\,\Omega$cm FZ p-Si wafers as a function of the refractive index of SiN_x films prepared by HF direct PECVD and remote PECVD (open and filled circles, deposition temperature $\sim$375 $^\circ$C) [142]. Also included are the results of $1\,\Omega$cm FZ p-Si samples passivated using HF direct PECVD (square x-hair, deposition temperature 400 $^\circ$C) published by Schmidt and Kerr [65].

The SRV as well as the chemical, mechanical, electrical and optical properties of the SiN_x films strongly depend on the preparation parameters used. Lauinger *et al.* optimised the deposition parameters of HF direct PECVD and remote PECVD SiN_x films and achieved very low SRVs at the Si/SiN_x interface [64, 142, 69]. An optimum deposition temperature in the range of $375 - 400\,^\circ$C was found. This can be seen in Fig. 4.1 (a) where τ_{eff} is shown as a function of the deposition temperature. Since identical silicon wafers were used, the differences in τ_{eff} can be ascribed to differences in surface passivation. Lauinger *et al.* also found that the impact of all deposition parameters on the refractive index n of the films

measured at 633 nm by ellipsometry is very similar to the impact on the passivation quality [69]. n is correlated with the effective carrier lifetime of the passivated silicon wafers in the manner that SiN_x films having high refractive indices result in very high effective carrier lifetimes (Fig. 4.1 (b)). This allows a fast and easy control of the passivation quality simply by measuring the refractive index of the SiN_x films. An increase of the refractive index n is correlated with a shift of the film composition towards silicon-rich films as was calculated by Robertson [143]. Experimentally, the stoichiometry of the films can be determined by Rutherford back scattering and elastic recoil detection. A compilation of data from different sources showing n as a function of the Si/N ratio (concentrations measured in atom%) can be seen in Fig. 4.2. Since n is easily accessible using ellipsometry, we use n throughout this study to assess the film composition.

Lauinger *et al.* found that the characteristics of SiN_x films deposited using a direct PECVD reactor are very similar to those prepared using a remote PECVD reactor (Fig. 4.1) [142]. Also included in Fig. 4.1 (b) are the results of $1\,\Omega$cm FZ p-Si samples passivated using HF direct PECVD and a deposition temperature of $400\,°C$ published by Schmidt and Kerr [65]. They used a modified process gas composition with a relatively high nitrogen concentration. The samples show a slightly different relation between the refractive index and the passivation quality they provide. Although the results for N-rich SiN_x films ($n = 1.8$) are very similar to those published by Lauinger *et al.* they found a maximum surface passivation for films with a ralatively low refractive index of $n \approx 1.9$. In contrast to our results published in this chapter and to those of Lauinger *et al.* the surface passivation decreases slightly towards higher refractive indices. The observed differences will be discussed in more detail at the end of this chapter.

Since SiN_x films prepared at a temperature of $400\,°C$ provide the most efficient surface passivation [69, 65], this temperature was used for all SiN_x depositions onto carrier lifetime test structures. The only parameter changed was the SiH_4 gas flow ($2 - 30\,sccm$). Doing so, the silicon content in the films could be adjusted from silicon-rich to nitrogen-rich films.

4.2   Capacitance-Voltage Measurements

4.2.1   High-Frequency C-V Measurements

The fixed charge density Q_f of dielectric films is usually obtained using capacitance-voltage (C-V) measurements carried out in the dark ([30, 31, 82]). Fig. 4.3 shows (a) the sample structure used, consisting of a metal-nitride-semiconductor (MNS) diode, and (b) the equivalent circuit for C-V measurements. The MNS samples were fabricated on shiny-etched $1.5\,\Omega$cm FZ p-Si wafers with (100) orientation. After an RCA cleaning, a PECVD SiN_x film was deposited on the front surface of the samples using identical deposition parameters as used for the carrier lifetime test structures (Tab. 3.1). Following the evaporation and sintering of the rear Al contact, the front Al contact was thermally evaporated in a vacuum chamber using a shadow mask to define the contact area. As a final step, an aluminium etch was performed to remove excess Al from parasitic evaporation at the Al dot edges. A Boonton 72B capacitance meter operating at high frequency (1 MHz) with a test signal
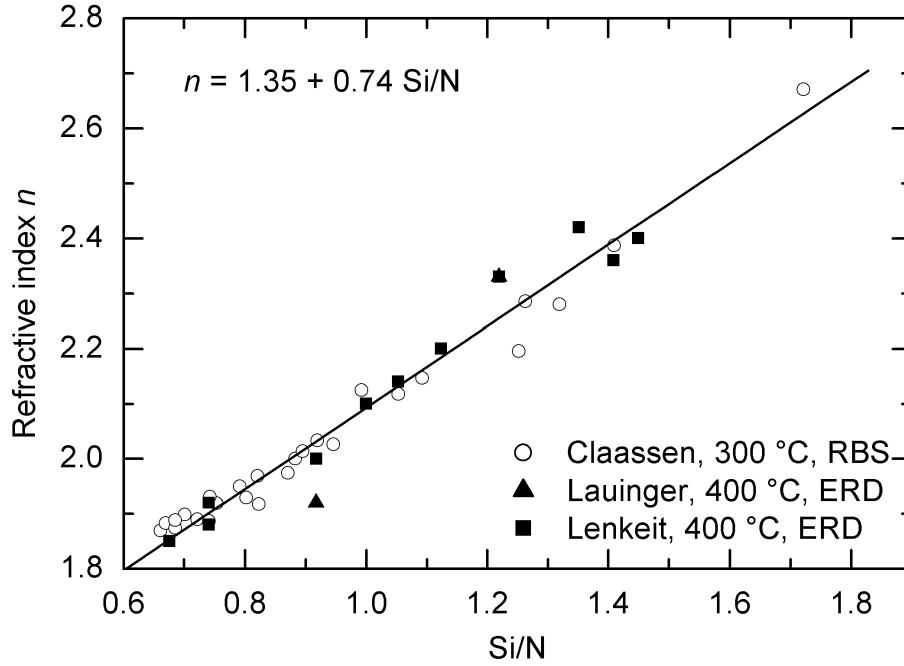
Figure 4.2: Empirically determined relationship between refractive index n and Si/N ratio. The data published by Claassen *et al.* were obtained with SiN_x films deposited at 300 °C using Rutherford back scattering (RBS) [144], while that by Lauinger [62] with SiN_x films deposited at 400 °C using elastic recoil detection (ERD). The refractive index was measured using ellipsometry with a wavelength of 633 nm.

of 100 mV was used for the measurements. The results of a typical high-frequency C-V measurement are shown in Fig. 4.4. The sample was prepared with a SiH_4 gas flow of 4.5 sccm and a deposition time of 2:50 min. The refractive index and the film thickness of the SiN_x layer was $n = 1.96$ and $d_{iG} = 63\,nm$, respectively. For the measurement, the bias voltage was ramped from 0 to -10 V (inversion to accumulation) first and then from -10 to 0 V (accumulation to inversion). A large hysteresis of about 2.1 V is observed in Fig. 4.4 which results from charging and discharging of bulk traps within the SiN_x film [145]. The charge density of the traps contributes to Q_f. This kind of behaviour is well-known and the basis for MNOS non-volatile memory structures [146]. For the insulator capacitance a value of $C_i = 86\,nF/cm^2$ was determined (dot size $A = 0.771\,mm^2$). Using $C_i = \epsilon_{SiN}/d_{iG}$, the dielectric permittivity was determined to be $\epsilon_{SiN} = 6.1\,\epsilon_0$. The total capacitance C_t of the MNS diode is a series connection of the insulator C_i and the semiconductor depletion-layer capacitance C_D (neglecting a contribution of the interface states) as is sketched in Fig. 4.3 (b):

$$C_t = \frac{C_i C_D}{C_i + C_D}. \tag{4.1}$$

At flatband, $C_D(V_{FB}) = \epsilon_{Si}/\lambda_D$ and, hence, $C_t(V_{FB}) = 64\,nF/cm^2$ ([31], p. 369). $\lambda_D = 42\,nm$ is the Debye length of the silicon substrate (Eq. 2.47) and ϵ_{Si} the permittivity of silicon.

From $C_t(V_{FB})$ and Fig. 4.4, a flatband voltage of $V_{FB} = -5.5\,\text{V}$ and $-7.6\,\text{V}$ is found for the virgin curve and for the reversely measured curve, respectively. For the determination of the fixed positive charge density, the work function difference between the metal and the silicon has to be taken into account using Eq. 2.59 and Eq. 2.60. With $\phi_m = 4.1\,\text{V}$ the work function of Al, $\chi_{Si} = 4.05\,\text{V}$ the electron affinity of silicon and $E_{C.b} - E_F = 0.92\,\text{eV}$ the difference between the conduction band edge and the Fermi level for $1.5\,\Omega\text{cm}$ silicon, a work function difference of $\Delta\phi_{ms} = -0.87\,\text{V}$ is calculated. Q_f can then be determined using Eq. 2.75, the condition of charge neutrality in the device (Eq. 2.36) and the conditions that hold for the flatband case, i.e., $\Psi_s = 0$ and $Q_{sc} = 0$:

$$Q_f = \frac{C_i/q\left(\Delta\phi_{ms} - V_{FB}\right) - Q_{it}}{1 - C_i\frac{d_{if}}{2\epsilon_{iG}}}. \tag{4.2}$$

Neglecting Q_{it} and assuming an equal order of magnitude for ϵ_{if} and ϵ_{iG} as well as $d_{if} \ll d_{iG}$, Eq. 4.2 simplifies to ([31], p. 395)

$$Q_f = C_i/q\left(\Delta\phi_{ms} - V_{FB}\right). \tag{4.3}$$

For the virgin (reverse) curve, a Q_f value of $2.5 \times 10^{12}\,\text{cm}^{-2}$ ($3.6 \times 10^{12}\,\text{cm}^{-2}$) is obtained. Note that for the given insulator capacitance, the work function difference is equivalent to a fixed positive charge density of $4.7 \times 10^{11}\,\text{cm}^{-2}$. The increase of the capacitance towards zero gate voltage in Fig. 4.4 is a measurement artifact due to the presence of an inversion layer underneath and in the vicinity of the contact. Due to the inversion layer conductivity, charge carriers next to the contact region contribute to the measured capacitance. Hence, the contact area is effectively increased.

In order to be able to achieve correspondence between experimental and theoretical data, Schmidt and Aberle [37, 38] proposed that Q_f decreases if the electron quasi-Fermi level is lifted towards the conduction band. However, although Q_f could be increased drastically by applying a negative voltage, it was not possible to decrease it significantly by applying positive voltages of up to $10\,\text{V}$. Furthermore, if strong inversion conditions at the surface and low injection conditions prevail, the difference between the conduction band edge at the surface $E_{C.s}$ and the electron quasi-Fermi level is independent of the illumination intensity which can be seen from the following derivation (note the opposite signs in the *energy* and *potential* image of the band diagram):

$$\begin{aligned}
\frac{E_{C.s}}{q} + \phi_{n.lgt} &= \frac{E_{C.b}}{q} + \phi_n - \Psi_s \\
&= \frac{E_{C.b}}{q} + \phi_p - \Psi_{s0} \\
&= \frac{E_{C.s}}{q} + \phi_{n.drk}, \tag{4.4}
\end{aligned}$$

where $\phi_{n.lgt}$, $\phi_{n.drk}$ and $E_{C.b}$ denote the electron quasi-Fermi potential under illumination and in the dark and the edge of the conduction band in the bulk, respectively. In the derivation, the relations $\Psi_s = \Psi_{s0} - V_{oc}$ (Eq. 2.62), $\phi_n = \phi_p - V_{oc}$ and $\phi_p = \phi_{n.drk}$ were used.

Hence, the assumption of Schmidt and Aberle [37, 38] that illumination changes the charge density of Q_f does not hold under low-level injection conditions. In Section 4.3, a novel technique is introduced to determine Q_f under illumination. With this method, it will be possible to check the assumption of Schmidt and Aberle for the first time experimentally.
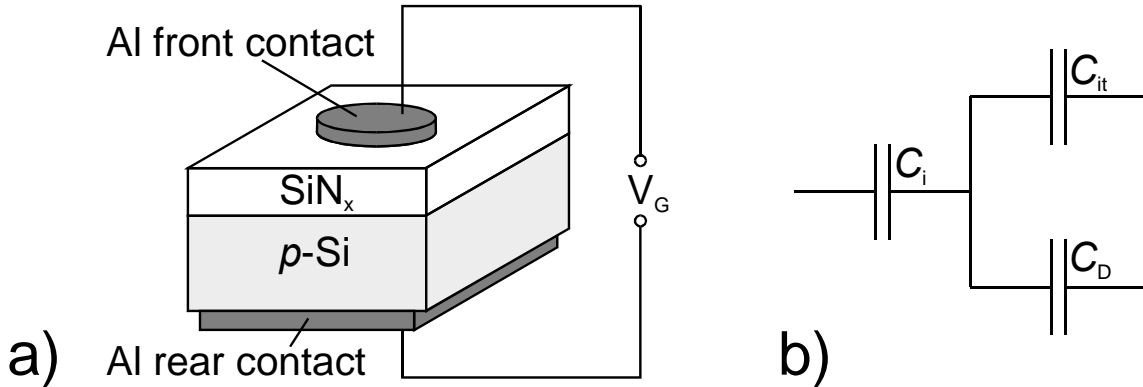

Figure 4.3: a) Schematic of the MNS sample structure used for C-V measurements. b) Equivalent circuit including the insulator capacitance C_i, the silicon depletion-region capacitance C_D and the capacitance associated with interface states C_{it}.

4.2.2   Combined High-Frequency and Quasi-Static C-V Measurements

Interface state densities can be determined with a higher degree of accuracy by simultaneously measure the high-frequency and the quasi-static C-V curves [30]. For these combined C-V measurements, the same sample structure as shown in Fig. 4.3 was used. The C-V curves were measured using a Keithley 595 combined quasi-static and a Keithley 590 high-frequency (1 MHz) C-V meter. Please refer to Ref. [30] for an introduction to the quasi-static capacitance technique and note that it is often referred to as low-frequency capacitance technique.

In order to examine the influence of the SiN_x film composition on the interface properties, two representative samples having different SiN_x films as gate insulators were examined. The samples were prepared using the parameters given in Tab. 3.1. SiH_4 gas flows of 2 sccm and 4.5 sccm and deposition times of 5 min and 2:50 min were used for sample A and B, respectively. This parameters resulted in SiN_x film having a refractive index of $n = 1.88$ for sample A and $n = 1.96$ for sample B, i.e., sample B was passivated with a SiN_x film having a higher silicon content. The measurement results for the two different MNS capacitors are shown in Fig. 4.5 (symbols). The plots (a1) and (b1) show the quasi-static capacitance C_{QS} and the high-frequency capacitance C_{HF} as a function of gate voltage V_G for sample A and B, respectively. As can be seen from the capacitance difference between the C_{QS} and the C_{HF} curve in the depletion range ($V_G \approx -3\,\mathrm{V}$ (sample A) and $V_G \approx -4\,\mathrm{V}$ (sample B)) the
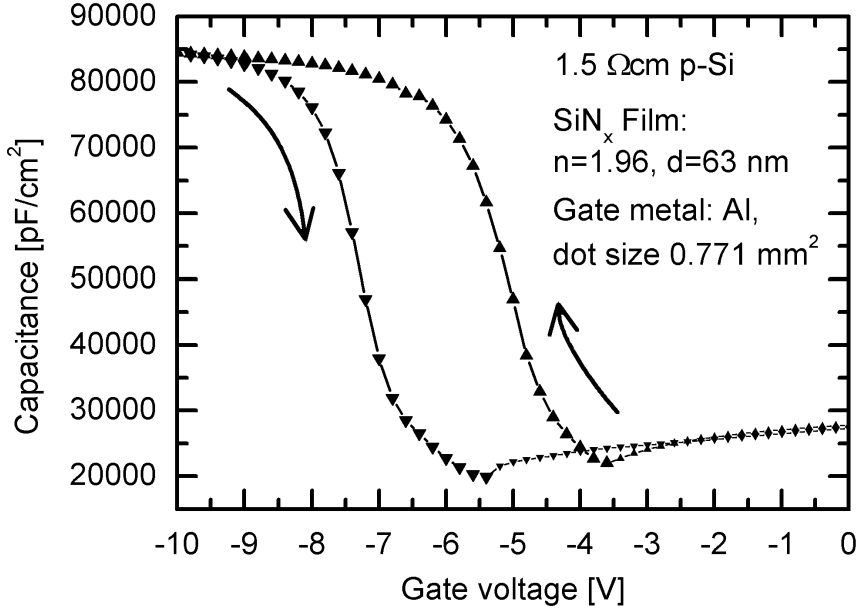
Figure 4.4: Measured high-frequency C-V curves of an MNS capacitor. A hysteresis of about 2.1 V is observed between the initial measurement (inversion to accumulation) and the reverse measurement (accumulation to inversion). The increase in capacitance towards zero voltage (small symbols) is a measurement artifact (see text).

interface state density is higher for sample A than for sample B. For a quantitative analysis, the C-V curves were modeled to determine Q_f and the interface state density $D_{it}(E)$ [147]. A model proposed by Brews was used for the high-frequency curve [148, 30]. For the quasi-static capacitance, the gate charge was calculated using the extended SRH formalism at a gate voltage of V_G and $V_G + \delta V_G$. C_{QS} was then calculated via

$$C_{QS} = \frac{Q_G(V_G + \delta V_G) - Q_G(V_G)}{\delta V_G}. \tag{4.5}$$

Sample	n	d_{iG}	Q_f	T_A	T_B	C	$D_{it.max}$	$D_{it.0}$	σ
		nm	cm^{-2}	cm^{-2}eV^{-1}	eV^{-1}	cm^{-2}eV^{-1}	cm^{-2}eV^{-1}	eV	eV
A	1.88	53.3	2.4×10^{12}	20×10^{11}	18	3×10^{11}	8.0×10^{11}	0.52	0.25
B	1.96	62.5	3.1×10^{12}	20×10^{11}	18	1×10^{11}	2.9×10^{11}	0.40	0.24

Table 4.1: Parameters of samples A and B determined from the complete C-V analysis.

A good correspondence between measured (symbols in Fig. 4.5 (a1) and (b1)) and calculated (solid lines) C-V curves has been achieved with the following interface state density
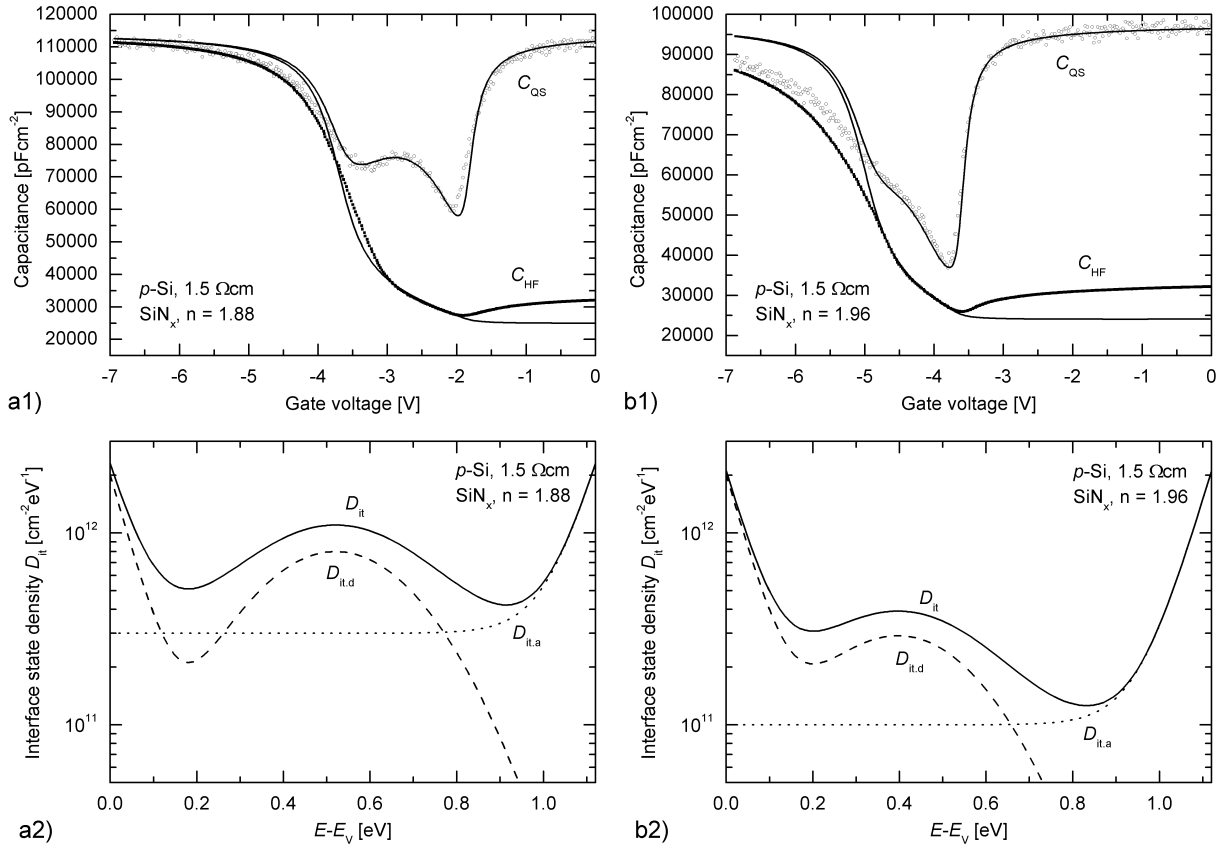
Figure 4.5: Measured (dotted) and calculated (solid lines) quasi-static and high-frequency C-V curves for MNS sample A (a1) and B (b1). The sample structure is shown in Fig. 4.3. The gate insulator in sample A was a N-rich SiN_x film, while that in sample B was slightly Si-rich. (a2) and (b2) show the corresponding D_{it} curves that were assumed for the calculation of the C-V curves. The interface state density D_{it} is divided into donor-like interface states with density $D_{it.d}$ and acceptor-like interface states with density $D_{it.a}$. See text for details regarding the applied calculation method.

distributions:

$$D_{it.d}(E) = T_A e^{-T_B(E-E_V)} + D_{it.max}e^{-((E-E_V)-D_{it.0})^2/\sigma^2} \quad (4.6)$$

$$D_{it.a}(E) = T_A e^{-T_B(E_C-E)} + C \quad (4.7)$$

and the parameters given in Tab. 4.1. The assumed interface state distributions consist of so-called tail states at the band edges (donor- and acceptor-like), a Gaussian profile within the bandgap (donor-like) and a constant contribution (acceptor-like). The distributions are following those identified at Si/SiO_2 interfaces [32, 33, 34]. The tail states result from stretched $Si - Si$ bonds while a Gaussian peak can be attributed to dangling silicon bonds. Depending on the type of remaining silicon bonds, different states have been identified at the Si/SiO_2 interface [34]. Due to statistical disorder in the bond angles and the distances to the next neighbour atoms, interface states show, in general, broad distributions. The

interface state distributions assumed in this work are plotted in Fig. 4.5 (a2) and (b2) for the sample A and B, respectively. The C-V curves of both samples could be modeled assuming a symmetrical tail state distribution for donor- and acceptor-like tail states. Moreover, identical densities of tail states for sample A and B were assumed. However, the sensitivity of the calculated C-V curves to changes in the tail-state density is less pronounced than that to changes in the interface state density located around midgap. The density of midgap interface states of sample A is by a factor of three higher than that of sample B. This important finding explains the tendency that samples passivated using Si-rich SiN_x films exhibit higher effective carrier lifetimes than those passivated using N-rich films (Fig. 4.1 b). The impact of the Si content on the passivation quality of the SiN_x films is studied in detail in Section 4.5. Considering the hysteresis effect introducing a relatively large uncertainty in the determination of the fixed positive charge density, the Q_f values found are comparable for both samples (Tab. 4.1).

The differences between the calculated and measured C_{HF} curves under inversion conditions is a measurement artifact that was already discussed in the previous section. Furthermore, the measured C-V curves exhibit a shallower slope than the calculated curves that is particularly visible in the voltage range of -5 to $-7\,V$ for sample B. This can be attributed to charging or discharging of traps that is also responsible for the hysteresis discussed in the previous section. SiN_x films with higher refractive indices corresponding to a higher Si content exhibit relatively high leakage currents and an even higher hysteresis than that shown in Fig. 4.4 when measured using the C-V method. Unfortunately, this makes the use of this method inappropriate for SiN_x films with $n > 2.0$.

4.3   Corona Charging and Lifetime Measurements

Carrier lifetime measurements are a very sensitive tool to determine the recombination rate at a semiconductor surface. By varying the surface potential Ψ_s, the surface recombination rate and, hence, the SRV can be drastically changed (Fig. 2.17). The surface potential can be changed using an MIS structure and varying the gate voltage [14, 16] or by the deposition of additional charges upon the insulating film [74]. The latter method has the inherent advantage that no metallic gate contacts are necessary. As metal contacts are usually opaque and exhibit a high conductivity, lifetime measurements relying on the measurement of excess photoconductance may be hampered. Furthermore, owing to the contactless nature of the measurement technique using additional charges, a metal contamination is avoided and the work function of the gate electrode has not to be taken into account for the evaluation of the measurement data. In this work, we used corona charges deposited upon insulating SiN_x films to vary the surface potential. The corona apparatus has been introduced in Section 3.1.5. The charge density Q_c deposited onto both surfaces of the samples was measured using a Kelvin probe [80, 82].

The simulation results shown in Fig. 2.17 can also be regarded as the SRV as a function of the *total* fixed charge density $Q_t = Q_f + Q_c$, where Q_c is the deposited corona charge density. Since the position of the peak occurs at $Q_t \approx 0$, the simple relation $Q_f = -Q_c$ is obtained at the peak. Hence, by measuring Q_c at the position of the peak, Q_f can be
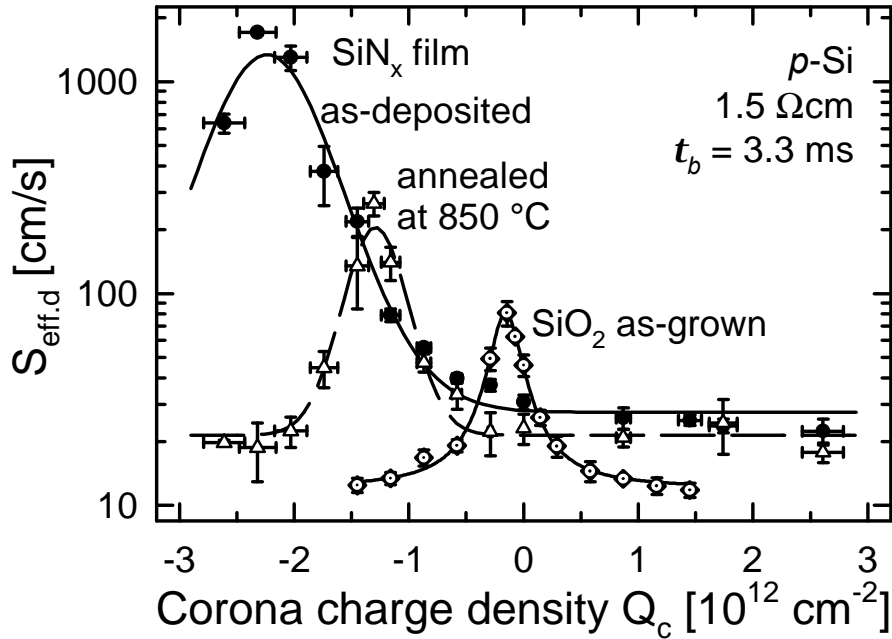
Figure 4.6: Differential effective SRV $S_{\text{eff.d}}$ as a function of the deposited corona charge density Q_c for Si/SiN$_x$ and Si/SiO$_2$ interfaces. The SiN$_x$ films have a refractive index of $n = 1.94$. The results for as-deposited (closed circles) and annealed (open triangles) SiN$_x$ films are shown. For comparison, the results of a sample with as-grown SiO$_2$ films on both surfaces is shown as well. Note that a constant white bias light intensity of about 40 mW/cm^2 was used during the lifetime measurements. As can be seen by the low SRV, inversion condition prevail for the SiN$_x$ samples for zero or positive corona charges. In order to achieve accumulation conditions, negative corona charge densities of less then -2 or -3×10^{12} cm^{-2} have to be applied.

determined easily.

The lifetime test structures in this work were prepared using double-side shiny-etched 300 μm thick 1.5 Ωcm p-type float-zone (FZ) silicon wafers. The wafers were given an RCA clean prior to SiN$_x$ deposition, including a final etch in diluted HF to remove any surface oxide layer that formed during the RCA cleaning process. The SiN$_x$ films were deposited using a remote PECVD reactor as described in Section 3.1.1. The deposition temperature was 400 °C. Further deposition parameters are summarised in Tab. 3.1. A SiH$_4$ gas flow of 4 sccm and a deposition time of 3 min were applied. The refractive index of the SiN$_x$ films was $n = 1.94$ and the thickness 70 nm as was determined by ellipsometry. Fig. 4.6 shows the results of a typical measurement using the MW-PCD technique described in Section 3.2.1 for the lifetime measurements. Note that a constant white bias light intensity of about 40 mW/cm^2 was used during the lifetime measurements. Thus, in contrast to the simulation (Fig. 2.17), the injection level is different for each measurement. Importantly, as the injection level depends not only on the bias light intensity but also on the lifetime, the position of the peak is only weakly affected by this. A Q_f value of 2.3×10^{12} cm^{-2} is

determined for the sample passivated using SiN_x (filled circles, as deposited) in accordance with the results of the C-V measurements presented above (Section 4.2). The absolute value of $S_{eff.d}$ at the position of the peak of nearly $2000\,cm/s$ illustrates the impact of the field-effect passivation provided by the fixed positive charges within the SiN_x films. In the past, there has been some discussion whether Q_f in SiN_x films is constant under illumination [37, 38]. In order to match theoretical and experimental data, it has been suggested that Q_f decreases under illumination. Our experimental results clearly prove for the first time that Q_f is constant under illumination and has the same value as in the dark. As the assumption of a reduced fixed charge density is in contradiction to our experimental results, a new theoretical model which explains the experimentally observed $S_{eff}(\Delta n)$ shape has been developed in Section 2.4.3 and will be applied in Section 4.5. The fixed charge density decreases after an annealing step in an infrared belt line furnace at $850\,°C$ for $20\,s$ (Fig. 4.6, annealed, open triangles). Such temperature cycles are used, for instance, to fire of screen-printed contacts. A decrease in Q_f to about $1.5 \times 10^{12}\,cm^{-2}$ is observed by annealing. The decrease of the SRV by annealing over the whole investigated charge density range can be attributed to a lower interface state density at the Si/SiN_x interface as well as a lower state density in the surface space-charge region. This may be caused by hydrogen diffusion towards the interface and its saturation of dangling bonds. For comparison, the results of a silicon wafer passivated using thermally grown SiO_2 is shown as well (Fig. 4.6, as grown, open diamonds). A fixed charge density of $Q_f \approx 1.5 \times 10^{11}\,cm^{-2}$ is found. This result is in perfect agreement with data published in the literature [30, 149, 16]. Also, the SRV at the position of the peak is much lower than that observed for the SiN_x film. This can be attributed to an inherently lower interface state density at the Si/SiO_2 interface in comparison with Si/SiN_x interfaces. By applying additional positive corona charges on top of the SiO_2 film, the SRV can be decreased from $S_{eff.d} = 46\,cm/s$ for $Q_c = 0$ to $12\,cm/s$ for $Q_c = 10^{12}\,cm^{-2}$. This finding is different to the results found for the SiN_x films where the fixed charge density within the films is already high enough to provide the maximum field-effect passivation ($S_{eff.d} = 31\,cm/s$ for $Q_c = 0$ and $22\,cm/s$ for $Q_c = 2.6 \times 10^{12}\,cm^{-2}$).

As was noted at the end of Section 4.2.2, SiN_x films with a refractive index $n > 2$ produce relatively high leakage currents in C-V measurements. This also excludes samples passivated using SiN_x films with $n > 2$ from the corona-lifetime measurement since stable corona charges require a well-insulating dielectric film. In fact, for samples with SiN_x films in the range of $n = 2.0 - 2.1$, a temporal variation of the effective carrier lifetime after the deposition of corona charges could be measured. For a sample with $n = 2.07$, we measured a temporal variation of the effective lifetime with a time constant of about $40\,s$. This finding can be attributed to the neutralisation of corona charges. For even higher refractive indices, no effect could be measured after the application of corona charges, i.e., the deposited corona charges disappear almost instantaneously.

4.4   Determination of the Sheet Resistance

In the last two sections, the interface properties of Si/SiN_x interfaces have been studied. However, since the conductivity of the SiN_x films increases strongly with the silicon content
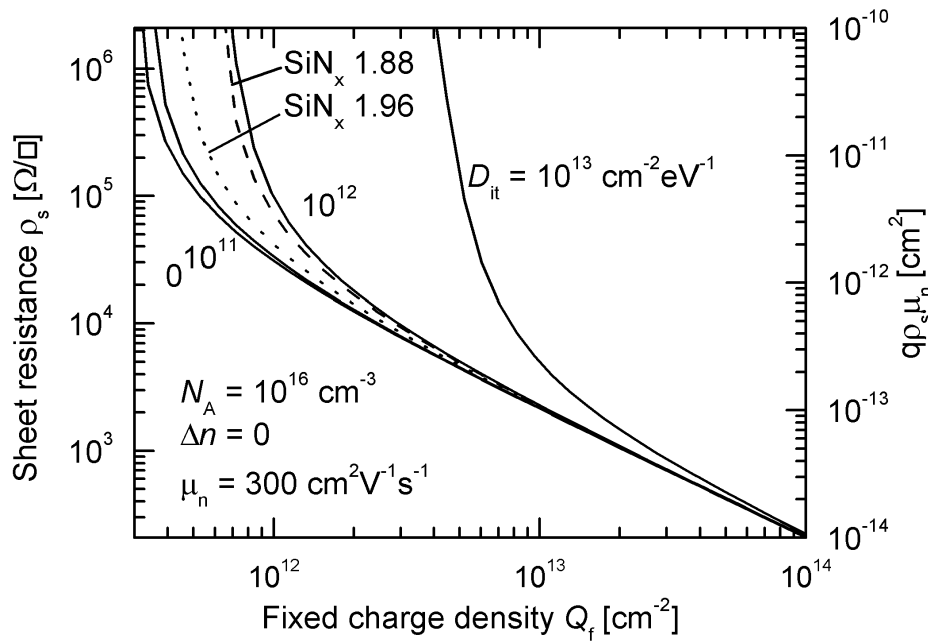
Figure 4.7: Calculated sheet resistance ρ_s (left axis) and normalised sheet resistance $\rho_s\mu_n q$ (right axis) as a function of fixed charge density Q_f for different interface state densities. The solid curves were calculated assuming constant interface state distributions while the curves marked with SiN_x 1.88 and SiN_x 1.96 were calculated using the D_{it} distributions as given in Section 4.2.2. Assumptions: p-Si, $N_A = 10^{16}\,cm^{-3}$, darkness, $\mu_n = 300cm^2V^{-1}s^{-1}$.
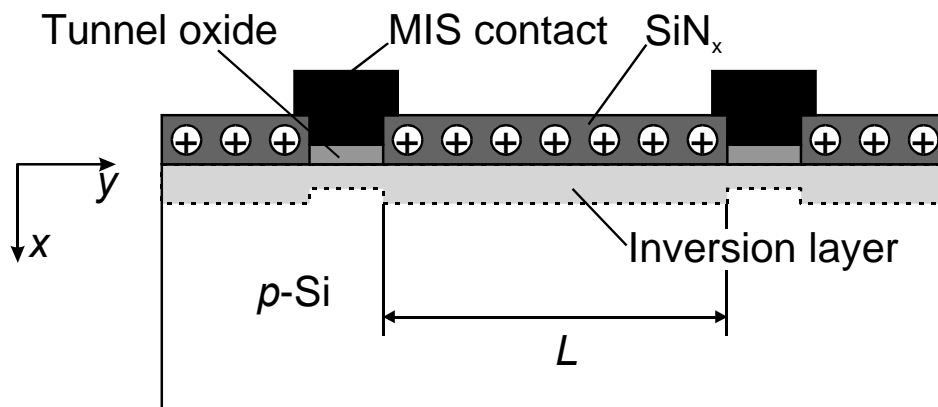
Figure 4.8: Schematic of the sample structure used to determine the sheet resistance. Note that the samples were annealed at $500\,°C$ for 10 min to grow the thin oxide for the MIS tunnel contacts. The SiN_x film properties remain constant during this treatment.

of the films [69], SiN_x films with higher silicon contents are neither experimentally accessible with the C-V method nor with the corona-lifetime method owing to high leakage currents through the film. The leakage current of films having a Si-to-N ratio above about 0.75, i.e., a refractive index $n > 2$ (Fig. 4.2), is too high for the quasi-static C-V method and the corona-lifetime method. Due to an increasing hysteresis, the high-frequency C-V method is also not applicable. On the other hand, SiN_x films having a high silicon content provide superior surface passivation compared with films with low silicon content. Hence, particular these films are of major interest for PV applications and an improved understanding is desirable. In this section, sheet resistance measurements of the induced inversion layer are presented. Since for a low sheet resistance of an inversion layer, both, a high Q_f as well as a low interface state density D_{it} is necessary, the sheet resistance of the inversion layers can be used as a vehicle for an improved understanding of the passivation mechanism of SiN_x films.

Fig. 4.7 shows the calculated sheet resistance ρ_s as a function of Q_f and D_{it} (left axis). ρ_s was calculated using

$$\rho_s = \frac{1}{q\mu_n |Q_{sc.n}|}, \tag{4.8}$$

where $Q_{sc.n}$ is determined using the extended SRH formalism and Eq. 2.51. For the sake of simplicity, we assumed a constant μ_n although this is in contrast to the experimental finding that μ_n depends on surface roughness and Coulomb scattering and, most important, on the transverse electric field which is perpendicular to the current flow [31, 150]. For simplicity, a value of $\mu_n = 300\,\text{cm}^2/\text{Vs}$ was assumed in accordance to data reported in the literature [151, 152, 150]. The quantity $\frac{1}{|Q_{sc.n}|} = q\rho_s\mu_n$ that is proportional to the sheet resistance but independent of the mobility is also plotted in Fig. 4.7 (same curves but right axis). However, a mobility being constant in the inversion layer is still assumed. The curves marked with 'SiN$_x$ 1.88' (dashed line) or 'SiN$_x$ 1.96' (dotted line) were calculated using the interface density distribution determined in Section 4.2.2 for sample A or B, respectively. The other curves (solid lines) were calculated using energy-independent interface state densities. As can be seen in Fig. 4.7, ρ_s becomes independent of the interface state density for high Q_f. This effect is exploited by MIS inversion layer solar cells fabricated at ISFH where Q_f is increased by Cs ions to decrease the sheet resistance of the emitter although an incorporation of the ions increases the interface state density [153, 154]. For low fixed charge densities, ρ_s depends strongly both on Q_f and D_{it} as can be seen by the steep increase of the curves towards low Q_f. For $D_{it} = 0$, the steep increase occurs at Q_f values slightly higher than what is required to drive the surface into strong inversion (cf. Fig. 2.13 with the assumption $Q_{sc} = Q_f$).

Fig. 4.8 shows the sample structure used to determine the sheet resistance of the inversion layer underneath the SiN_x films. The samples were fabricated on the same material as used for the C-V and the corona-lifetime measurements (1.5 Ωcm FZ p-Si wafers with (100) orientation) and additionally on 180 Ωcm FZ p-Si wafers with the same orientation. As can be seen from Fig. 2.13, lower fixed positive charge densities are required to drive higher resistivity material into inversion. Hence, the 180 Ωcm ($N_A = 7.4 \times 10^{13}\,\text{cm}^{-3}$) is more appropriate to investigate the sheet resistance underneath films with a lower fixed charge density. After an RCA cleaning step, a PECVD SiN_x film was deposited on the front surface

Sample	SiH$_4$	t	n	d
	sccm	min		nm
1.89	2	5:00	1.89	63
1.97	4.5	2:50	1.97	64
2.01	6	2:50	2.01	70
2.13	8	2:50	2.13	67
2.15	8	2:50	2.15	67
2.40	11	2:50	2.40	64
2.41	11	2:50	2.41	66
3.29	30	2:50	3.29	75
3.30	30	2:50	3.30	71

Table 4.2: Deposition parameters of the SiN$_x$ samples (1.5 Ωcm) used for the sheet resistance measurements in addition to those given in Tab. 3.1, namely the SiH$_4$ gas flow and the deposition time t. Furthermore, the film thickness d and the refractive index n as determined by ellipsometry are given. The samples on 180 Ωcm Si wafers were prepared with corresponding deposition parameters.
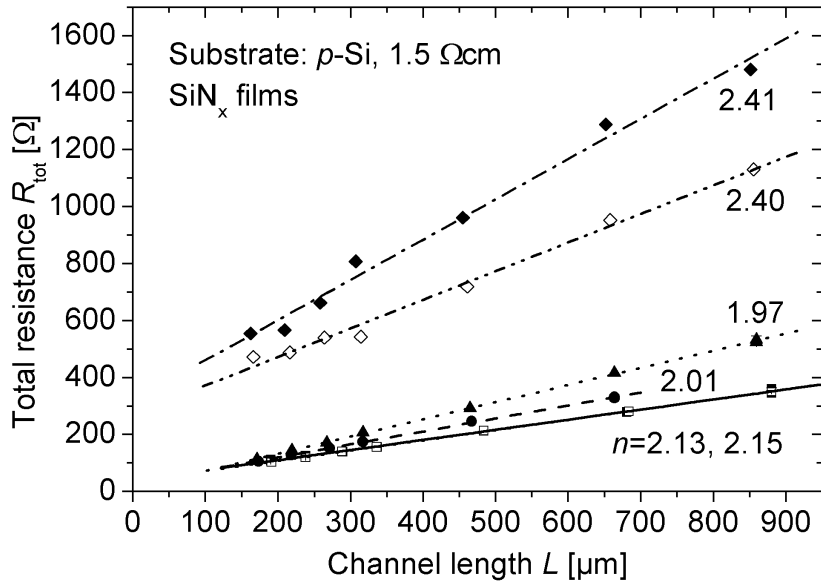
Figure 4.9: Measured total resistance R_{tot} as a function of channel length L for samples with different SiN$_x$ films on top of a p-Si substrate. The sample structure is shown in Fig. 4.8. The refractive index n of the SiN$_x$ films is also given. The lines are linear fits to the measured data.
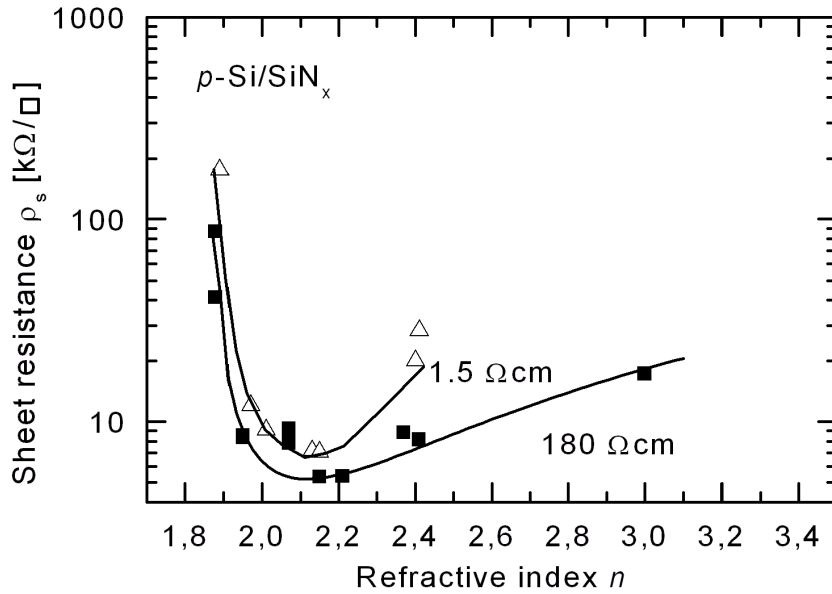
Figure 4.10: Measured sheet resistance ρ_s as a function of the refractive index n of the SiN_x film on top of the p-Si substrate. The sample structure is shown in Fig. 4.8.

of the samples using the parameters given in Tab. 4.2. The film thickness was greater than 60 nm for all samples to ensure that the interface properties as well as Q_f are independent of the actual film thickness. In this respect, Elmiger *et al.* have reported that Q_f reaches a constant value above a film thickness of about 20 nm [155]. The contact lines in the SiN_x films of the test devices were opened using photolithography and chemical etching. Subsequently, a tunnel oxide was grown on the bare silicon at 500 °C for 10 min. On top of the front structure, Al was evaporated in a vacuum chamber. As a final step, the Al contact lines were defined by photolithography and the Al on top of the SiN_x films was etched off. A small voltage (< 150 mV) was applied to the MIS contacts to determine the total resistance R_{tot} being composed of the contact resistance R_C and the inversion layer sheet resistance ρ_s according to

$$R_{tot} = 2\frac{R_C}{Z} + \frac{\rho_s L}{Z}, \tag{4.9}$$

where L and Z are the channel length and the length of the contact lines, respectively. In order to determine ρ_s, the sample consisted of several MIS contacts with different spacings. This measurement technique is known as the *transfer length* method [82].

A plot of R_{tot} versus the channel length L is shown in Fig. 4.9 for SiN_x films of varying composition. The refractive index n is taken for film distinction. The slope of the curves determines ρ_s while the y-axis offset can be used to determine the contact resistance (Eq. 4.9). However, in this work, the y-axis offset could only be evaluated with an insufficient accuracy. Hence, it was not considered for analysing the contact resistance. The determined sheet

resistance as a function of the refractive index of the SiN_x films is depicted in Fig. 4.10. $1.5\,\Omega$cm and $180\,\Omega$cm p-type Si wafers were used as substrate. The higher resistivity material is advantageous since it is driven into inversion by a lower fixed positive charge density (Fig. 2.13). As can be seen, the minimum values for ρ_s are found for SiN_x films with a refractive index in the range $1.95 - 2.20$. For lower refractive indices, ρ_s increases. This can be attributed to the increased interface state density in correspondence with the results determined from the C-V measurements in Section 4.2.2. Due to the higher interface state density, Q_f is compensated partly by the interface trapped charge Q_{it} and, hence, $Q_{sc.n}$ is smaller. Also, for higher refractive indices, ρ_s increases, but we attribute this to a different reason: Since the surface passivation provided by films with a higher refractive index is superior to that of films with n in the range $1.95 - 2.20$ (Fig. 4.1 and Section 4.5), the higher sheet resistance cannot be attributed to a higher interface state density but to lower Q_f values. It should be noted that the $R_{tot}(L)$ measurements on the $1.5\,\Omega$cm material with $n < 1.9$ and $n > 3.0$ resulted in straight lines with some scattering, introducing an error into the determined sheet resistance. This can be attributed to a lower fixed charge density or a higher interface state density since ρ_s relates very sensitive to Q_f for low Q_f and high D_{it} values (steep increase in ρ_s in Fig. 4.7). Since the surface of the $180\,\Omega$cm material can be driven into inversion condition with lower Q_f values, the sheet resistance of the inversion layer at the wafer surface can be measured down to lower Q_f values in the SiN_x films. In fact, the $R_{tot}(L)$ measurements for all investigated SiN_x films resulted in perfect straight lines. Hence, we attribute the differences in ρ_s found for the different materials and the films with $n > 2.4$ to measurement uncertainties of the results of the $1.5\,\Omega$cm material.

The mobile electron density within the inversion layer can be calculated from the data given in Fig. 4.10 according to

$$|Q_{sc.n}| = \frac{1}{q\rho_s\mu_n}. \tag{4.10}$$

If we assume that the Q_f within the SiN_x films is fully compensated by $Q_{sc.n}$, i.e., strong inversion conditions and negligible Q_{it}, the data shown in Fig. 4.11 can be used as a further method to estimate Q_f within the SiN_x films. As can be seen from Fig. 4.11, Q_f values of $2 - 3 \times 10^{11}$ cm^{-2} are obtained for films having a refractive index in the range of $1.95 - 2.2$ which is in perfect agreement with the values determined by the C-V method and the corona-lifetime method in Section 4.2.1 and 4.3, respectively. This finding also proves the assumed electron mobility of $\mu_n = 300\,\text{cm}^2/\text{Vs}$. For films with $n = 1.88$ and $n > 3$ on the $1.5\,\Omega$cm material, the Q_f values determined are below what is theoretically meaningful since $Q_f > 2 \times 10^{11}$ cm^{-2} must be ensured in order to induce inversion conditions at the surface (Fig. 2.13). The erroneous values arise from the inappropriate assumption $Q_f = -Q_{sc.n}$ and inaccuracies due to the fact that rather small changes in Q_f give rise to a dramatic change in ρ_s as can be seen in Fig. 4.7. On the $180\,\Omega$cm material, the assumption $Q_f = -Q_{sc.n}$ requires $Q_f > 1.5 \times 10^{10}$ cm^{-2} (Fig. 2.13) which is fulfilled by all SiN_x films investigated.
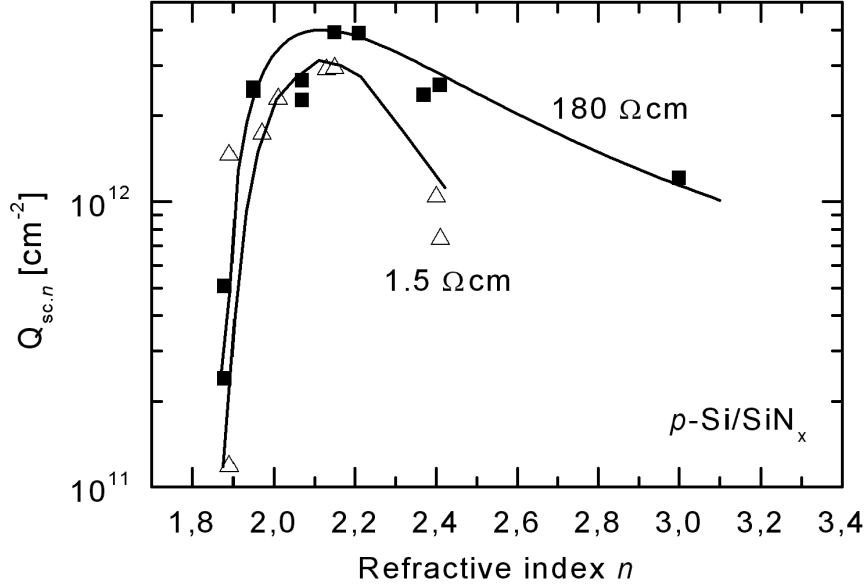
Figure 4.11: Calculated mobile inversion layer charge density $Q_{\text{sc}.n}$ using $|Q_{\text{n.sc}}| = \frac{1}{q\mu_n\rho_\text{s}}$ and the measured ρ_s values shown in Fig 4.10. An electron mobility of $\mu_n = 300\,\text{cm}^2/\text{Vs}$ was assumed.

4.5   Surface Recombination at the Si/SiN$_\text{x}$ Interface

Symmetrical SiN$_\text{x}$/Si/SiN$_\text{x}$ lifetime test structures were fabricated to investigate the surface passivation quality of the SiN$_\text{x}$ films. As for the other measurements in this chapter, double-side shiny-etched $300\,\mu\text{m}$ thick $1.5\,\Omega\text{cm}$ p-type float-zone (FZ) wafers were used for the silicon substrates. Silicon wafers of this type and resistivity are typically used for silicon solar cell fabrication. The silicon wafers were given an RCA clean prior to SiN$_\text{x}$ deposition. The SiN$_\text{x}$ films were prepared using a remote PECVD reactor as described in Section 3.1.1. The deposition temperature was $400\,^\circ\text{C}$. By changing the SiH$_4$ gas flow, the film composition was varied from N-rich to Si-rich SiN$_\text{x}$ films. The deposition parameters were identical to those given in Tab. 4.2 with slightly different refractive indices obtained.

The effect of the refractive index on the effective carrier lifetime measured using the QSSPC method described in Section 3.2.2 is shown in Fig. 4.12 (a). The effective lifetime increases with the refractive index, particularly in the injection range $10^{14} - 10^{16}\,\text{cm}^{-3}$. Samples passivated with N-rich films ($n = 1.88$) exhibit the lowest measured effective lifetime of about $100\,\mu\text{s}$. For Si-rich films, effective lifetimes as high as $1.3\,\text{ms}$ at $\Delta n = 10^{15}\,\text{cm}^{-3}$ were obtained. Towards lower and higher injection levels the different curves approach for different reasons. Towards high injection the intrinsic bulk lifetime determines the effective carrier lifetime as can be seen from the included curve showing τ_intr. In contrast, towards lower injection levels, the lower effective lifetime is determined by surface recombination as is seen from the difference between τ_intr and τ_eff. For τ_intr the parameterisation of Kerr
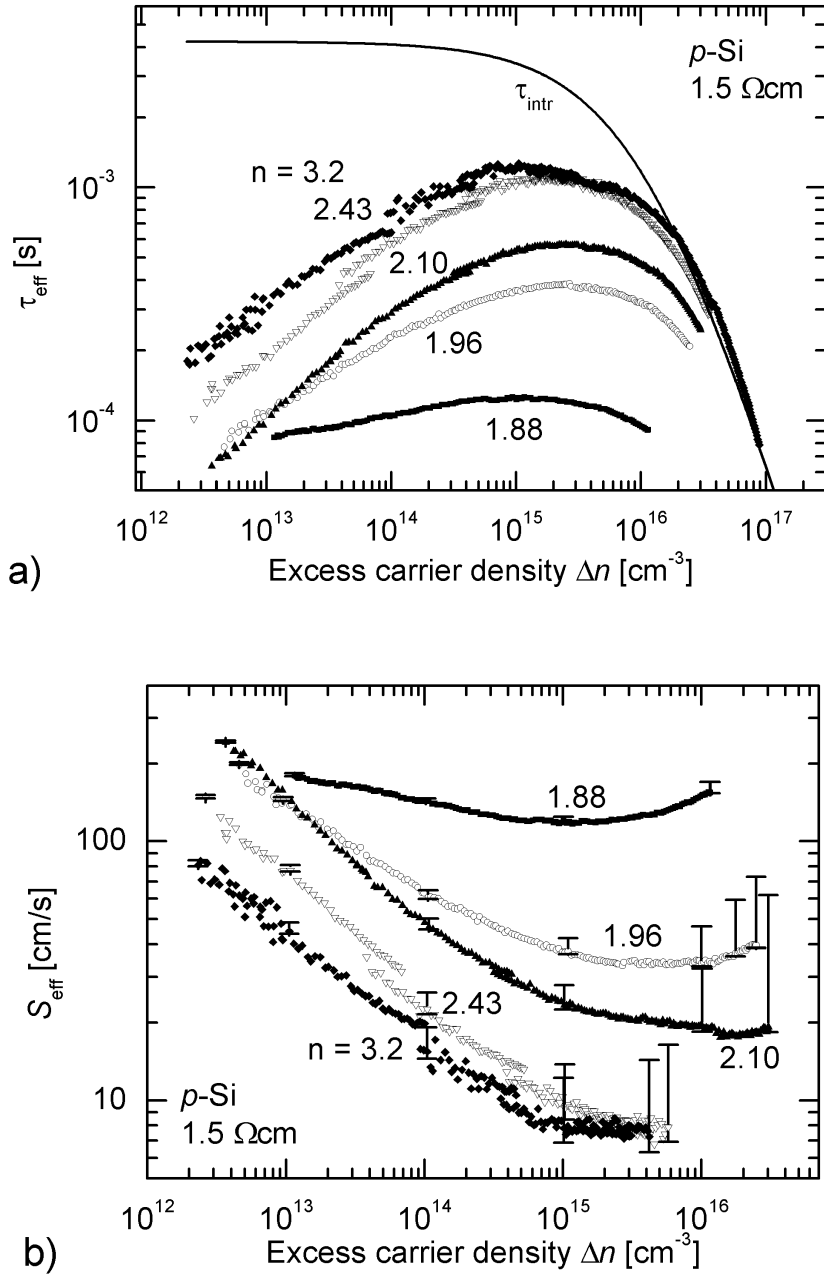
Figure 4.12: a) τ_{eff} as a function of the excess carrier density Δn for SiN_x passivated silicon wafers with different refractive indices n of the SiN_x films. The value of n is marked at the corresponding curve. Also included is the intrinsic carrier lifetime calculated using Eq. 2.25. For $\Delta n > 2 \times 10^{16}\,\mathrm{cm}^{-3}$, $\tau_{\mathrm{eff}} > \tau_{\mathrm{intr}}$ which is physically not possible. It follows that the intrinsic carrier lifetime was underestimated in previous studies. b) Corresponding effective SRV calculated using Eq. 2.98 and the intrinsic carrier lifetime shown in (a).

and Cuevas was used [20] (Eq. 2.25). However, as can be seen for the data of the $n = 2.43$ and $n = 3.2$ SiN$_x$ films, the measured effective lifetime exceeds τ_{intr} for Δn in the range of $10^{16} - 10^{17}\,\text{cm}^{-3}$ which is physically not realistic. Also, the intrinsic lifetime published by Schmidt *et al.* [23] is lower in this range. Hence, it follows, that τ_{intr} has to be higher in this injection range than the data published previously in the literature. However, a detailed investigation and reassessment of τ_{intr} is beyond the scope of this work. Note that the difficulties arising from an excess conductance in an inversion layer as was discussed in Section 3.2.2 were not taken into account. Since severe differences between the apparent and the true effective lifetime occur for excess carrier densities below $10^{13}\,\text{cm}^{-3}$, the simplification is justified by the considered injection range above $10^{13}\,\text{cm}^{-3}$.

In order to determine the surface passivation quality, the effective surface recombination velocity at the Si/SiN$_x$ interfaces was calculated according to Eq. 2.98 (Fig. 4.12 (b)). The poorest surface passivation is provided by the SiN$_x$ film with the lowest refractive index ($n = 1.88$) resulting in an S_{eff} between 120 and 200 cm/s. In contrast, S_{eff} values well below $10\,\text{cm/s}$ are obtained for SiN$_x$ films with higher refractive indices. The indicated errors bars arise from the uncertainty in τ_{b}. In the worst case scenario, an infinite bulk lifetime was assumed and higher S_{eff} values are obtained. At higher injection levels where Auger recombination in the bulk contributes essentially to the effective lifetime, this assumption gives a rather high upper limit for S_{eff}. If, on the other hand, in addition to the intrinsic recombination, a defect recombination is assumed with $\tau_{\text{SRH}} = 16\,\text{ms}$, a minimum S_{eff} of $6\,\text{cm/s}$ is obtained. It should be noted that the value used here for τ_{SRH} is significantly larger than what was typically been used in previous studies which was $\leq 4\,\text{ms}$ [56, 64, 37]. The effect is that the values determined for the lower limit of S_{eff} are more conservative, i.e., higher, compared with the values that would have been determined assuming $\tau_{\text{SRH}} \leq 4\,\text{ms}$ (Section 2.5).

Next, the different $S_{\text{eff}}(\Delta n)$ curves are modeled considering interface recombination and recombination in the surface space-charge region. Fig. 4.13 - 4.15 show the measured and calculated data. The interface recombination (dotted lines) was calculated using the extended Shockley-Read-Hall formalism outlined in Section 2.4.2 while the recombination in the space-charge region (dashed lines) was calculated using the theory outlined in Section 2.4.3. The sum of both contributions to S_{eff} is shown by solid lines in the figures.

First, the sample with $n = 1.96$ was modeled. $Q_{\text{f}} = 2 \times 10^{12}\,\text{cm}^{-2}$ and the D_{it} distribution determined by C-V measurements in Section 4.2.2 were used to calculate S_{it}. The capture cross sections of the interface states, σ_n and σ_p, respectively, could not be determined by the previous measurements. Schmidt *et al.* investigated Si/SiN$_x$ interfaces by small-pulse deep-level transient spectroscopy (DLTS) to determine values for σ_n and σ_p [156]. However, the data could only be determined with an error range of about two orders of magnitude. For simplicity, we assumed energy-independent capture cross sections and adjusted their values in order to achieve the best correspondence with the experimental data. The best agreement was achieved with $\sigma_n = \sigma_p = 4 \times 10^{-15}\,\text{cm}^2$. Since the capture cross sections are believed to be independent of the D_{it} values, these values were assumed for all investigated samples. As can be seen in Fig. 4.13, S_{it} contributes only for $\Delta n > 10^{16}\,\text{cm}^{-3}$ significantly to the effective SRV. In the past, this finding has tempted to change the interface properties in order to match the experimental data by the calculated S_{it}. Schmidt and Aberle argued
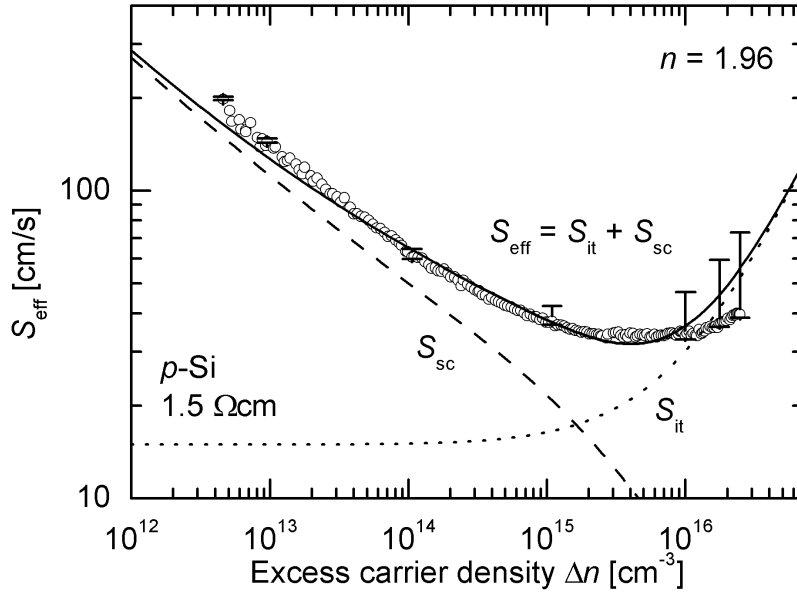
Figure 4.13: Measured and calculated S_{eff} as a function of excess carrier density Δn for a $1.5\,\Omega$cm p-Si wafer passivated on both sides using PECVD SiN$_{\text{x}}$ films with a refractive index of $n = 1.96$. The deposition parameters are given in Tab. 4.2. The dotted curve S_{it} was calculated using the extended SRH formalism while the dashed curve S_{sc} shows the contribution of recombination in the space-charge region. The parameters used in the calculation are given in Tab. 4.3. The solid curve represents the sum of S_{it} and S_{sc}.

that Q_{f} depends strongly on the operating conditions and proposed a lower value for Q_{f} under illumination in order to achieve good correspondence with the SRV calculated using the extended Shockley-Read-Hall formalism and the experimental data [37, 38]. However, as this assumption was rejected in this study (Section 4.2.1 and Section 3.1.5), a further contribution to S_{eff} has to be introduced. Considering the experimental data, the most likely contribution is from recombination in the surface space-charge region. The theoretical foundations have been outlined in Section 2.4.3. Assuming a band-bending defined by Q_{f} and D_{it}, an excellent agreement with the measured data could be achieved with capture time constants of the states in the surface space-charge region of $\tau_{n0} = \tau_{p0} = 1\,\mu$s. In fact, the larger part of the measured S_{eff} is determined by the recombination in the space charge region. A remarkable result is the fact that the capture time constants determined for the space-charge region are by at least four orders of magnitude lower than those in the bulk. The reasons for theses low lifetime values in the space-charge region remain unclear. A plasma damage at the surface caused during the deposition can be excluded since the samples are not in direct contact with the plasma (remote PECVD) and a very similar relation between S_{eff} and Δn is observed for SiN$_{\text{x}}$ passivated samples using thermo-catalytic CVD instead of plasma-enhanced CVD [60].

Fig. 4.14 and Fig. 4.15 show the experimental and calculated $S_{\text{eff}}(\Delta n)$ curves of different samples. The corresponding parameters are shown in Table 4.3. In addition to the given parameters, energy-independent capture cross sections of $\sigma_n = \sigma_p = 4 \times 10^{-15}\,\text{cm}^2$ were assumed for all SiN$_x$ films. Since the data, particularly at lower injection levels, are determined by recombination in the space-charge region, it is rather difficult to extract Q_f and D_{it} from the modeled data. For the sample with $n = 1.88$ an excellent agreement with the experimental data is obtained if the parameters determined in the previous sections are used in the calculation. Since the energy-resolved D_{it} values could not be determined for SiN$_x$ films with $n > 2$, energy-independent values were assumed for the samples with $n = 2.10$, 2.43 and 3.2. As determined from the sheet resistance data, Q_f decreases for increasing refractive index. Hence, for the films with a higher refractive index, lower Q_f and D_{it} values were assumed. However, since $S_{\text{it}} \propto \frac{S}{Q_f^2}$ (Eq. 2.78), where S depends on σ_n, σ_p and D_{it}, the interface parameters and the fixed charge density cannot be determined individually from the S_{eff} data.

For excess carrier densities $\Delta n > 6 \times 10^{15}\,\text{cm}^{-3}$ ($n = 2.43$) or $\Delta n > 4 \times 10^{15}\,\text{cm}^{-3}$ ($n = 3.2$), respectively, the S_{eff} curves drastically bend downwards (Fig. 4.15). For even higher injection levels, the measured effective carrier lifetimes are larger than the intrinsic bulk lifetime proposed by Kerr and Cuevas [20] and S_{eff} becomes negative if it is calculated according to Eq. 2.97. This behaviour, which is not physically realistic, is due to the fact that the intrinsic bulk lifetime was underestimated in previous studies. Since Auger recombination is the dominant recombination mechanism in this injection range, the determination of the accurate contribution by surface recombination is rather difficult. Hence, we did not consider the data obtained for Δn greater than the above values for the modeling. For the Si-rich SiN$_x$ films, higher values for the capture time constants τ_n and τ_p are found. However, since the uncertainties in the determination of the capture time constants are rather large, this finding should not be overrated.

Sample		Interface				Space-charge	
n	Q_f	D_{it} distrib.	$D_{\text{it.a}}$	$D_{\text{it.d}}$	τ_{n0}	τ_{p0}
	cm^{-2}		cm^{-2}eV^{-1}	cm^{-2}eV^{-1}	μs	μs
1.88	1.53×10^{12}	given in Fig. 4.5 (a2)			1	1
1.96	2.00×10^{12}	given in Fig. 4.5 (b2)			1	1
2.10	3.00×10^{12}	const.	15.00×10^{10}	15.00×10^{10}	1	1
2.43	1.00×10^{12}	const.	1.00×10^{10}	1.00×10^{10}	2.5	2.5
3.20	0.50×10^{12}	const.	0.15×10^{10}	0.15×10^{10}	3	3

Table 4.3: Parameters used for the calculation of $S_{\text{eff}} = S_{\text{it}} + S_{\text{sc}}$ for the data shown in Fig. 4.13 - 4.15. The refractive index n of the SiN$_x$ films given in the first column is used for sample distinction. The columns entitled with 'Interface' give the parameters for the interface state distribution. In addition to the given parameters, capture cross sections of the interface states $\sigma_n = \sigma_p = 4 \times 10^{-15}\,\text{cm}^2$ were assumed (Section 2.4.2). The columns entitled with 'Space-charge' give the capture time constants used for the calculation of the recombination in the space-charge region (Section 2.4.3).
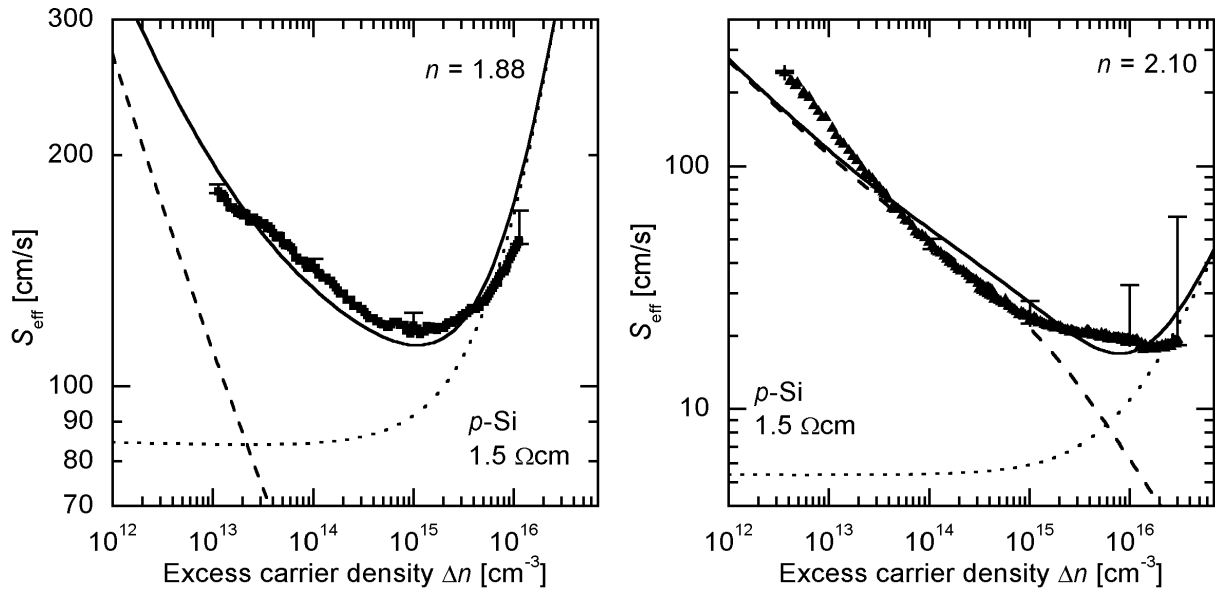
Figure 4.14: Measured and calculated $S_{\mathrm{eff}}(\Delta n)$ curves for p-Si samples passivated using PECVD SiN$_{\mathrm{x}}$ films with $n = 1.88$ and 2.10, respectively. The deposition parameters are given in Tab. 4.2 and the parameters for data modeling in Tab. 4.3. Please refer to Fig. 4.13 for further explanations.
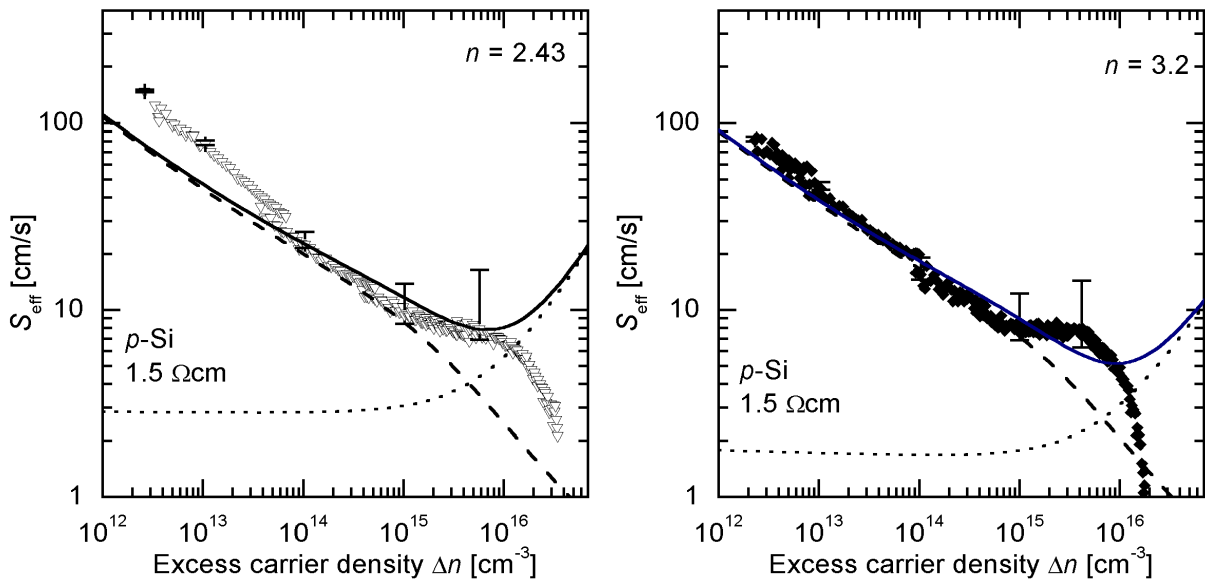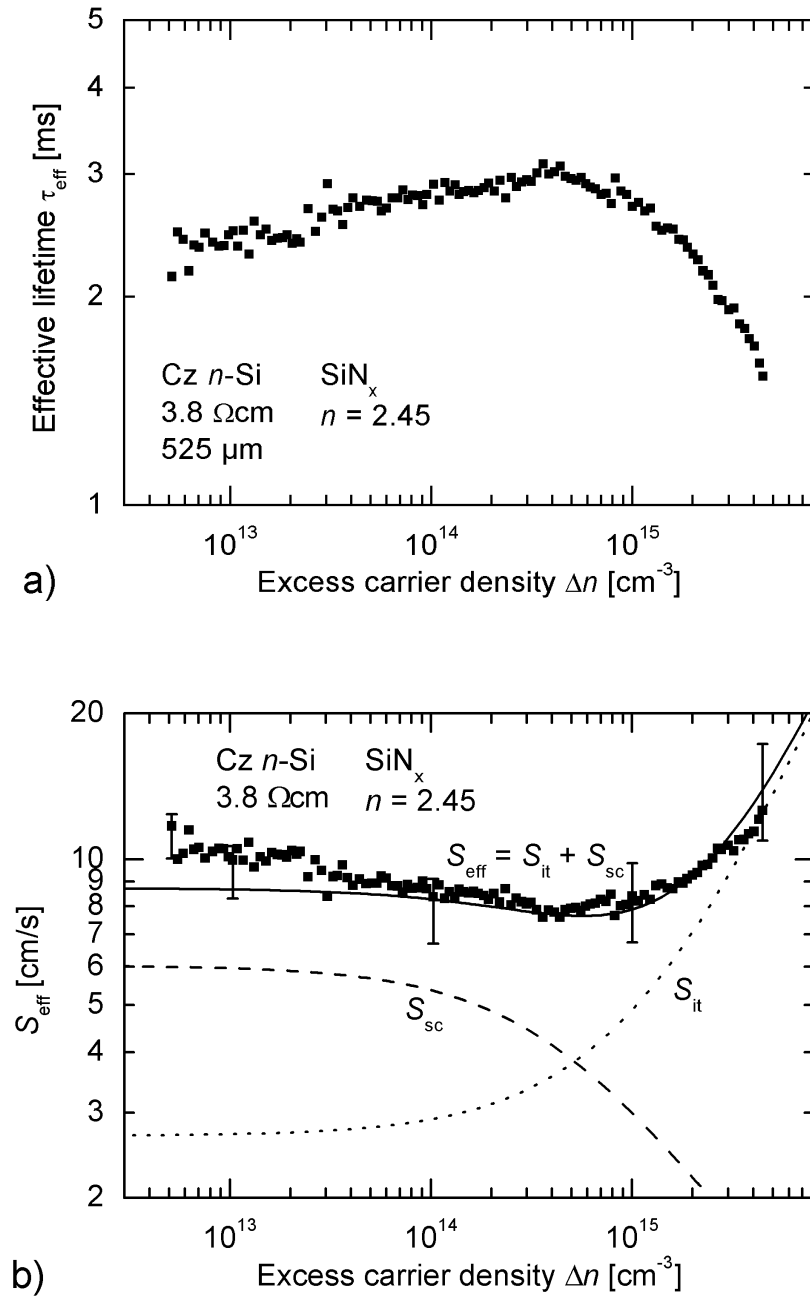

Figure 4.15: Measured and calculated $S_{\mathrm{eff}}(\Delta n)$ data for p-Si samples passivated using SiN$_{\mathrm{x}}$ films with $n = 2.43$ and 3.2, respectively. The deposition parameters are given in Tab. 4.2 and the parameters for data modeling in Tab. 4.3. Please refer to Fig. 4.13 for further explanations.

Figure 4.16: a) τ_{eff} as a function of the excess carrier density Δn) for a $3.8\,\Omega\text{cm}$ Cz n-Si sample passivated on both surfaces using PECVD SiN$_x$ films with a refractive index n of 2.45. b) Corresponding effective SRV calculated using Eq. 2.98 and the intrinsic carrier lifetime given in Eq. 2.25.

Sample		Interface			Space-charge	
	Q_{f}	D_{it} distrib.	$D_{\mathrm{it.a}}$	$D_{\mathrm{it.d}}$	τ_{n0}	τ_{p0}
	cm^{-2}		cm^{-2}eV^{-1}	cm^{-2}eV^{-1}	μs	μs
n-Si	1×10^{12}	const.	7×10^{10}	7×10^{10}	5	5

Table 4.4: Fit parameters for the $3.8\,\Omega$cm Cz n-Si sample passivated with SiN$_{\mathrm{x}}$ films on both surfaces ($n = 2.45$). The columns entitled with 'Interface' give the parameters for the interface state distribution. In addition to the given parameters, capture cross sections of $\sigma_n = \sigma_p = 4 \times 10^{-15}$ cm^2 were assumed (Section 2.4.2). The columns entitled with 'Space-charge' give the capture time constants used for the calculation of the recombination in the space-charge region (Section 2.4.3).

In order to investigate whether the parameters determined for p-type Si/SiN$_{\mathrm{x}}$ interfaces can also be applied to n-Si/SiN$_{\mathrm{x}}$ interfaces, an n-type wafer has been passivated using SiN$_{\mathrm{x}}$. The material used was a $3.8\,\Omega$cm Cz Si wafer of $525\,\mu$m thickness. The deposited SiN$_{\mathrm{x}}$ films had a refractive index of $n = 2.45$. Fig. 4.16 (a) shows the the effective lifetime as a function of the excess carrier density. Effective lifetimes of $2 - 3\,$ms were achieved for Δn in the range of $10^{13} - 10^{15}$ cm^{-3}. The τ_{eff} values correspond to S_{eff} values of about $10\,$cm/s as can be seen in Fig. 4.16 (b). Again, for τ_{b}, the parameterisation of Kerr and Cuevas [20] was used and the indicated error bars arise from the uncertainty in τ_{b}. The solid line is the calculated $S_{\mathrm{eff}} = S_{\mathrm{it}} + S_{\mathrm{sc}}$ curve. S_{it} was calculated assuming $Q_{\mathrm{f}} = 10^{12}$ cm^{-2} and energy-independent interface recombination parameters (dotted line) as given in Table 4.4. The capture cross sections of the interface states were assumed to be equal to 4×10^{-15} cm^2 as for the p-Si/SiN$_{\mathrm{x}}$ interfaces. Again, a surface space-charge region with a rather high recombination rate has to be assumed to achieve correspondence with the measured data. A good agreement was achieved if capture time constants of $5\,\mu$s were assumed. In contrast to p-type semiconductors, for n-type semiconductors only a high-low junction is induced rather than a p-n junction. Hence, the calculated S_{sc} curve is at a distinctly lower level and remains flat towards low injection. The slopes and the flat S_{eff} curves in low injection are a typical difference for p- and n-type Si samples passivated using SiN$_{\mathrm{x}}$ films as was published without explanation by Kerr and Cuevas for a variety of Si doping concentrations [138].

A comparison of the S_{eff} data obtained using SiN$_{\mathrm{x}}$ films fabricated in different labs is shown in Fig. 4.17. The results of Lauinger $et\ al.$ were measured using the MW-PCD technique unlike the results in this study where the QSSPC technique was used. This may explain the differences that can be seen in the Fig. 4.17 since their films and those fabricated in this study were deposited in the same PECVD reactor. As was discussed at the beginning of this section, the shape of the S_{eff} curve for $\Delta n > 10^{15}$ cm^{-3} for the films prepared in this work is physically not realistic and is due to the underestimation of the intrinsic lifetime. This finding implies that the surface passivation in this injection range is substantially better than what has been used to determine the intrinsic lifetime [20]. The data of Kerr and Cuevas [138] shown in Fig. 4.17 were measured using the QSSPC technique as well and the results are fairly similar to ours. However, the film composition is reported to be rather different from ours. The SiN$_{\mathrm{x}}$ films fabricated by Kerr and Cuevas have a low refractive index, that is, the Si/N ratio is approximately the same as for stoichiometric SiN$_{\mathrm{x}}$
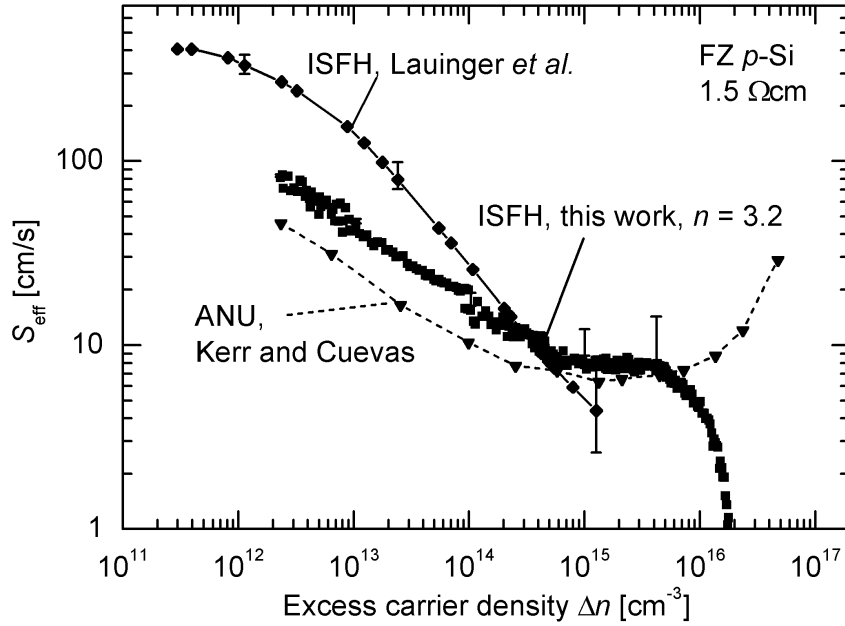
Figure 4.17: Comparison of $S_{\mathrm{eff}}(\Delta n)$ curves from this study with literature data for $1.5\,\Omega$cm p-type silicon passivated with different types of PECVD SiN$_x$ films. The data of Lauinger et $al.$ [64] was measured using an MW-PCD system while the data of Kerr and Cuevas [138] and the data of this study were measured using the QSSPC method.

films. However, in contrast to stoichiometric Si$_3$N$_4$, the films contain substantial amounts of hydrogen. The fact that Kerr and Cuevas are able to produce well-passivating stoichiometric SiN$_x$ films is rather interesting since SiN$_x$ films deposited with other CVD techniques in our lab and films fabricated in other labs generally provide a lower degree of surface passivation at low refractive indices and reach the excellent SRVs for n larger than at least 2.3 [60, 139]. In this respect, it is noteworthy that it is possible to achieve an excellent surface passivation with films where only during the first seconds of the deposition a high SiH$_4$ gas flow is adjusted. This has been investigated with lifetime test structures covered by a double layer of SiN$_x$ films (see inset in Fig. 4.18). The first film was deposited with a very high gas flow of SiH$_4$ while the capping SiN$_x$ film was deposited with a lower gas flow resulting in a stoichiometric SiN$_x$ film ($n = 1.95$). As can be seen in Fig. 4.18, the effective lifetime for a sample covered with the stoichiometric film only (SiN$_x$ $n = 3$ film thickness equal zero) is only $400\,\mu$s. However, as soon as the film thickness of the Si-rich SiN$_x$ film is thicker than $2\,$nm, the full surface passivation with $\tau_{\mathrm{eff}} \approx 1.3\,$ms is achieved. Note that the covering SiN$_x$ film is indispensable for an efficient surface passivation since a minimum total SiN$_x$ film thickness of about $30\,$nm is required to achieve the optimum surface passivation, which is likely to be due to the necessity of a field-effect passivation provided by Q_{f} within the SiN$_x$ films. As Elmiger et $al.$ have shown, Q_{f} increases with the film thickness until a constant value is reached at a film thickness of about $20\,$nm [155].

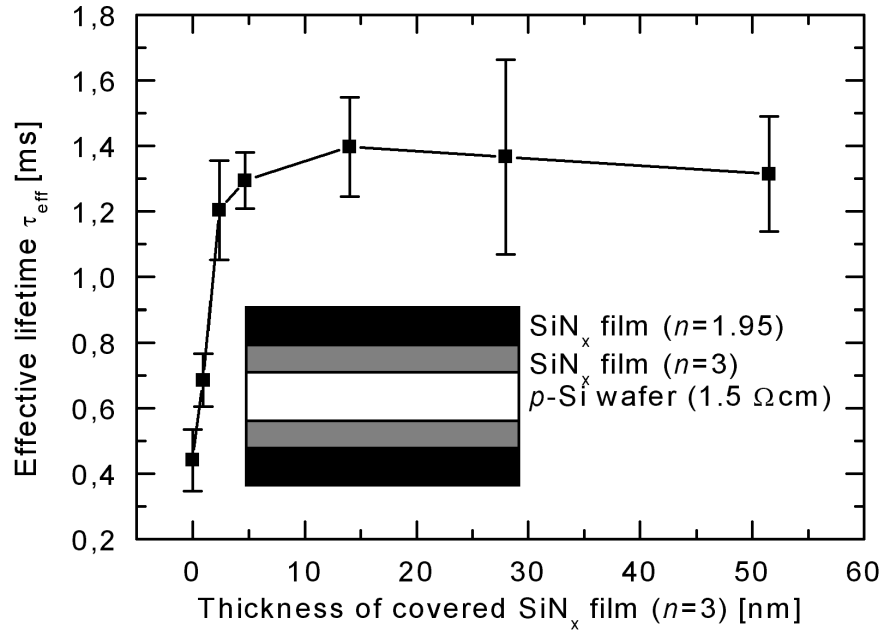   This result demonstrates that a high SiH$_4$ gas flow or at least an effective utilisation of

Figure 4.18: τ_{eff} as a function of the thickness of the passivating Si-rich SiN_x film ($n = 3$). This film is covered by an additional stoichiometric SiN_x film ($n = 1.95$) with a thickness of 50 nm as is sketched in the graph.

the precursor gas SiH_4 is necessary only at the very beginning of the deposition while during the remaining time of the film deposition the conditions imposed on the gas composition are less restrictive. This may explain the differences among the surface passivation of SiN_x films fabricated in different labs. As has been shown in this work and reported in the literature, the degree of surface passivation provided by N-rich SiN_x films is generally lower than that found for Si-rich SiN_x films [60, 65, 139][1]. The main difference is the Si/N ratio (or the refractive index n) at which the surface passivation increases to the degree found for Si-rich SiN_x films. Considering our results, we attribute this to a different degree of utilisation of the precursor gas SiH_4 for the different deposition reactors at the beginning of the deposition. Depending on the reactor geometry and process pressure, some reactors allow for a relatively low SiH_4 gas flow for an effective passivation of the dangling bonds at the surface by hydrogen while others seem to require a higher SiH_4 gas flow. The different Si/N ratios at which the surface passivation increases can be explained by the fact that the ellipsometry measurements detect the overall refractive index of the SiN_x film while the surface passivation is partly determined by the film composition at the very silicon surface.

---

[1]Note that the τ_{eff} values published in Ref. [65] (Fig. 4.1) decrease slightly for higher refractive indices. However, the surface passivation provided by Si-rich films is still far better than that provided by N-rich films.

Chapter 5

Recombination at the a-Si/c-Si Interface

In the previous chapter, SiN_x films with different Si/N ratios have been investigated. A limiting case would be an infinite Si/N ratio, resulting in amorphous hydrogenated silicon (a-Si:H) films. Since the properties of a-Si:H films are somewhat different to those of SiN_x films we will discuss them separately in this chapter. Recently, a-Si:H films have been incorporated into heterojunction silicon solar cells consisting of an a-Si:H film on top of a crystalline silicon (c-Si) substrate. These solar cell type has gained large interest among the photovoltaic community due to the unique combination of a very low deposition temperature ($\sim 200\,°C$) at which the junction is formed and the high conversion efficiencies that have been obtained [67, 157]. The highest efficiency obtained so far for this cell type is $21.0\,\%$ [157]. Moreover, very high open-circuit voltages of up to $V_{oc} = 719\,mV$ [158] have been reached for these so-called HIT (heterojunction with intrinsic thin-layer) cells having an intrinsic a-Si:H/p-type a-Si:H layer stack on an n-type c-Si substrate. This result demonstrated the excellent electronic properties of the a-Si/c-Si(n) interface. For the inverse structure that uses p-type c-Si, the highest open-circuit voltage that has been reported so far is $655\,mV$ with an efficiency of $14.1\,\%$ [159]. The highest independently confirmed conversion efficiency reported so far is $\eta = 16.2\,\%$ [160]. From a compilation of solar cell results given in Ref. [159], it can be seen that, in general, the results obtained with a-Si:H(n)/c-Si(p) heterojunction solar cells are by far inferior to those attained on n-type c-Si. It has been proposed that this finding is due to the higher band offset in the minority-carrier band in case of the p/n-type a-Si/c-Si structure leading to a more efficient suppression of interface recombination [161].

Apart from the more indirect conclusion that a high efficiency relies on excellent properties of the a-Si/c-Si interface, direct investigations of the surface recombination velocity are rare [67, 162, 163, 83]. In Ref. [67], the surface recombination velocity was estimated to be lower than $100\,cm/s$ for the a-Si:H(p)/a-Si:H(i)/c-Si(n) structure. $1\,\Omega cm$ n-type Czochralski (Cz) Si material was used as substrate material. A SRV well below $100\,cm/s$ was reported in Ref. [162] using high-resistivity $10\,\Omega cm$ p-type Cz Si material. In Ref. [163], $1\,\Omega cm$ p-type silicon substrates were used and SRVs of $68\,cm/s$ and $44\,cm/s$ were reported for an intrinsic a-Si:H layer and an a-Si:H(i)/a-Si:H(p^+) layer stack, respectively. A SRV of $55\,cm/s$ was reported in Ref. [83] on $3.3\,\Omega cm$ p-Si.

In this chapter, the optimum deposition temperature for the deposition of well-passivating a-Si:H films and the thermal stability of the surface passivation is investigated (Section 5.2). Furthermore, the surface recombination velocity as a function of injection level is investigated for p- and n-type Si substrates passivated by a-Si:H films (Section 5.3).

5.1 Experimental

Symmetrical a-Si:H/c-Si/a-Si:H lifetime test structures were fabricated to investigate the surface passivation quality of the a-Si:H films. The substrate material used was single-crystalline, shiny-etched, (100)-oriented FZ p-type silicon. The wafers were $300\,\mu$m thick and had a resistivity of $1.6\,\Omega$cm. Additionally, $525\,\mu$m thick, $3.4\,\Omega$cm n-type Cz silicon wafers with one polished and one shiny-etched surface were used. Prior to the deposition of about $30\,$nm thick a-Si:H films, the wafers received a standard RCA clean. The a-Si:H films were deposited onto both wafer surfaces in a parallel-plate plasma-enhanced chemical vapour deposition (PECVD) chamber as described in Section 3.1.2. The following deposition parameters were applied (Table 3.1): Temperature $150 - 350\,^\circ$C, gas flow $30\,$sccm SiH$_4$, rf power $100\,$W, pressure $450\,$mTorr. Additional samples were fabricated with dilution of the silane by helium. However, the passivation properties of the films deposited with helium dilution were found to be quite similar to those fabricated with the above parameter set and the results obtained with helium dilution are therefore omitted in the following. A deposition time of $1\,$min resulted in a film thickness of about $30\,$nm. The film thickness was determined by ellipsometry (wavelength $633\,$nm) using a-Si:H/glass samples instead of a-Si:H/c-Si samples since the latter sample type is difficult to measure due to the similar refractive indices of a-Si:H and c-Si. Absorption within the a-Si:H film was neglected for the evaluation of the ellipsometry data.

The effective carrier lifetime τ_{eff} of the samples was measured using the QSSPC technique described in Section 3.2. The effective surface recombination velocity S_{eff} at the a-Si/c-Si interface was calculated from the measured lifetime τ_{eff} using Eq. 2.98 and the ambipolar diffusion coefficient $D_{\mathrm{a}} = \frac{(n+p)}{(n/D_p + p/D_n)}$ instead of the electron diffusion coefficient D_{n}. For the $1.6\,\Omega$cm p-type ($3.4\,\Omega$cm n-type) Si, an electron diffusion coefficient of $D_{\mathrm{n}} = 29\,$cm^2/s ($35\,$cm^2/s) and a hole diffusion coefficient of $D_{\mathrm{p}} = 11\,$cm^2/s ($12\,$cm^2/s) were used. For the bulk lifetime τ_{b}, only intrinsic recombination, including radiative and Auger recombination, was considered using the parameterisation given in Eq. 2.25. An upper limit for the effective SRV was estimated by assuming that no bulk recombination takes place ($\tau_{\mathrm{b}} \to \infty$) and a lower limit was determined by assuming an additional recombination via defects with a lifetime of $\tau_{\mathrm{SRH}} = 16\,$ms and $32\,$ms for the p and n-type material, respectively. The assumption for the bulk lifetime is rather conservative in the sense that previous publications used lower bulk lifetimes which led to a significant underestimation of the SRVs. In order to investigate the thermal stability of the surface passivation, the samples were annealed on a hotplate in an atmospheric ambient.

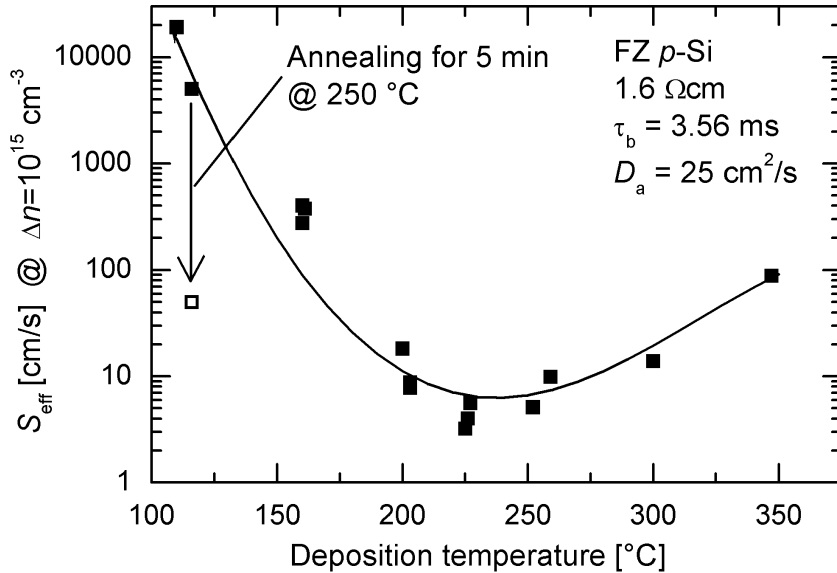# 5.2 Optimum Deposition Temperature and Thermal Stability

Figure 5.1: Measured effective SRV S_{eff} as a function of deposition temperature. The $1.6\,\Omega\mathrm{cm}$ FZ p-Si wafers were passivated on both surfaces using a-Si:H films deposited in a parallel-plate PECVD system.

For the determination of the optimal deposition temperature, the deposition temperature was varied while all other deposition parameters were kept constant. The effective carrier lifetimes of the samples were determined at a fixed injection level of $\Delta n = 10^{15}\,\mathrm{cm}^{-3}$ using the QSSPC method described in Section 3.2. As can be seen in Fig. 5.1, a broad minimum of S_{eff} is obtained in the temperature range between $200\,^{\circ}\mathrm{C}$ and $250\,^{\circ}\mathrm{C}$. Lifetime values as high as $2\,\mathrm{ms}$ have been measured. Using Eq. 2.98 with $\tau_{\mathrm{b}} = 3.56\,\mathrm{ms}$ and $D_{\mathrm{a}} = 25\,\mathrm{cm}^2/\mathrm{s}$ for the injection level of $\Delta n = 10^{15}\,\mathrm{cm}^{-3}$, S_{eff} values as low as $3\,\mathrm{cm/s}$ were achieved. The lifetime depends strongly on the deposition temperature for lower and higher temperatures. For example, a deposition temperature of $116\,^{\circ}\mathrm{C}$ results only in a very low τ_{eff} value of $6\,\mu\mathrm{s}$ ($S_{\mathrm{eff}} = 5000\,\mathrm{cm/s}$). At low temperatures ($\leq 200\,^{\circ}\mathrm{C}$), a lower mobility of the species adsorbed on the surface during the PECVD process and the reduced hydrogen diffusivity result in a poorer quality of the a-Si:H films [164]. Both effects result in an increased density of unsaturated bonds at the c-Si surface and therefore in a higher interface state density. Interestingly, we found that subsequent annealing of the samples at about $250\,^{\circ}\mathrm{C}$ drastically increases the effective carrier lifetime (Fig. 5.1). We attribute this increase to the diffusion of hydrogen to the interface and the effective passivation of dangling bond states. Higher deposition temperatures ($\geq 300\,^{\circ}\mathrm{C}$) also result in poorer surface passivation,

but for a different reason. In this case, the samples show blistering caused by molecular hydrogen accumulated in voids. Due to the blisters, the films provide a rather poor overall passivation. The blistering can be reduced by depositing thinner a-Si:H films, however, the excellent lifetimes that are obtained in the range of $200 - 250\,^\circ$C cannot be attained.
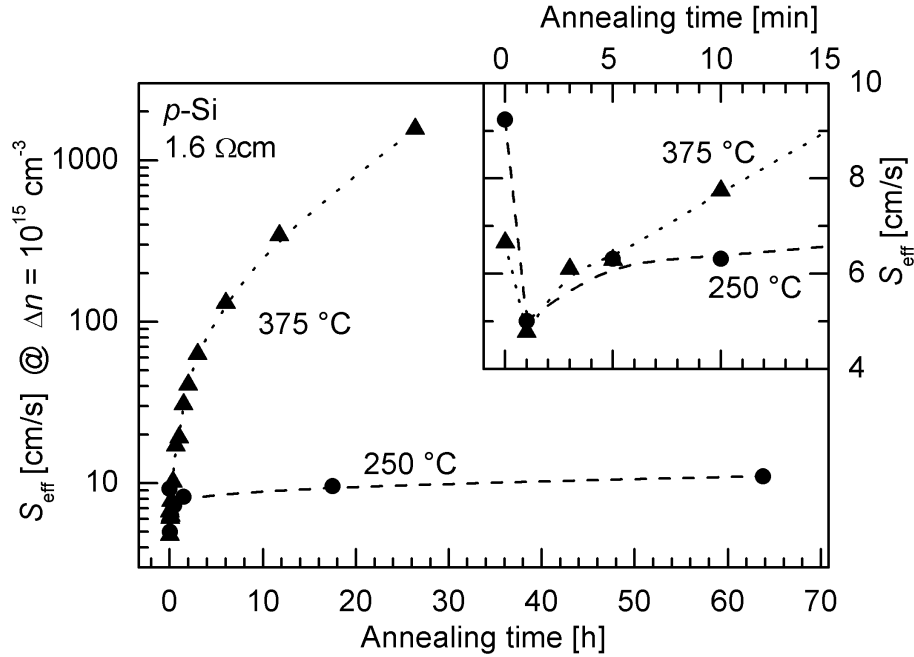

Figure 5.2: Measured effective SRV S_{eff} of a-Si:H passivated $1.6\,\Omega$cm FZ p-Si wafers annealed at $375\,^\circ$C and $250\,^\circ$C as a function of annealing time.

In order to examine the thermal stability of the surface passivation, some of the p-type samples passivated on both surfaces with an a-Si:H film deposited at $225\,^\circ$C were annealed at different temperatures. At $250\,^\circ$C as well as at $375\,^\circ$C, the surface passivation improves during the first minute of annealing, as can be seen in the inset of Fig. 5.2. We attribute this to hydrogen diffusion to the interface where it saturates dangling bond states. For longer annealing times, the passivation quality is nearly constant at $250\,^\circ$C and decreases within 30 hours by about two orders of magnitude at $375\,^\circ$C. The degradation of the surface passivation at higher temperatures is likely to be due to the effusion of hydrogen out of the films [165].

5.3   Injection Level Dependence of the Surface Recombination Velocity

Fig. 5.3 shows the injection level dependence of the effective SRV for a sample passivated on both surfaces using an a-Si:H film deposited at $225\,^\circ$C for 2 min. For an injection level
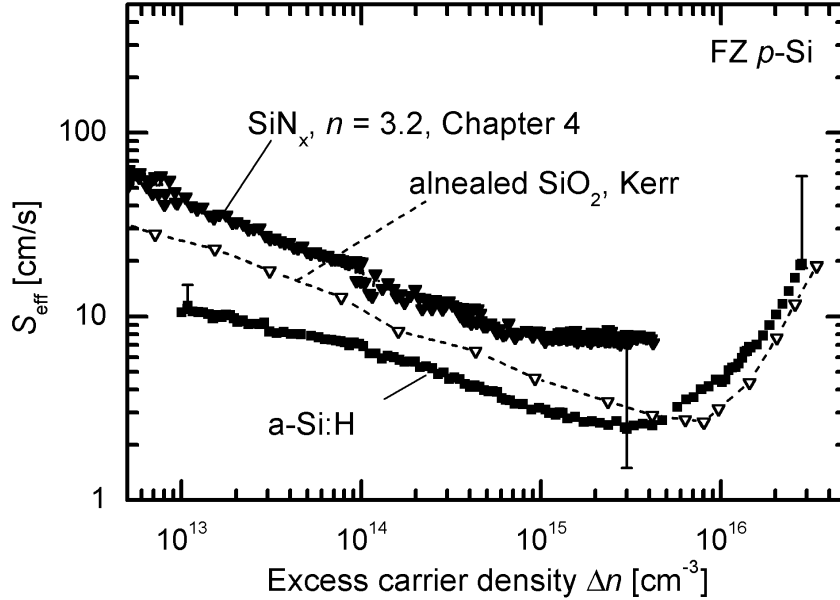
Figure 5.3: Measured effective SRV S_{eff} in dependence of the excess carrier density Δn of a $1.6\,\Omega\mathrm{cm}$ FZ p-Si wafer passivated by an a-Si:H film on both surfaces. For comparison, the $S_{\mathrm{eff}}(\Delta n)$ dependence for samples passivated using an alnealed high-temperature SiO_2 ($1\,\Omega\mathrm{cm}$ FZ p-Si substrate [166]) and a PECVD SiN_x film ($1.5\,\Omega\mathrm{cm}$ FZ p-Si, Chapter 4), respectively, are also included.

of about $\Delta n = 10^{15}\,\mathrm{cm}^{-3}$, an effective SRV as low as $3\,\mathrm{cm/s}$ is obtained. The error bars in Fig. 5.3 arise from the uncertainty in τ_{b}. In the worst case scenario, i.e., assuming an infinite bulk lifetime, $S_{\mathrm{eff}} = 8\,\mathrm{cm/s}$ was determined. If, on the other hand, in addition to the intrinsic recombination, a defect recombination was assumed with $\tau_{\mathrm{SRH}} = 16\,\mathrm{ms}$, $S_{\mathrm{eff}} = 2\,\mathrm{cm/s}$ was obtained. Even for a lower injection level of $\Delta n = 10^{13}\,\mathrm{cm}^{-3}$, the SRV was only $13\,\mathrm{cm/s}$. For comparison, the injection-level dependent SRVs of samples passivated using PECVD SiN_x and high-temperature grown alnealed SiO_2 are also included in Fig. 5.3 (cf. Fig. 4.17, [166]). It can be seen that the passivation quality of the a-Si:H films can easily compete with that of high-temperature ($\sim 1000\,^\circ\mathrm{C}$) grown SiO_2 that needs to be annealed with a capping layer of Al (the so-called 'alneal') to provide excellent passivation. Also, the passivation quality provided by our a-Si:H films exceeds that of optimised PECVD SiN_x deposited at 400°C.

As already mentioned above, there is some discussion regarding the quality of a-Si:H passivation on silicon wafers of different conduction type. In order to examine the passivation properties of a-Si:H on n-type c-Si wafers, a-Si:H films were deposited onto both surfaces of $3.4\,\Omega\mathrm{cm}$ n-type Cz Si material using the same deposition parameters as used above on p-type Si. The injection level dependence of the measured SRV is shown in Fig. 5.4. A measured τ_{eff} of $3.0\,\mathrm{ms}$ at an injection level of $\Delta n = 1.5 \times 10^{15}\,\mathrm{cm}^{-3}$ corresponds to an S_{eff} value
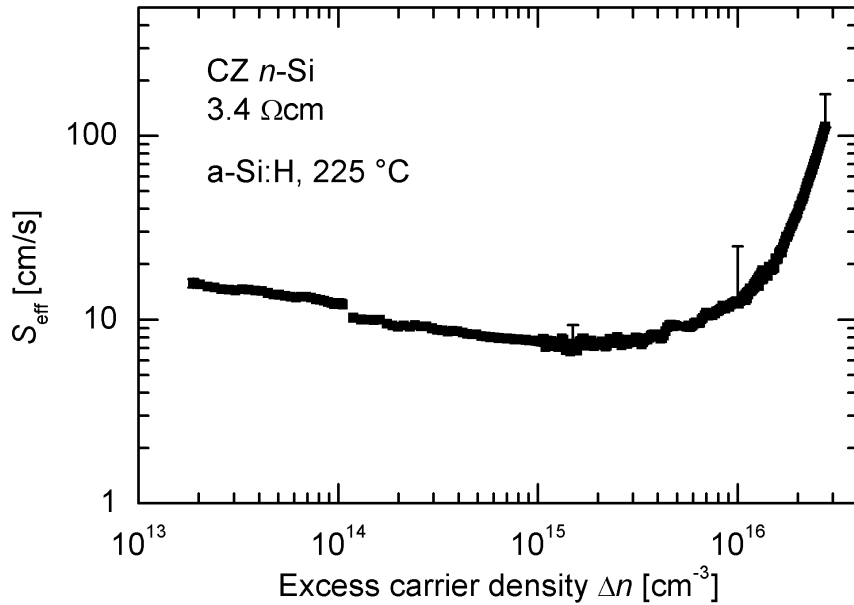
Figure 5.4:   Measured injection level dependence of the effective SRV S_{eff} at the a-Si:H/c-Si(n) interface of a $3.4\,\Omega$cm Cz n-Si wafer.

of $7\,\mathrm{cm/s}$, assuming intrinsic bulk recombination only. If no bulk recombination is assumed, the upper limit for S_{eff} is calculated to be $9\,\mathrm{cm/s}$. A lower limit for S_{eff} is determined to be $6\,\mathrm{cm/s}$ if an additional defect recombination with $\tau_{\mathrm{SRH}} = 32\,\mathrm{ms}$ is assumed. A very small increase of the SRV with decreasing injection level is observed, resulting in $S_{\mathrm{eff}} = 15\,\mathrm{cm/s}$ ($\tau_{\mathrm{eff}} = 1.6\,\mathrm{ms}$) at $\Delta n = 2 \times 10^{13}\,\mathrm{cm}^{-3}$.

5.4   a-Si:H Conductivity

In order to determine the conductivity of the a-Si:H films, the following sample structure was used: parallel Al contact lines of different spacings were evaporated on a glass substrate. Subsequently, a-Si:H films were deposited onto the Al-glass substrate structure. The structure is similar to that shown in Fig. 4.8, although a glass substrate rather than a p-Si substrate was used, a-Si:H films rather than SiN$_{\mathrm{x}}$ films were deposited and the tunnel oxide was omitted. Since the contact spacings were of different length, the sheet resistance without the contact resistance between the Al contacts and the a-Si:H films could be determined (transfer length method) (cf. Section 4.4). Using the film thickness determined by ellipsometry, the resistivity of the a-Si:H films was determined. Owing to some scattering of the data, the resistivity could only be determined to be in the range of $10^5 - 10^7\,\Omega$cm which is in accordance with data published in the literature for intrinsic amorphous silicon [167, 168, 169].

5.5   Discussion

In conclusion, the investigated a-Si:H films provide excellent surface passivation with effective SRVs below $10\,\mathrm{cm/s}$ on both n- and p-type crystalline silicon material that is typically used for solar cell manufacturing. The very low deposition temperature $(200-250°C)$ has two major advantages: first, a lower energy budget for cell processing and second, a reduced risk of impurity diffusion into the substrate. The films can be readily used as a rear surface passivation for crystalline silicon solar cells. Compared with SiN_x rear surface passivation, a further advantage is expected: since SiN_xpassivation relies on the field-effect passivation provided by the fixed positive charges in the films, parasitic shunting between the inversion layer underneath the films and the rear metal contacts deteriorates the cell performance (Section 6.3). In this respect, a possible inversion layer sheet conductance was investigated with a sample structure similar to that shown in Fig. 4.8 with the only difference that a-Si:H films instead of SiN_x films were used. Unfortunately, a clear result of a sheet conductance parallel to the junction interface that can be attributed to the a-Si/c-Si heterojunction could not be obtained. However, published values for the band-bending are about $0.7\,\mathrm{V}$ [159, 170] and, hence, the free electron charge available in p-type c-Si is small ($Q_{sc.n} \approx 10^{10}\,\mathrm{cm}^{-2}$) and can only support a rather small current. Thus, using a-Si:H films as rear surface passivation, the parasitic shunting found for SiN_x rear surface passivation is circumvented and the deposition temperature is even decreased. This will be further discussed in Section 6.4.2.

The important finding that silicon material of both conduction types can be effectively passivated, demonstrates that both heterojunction cell structures (a-Si(p)/c-Si(n) as well as a-Si(n)/c-Si(p)) are equally promising considering interface recombination only. In this context, it is worth mentioning that although V_{oc} values at least $60\,\mathrm{mV}$ lower are reported for the a-Si(n)/c-Si(p) type structure, the highest V_{oc} value that was reported so far was not limited by interface recombination at the a-Si/c-Si interface [159]. However, one of the structures may be more favourable due to the different carrier mobilities of holes and electrons [161], due to the light-induced degradation of the bulk lifetimes reported for boron-doped Cz but not for n-type Cz c-Si material [171] or in terms of technological aspects. It is noteworthy that the optimal deposition temperature for a-Si:H films is about $150\,°C$ lower than that found for SiN_x films. However, SiN_x passivation can withstand higher annealing temperatures. These differences may be due to different hydrogen contents, hydrogen bonding types or hydrogen diffusivities and further investigations would be interesting.

Chapter 6

Solar Cell Results

The future trend towards lower cell thickness for crystalline silicon solar cells exhibiting diffusion lengths exceeding the cell thickness has increased the demand for low-cost, yet effective rear surface passivation schemes. As was demonstrated in Chapter 4, SiN_x deposited by low-temperature ($400\,°C$) PECVD is a promising candidate for achieving this goal since thin SiN_x films provide very low surface recombination velocities [64, 172]. Also, a-Si:H films deposited using PECVD at even lower temperature ($200 - 250\,°C$) provide excellent surface passivation as was demonstrated in Chapter 5. The surface passivation properties are comparable for SiN_x, a-Si:H and alnealed SiO_2 films as can be seen from Fig. 5.3. This chapter examines the applicability of these films as a rear surface passivation scheme for crystalline silicon solar cells. After a brief review of previous work in Section 6.1, the first solar cell results are presented in Section 6.2. SiN_x passivated solar cells exhibit an unexpected performance loss compared with solar cells passivated with SiO_2 at the rear surface. This SiN_x-specific loss mechanism is is investigated in detail in Section 6.3. Section 6.4 deals with the avoidance of the performance loss found for SiN_x passivated solar cells and the application of a-Si:H films as a new rear surface passivation scheme.

6.1   Previous Work

Optimised SiN_x films were first applied to bifacial silicon solar cells as surface passivating anti-reflection coatings [173, 174]. The high open-circuit voltage of $649\,mV$ that was achieved for solar cells having both surfaces passivated with SiN_x films demonstrates the excellent surface passivation provided by the SiN_x films [175]. Recently, the results of solar cells incorporating SiN_x films for rear surface passivation were compared with results of cells incorporating a high-temperature-grown silicon dioxide [176, 177]. Since the passivation of silicon surfaces by thermally grown oxide films is the most common passivation scheme for laboratory high-efficiency solar cells today, these cells can be regarded as references. It was found that the open-circuit voltages of the SiN_x rear surface passivated cells are comparable to the respective silicon dioxide passivated reference cells differing only about $1.0\,\%$ at the most: Kerr *et al.* reported open-circuit voltages of $667.3\,mV$ for a planar, all-nitride passivated solar cell and $661\,mV$ for the respective reference cell [176, 178]. The

rear contact openings in these cells were defined by photolithography and chemical etching. Glunz *et al.* published values of 660 mV for SiN$_x$ and 661 mV for oxide rear surface passivated solar cells [177]. They performed the patterning of the rear dielectric layer by laser ablation. In the same paper, they reported on open-circuit voltages of 674 and 678 mV, respectively, for solar cells with contact patterns formed by plasma etching. In Section 6.2, we report 654 and 657 mV for cells with contact openings defined by mechanical abrasion. Despite these remarkably high open-circuit voltages for SiN$_x$ rear surface passivated cells, the obtained short-circuit current densities are—in some cases exceptionally—lower compared with the oxide passivated cells. In this respect, Glunz *et al.* reported, in the case of cells having the laser-ablated rear contact pattern, 37.4 mA/cm^2 for the SiN$_x$ and 39.7 mA/cm^2 for the oxide rear surface passivated cells [177] while we found 37.1 mA/cm^2 compared with 39.2 mA/cm^2 (Section 6.2). It is noteworthy that such a significant current loss is not observed in all relevant cases, indicating that the efficiency losses might be eliminated by using SiN$_x$ films of varying composition or a different method to perform the contact opening [176, 177].

6.2   First Cell Results
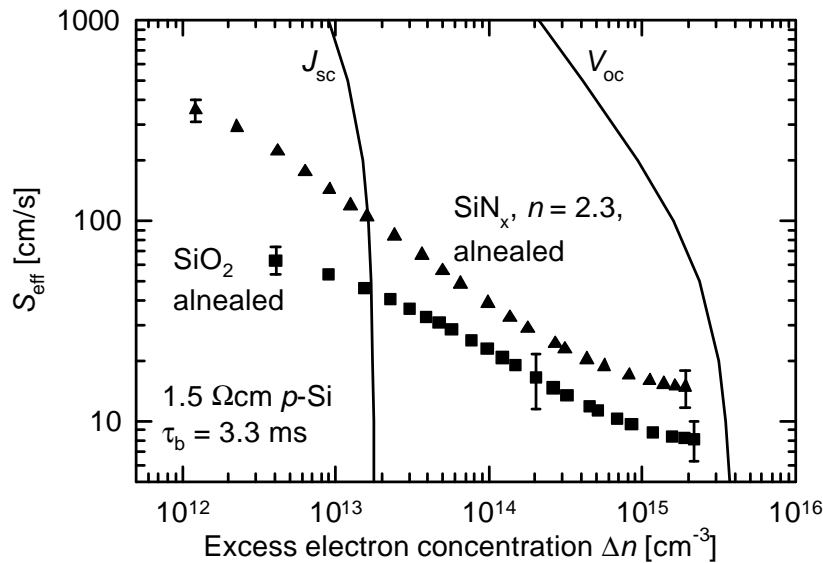
Figure 6.1: SRV as a function of the excess carrier density Δn determined using carrier lifetime test structures passivated using SiO$_2$ and SiN$_x$ films. The SiO$_2$ films were grown at high temperature (1050 °C) while the SiN$_x$ films were deposited using PECVD at 400 °C. After film preparation the samples were covered with Al and annealed at 500 °C for 10 min (alneal). The effective carrier lifetime was determined using MW-PCD measurements. Also shown is the calculated bulk excess carrier density as a function of the SRV for J_{sc} and V_{oc} conditions (turn graph by 90 °) of a typical solar cell using the following assumptions: $N_A = 10^{16}$ cm^{-3}, 300 μm thick wafer, $\tau_b = 3.3$ ms, illumination intensity 100 mW/cm^2, 16 % front surface reflectance, SRV at front surface $S_f = 1000$ cm/s, SRV at rear surface as shown on the y-axis.

In order to compare the surface passivation quality of SiO_2 and SiN_x films, symmetrical carrier lifetime test structures were fabricated according to the process sequence outlined in Section 4.5. Fig. 6.1 shows a comparison of the measured SRV for lifetime test structures passivated with SiO_2 grown at high temperature (1050 °C) and with SiN_x films deposited by PECVD (400 °C) as described in Section 3.1.1. The samples were annealed for 20 min at 500 °C, with a capping layer of Al, process referred to as 'alneal' ([57], p. 169). This alnealing step serves to distinctly improve the passivation quality at Si/SiO_2 interfaces and to form the ohmic back contact for the solar cells discussed later in this section. The capping layers of the alnealed samples were removed and the effective lifetime τ_{eff} was subsequently measured at various bias light intensities using light-biased MW-PCD measurements as described in Section 3.2.1. While an alneal drastically reduces the SRV at the Si/SiO_2 interfaces, the SRV remains constant at Si/SiN_x interface after the alnealing. As can be seen from Fig. 6.1, alnealed SiO_2 films provide a slightly better surface passivation compared with SiN_x films. Also shown are the calculated bulk excess carrier densities as a function of the rear SRV for J_{sc} and V_{oc} conditions, respectively. The Δn value at V_{oc} conditions is about two orders of magnitude higher compared with Δn at J_{sc} conditions. An estimation of the expected solar cell results using the measured SRVs for the cell rear gives for both passivation schemes very similar parameters: Assuming a rear SRV of $S_r = 46$ cm/s ($S_r = 104$ cm/s), corresponding to J_{sc} conditions, results in $J_{sc} = 39.1$ mA/cm^2 ($J_{sc} = 39.0$ mA/cm^2) for SiO_2 (SiN_x) rear surface passivation. For V_{oc} conditions, $S_r = 8$ cm/s ($S_r = 15$ cm/s) was assumed for the SiO_2 (SiN_x) passivation and $V_{oc} = 663$ mV was calculated for both passivation schemes. Note that the SRV in real devices will be higher since the recombination at the rear metal contacts was neglected in this calculation. The important result is that with both passivation schemes similar solar cell results may be expected.

		SiO_2 $n = 1.46$	SiN_x $n=2.3$
V_{oc}	[mV]	657 ±1	654 ±1
J_{sc}	[mA/cm^2]	39.2±0.2	37.1±0.1
FF	[%]	81.0±0.2	80.2±0.8
η	[%]	20.9±0.0	19.5±0.1

Table 6.1: Experimental results for oxide and nitride rear surface passivated MIS-n^+p solar cells (textured front surface, 0.5 Ωcm FZ p-Si).

Table 6.1 shows the experimental results of the processed cells on 0.5 Ωcm FZ p-type silicon with front surface texture, fabricated as described in Section 3.3. The rear surface of the cells was either passivated using SiO_2 films thermally grown at high temperature (1050 °C) or using PECVD SiN_x films deposited at 400 °C. The mean values of a set of four identically processed samples are shown in Table. 6.1. The conversion efficiency of the SiN_x passivated cells is 1.4 % smaller compared with the SiO_2 passivated cells. The decrease in efficiency can mainly be attributed to a lower short-circuit current density of 2.1 mA/cm^2. This result cannot be explained by the small differences in the SRVs that was discussed in
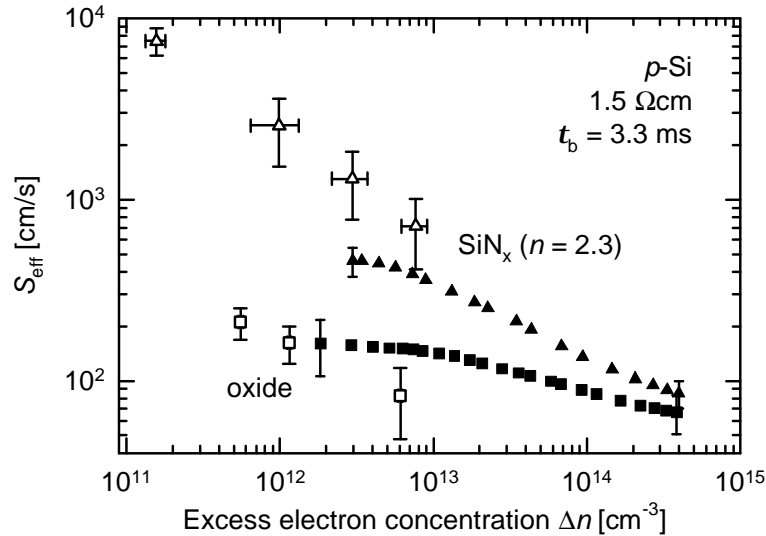
Figure 6.2: Measured area-averaged S_{eff} as a function of Δn at SiO_2 and SiN_x passivated p-Si wafers using the MW-PCD technique (filled symbols). The lifetime test structures received an alneal step after film preparation. In order to be comparable to solar cells, contact openings were introduced by mechanical abrasion into the passivating films (unlike Fig. 6.1). Also shown are the $S_r(\Delta n)$ values at the rear surface of finished solar cells determined by SR measurements (open symbols, Section 6.3.4). $300\,\mu$m thick $1.5\,\Omega$cm p-Si wafers were used as substrate material for the lifetime test structures and the solar cells.

the previous paragraph.

The SRV can be determined from photoconductance measurements of lifetime test structures (Section 3.2) as well as from spectral response measurements of solar cells (Section 3.4.2 and Section 6.3.4). In order to examine the differences between SiO_2 and SiN_x passivated cells in more detail, both methods were applied to investigate the SRV. Again, the lifetime test structures used received an alneal after film preparation. In contrast to the lifetime samples investigated before (Fig. 6.1), lines were cut into the dielectric layers by means of mechanical abrasion. These lines correspond to the highly recombinative metal contact areas at the rear surface of solar cells. The SRV as a function of Δn determined on these structures is shown in Fig. 6.2 (filled symbols). In contrast to the results shown in Fig. 6.1, the injection level dependence of S_{eff} at the Si/SiN_x interface is more pronounced. This important finding becomes particularly obvious if the low-injection regime is considered. However, due to signal-to-noise problems, the SRV cannot be determined by MW-PCD measurements in very low injection. Hence, SR measurements of finished solar cells were used instead.[1] Planar solar cells on the same $1.5\,\Omega$cm substrate material as used for the carrier lifetime test structures were used for the SR measurements. The effective diffusion length L_{eff} was determined according to Eq. 3.32 and the rear effective SRV S_r was calculated using Eq. 3.33. Subsequently, the excess carrier density Δn at J_{sc} conditions

---

[1]The limit for the accessible injection range towards low injection is even more restricted when the QSSPC method is used.

was determined using the simulation program PC1D with S_r as parameter. Fig. 6.2 shows the results of the SR measurements (open symbols). Although the SRV is determined at completely different samples, carrier lifetime test structures and solar cells, respectively, the S_{eff} values correspond reasonably well. As can be seen from Fig. 6.2, the SRV at the Si/SiO$_2$ interface saturates for low injection levels while for the Si/SiN$_x$ interface it further increases with decreasing injection level.

In first explanations the differences in cell performance were attributed to pinholes in the SiN$_x$ film [179], to the injection level dependence of the SRV [180] and to optical effects due to a different internal rear reflectance [181]. However, as will be discussed in detail in the next section, the performance loss found for the SiN$_x$ passivated solar cells and the pronounced injection level dependence of the SRV observed for the SiN$_x$ passivated samples with highly recombinative areas can predominantly be attributed to a parasitic shunting between the induced floating junction underneath the SiN$_x$ films and the rear metal contacts. For the identification of the loss mechanisms, a comparative experiment was carried out.

6.3   Loss Mechanisms in SiN$_x$ Passivated Silicon Solar Cells

In this section, experimental evidence is presented that the predominant reason for low J_{sc} values obtained forSiN$_x$ rear surface passivated solar cells is shunting across the induced floating junction (FJ) at the rear surface (Section 6.3.2). Results of a solar cell test structure that features a separation of the inversion layer from the metal contacts are presented. This test structure allows for the identification of the main loss mechanism. Besides the dominant loss in the short-circuit current, a further characteristic trait of a shunt across a rear FJ is a shoulder observed in the corresponding dark I-V curve of the cell [182]. We report on shoulders in dark I-V curves of SiN$_x$ rear surface passivated solar cells (Section 6.3.3). Since shoulders in dark I-V curves can be attributed to an injection-level-dependent SRV of the Si/SiN$_x$ interface as well, an estimation is given for the relevance of each effect. Furthermore, spectral response (Section 6.3.4) and LBIC (Section 6.3.5) measurements are used as a further proof for the parasitic shunting.

6.3.1   Experimental

The MIS-n^+p process as described in Section 3.3 was used for fabricating the front of the test cells. The cells have an active area of $4\,cm^2$. Three different sets of cells were fabricated differing only in the rear surface passivation scheme. For the first cell type, SiN$_x$ films were used to passivate the whole non-metalised area at the rear surface of the cells. These are referred to as PR-SiN cells (passivated rear with SiN$_x$) in the following. As reference, a second set of cells having a high-temperature ($\sim$1000 °C) grown silicon dioxide rear surface passivation were fabricated, referred to as PR-SiO cells in the text. The rear of the solar cells is schematically shown in Fig. 6.3. For a detailed investigation of two-dimensional effects, additional solar cell test structures were fabricated characterised by photolithographically defined oxide lines between the SiN$_x$ films and the contact lines,
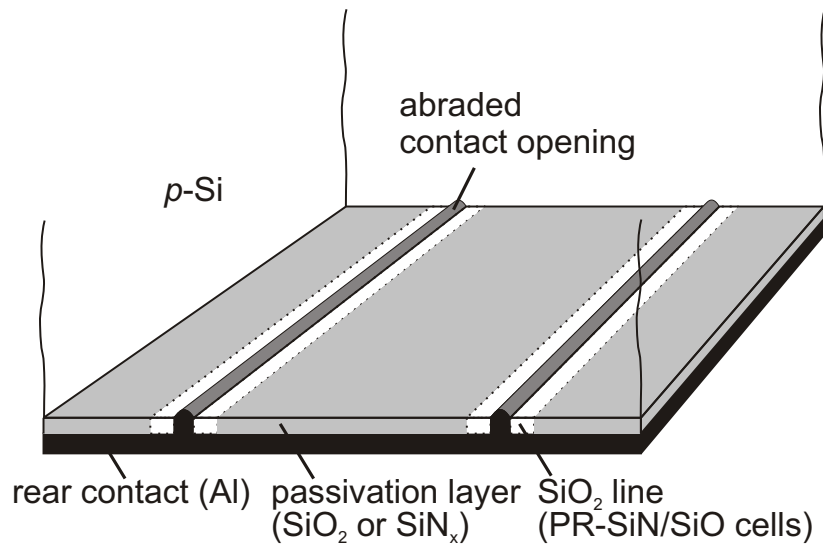
Figure 6.3: Schematic sketch of the rear region of the MIS-n^+p solar cells fabricated to identify losses found for SiN$_x$ passivated solar cells. Silicon nitride passivated rear surface cells (PR-SiN) incorporate a SiN$_x$ film for rear surface passivation, silicon dioxide passivated rear solar cells (PR-SiO) a SiO$_2$ film, while in the case of the PR-SiN/SiO cells the passivating SiN$_x$ film is separated by oxide lines from the rear metal contacts (indicated by dotted lines).

leaving about 88 % of the rear surface passivated by SiN$_x$ (3 % contact area and 9 % oxide passivation). Oxide lines of about 200 μm width separate the SiN$_x$ passivated areas from the metal contacts as is sketched by the dotted lines in Fig. 6.3. These cells are referred to as PR-SiN/SiO in the following. In this test structure, the inversion layer underneath the SiN$_x$ films is separated from the rear metal contact. The rear contacts are formed by mechanical abrasion for all fabricated solar cells. For a sound comparison of the different cell structures all cells were fabricated in the same run. It should be noted that since the contact openings are formed by mechanical abrasion, defects are introduced in the crystal between the inversion layer and the contact. The defects may cause current paths thus enhancing the parasitic shunt conductance. However, PR-SiN cells with rear contact openings realised by photolithography and chemical etching that have been fabricated at ISFH show the same non-idealities as those for which the contact openings were formed by mechanical means. Also, samples that received an additional saw damage etch after the abrasion step give the same results. For simplicity, this damage etch was omitted for all cells described in this work.

Type	V_oc [mV]	J_sc [mA/cm^2]	FF [%]	η [%]
PR-SiO	649 ± 1	34.5 ± 0.2	80.0 ± 0.2	17.9 ± 0.2
PR-SiN	643 ± 1	33.1 ± 0.1	78.9 ± 0.3	16.8 ± 0.1
PR-SiN/SiO	646 ± 1	34.3 ± 0.2	80.2 ± 0.2	17.8 ± 0.1

Table 6.2: Measured cell parameters of planar PR-SiO, PR-SiN and PR-SiN/SiO MIS-n^+-p solar cells under AM1.5G, 100 mW/cm^2 illumination at 25 °C. All samples were processed in the same run. Mean values of four identically processed samples are shown. The substrate material used was 1.5 Ωcm FZ p-type Si. Note that the significantly lower short-circuit current densities compared with those in Table 6.1 are due to the planar cell structure.

6.3.2   Analysis of Illuminated I-V Curves

The measured cell parameters of the fabricated MIS-n^+-p solar cells are summarised in Table 6.2. The results are mean values of a set of four identically processed samples. For PR-SiN cells, V_oc is only 6 mV (0.9 % relative) smaller than for the reference PR-SiO cells. This can be attributed to the excellent surface passivation of SiO$_2$ and SiN$_\mathrm{x}$ films at injection levels corresponding to V_oc conditions (about 10^{15} cm^{-3}, Fig. 6.1). In contrast, for the short-circuit current density (J_sc) a significant reduction of 1.4 mA/cm^2 (4 % relative) is observed for the PR-SiN cells compared with the PR-SiO reference cells. By introducing narrow oxide lines to separate the SiN$_\mathrm{x}$ passivated areas from the metal contacts, this reduction in J_sc decreases to only 0.2 mA/cm^2, i.e., it is nearly eliminated. The same trend can be seen for the fill factor, however, to a lesser extent. The results for the PR-SiN/SiO cells provide clear experimental evidence that two-dimensional effects affect the cell performance predominantly.

An explanation of the experimental results follows from the high amount of fixed positive charges that SiN$_\mathrm{x}$ films contain ($Q_\mathrm{f} \approx (2-3) \times 10^{12}$ cm^{-2}) inducing a strong band-bending and resulting in an inversion layer in the silicon beneath (Chapter 4). Note, that in contrast to SiN$_\mathrm{x}$ the oxide films contain a fixed charge density of only about $Q_\mathrm{f} \approx 10^{11}$ cm^{-2} (Section 4.3) resulting in no or only a weak inversion layer. A band-bending in thermal equilibrium is often referred to as a junction. Since the junction is covered by a dielectric layer, the potential is floating, i.e., for silicon nitride passivation the same principles as in FJ passivation incorporating a diffused junction will apply [183]. No precautions are taken in the case of PR-SiN cells to separate the inversion layer from the metal contacts. Thus, lateral current flow in the n-type layer toward the rear contacts reduces the cell performance of the PR-SiN cells. This current path can be regarded as a shunt between the inversion layer and the rear metal contact.

Fig. 6.4 shows a one-dimensional band diagram representing a solar cell with a shunted floating junction at the rear surface. Under illumination, electrons are photogenerated throughout the base resulting in a separation of the quasi-Fermi levels. Electrons in the inversion layer at the rear can either be injected into the p-type base of the cell, or they can flow through the parasitic shunt resistance into the rear contact, in which case they do not contribute to the cell current. Like any junction, if the voltage V_r across the FJ
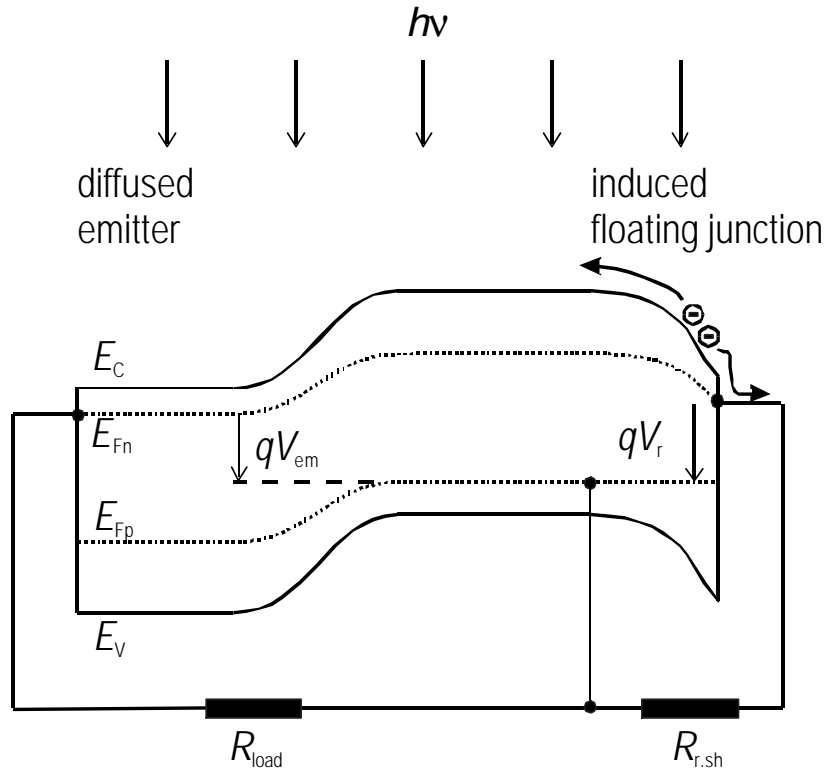
Figure 6.4: Schematic energy band diagram of an illuminated solar cell with an induced junction at the rear surface and a parasitic shunt $R_{\rm r.sh}$ between the inversion layer and the rear contact.

is small, practically all of the current flows through the shunt resistance, whereas if the voltage is high, the main part of the current flows through the diode. The excess carrier density Δn under $J_{\rm sc}$ conditions is about two orders of magnitude lower than under $V_{\rm oc}$ conditions (Fig. 6.1), i.e., $V_{\rm r}$ is smaller under $J_{\rm sc}$ conditions compared with $V_{\rm oc}$ conditions. Thus, the ratio of the shunt to the diode current will be larger under $J_{\rm sc}$ compared with $V_{\rm oc}$ conditions. In order to quantify the effect, PC1D simulations [35] were carried out. The results are shown in Fig. 6.5. As can be seen, a parasitic shunt across a FJ reduces $J_{\rm sc}$ even for a small value of the shunt conductance, while $V_{\rm oc}$ will remain unaffected unless the conductance is larger. This is in accordance with the experimental results of the PR-SiN cells if an intermediate shunt conductance is assumed. The shunt conductance is prevented or at least significantly decreased in case of the PR-SiN/SiO cells since SiO_2 films contain a lower density of fixed positive charges compared with SiN_x films. Besides a small shunt conductance that might still be present, a further reason for the small loss in short-circuit current (0.2 mA/cm^2) observed for the PR-SiN/SiO cells compared with the PR-SiO cells is the poorer passivation of the SiN_x films at low injection levels which are typical for $J_{\rm sc}$ conditions. It is noteworthy, that an additional two-dimensional effect due to the injection-level-dependent SRV at the Si/SiN$_x$ interface decreases the cell performance of the PR-
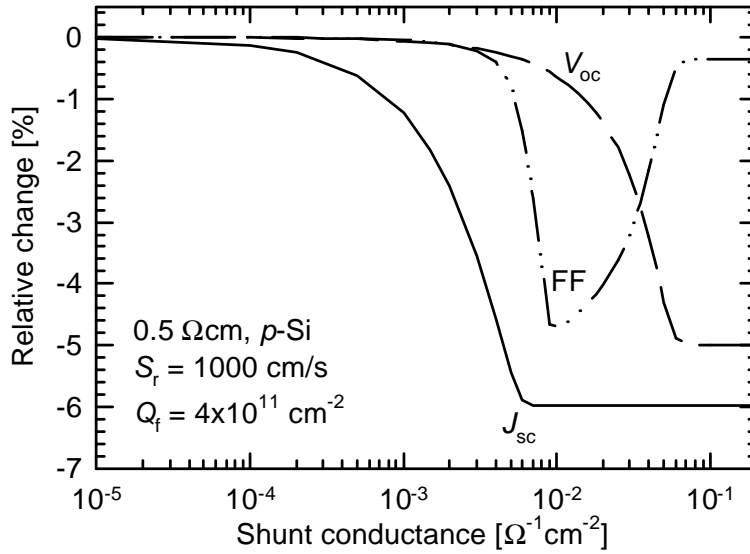
Figure 6.5: Calculated relative changes in J_sc, V_oc and FF as a function of the shunt conductance $1/R_\text{r.sh}$. The assumed fixed charge density in the dielectric rear film of $Q_\text{f} = 4 \times 10^{11}\,\text{cm}^{-2}$ causes a weak inversion in thermal equilibrium (Fig. 2.13). For zero shunt conductance the calculated values are: $J_\text{sc} = 38.7\,\text{mA/cm}^2$, $V_\text{oc} = 684\,\text{mV}$, FF $= 81.4\,\%$. Assumptions: AM1.5G, 300 K, $300\,\mu$m thick $0.5\,\Omega$cm p-type Si wafer, $\tau_\text{b} = 500\,\mu$s, $S_\text{f} = 0\,\text{cm/s}$, $S_\text{r} = 1000\,\text{cm/s}$.

SiN cells. However, this effect is of minor importance as will be clarified in the following discussion. Since metal contacts show a high recombination, the injection level is reduced in the areas surrounding the contacts. For both dielectric passivation films, SiO$_2$ and SiN$_\text{x}$, the SRV is higher the lower the injection level, thus the reduction of the injection level is further enhanced. These recombination losses are higher for SiN$_\text{x}$ passivated surfaces since the SRV is higher for Si/SiN$_\text{x}$ passivated interfaces compared with Si/SiO$_2$ interfaces (Fig. 6.1). Hence, replacing SiN$_\text{x}$ by SiO$_2$ in contact-adjacent regions reduces recombination and thereby additionally improves the cell performance. However, a major impact of this effect can be excluded since the SRV at the Si/SiN$_\text{x}$ interface is only slightly more than twice as high as the SRV at the Si/SiO$_2$ interface (104 cm/s versus 46 cm/s for Δn of about $10^{13}\,\text{cm}^{-3}$ corresponding to J_sc conditions, Section 6.2) whereas metal contacts exhibit SRVs in the order of $10^4 - 10^6\,\text{cm/s}$. Thus, current flow from the inversion layer into the metal contacts is the dominant parasitic effect for PR-SiN cells.

In order to demonstrate the potential of SiN$_\text{x}$ passivated cells, the contact spacing at the rear surface was enlarged to focus on the passivation quality. A lower fill factor due to a higher series resistance is disregarded. Due to an improved rear surface passivation, both V_oc and J_sc increase with increasing contact spacing, as can be seen in Table 6.3. The relative increase in the short-circuit current of the PR-SiN cells is nearly by a factor of five higher than that of the PR-SiO cells. Again, this can be explained by a shunt resistance across the electrostatically induced FJ. Due to the relatively high sheet resistance of the inversion layer, less electrons from the inversion layer are collected if the distance to the

Cell type	Cell parameter		Contact spacing		Relative changes
			standard	wide	between 7 and 3 mm cells
			3 mm	7 mm	[%]
PR-SiO	V_{oc}	[mV]	655.6±0.9	657.0±2.0	0.2
	J_{sc}	[mA/cm²]	39.01±0.03	39.33±0.16	0.8
	FF	[%]	80.2 ±0.7	78.8 ±0.4	-1.7
	η	[%]	20.5 ±0.2	20.4 ±0.1	-0.5
PR-SiN	V_{oc}	[mV]	652.0±3.7	655.9±2.4	0.6
	J_{sc}	[mA/cm²]	36.76±0.61	38.17±0.17	**3.8**
	FF	[%]	80.8 ±0.2	78.7 ±0.4	-2.6
	η	[%]	19.4 ±0.4	19.7 ±0.2	1.5

Table 6.3: Cell parameters for PR-SiO and PR-SiN cells with different rear contact spacings. 3 mm is the optimum contact spacing for PR-SiO cells made on $0.5\,\Omega$cm FZ p-type Si. The cells with 7 mm contact spacing have only three rear contact lines. Mean values of 4 cells per cell type are shown. The substrate material used is $0.5\,\Omega$cm FZ p-type Si with textured front surface. In-house measurement under standard AM1.5G, 100 mW/cm² illumination at 25 °C.

contact increases. It is important to note that a major influence of pinholes in the SiN_x films, short-circuiting the inversion layer with the overlying metal film, can be excluded due to the higher J_{sc} of the PR-SiN/SiO (Table 6.2) and the PR-SiN cells with wider contact spacing (Table 6.3) compared with PR-SiN cells. For the same reasons a major influence of optical effects arising from the different internal reflectance of the rear layer structures can be excluded.

6.3.3   Analysis of Dark I-V Curves

Fig. 6.6 (a) shows the dark I-V curves of one sample of each solar cell set (PR-SiN, PR-SiO, PR-SiN/SiO). Shoulders in dark I-V curves can be highlighted as a bump if the inverse slope of the $\log(I)$-V curve is considered, that is the local ideality factor m_{loc} against V (m_{loc}-V) curve (Fig. 6.6 (b) and Section 3.4.1). The saturation current for the PR-SiO cell is the lowest and no bump is seen in the m_{loc}-V curve. For the PR-SiN and the PR-SiN/PR-SiO cells, a shoulder is clearly visible that is seen as a bump in the respective m_{loc}-V curves. The peak of the bump is located at 570 mV (510 mV) for the PR-SiN (PR-SiN/SiO) cell. The decreasing slope in the dark I-V curves (increasing local ideality factor) at higher voltages can be attributed to the series resistance of the cells.

Shoulders in the dark I-V curve are characteristic of a strongly injection-level-dependent SRV at the rear surface. SRVs that are significantly higher at low external voltages, i.e., at low injection levels, than at higher voltages and a transition from high to low SRV occurring over a relatively small injection range, give rise to shoulders in dark I-V curves. Two very different causes have been proposed for these non-ideal characteristics [184, 73]: The first cause is the trivial case that the effective SRV of the passivating film/Si interface shows an injection level dependence as in the case of SiO_2 rear surface passivated solar cells.
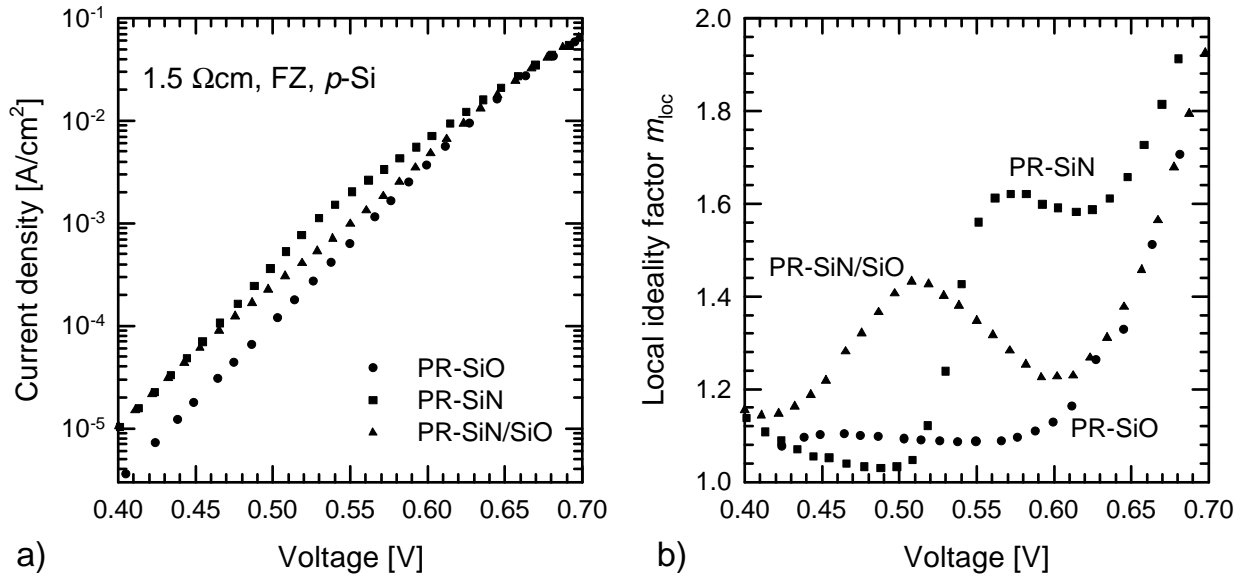
Figure 6.6: (a) Dark IV curves and (b) local ideality factor as a function of voltage ($m_{loc} - V$) measured on a PR-SiO, PR-SiN, PR-SiN/SiO cell of the cells from table 6.2.

Shoulders in dark I-V curves have been reported for high-temperature SiO$_2$ passivated PERL (passivated emitter and rear) solar cells, due to the transition from high to low effective SRV with increasing injection level for Si/SiO$_2$ interfaces [184]. A second very different cause for the transition from high to low SRV with increasing voltage is a parasitic shunt across a rear FJ [73, 182]. The shunt causes an overall SRV that is injection-level-dependent even if the interface itself does not show any injection level dependence of the SRV. This can be explained in analogy to the interpretations given for the illuminated case in the previous section. In the shunt-dominated case at low V_r (Fig. 6.4), electrons in the inversion layer flow through the parasitic shunt resistance into the rear contact. In this case they do not contribute to the cell current corresponding to a very high overall SRV [182]. In contrast, in the diode-dominated case, the overall SRV is determined by the SRV of the passivation layer at the rear surface. The voltage required to cause the transition from shunt-dominated to diode-dominated current flow depends primarily on the magnitude of the shunt resistance [182].

A relationship between the voltage across the FJ (V_r) and the voltage across the emitter (V_{em}) was calculated by Altermatt *et al.* [185]. In the ideal case of no recombination, V_r equals V_{em}. If current is lost due to shunts or recombination at the rear surface, V_r is smaller than V_{em} at low V_{em} and approaches V_{em} for higher voltages across the emitter. The higher the current loss the higher V_{em} (and therefore external voltage) is required for the transition from shunt- to diode-dominated current flow. Thus, for a small shunt resistance the shoulder occurs at a higher external voltage in the dark I-V curve.

Although the underlying physics is very different for the two possibilities that cause a shoulder in the dark I-V curve, the exhibited non-idealities are very similar, making it

difficult to assign certain amounts of the observed non-idealities to either of both effects. However, the different voltages at which the bumps for the PR-SiN or PR-SiN/SiO cell, respectively, occur (Fig. 6.6) make it possible to distinguish between the effects. Since the rear effective SRV of the PR-SiN/SiO cells is almost the same as that of the PR-SiN cells, the difference between the two cell types lies only in the increased shunt resistance due to the separation of the inversion layer from the metal contacts. Thus, it can be concluded that the shunting across the FJ is the more significant effect for the PR-SiN cell in accordance with the results presented in the previous section. Owing to the increased shunt resistance in the PR-SiN/SiO cells, the transition from shunt to diode-dominated behaviour occurs at lower voltages. However, in contrast to the PR-SiN cell, the shoulder in the dark I-V curve of the PR-SiN/SiO cell is additionally affected by the injection-level-dependent SRV of the Si/SiN$_\mathrm{x}$ interface.

6.3.4   Spectral Response Measurements
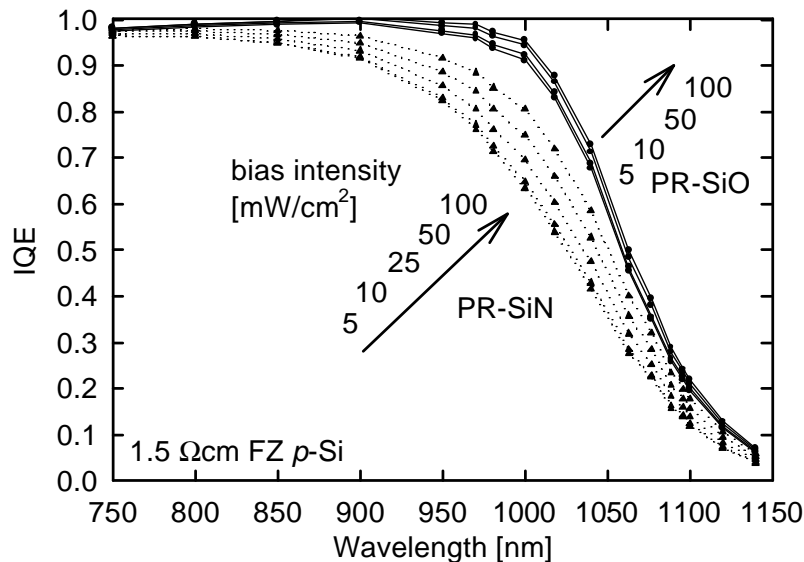
Figure 6.7: Internal quantum efficiency (IQE) of SiO$_2$ passivated and SiN$_\mathrm{x}$ passivated ($n = 2.3$) planar solar cells at different bias light intensities. $300\,\mu$m thick $1.5\,\Omega$cm FZ p-Si wafers were used as substrate material. The IQE values in the range $800 - 1000\,$nm were used to calculate the S_r values shown in Fig. 6.2.

Spectral response measurements were performed to examine the rear surface recombination in solar cells (Section 3.4.2). As can be seen from Fig. 6.7, the current loss found for the PR-SiN cells arises from a poorer quantum efficiency in the long wavelength regime $(800 - 1100\,$nm$)$ which can be attributed to an increased rear SRV. Furthermore, the quantum efficiency shows a more pronounced dependence on the bias light intensity for PR-SiN cells compared with PR-SiO cells. This behaviour is studied in more detail in the following. Fig. 6.8 shows the EQE at $1000\,$nm for the three different cell types (PR-SiO, PR-SiN and
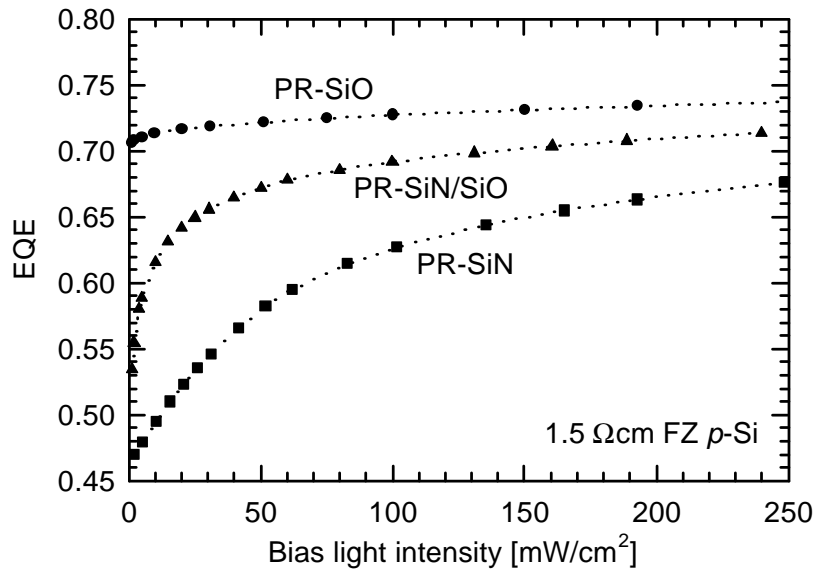
Figure 6.8: Measured external quantum efficiency (EQE) at 1000 nm as a function of bias light intensity for a PR-SiO, PR-SiN/SiO and PR-SiN cell from Table 6.2.
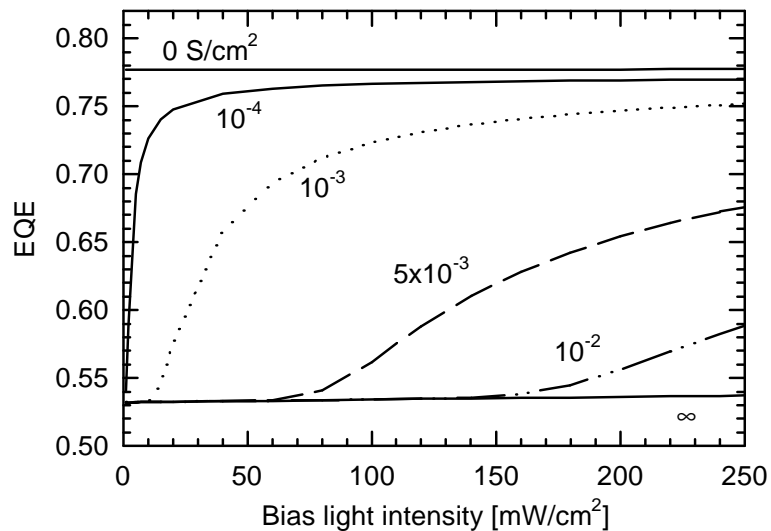

Figure 6.9: Calculated EQE at 1000 nm as a function of bias light intensity with the shunt conductance $(1/R_\text{r.sh})$ as parameter. Assumptions: $1.5\,\Omega$cm p-Si, for further parameters see Fig. 6.5 for other parameters.

PR-SiN/SiO). The absorption length for light of wavelength $1000\,$nm is about $150\,\mu$m resulting in a relatively homogeneous absorption throughout the base. Using this wavelength, the passivating properties of the rear surface scheme can be highlighted. The PR-SiO cell shows the highest EQE with only a weak bias light (or injection level) dependence. In contrast,

the EQE of the PR-SiN cell is generally lower particularly at small bias light intensities. This can be attributed to a strong injection-level dependence of the rear passivation. The EQE of the PR-SiN/SiO cell lies between both cases. Although at low bias light intensities the EQE is rather poor, a steep increase occurs at intensities below $50\,\mathrm{mW/cm^2}$. Owing to oxide lines between the contact and the SiN_x passivated areas the shunt conductance is eliminated or at least drastically reduced. These results agree well with the explanations given in the previous two sections on the parasitic shunting between the inversion layer underneath the SiN_x film and the rear contact. For a quantification of the observed EQE results, PC1D calculations were used for further analysis.

The simulations were performed according to the experimental conditions, i.e., using bias light to set the injection level and a weak monochromatic ($\lambda = 1000\,\mathrm{nm}$) perturbation to determine the EQE. Fig. 6.9 shows that a shunt conductance results generally in a reduced EQE. With increasing bias light intensity the effect of the shunt becomes smaller, resulting in a strongly injection-level-dependent EQE. The greater the shunt conductance the higher intensities are required to increase the EQE. Again, this can be explained by a parasitic shunt resulting in a strongly injection-level-dependent rear SRV. By increasing the bias light the separation and thus the voltage across the FJ (V_r in Fig. 6.4) is increased thereby changing from the shunt-dominated to the diode-dominated behaviour. The calculations explain the results obtained for the PR-SiO, PR-SiN and PR-SiN/SiO cells. Owing to the decreased shunt conductance in the PR-SiN/SiO cells, the transition from shunt to diode-dominated behaviour occurs at lower bias light intensities compared with the PR-SiN cells.

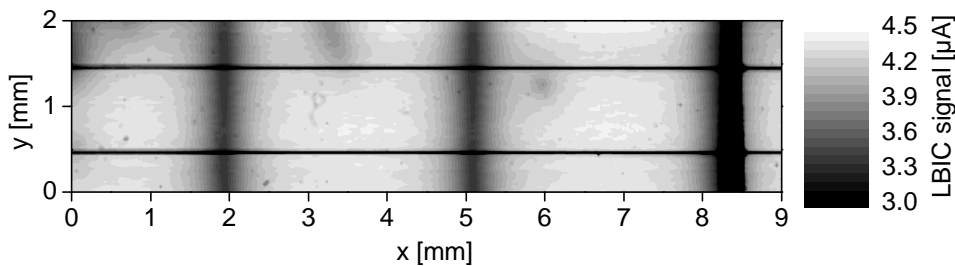### 6.3.5   Light Beam Induced Current Measurements

Figure 6.10: LBIC mapping of a PR-SiO cell at $980\,\mathrm{nm}$ with a bias light intensity of $5\,\mathrm{mW/cm^2}$. The horizontal black lines and the vertical black bar arise from shading of the front contact fingers and the busbar, respectively. The vertical dark lines parallel to the busbar arise from recombination at the rear contact lines.

For the investigation of two-dimensional effects at the cell rear, light beam induced current (LBIC) measurements were carried out at a wavelength of $980\,\mathrm{nm}$. Fig. 6.10 shows a typical LBIC mapping. Due to the shading underneath the front metal grid lines a black bar at the right side from top to bottom (busbar) and two fine lines from left to right (fingers) are seen. The dark grey lines left of the busbar and parallel to it arise from the
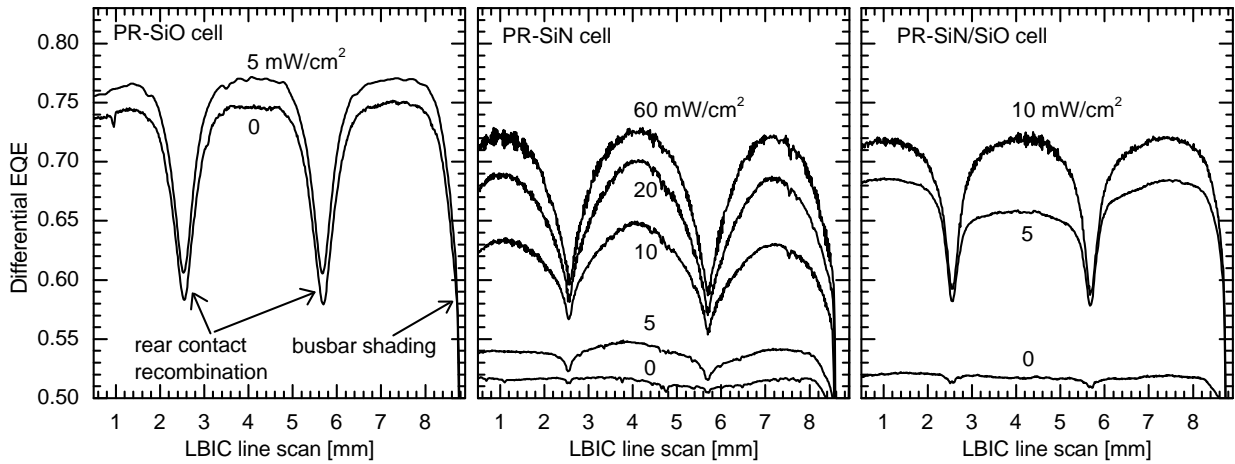
Figure 6.11: LBIC ($\lambda = 980\,\mathrm{nm}$) line scans for a PR-SiO, PR-SiN and a PR-SiN/SiO cell at different bias light intensities.

contact recombination at the rear surface. For an absolute comparison of the local EQE values, line scans along the x-axis are shown in Fig. 6.11. Note that in contrast to the results in the last section, differential EQE values are shown. Although the local EQE of the PR-SiO cell drops to about 0.6 at the contacts, a steep increase causes a plateau-like shape between them. Curves taken at bias light intensities greater than $5\,\mathrm{mW/cm^2}$ lie all on the top curve and are not shown for the sake of clearness. The weak bias light dependence of the local EQE is in accordance with the results of the previous section. In contrast, the local EQE of the PR-SiN cell shows the expected strong bias light dependence. A further striking difference is the relatively shallow slope of the EQE from the contacts toward the non-metalised areas, particularly at low bias light intensities. This is a consequence of a lateral current flow from the inversion layer towards the contacts that is most pronounced at low injection levels. The PR-SiN/SiO cell shows a slope from the contacts to the non-metalised regions that is nearly as steep as that of the PR-SiO cells. This can be attributed to the elimination of the shunt by the oxide lines. A strong injection-level dependence for low bias light intensities is observed while for intensities greater than about $10\,\mathrm{mW/cm^2}$ hardly any intensity dependence is measured. We attribute the shallower slope and the more pronounced injection level dependence of the EQE observed for the PR-SiN cell compared with the PR-SiN/SiO cell to the parasitic shunt between the rear contact lines and the inversion layer underneath the $\mathrm{SiN_x}$ films. This finding is a further proof of the parasitic shunting.

6.4   Means to Decrease the Parasitic Current Loss

From the above analysis, different means become evident to avoid non-idealities in PR-SiN cells. First, if the inversion layer sheet resistance is increased by keeping the same

low effective SRV shunting problems can be reduced. This possibility can be realised with optimised SiN_x or a-Si:H films, respectively, having an excellent SRV and a high inversion layer sheet resistance. From the findings in Section 4.4 and Section 4.5, Si-rich SiN_x films are very promising. A different solution is the introduction of a barrier for electrons between the inversion layer and the metal contact since the interface between the inversion layer and the contact is a crucial point for the improvement of PR-SiN cells. For this purpose, a local back surface field (LBSF) can be implemented. The potential step between the p^{++} region underneath the contact and the n^+ inversion layer repels electrons from the back contact. Note that the injection level in contact-adjacent regions is increased due to the LBSF, thus decreasing the SRV.

6.4.1   Implementing a Local Back Surface Field
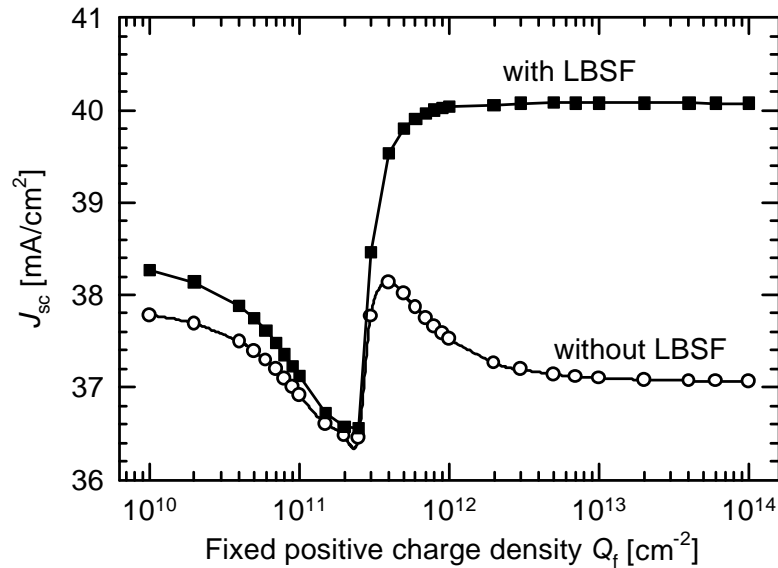
Figure 6.12: DESSIS simulated short-circuit current density J_{sc} as a function of the rear fixed charge density Q_f. Simulations with and without an LBSF below the rear metal contact lines are plotted. Please refer to Table 6.4 for the simulation parameters used [186].

A two-dimensional simulation study was performed by Mittelstädt *et al.* to quantitatively investigate the effect of the fixed positive charge density Q_f within the rear dielectric layer and the beneficial effect of an LBSF on J_{sc} [186]. The simulation was performed using the software package DESSIS [36] and the parameters given in Table 6.4. The results are presented in Fig. 6.12. If Q_f is increased from 10^{10} cm^{-2} to 2×10^{11} cm^{-2} J_{sc} decreases. This is due to the transition from flat-band ($p_s \gg n_s$) to the case where $p_s = n_s$ at the rear surface. n_s (p_s) is the surface electron (hole) density. As was discussed in Section 2.4.2.4, the SRV peaks for the latter case assuming equal capture cross sections. Due to a reduced carrier recombination at the contacts in the case of an implemented LBSF, J_{sc} is slightly higher at $Q_f = 10^{10}$ cm^{-2}. Increasing Q_f to values higher than 2×10^{11} cm^{-2} increases J_{sc} since

Device geometry:	unit cell width	500	μm
	thickness	300	μm
Front:	finger spacing	1000	μm
	S_f	5000	cm/s
Rear:	S_r	1000	cm/s
	surface charge	$10^{10} - 10^{14}$	cm^{-2}
	LBSF $N_{A.peak}$	10^{18}	cm^{-3}
	LBSF depth	5	μm
Bulk:	resistivity	1.5	Ωcm
	lifetime (τ_b at $N_A = 10^{16}$ cm^{-3})	1260	μs
Optics:	AM1.5G		
	random pyramids		
	internal front surface reflectance	70	%
	internal rear surface reflectance	93	%

Table 6.4: DESSIS parameters used for the two dimensional device simulation of the SiN$_x$ passivated solar cells.

n_s becomes greater than p_s. However, as soon as strong inversion conditions are reached, J_{sc} decreases again in the case without LBSF. This can be attributed to the inversion layer conductance and the carrier flow from the inversion layer to the contacts. In contrast, J_{sc} increases significantly by nearly 4 mA/cm^2 if an LBSF is implemented which is due to both, the cut off of the parasitic shunt and the reduced carrier recombination at the rear contact.

In order to experimentally verify the beneficial effect of an LBSF, MIS-n^+p solar cells were fabricated including an LBSF. The process details given in Section 3.3 were slightly modified. After emitter diffusion and etching off the rear SiO$_2$ film, the Al rear contact grid was evaporated through a shadow mask (metallisation fraction about 5 %). Subsequently, the Al-LBSF was formed at an alloying temperature of 850 °C (Section 3.1.3) and the rear surface was passivated using a PECVD SiN$_x$ film deposited at 400° (Section 3.1.1). The results of the best cell is shown in Table 6.5. The results were independently confirmed by the Fraunhofer ISE CalLab [187]. The V_{oc} value is 4 mV (0.6 %) and J_{sc} is about 2 mA/cm^2 (5 %) higher with the LBSF compared with the PR-SiN cells in Table 6.1. Note that the LBSF cell has a double layer antireflection coating in order to minimise optical losses. This accounts for an increase in J_{sc} of about 0.5 mA/cm^2. The additional increase in J_{sc} is mainly due to the cut off of the parasitic shunt. In summary, a conversion efficiency of 20.6 % was obtained. To our knowledge, this is the highest independently confirmed efficiency for an all-SiN$_x$ passivated silicon solar cell. The beneficial effect of an LBSF on the conversion efficiency of SiN$_x$ passivated solar cells could also be demonstrated on multicrystalline silicon solar cells for which an independently confirmed efficiency of 18.1 % was obtained [188].

Cell type and rear surface	η	V_{oc}	J_{sc}	FF
passivation	[%]	[mV]	[mA/cm²]	[%]
SiN$_x$ + LBSF[2]	20.6	658	38.9	80.5
SiN$_x$ (Si-rich)	20.2	661	38.0	80.6
a-Si:H	19.2	651	38.5	76.7

Table 6.5: Measured cell parameters of MIS-n^+p silicon solar cells having an area of 4 cm². The active cell area of the cells is passivated with either PECVD SiN$_x$ or a-Si:H. The cell with an LBSF and that passivated using a Si-rich SiN$_x$ film have a double-layer antireflection coating on the front surface in order to minimise optical losses. The substrate material used is 0.5 Ωcm FZ p-type Si with textured front surface. The parameters were determined under standard AM1.5G, 100 mW/cm² illumination at 25 °C. Those of the LBSF cell were independently determined by the Fraunhofer ISE CalLab while the other parameters were determined by in-house measurements.

6.4.2   Application of Optimised Films as Rear Surface Passivation

In Section 4.4 it was shown that Si-rich SiN$_x$ films provide excellent surface passivation but produce a reduced inversion layer sheet resistance compared with stoichiometric or slightly Si-rich SiN$_x$ films. Hence, Si-rich SiN$_x$ films are expected to decrease the parasitic shunt as well. The results of a solar cell with a Si-rich SiN$_x$ film (refractive index $n = 3.0$) for rear surface passivation is included in Table 6.5. A conversion efficiency exceeding 20 % was obtained by application of the SiN$_x$ film. The V_{oc} value is 7 mV (1.0 %) and the J_{sc} value is about 1 mA/cm² (2.4 %) higher compared with those of the SiN$_x$ passivated cells in Table 6.1. Again, a double layer antireflection coating was used for the Si-rich SiN$_x$ cell in order to minimise optical losses that accounts for an increase in J_{sc} of about 0.5 mA/cm².

Also included in Table 6.5 is the result of a solar cell passivated using an a-Si:H film deposited at 225 °C. The solar cell processing sequence (Section 3.3) had to be adjusted since the surface passivation provided by the a-Si:H films degrades during the thermal oxidation step at 500 °C. According to process C in Fig. 3.8, an Al rear contact grid was evaporated through a shadow mask (metallisation fraction about 5 %) before the oxidation step. The last two steps of the processing sequence were an HF dip to prepare a hydrogen terminated silicon surface between the rear Al contact lines and the deposition of a-Si:H films at 225 °C as described in Section 3.1.2. Note that the HF dip was performed with already metalised samples involving the risk of contaminating the bare silicon surface. Unfortunately, owing to the low fill factor of 76.7 %, only 19.2 % efficiency is obtained. However, the measured V_{oc} and J_{sc} values of 651 mV and 38.5 mA/cm², respectively, demonstrate that the rear surface is very well passivated by the a-Si:H film and that efficiencies above 20 % are achievable. Particularly the J_{sc} value is higher (1.4 mA/cm²) for the a-Si:H passivated cells compared with SiN$_x$ passivated cells (Table 6.1). As the low J_{sc} value observed for the SiN$_x$ passivated cell is a characteristic for parasitic shunting, the parasitic shunt seems to be eliminated using a-Si:H films as rear surface passivation. This behaviour is expected from the results presented in Chapter 5 and Section 5.5. It will be investigated further by an analysis of the

---

[2]independently confirmed by Fraunhofer ISE

dark *I-V* curve. As can be seen in Fig. 6.13, no shoulder is found in the dark *I-V* curve (a) and no bump in the m_{loc}-*V* curve (b). This finding is a further proof that solar cells with a-Si:H films implemented as rear surface passivation are not adversely affected by a parasitic shunt.

The surface passivation provided by the a-Si:H films may not be optimal due to the presence of Al during the HF dip. A solution to this problem and to the difficulty that a-Si:H films degrade during the rear contact sintering process would be the deposition of a-Si:H prior to the Al evaporation. The subsequent ohmic contact formation to the silicon base could be done by a laser firing through process [189]. An inherent advantage of this processing sequence is the possible silicon surface passivation by a-Si:H without metal contamination. However, preliminary experiments were not successful and further investigations are desirable.
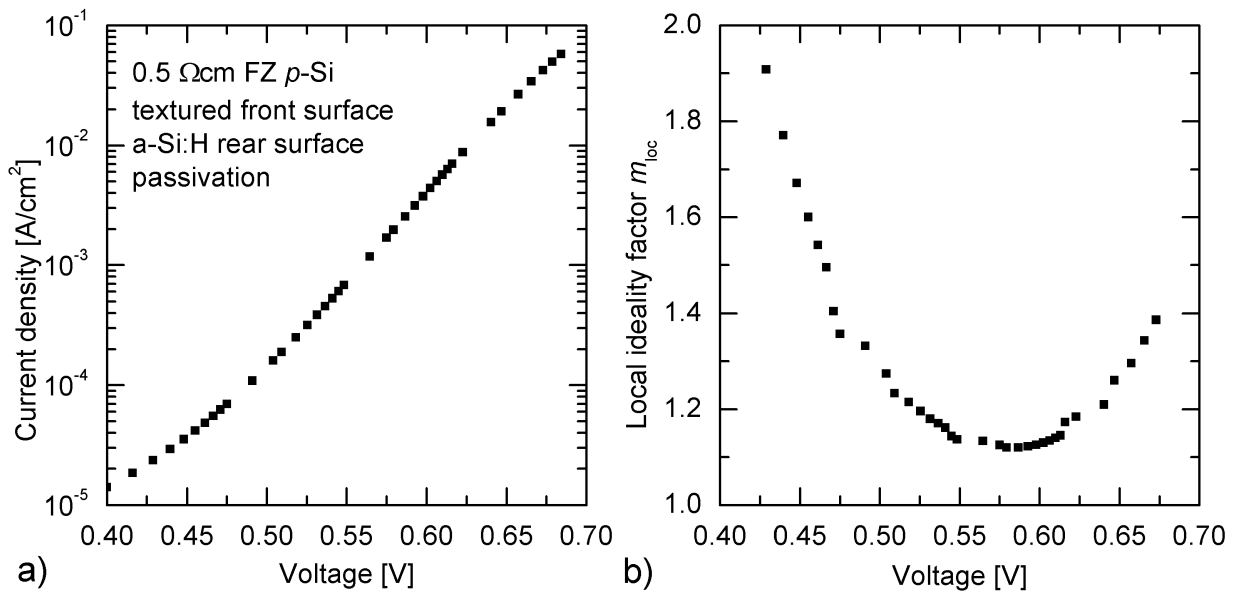
Figure 6.13: (a) Dark IV curve and (b) local ideality factor as a function of voltage ($m_{loc} - V$) measured on a cell passivated with an a-Si:H film at the rear surface.

Chapter 7

Summary, Conclusions and Further Work

The energy conversion efficiency of crystalline silicon solar cells is substantially determined by the recombination probability of light-generated electron-hole pairs. Carrier recombination, both within the bulk and at the surfaces of the solar cell, has to be minimised in order to maximise the conversion efficiency. The main focus of this work has been on investigating and reducing the surface recombination. The standard technique for reducing surface recombination losses (also known as surface passivation) is thermal oxidation of the silicon surface at high temperatures ($\sim$1000 °C). For a number of reasons, high-temperature processing steps should be avoided in solar cell manufacturing. Two prominent alternatives to the high-temperature oxidation that are based on the plasma-enhanced chemical vapour deposition (PECVD) of thin films at low temperature have been investigated in this work. These were amorphous hydrogenated silicon nitride (SiN_x) deposited at 400 °C and amorphous hydrogenated silicon (a-Si:H) deposited at 225 °C. The SiN_x films have been optimised and studied extensively in previous studies. However, no ultimate explanation for the outstanding surface passivation provided by SiN_x films was found in theses studies. This work tries to fill this gap by gaining an improved physical understanding of the passivation mechanism at the Si/SiN_x interface. A second objective was the thorough optimisation of a-Si:H films with respect to silicon surface passivation. Finally, the optimised SiN_x and a-Si:H films were implemented as low-temperature rear surface passivation schemes into cell structures to verify their excellent surface passivation properties on real high-efficiency solar cells.

The recombination strength at a semiconductor surface can be quantified by the so-called surface recombination velocity (SRV). **Chapter 2** summarised the fundamental theoretical background required for the calculation of the surface recombination rate and the SRV at a semiconductor surface. In order to clarify the impact of the most important properties of the surface states on the SRV, first, the specific case of flatband conditions at the surface has been discussed. Since in the case of real surfaces the energy bands at semiconductor surfaces are usually bent as a result of electrical charges at the surface, the so-called 'extended Shockley-Read-Hall formalism' has been used to reveal the significant modifications of the surface recombination rate due to the surface band-bending. Using this quasi-exact formal-

ism, the surface band-bending was calculated which also uniquely determines the shape of the potential barrier at the surface. For the case of strong inversion, an approximate expression for surface band-bending as well as the SRV was derived which simplifies the calculation significantly. The recombination in the surface space-charge region, an important additional recombination path, has been discussed to an extent that has not yet been seen elsewhere. Quantitative calculations were performed using the theory of recombination via defect levels developed by Shockley, Read and Hall considering the rapid variation of the carrier concentrations in the space-charge region. The recombination in the surface space-charge region has been neglected in the past but, as was shown in Chapter 4, must be included in order to match experimental SRV data. The sum of both recombination paths, recombination via surface states and recombination in the space-charge region via bulk defects, contributes to the effective surface recombination velocity S_{eff} at a semiconductor surface.

In **Chapter 4** previously determined characteristics of Si/SiN$_{\mathrm{x}}$ interfaces have been used as a basis for further investigations. Using capacitance-voltage (C-V) measurements performed in the dark, the energy-dependent interface state density $D_{\mathrm{it}}(E)$ and the positive fixed insulator charge density Q_{f} have been measured for SiN$_{\mathrm{x}}$ films of different compositions. For the first time, Q_{f} has also been measured *under illumination* by applying a novel measuring technique developed in the course of this work. It is based on adjusting the surface band-bending by depositing corona charges and determining the SRV from contactless lifetime measurements. A value of $Q_{\mathrm{f}} \approx 2 \times 10^{12}\,\mathrm{cm}^{-2}$ has been unambiguously determined both under illumination and in the dark in contrast to a proposed Q_{f} being lower under illumination as was reported in previous publications. Silicon-rich SiN$_{\mathrm{x}}$ films that are neither accessible with C-V nor with the corona-lifetime measurements due to high leakage currents have been investigated by measuring the sheet resistance of the underlying inversion layer. Stochiometric and slightly Si-rich SiN$_{\mathrm{x}}$ films provide the lowest sheet resistance of the inversion layer. The surface state density at the Si/SiN$_{\mathrm{x}}$ interface was found to be higher for N-rich SiN$_{\mathrm{x}}$ films compared with slightly Si-rich SiN$_{\mathrm{x}}$ films. This finding nicely explains the higher sheet resistance of the inversion layer induced by nitrogen-rich SiN$_{\mathrm{x}}$ films. In contrast, a lower Q_{f} is the reason for the lower sheet resistance found for inversion layers underneath SiN$_{\mathrm{x}}$ films with a very high Si content. Finally, the results of S_{eff} as a function of the excess carrier density Δn have been measured for SiN$_{\mathrm{x}}$ films of different composition. Using the experimentally determined interface parameters and the surface recombination model introduced in Chapter 2, the $S_{\mathrm{eff}}(\Delta n)$ curves have been modeled successfully. Si-rich SiN$_{\mathrm{x}}$ films were found to provide the highest degree of surface passivation, a result which is consistent with previous studies. However, in this work it has been shown for the first time that particularly in the low-injection range, the injection level dependence of the SRV is mainly due to recombination within the space-charge region close to the Si/SiN$_{\mathrm{x}}$ interface. Very low capture time constants of only a few μs have been found for the dominant recombination centre in the space-charge region. The reason for the low values are still unclear and further examination is required to draw final conclusions.

In **Chapter 5** the surface passivation provided by PECVD a-Si:H films[1] has been examined. At deposition temperatures in the range of $200-250\,^{\circ}\mathrm{C}$, record low SRVs with values

---

[1]Note that a-Si:H films can be regarded as SiN$_{\mathrm{x}}$ films with an infinite Si/N ratio

well below 10 cm/s have been achieved with a-Si:H films both on n- and p-type Si material. The surface passivation can easily compete with state-of-the-art high-temperature thermally grown SiO_2 as well as with the best PECVD SiN_x films. Investigations regarding the thermal stability of the passivation quality of the a-Si:H films show that the passivation is stable for temperatures not significantly exceeding the deposition temperature. It is noteworthy that the optimal deposition temperature for a-Si:H films is about 150 °C below that found for SiN_x films. However, SiN_x passivation can withstand higher annealing temperatures. These differences may be due to different hydrogen contents, hydrogen bonding types or hydrogen diffusivities. Further investigations have not been possible within the timeframe of this thesis, however, it would be interesting to identify the predominant physical causes for the differences.

In **Chapter 6** the results of applying SiN_x and a-Si:H films as rear surface passivation schemes to crystalline silicon solar cells have been presented and discussed. By direct comparison with SiO_2 passivated cells, characteristic loss mechanisms found in SiN_x passivated solar cells have been identified. The predominant loss arises from a parasitic shunt between the inversion layer underneath the SiN_x film and the rear metal contacts. As found in the SiN_x passivated solar cells and as verified by one-dimensional simulations, the parasitic shunt causes (i) a reduced conversion efficiency, particularly a lower short-circuit current density, (ii) a shoulder in the dark I-V curves, (iii) lower quantum efficiencies for infrared light, particularly at low bias light intensities, and (iv) lower quantum efficiencies for infrared light close to the metal contacts. Two different means to reduce the parasitic shunt have been proposed and successfully applied to high-efficiency solar cells. First, SiN_x films with a relatively low fixed charge density and, second, the incorporation of a local back surface field (LBSF) underneath the metal contact have been implemented. The efficiency of the SiN_x passivated solar cells could be increased to values above 20 % by either means. By incorporation of an LBSF, an independently confirmed efficiency of 20.6 % has been achieved for an all-SiN_x passivated silicon solar cell. Furthermore, results of solar cells having an a-Si:H passivated rear surface have been presented for the first time. Conversion efficiencies of 19.2 % have demonstrated the excellent surface passivation properties provided by the a-Si:H films. Due to the reduced thermal stability of the a-Si:H films, the rear contact sintering was performed before the a-Si:H film deposition. A different solution would be the selective sintering of the contacts by means of a laser after a-Si:H and rear metal deposition. This approach would be an interesting starting point for further investigations.

In conclusion, the SiN_x and a-Si:H films investigated in this work have an enormous potential for the application as surface passivation layers in commercial high-efficiency silicon solar cells. Since PECVD machines for the low-temperature deposition of SiN_x films (which can just as well be used for a-Si:H film deposition) have already been introduced into the industrial solar cell manufacturing process to deposit front antireflection coatings, an additional incorporation of these films for rear surface passivation could now easily be implemented into industrial solar cell processes. As shown in this work, an incorporation of SiN_x and a-Si:H films at the solar cell rear allows to obtain energy conversion efficiencies above 20 %. Since all area-related costs of a PV module decrease if the solar cell efficiency is increased, the application of the films as a rear surface passivation scheme investigated in this work is a promising route to increase the cost-effectiveness of PV generated power.

List of Symbols and Acronyms

Symbol	Description	Unit
β	q/kT	V^{-1}
δ	δ distribution	
$\Delta\sigma$	Excess photoconductance	Ω^{-1}
$\Delta\phi_{\mathrm{ms}}$	Potential difference $\phi_{\mathrm{ms}} = \phi_{\mathrm{m}} - \phi_{\mathrm{s}}$	V
δn	Excess electron density (small perturbation)	cm^{-3}
Δn, Δp	Excess electron and hole density	cm^{-3}
Δn_0	Excess electron density at $t = 0$	cm^{-3}
Δn_{b}	Excess electron density in the bulk	cm^{-3}
$\Delta n_{\mathrm{d_{sc}}}$	Excess electron density at the edge of the SCR	cm^{-3}
Δn_{s}, Δp_{s}	Excess electron, hole density at the semiconductor surface	cm^{-3}
Δn_{li}	Low-injection excess electron density	cm^{-3}
ΔV_{oc}	Difference between two V_{oc} values	V
ϵ_0	Permittivity in vacuum	As/Vcm
ϵ_{s}	Semiconductor permittivity	As/Vcm
ϵ_{if}	Insulator permittivity in the range $-d_{\mathrm{if}}$ to 0	
ϵ_{iG}	Insulator permittivity in the range $-d_{\mathrm{iG}}$ to $-d_{\mathrm{if}}$	
ϵ_{Si}	Silicon permittivity	$11.9\,\epsilon_0$
ϵ_{SiN}	$\mathrm{SiN_x}$ permittivity	$(6-7)\,\epsilon_0$
η	Conversion efficiency	%
λ_{D}	Steady-state extrinsic Debye length	cm
λ_{D0}	Extrinsic Debye length	cm
μ_n, μ_p	Mobility of electrons, holes	$\mathrm{cm^2V^{-1}s^{-1}}$
ρ	Charge density	$\mathrm{C/cm}^{-3}$
ρ_{s}	Sheet resistance	$\Omega/\square$
σ	Coefficient for interface state distribution	eV
σ_n, σ_p	Capture cross section for electrons, holes	cm^2
τ	Carrier lifetime	s
τ_{A}	Auger carrier lifetime	s

Symbol	Description	Unit
τ_{b}, $\tau_{\mathrm{b.diff}}$	Bulk carrier lifetime, differential	s
τ_{eff}	Effective carrier lifetime	s
τ_{intr}	Intrinsic carrier lifetime	s
τ_{n0}, τ_{p0}	Capture time constant for electrons, holes	s
τ_{rad}	Radiative carrier lifetime	s
τ_{SRH}	SRH carrier lifetime	s
ϕ_n, ϕ_p	Quasi-Fermi level for electrons, holes	V
$\phi_{n_{\mathrm{s}}}$, $\phi_{n_{\mathrm{b}}}$	Quasi-Fermi level for electrons at surface, in bulk	V
ϕ_{m}	Potential according to metal work-function: $\phi_{\mathrm{m}} = W_{\mathrm{m}}/q$	V
ϕ_{s}	Potential according to semic. work-function: $\phi_{\mathrm{m}} = W_{\mathrm{m}}/q$	V
χ	Electron affinity	V
Ψ	Potential	V
Ψ_{B}	Potential difference: $\Psi_{\mathrm{B}} = (E_{\mathrm{i}} - E_{\mathrm{F}})/q$	V
Ψ_{s}, Ψ_{s0}	Surface potential (band-bending), in thermal equilibrium	V
A	Area, e.g. gate electode area	cm^2
AM1.5G	Air mass 1.5 global	
APCVD	Atmospheric pressure chemical vapour deposition	
a-Si:H	Amorphous hydrogenated silicon	
B	Radiative recombination coefficient	cm^{3}s^{-1}
BSF	Back surface field	
c	Speed of light in vacuum	cm/s
C	Coefficient for interface state distribution	cm^{-2}eV^{-1}
C_n, C_p	Auger coefficients	cm^{6}s^{-1}
C_{a}	Ambipolar Auger coefficient	cm^{6}s^{-1}
C_n^*, C_p^*	Auger coefficients including Coulomb interaction	cm^{6}s^{-1}
C_a^*	Ambipolar Auger coefficient including Coulomb interaction	cm^{6}s^{-1}
C_{D}	Semiconductor depletion-region capacitance	F/cm^2
C_{i}	Insulator capacitance	F/cm^2
C_{t}	Total capacitance	F/cm^2
$C\text{-}V$	Capacitance-voltage	
Cat-CVD	Thermo-catalytic chemical vapour deposition	
c-Si	Crystalline silicon	
CVD	Chemical vapour deposition	
Cz	Czochralski	
D_{a}, D_n, D_p	Ambipolar, electron, hole diffusion constant	cm^{2}s^{-1}
D_{H}	Hydrogen diffusivity	cm^{2}s^{-1}
D_{it}	Interface state density	cm^{-2}eV^{-1}

Symbol	Description	Unit
$D_{\text{it.a}}$	Density of acceptor-like interface states	$\text{cm}^{-2}\text{eV}^{-1}$
$D_{\text{it.d}}$	Density of donor-like interface states	$\text{cm}^{-2}\text{eV}^{-1}$
$D_{\text{it.max}}$	Coefficient for interface state distribution	$\text{cm}^{-2}\text{eV}^{-1}$
$D_{\text{it.0}}$	Coefficient for interface state distribution	eV
d_{iG}, d_{if}	Thickness of insulators (cf. Fig. 2.11)	cm
d_{sc}	Width of the space-charge region	cm
DESSIS	Simulation package [36]	
E	Energy	eV
E	Incident power density	W/cm^2
$\mathcal{E}$	Electric field	V/cm
$\mathcal{E}_{\text{s}}$	Electric field at surface	V/cm
E_{C}, $E_{\text{C.b}}$, $E_{\text{C.s}}$	Conduction band edge, in the bulk, at the surface	eV
E_{F}, $E_{\text{F}.n}$, $E_{\text{F}.p}$	Fermi level, for electrons, for holes	eV
E_{g}	Forbidden energy gap	eV
E_{i}	Intrinsic energy level	eV
E_{t}	Trap energy level	eV
E_{V}	Valence band edge	eV
E_{Vb}	Valence band edge in the bulk	eV
EQE	External quantum efficiency	
ERD	Elastic recoil detection	
F	Function	
f_{a}, f_{d}	Occupancy (Fermi-function) of acceptor-, donor-like states	
FF	Fill factor	%
FZ	Float zone	
G	Generation rate	$\text{cm}^{-3}\text{s}^{-1}$
g_{eeh}, g_{ehh}	Enhancement factors for eeh, ehh Auger recombination process	
$g_{\text{max},n}$, $g_{\text{max},p}$	Temperature-dependent coefficients in the expressions for g_{eeh} and g_{ehh}	
h	Planck constant	Js
HF	High frequency (also hydrofluoric acid)	
HIT	Heterojunction with intrinsic thin-layer	
I	Current	A
I_{sc}	Short-circuit current	A
IQE	Internal quantum efficiency	
ISFH	Institut für Solarenergieforschung Hameln/Emmerthal	
I-V	Current-voltage	
J_{02}	Recombination saturation current	Acm^{-2}
$J_{0\text{E}}$	Emitter saturation current density	Acm^{-2}

Symbol	Description	Unit
J_2	Recombination current density	Acm^{-2}
J_{drk}, J_{lgt}	Current density in the dark, under illumination	Acm^{-2}
$J_{0.\mathrm{drk}}$, $J_{0.\mathrm{lgt}}$	Saturation current density in the dark, under illumination	Acm^{-2}
J_n	Electron current density	Acm^{-2}
J_{sc}	Short-circuit current density	Acm^{-2}
J_{S}	Current density flowing towards the surface	Acm^{-2}
k	Boltzmann constant	J/K
L	Channel length	cm
L_{eff}	Effective carrier diffusion length	cm
L_n	Electron diffusion length	cm
LBIC	Light beam induced current	
LBSF	Local back surface field	
LPCVD	Low pressure chemical vapour deposition	
m, m_{drk}, m_{lgt}	Diode ideality factor, in the dark, under illumination	
m_{loc}	Local diode ideality factor	
MIS	Metal-insulator-semiconductor	
MNS, MNOS	Metal-nitride-(oxide-)semiconductor	
MW-PCD	Microwave-detected photoconductance decay	
n	Electron concentration	cm^{-3}
n	Refractive index	
n_0	Electron concentration in thermal equilibrium	cm^{-3}
n_1	Parameter in SRH recombination (cf. Eq. 2.27)	cm^{-3}
N_{A}	Acceptor concentration	cm^{-3}
n_{b}	Bulk electron concentration	cm^{-3}
N_{C}	Effective density of states in conduction band	cm^{-3}
N_{D}	Donor concentration	cm^{-3}
N_{dot}	Doping concentration	cm^{-3}
n_{i}	Intrinsic carrier density	cm^{-3}
n_{s}	Electron concentration at surface	cm^{-3}
N_{t}	Concentration of recombiation centres	cm^{-3}
N_{V}	Effective density of states in valence band	cm^{-3}
p	Hole concentration in valence band	cm^{-3}
P	Microwave intensity	$\mathrm{W/cm}^2$
p_0	Hole concentration in thermal equilibrium	cm^{-3}
p_1	Parameter in SRH recombination (cf. Eq. 2.27)	cm^{-3}
p_{b}	Bulk hole concentration	cm^{-3}
P_{out}	Output power	$\mathrm{W/cm}^2$

Symbol	Description	Unit
p_s	Hole concentration at surface	cm^{-3}
p_{s0}	Hole concentration at surface in thermal equilibrium	cm^{-3}
PECVD	Plasma-enhanced chemical vapour deposition	
PERL	Passivated emitter and rear	
PC1D	One dimensional simulation program for solar cells	
PR-SiO	Solar cells passivated at the rear surface using SiO_2 films	
PR-SiN	Solar cells passivated at the rear surface using SiN_x films	
PR-SiN/SiO	PR-SiN cells with thin oxide lines next to the rear contacts	
q	Elementary charge	C
Q_c	Corona charge density	cm^{-2}
Q_f	Fixed charge density	cm^{-2}
Q_G	Charge density in metal electrode	cm^{-2}
Q_{it}	Charge density in interface states	cm^{-2}
Q_{sc}	Charge density in space-charge region	cm^{-2}
$Q_{sc.f}$	Charge density of acceptor ions in space-charge region	cm^{-2}
$Q_{sc.n}$	Charge density of free electrons in space-charge region	cm^{-2}
$Q_{sc.p}$	Charge density of free holes in space-charge region	cm^{-2}
QSSPC	Quasi steady-state photoconductance	
R^*	Reflection coefficient (also accounts for transmission and absorption losses)	
R_A	Auger recombination rate	$cm^{-3}s^{-1}$
R_C	Contact resistance	Ωcm
R_{intr}	Intrinsic recombination rate	$cm^{-3}s^{-1}$
R_{load}	Load resistance	Ω
R_{rad}	Radiative recombination rate	$cm^{-3}s^{-1}$
$R_{r.sh}$	Shunt resistance across rear FJ	Ω
R_{tot}	Total resistance	Ω
RBS	Rutherford back scattering	
RCA clean	Standard cleaning procedure [121] (after *Radio Corporation of America*)	
rf	Radio frequency	
S	Surface recombination velocity (SRV)	cm/s
S_{eff}, $S_{eff.diff}$	Effective SRV, differential	cm/s
S_f	SRV at front surface	cm/s
S_{it}	SRV at the actual interface including band-bending (S_{it} is calculated using the extended SRH formalism	cm/s
$S_{li.max}$	Maximum SRV under low-injection conditions	cm/s
S_{n0}, S_{p0}	SRV parameter for electrons, holes	cm/s
S_r	SRV at rear surface	cm/s
S_{sc}	SRV considering SRH recombination in the SCR	cm/s

Symbol	Description	Unit
SCR	Space-charge region	
SiN_x	Amorphous hydrogenated silicon nitride	
SR, SR_{diff}	Spectral response, differential	
SRV	Surface recombination velocity	
SRH	Shockley-Read-Hall	
T	Temperature	K
t	Time	s
T_A	Coefficient for interface state distributions (tail states)	$cm^{-2}eV^{-1}$
T_B	Coefficient for interface state distributions (tail states)	eV^{-1}
T_{eff}	Coefficient that accounts for different generation rates in QSSPC measurement	
U	Net recombination rate	$cm^{-3}s^{-1}$
U_A	Net Auger recombination rate	$cm^{-3}s^{-1}$
U_{it}	Net surface recombination rate calculated using extended SRH formalism	$cm^{-2}s^{-1}$
U_{rad}	Net radiative recombination rate	$cm^{-3}s^{-1}$
U_{SRH}	Net SRH recombination rate	$cm^{-3}s^{-1}$
U_s	Net recombination rate at actual surface	cm^{-2}/s
$U_{z<d_{sc}}$	Net surface recombination rate at actual surface and in SCR	cm^{-2}/s
V	Voltage	V
V_a	Applied voltage	V
V_{bi}	Built-in voltage	V
V_{em}, V_r	Voltage across emitter, rear junction	V
V_{FB}	Flatband voltage	V
V_G	Gate voltage	V
V_{oc}	Separation of quasi-Fermi levels	V
v_{th}	Thermal carrier velocity	cm/s
W, W_{cell}	Sample width, cell width	cm
W_m	Metal work-function	eV
W_s	Semiconductor work-function	eV
z	Coordinate of position	cm
Z	Length of contact line	cm

Bibliography

[1] A.E. Becquerel. *Compt. Rend. Acad. Sci.*, **9**:561, 1839.

[2] D.M. Chapin, C.S. Fuller and G.L. Pearson. A new silicon *p-n* junction photocell for converting solar radiation into electrical power. *J. Appl. Phys.*, **25**(5):676–677, 1954.

[3] A. Goetzberger, C. Hebling and H.-W. Schock. Photovoltaic materials, history, status and outlook. *Mat. Sci. Eng.*, **R40**(1):1–46, 2003.

[4] IWR - Internationales Wirtschaftsforum Regenerative Energien. www.iwr.de.

[5] Energy Information Administration, Official Energy Statistics from the U.S. Government. www.eia.doe.gov.

[6] German Bundesministerium für Wirtschaft und Arbeit. www.bmwi.de/Homepage/Politikfelder/Energiepolitik/Energiedaten.

[7] M. Schmela. PV in the fast lane. *Photon International*, **3**:32–35, 2001.

[8] J. Zhao, A. Wang and M.A. Green. 24.5 % efficiency silicon PERT cells on MCZ substrates and 24.7 % efficiency PERL cells on FZ substrates. *Prog. Photovolt. Res. Appl.*, **7**(6):471–474, 1999.

[9] A. Metz and R. Hezel. Record efficiencies above 21 % for MIS-contacted diffused junction silicon solar cells. *Proc. 26th IEEE Photovoltaic Specialists Conf., Anaheim*, pp. 283–286, 1997.

[10] S.W. Glunz, J. Knobloch, C. Hebling and W. Wettling. The range of high-efficiency silicon solar cells fabricated at Fraunhofer ISE. *Proc. 26th IEEE Photovoltaic Specialists Conf., Anaheim*, pp. 231–234, 1997.

[11] C.Z. Zhou, P.J. Verlinden, R.A. Crane and R.M. Swanson. 21.9 % efficient silicon bifacial solar cells. *Proc. 26th IEEE Photovoltaic Specialists Conf., Anaheim*, pp. 287–290, 1997.

[12] J. Schmidt. *Untersuchungen zur Ladungsträgerrekombination an den Oberflächen und im Volumen von kristallinen Silicium-Solarzellen.* Ph. D. thesis (in German), University of Hannover, Germany. Published by Shaker Verlag, Aachen, 1998.

[13] M. A. Green. *Solar Cells: Operating Principles, Technology and System Applications.* The University of New South Wales, 1992.

[14] R.B.M. Girisch, R.P. Mertens and R.F. de Keersmaecker. Determination of Si-SiO$_2$ interface recombination parameters using a gate-controlled point-junction diode under illumination. *IEEE Trans. Electron Devices*, **35**(2):203–222, 1988.

[15] A. Many, Y. Goldstein and N.B. Grover. *Semiconductor surfaces.* North-Holland Publishing Company, Amsterdam, 1965.

[16] A.G. Aberle, S. Glunz and W. Warta. Impact of illumination level and oxide parameters on Shockley-Read-Hall recombination at the Si-SiO$_2$ interface. *J. Appl. Phys.*, **71**:4422–4431, 1992.

[17] A.L. Fahrenbruch and R.H. Bube. *Fundamentals of Solar Cells - Photovaltaic Solar Energy Conversion.* Academic Press, New York, 1983.

[18] H. Schlangenotto, H. Maeder and W. Gerlach. Temperature dependence of the radiative recombination coefficient in silicon. *Phys. Stat. Sol. (a)*, **21**(1):357–367, 1974.

[19] J. Dziewior and W. Schmid. Auger coefficients for highly doped and highly excited silicon. *Appl. Phys. Lett.*, **31**(5):346–348, 1977.

[20] M.J. Kerr and A. Cuevas. General parameterization of Auger recombination in crystalline silicon. *J. Appl. Phys.*, **91**(4):2473–2480, 2002.

[21] A. Hangleiter and R. Häcker. Enhancement of band-to-band Auger recombination by electron-hole correlations. *Phys. Rev. Lett.*, **65**(2):215–218, 1990.

[22] P.P. Altermatt, J. Schmidt, G. Heiser and A.G. Aberle. Assessment and parameterisation of Coulomb-enhanced Auger recombination coefficients in lowly injected crystalline silicon. *J. Appl. Phys.*, **82**(10):4938–44, 1997.

[23] J. Schmidt, M. Kerr and P.P. Altermatt. Coulomb-enhanced Auger recombination in crystalline silicon at intermediate and high-injection densities. *J. Appl. Phys.*, **88**(3):1494–97, 2000.

[24] W. Shockley and W.T. Read. Statistics of the recombination of holes and electrons. *Phys. Rev.*, **87**(5):835–842, 1952.

[25] R.N. Hall. Electron-hole recombination in germanium. *Phys. Rev.*, **87**(2):387, 1952.

[26] M.A. Green. Intrinsic concentration, effective densities of states, and effective mass in silicon. *J. Appl. Phys.*, **67**(6):2944–54, 1990.

[27] I.E. Tamm. Über eine mögliche Art der Elektronenbindung an Kristalloberflächen. *Physik. Z. Sowjetunion*, **1**:733, 1932.

[28] W. Shockley. On the surface states associated with a periodic potential. *Phys. Rev.*, **56**:317–323, 1939.

[29] W. Mönch. *Semiconductor Surfaces and Interfaces*. Springer series in surface sciences. Springer-Verlag Berlin Heidelberg, 3rd edition, 2001.

[30] E.H. Nicollian and J.R. Brews. *MOS (Metal Oxide Semiconductor) Physics and Technology*. John Wiley & Sons, New York, 1982.

[31] S.M. Sze. *Physics of Semiconductor Devices*. Wiley-Interscience, 2nd edition, 1981.

[32] W. Füssel, R. Könenkamp, M. Schmidt and H. Flietner. Degradation effects at Si/SiO_2 interfaces compared to those in a-Si. *Proc. 11th European Photovoltaic Solar Energy Conf., Montreux*, pp. 746–749, 1992.

[33] H. Flietner. Passivity and electronic properties of the silicon/silicon dioxide interface. *Materials Science Forum*, **185-188**:73–82, 1995.

[34] W. Füssel, M. Schmidt, H. Angermann, G. Mende and H. Flietner. Defects at the Si/SiO_2 interface: their nature and behaviour in technological processes and stress. *Nucl. Inst. and Meth. in Phys. Res. A*, **377**(2-3):177–183, 1996.

[35] D.A. Clugston and P.A. Basore. PC1D version 5: 32-bit solar cell modeling on personal computers. *Proc. 26th IEEE Photovoltaic Specialists Conf., Anaheim*, pp. 207–210, 1997.

[36] DESSIS 6.1. *ISE Integrated Systems Engineering AG*. Zürich, Switzerland, 2000. www.ise.com.

[37] J. Schmidt and A.G. Aberle. Carrier recombination at silicon-silicon nitride interfaces fabricated by plasma-enhanced chemical vapor deposition. *J. Appl. Phys.*, **85**(7):3626–3633, 1999.

[38] A.G. Aberle. *Crystalline silicon solar cells: Advanced surface passivation and analysis*. Habilitation thesis, University of Hannover. Published by the Centre for Photovoltaic Engineering, University of New South Wales, Sydney, Australia, 1999.

[39] J.R. Schrieffer. Effective carrier mobility in surface-space charge layers. *Phys. Rev.*, **97**(3):641–646, 1955.

[40] C.G.B. Garrett and W.H. Brattain. Physical theory of semiconductor surfaces. *Phys. Rev.*, **99**(2):376–387, 1955.

[41] W.H. Brattain and J. Bardeen. *Bell System Technical Journal*, **32**:1, 1953.

[42] A.S. Grove and D.J. Fitzgerald. Surface effects on *p-n* junctions: Characteristics of surface space-charge regions under non-equilibrium conditions. *Solid State Electron.*, **9**:783–806, 1966.

[43] D.J. Fitzgerald and A.S. Grove. Surface recombination in semiconductors. *Surf. Sci.*, **9**:347–369, 1968.

[44] B. Kuhlmann. *Charakterisierung und mehrdimensionale Simulation von MIS-Inversionsschichtsolarzellen.* Ph. D. thesis (in German), University of Hannover, Germany. Published by Shaker Verlag, Aachen, 1998.

[45] W.H. Press, S.A. Teukolsky, W.T. Vetterling and B.P. Flannery. *Numerical recipes in C: The art of scientific computing.* Cambridge University Press, 3rd edition, 1992.

[46] J. Brody and A. Rohatgi. Analytical approximation of effective surface recombination velocity of dielectric-passivated *p*-type silicon. *Solid State Electron.*, **45**(9):1549–57, 2001.

[47] D.E. Kane and R.M. Swanson. Measurement of the emitter saturation current by a contactless photoconductivity decay method. *Proc. 18th IEEE Photovoltaic Specialists Conf., Las Vegas*, pp. 578–583, 1985.

[48] A. Cuevas. The effect of emitter recombination on the effective lifetime of silicon wafers. *Sol. Energy Mater. Sol. Cells*, **57**(3):277–290, 1999.

[49] S.C. Jain and R. Muralidharan. Effect of emitter recombinations on the open circuit voltage decay of a junction diode. *Solid State Electron.*, **24**(12):1147–54, 1981.

[50] S. W. Glunz, D. Biro, S. Rein and W. Warta. Field-effect passivation of the SiO$_2$-Si interface. *J. Appl. Phys.*, **86**(1):683–691, 1999.

[51] K.R. McIntosh, Pietro P. Altermatt and Gernot Heiser. Depletion region recombination in silicon solar cells: When does $m_{dr} = 2$? *Proc. 16th European Photovoltaic Solar Energy Conf., Glasgow*, pp. 251–254, 2000.

[52] K.L. Luke and Li-Jen Cheng. Analysis of the interaction of a laser pulse with a silicon wafer: Determination of bulk lifetime and surface recombination velocity. *J. Appl. Phys.*, **61**:2282–2293, 1987.

[53] A. B. Sproul. Dimensionless solution of the equation describing the effect of surface recombination on carrier decay in semiconductors. *J. Appl. Phys.*, **76**(5):2851–54, 1994.

[54] S.M. Sze. *Semiconductor Devices, Physics and Technology.* John Wiley & Sons, 1985.

[55] S.W. Glunz, A.B. Sproul, W. Warta and W. Wettling. Injection-level-dependent recombination velocities at the Si-SiO$_2$ interface for various dopant concentrations. *J. Appl. Phys.*, **75**(3):1611–15, 1994.

[56] A.W. Stephens, A.G. Aberle and M.A. Green. Surface recombination velocity measurements at the silicon-silicon dioxide interface by microwave-detected photoconductance decay. *J. Appl. Phys.*, **76**(1):363–370, 1994.

[57] M. A. Green. *Silicon Solar Cells: Advanced Principles and Practice.* Centre for Photovoltaic Devices and Systems, 1995.

[58] A. Sherman. *Chemical vapor deposition for microelectronics.* Noyes Publications, Park Ridge, New Jersey, U.S.A, 1987.

[59] H. Matsumura. Formation of silicon-based thin films prepared by catalytic chemical vapor deposition (Cat-CVD) method. *Jpn. J. Appl. Phys., Part 1*, **37**(6a):3175–87, 1998.

[60] J.D. Moschner, J. Schmidt and R. Hezel. Thermo-catalytic deposition of silicon nitride - a new method for excellent silicon surface passivation. *Proc. 29th IEEE Photovoltaic Specialists Conf., New Orleans*, pp. 174–177, 2002.

[61] D.L. Smith. *Thin-film depostion: Principles and practice.* McGraw-Hill, Inc., 1995.

[62] T. Lauinger. *Untersuchung und Optimierung neuartiger Plasmaverfahren zur Silici-umnitrid-Beschichtung von Silicium-Solarzellen.* Ph. D. thesis (in German), University of Hannover, Germany. Published by Shaker Verlag, Aachen, 2001.

[63] J.D. Moschner. Ph.D thesis (in German), University of Hannover, Germany, in preparation.

[64] T. Lauinger, J. Schmidt, A.G. Aberle and R. Hezel. Record low surface recombination velocities on 1 Ωcm p-silicon using remote plasma silicon nitride passivation. *Appl. Phys. Lett.*, **68**(9):1232–1234, 1996.

[65] J. Schmidt and M.J. Kerr and. Highest-quality surface passivation of low-resistivity p-type silicon using stoichiometric PECVD silicon nitride. *Sol. Energy Mater. Sol. Cells*, **65**(1-4):585–591, 2001.

[66] T. Lauinger. Duschkopf zur großflächigen Gasphasenbehandlung. German patent No. De 197 57 150 A1. *Patent*, 1997.

[67] M. Taguchi, K. Kawamoto, S. Tsuge, T. Baba, H. Sakata, M. Morizane, K. Uchihashi, N. Nakamura, S. Kiyama and O. Oota. HIT$^{\text{TM}}$ cells - high-efficiency crystalline Si cells with novel structure. *Prog. Photovolt. Res. Appl.*, **8**(5):503–513, 2000.

[68] M. Rammensee. *Nachweis und Elimination der Oberflächenschädigung bei der Plasma-Siliziumnitridbeschichtung von Silizium-Inversionsschicht-Solarzellen.* Ph. D. thesis (in German), University of Erlangen-Nürnberg, Germany, 1995.

[69] T. Lauinger, J. Moschner, A.G. Aberle and R. Hezel. Optimization and characterization of remote plasma-enhanced chemical vapor deposition silicon nitride for the passivation of p-type crystalline silicon surfaces. *J. Vac. Sci. Technol. A*, **16**(2):530–543, 1998.

[70] J. Mandelkorn and J.H. Lamneck, Jr. Simplified fabrication of back surface electric field silicon cells and novel characteristics of such cells. *Proc. 9th IEEE Photovoltaic Specialists Conf., Silver Springs, MD*, pp. 66–71, 1972.

[71] J. Mandelkorn, J.H. Lamneck and L.R. Scudder. Design, fabrication and characteristics of new types of back surface field cells. *Proc. 10th IEEE Photovoltaic Specialists Conf., Palo Alto*, pp. 207–211, 1973.

[72] M.Y. Ghannam. A new n^+pn^+ structure with back side floating junction for high efficiency silicon solar cells. *Proc. 22nd IEEE Photovoltaic Specialists Conf., Las Vegas*, pp. 284–289, 1991.

[73] S.R. Wenham, S.J. Robinson, X. Dai, J. Zhao, A. Wang, Y.H. Tang, A. Ebong, C.B. Honsberg and M.A. Green. Rear surface effects in high efficiency silicon solar cells. *Proc. 1st World Conf. Photovoltaic Energy Conversion, Hawaii*, pp. 1278–1282, 1994.

[74] M. Schöfthaler, R. Brendel, G. Langguth and J.H. Werner. High-quality surface passivation by corona-charged oxides for semiconductor surface characterization. *Proc. 1st World Conf. Photovoltaic Energy Conversion, Hawaii*, pp. 1509–12, 1994.

[75] M. Schöfthaler. *Transiente Mikrowellenreflexion zur kontaktlosen Trägerlebensdauermessung an Silizium für Solarzellen.* Ph. D. thesis (in German), University of Stuttgart, Germany. Published by Shaker Verlag, Aachen, 1995.

[76] J. Schmidt and A.G. Aberle. Easy-to-use surface passivation technique for bulk carrier lifetime measurements on silicon wafers. *Prog. Photovolt. Res. Appl.*, **6**(4):259–263, 1998.

[77] A. Beyer, M. Rennau and G. Ebest. Corona charging of insulated surfaces and the application in the photovoltaic. *Proc. 13th European Photovoltaic Solar Energy Conf., Nice*, pp. 1254–1257, 1995.

[78] M.M. Shahin. Mass spectrometric studies of corona discharges in air at atmospheric pressures. *J. Chem. Phys.*, **45**(7):2600, 1966.

[79] R.B. Comizzoli. Uses of corona discharges in the semiconductor industry. *J. Electrochem. Soc.*, **134**(2):424–429, 1987.

[80] Lord Kelvin. Contact electricity of metals. *Philos. Magaz.*, **46**:82–120, 1898.

[81] C.W. Reedyk and M.M. Perlman. The measurement of surface charge. *J. Electrochem. Soc.*, **115**(1):49, 1968.

[82] D.K. Schroder. *Semiconductor material and device characterization.* Wiley-Interscience, 2nd edition, 1998.

[83] I. Martín, M. Vetter, A. Orpella, J. Puigdollers, A. Cuevas and R. Alcubilla. Surface passivation of p-type crystalline Si by plasma enhanced chemical vapor deposited amorphous SiC_x:H films. *Appl. Phys. Lett.*, **79**(14):2199–2201, 2001.

[84] B.S. Richards, S.F. Rowlands, C.B. Honsberg and J.E. Cotter. TiO$_2$ DLAR coatings for planar silicon solar cells. *Prog. Photovolt. Res. Appl.*, **11**(1):27–32, 2003.

[85] L.M. Doeswijk, P. Laloli, D.H.A. Blank and H. Rogalla. Passivating TiO$_2$ coatings for silicon solar cells by a pulsed laser deposition. *Proc. 16th European Photovoltaic Solar Energy Conf., Glasgow*, pp. 154–157, 2000.

[86] B.S. Richards, J.E. Cotter and C.B. Honsberg. Enhancing the surface passivation of TiO$_2$ coated silicon wafers. *Appl. Phys. Lett.*, **80**(7):1123, 2002.

[87] T.M. Buck and F.S. McKim. Effects of certain chemical treatments and ambient atmospheres on surface properties of silicon. *J. Electrochem. Soc.*, **105**(12):709–714, 1958.

[88] E. Yablonovitch, D.L. Allara, C.C. Chang, T. Gmitter and T.B. Bright. Unusually low surface-recombinatino velocity on silicon and germanium surfaces. *Phys. Rev. Lett.*, **57**(2):249–252, 1986.

[89] K.L. Luke and L.-J. Cheng. A chemical/microwave technique for the measurement of bulk minority carrier lifetime in silicon wafers. *J. Electrochem. Soc.*, **135**(4):957–961, 1988.

[90] T.S. Horányi, T. Pavelka and P. Tüttö. In situ bulk lifetime measurement on silcon with a chemically passivated surface. *Appl. Surf. Sci.*, **63**:306–311, 1993.

[91] A.W. Stephens and M.A. Green. Effectiveness of 0.08 molar iodine in ethanol solution as a means of chemical surface passivation for photoconductance decay measurements. *Sol. Energy Mater. Sol. Cells*, **45**:225–265, 1997.

[92] A. Schönecker, K. Heasman, J. Schmidt, J. Poortmans, T. Bruton and W. Koch. Results of five solar silicon wafer minority carrier lifetime round robins organised by the SEMI M6 solar silicon standardisation task force. *Proc. 14th European Photovoltaic Solar Energy Conf., Barcelona*, pp. 666–671, 1997.

[93] H. Takato, I. Sakata and R. Shimokawa. Surface passivation effect of silicon substrates due to quinhydrone/ethanol treatment. *Jpn. J. Appl. Phys., Part 2*, **40**(10a):L1003–04, 2001.

[94] D. Biro and W. Warta. Low temperature passivation of silicon surfaces by polymer films. *Sol. Energy Mater. Sol. Cells*, **71**(3):369–374, 2002.

[95] K. Katayama, Y. Kirino, K. Iba and F. Shimura. Effect of ultraviolet light irradiation on noncontact laser microwave lifetime measurement. *Jpn. J. Appl. Phys., Part 2*, **30**(11b):L1907–10, 1991.

[96] S. Deb and B.R. Nag. Measurement of carriers in semiconductors through microwave reflection. *J. Appl. Phys.*, **33**(4):1604, 1962.

[97] M. Kunst and G. Beck. The study of charge carrier kinetics in semiconductors by microwave conductivity measurements. *J. Appl. Phys.*, **60**:3558–66, 1986.

[98] M. Kunst and G. Beck. The study of charge carrier kinetics in semiconductors by microwave conductivity measurements. II. *J. Appl. Phys.*, **63**:1093–98, 1988.

[99] N.J. Harrick. Lifetime measurements of excess carriers in semiconductors. *J. Appl. Phys.*, **27**(12):1439–42, 1956.

[100] T. Warabisako, T. Saitoh, T. Motooka and T. Tokuyama. Contactless measurements of wafer lifetime by free carrier infrared absorption. *Jpn. J. Appl. Phys., Part 1*, **22**(Suppl. 22-1):557, 1983.

[101] Z.G. Ling and P.K. Ajmera. Measurement of bulk lifetime and surface recombination velocity by infrared absorption due to pulsed optical excitation. *J. Appl. Phys.*, **69**(1):519–521, 1991.

[102] V. Grivickas, J. Linnros, A. Vigelis, J. Šeckus and J.A. Tellefsen. A study of carrier lifetime in silicon by laser-induced absorption: a perpendicular geometry measurement. *Solid State Electron.*, **35**(3):299–310, 1992.

[103] R. Brendel, M. Bail, B. Bodmann, J. Kentsch and M. Schulz. Analysis of photoexcited charge carrier density profiles in Si wafers by using an infrared camera. *Appl. Phys. Lett.*, **80**(3):437–439, 2002.

[104] T. Tiedje, J.I. Habermann, R.W. Francis and A.K. Ghosh. An rf bridge technique for contactless measurement of the carrier lifetime in silicon wafers. *J. Appl. Phys.*, **54**(5):2499–2503, 1983.

[105] F. Dannhäuser. The dependence of carrier mobility in Si of the concentration of free charge carriers. *Solid State Electron.*, **15**:1371, 1972.

[106] J. Krausse. The dependence of carrier mobility in Si on the concentration of free charge carriers. *Solid State Electron.*, **15**(12):1377–81, 1972.

[107] Grivitskas V., Willander M. and Vaitkus J. The role of intercarrier scattering in excited silicon. *Solid State Electron.*, **27**(6):565–72, 1984.

[108] Jan Schmidt, Thomas Lauinger, Armin G. Aberle and Rudolf Hezel. Light-biased photoconductance decay measurements on silicon nitride passivated silicon wafers. *Proc. 13th European Photovoltaic Solar Energy Conf., Nice*, pp. 1287–90, 1995.

[109] R. Brendel. Note on the interpretation of injection-level-dependent surface recombination velocities. *Appl. Phys. A*, **60**(5):523–524, 1995.

[110] A.G. Aberle, J. Schmidt and R. Brendel. On the data analysis of light-biased photoconductance decay measurements. *J. Appl. Phys.*, **79**(3):1491–96, 1996.

[111] J. Schmidt. Measurement of differential and actual recombination parameters on crystalline silicon wafers. *IEEE Trans. Electron Devices*, **46**(10):2018–25, 1999.

[112] F. M. Schuurmans, A. Schönecker, A. R. Burgers and W. C. Sinke. Simplified evaluation method for light-biased effective lifetime measurements. *Appl. Phys. Lett.*, **71**(13):1795–97, 1999.

[113] R.A. Sinton and A. Cuevas. Contactless determination of current-voltage characteristics and minority-carrier lifetimes in semiconductors from quasi-steady-state photoconductance data. *Appl. Phys. Lett.*, **69**(17):2510–2512, 1996.

[114] H. Nagel, C. Berge and A.G. Aberle. Generalized analysis of quasi-steady-state and quasi-transient measurements of carrier lifetimes in semiconductors. *J. Appl. Phys.*, **86**(11):6218–21, 1999.

[115] Sinton Consulting, Inc. 1132 Green Circle, Boulder, CO 80305.

[116] H. Nagel, B. Lenkeit, R. A. Sinton, A. Metz and R. Hezel. Relationship between effective carrier lifetimes in silicon determined under transient and steady-state illumination. *Proc. 16th European Photovoltaic Solar Energy Conf., Glasgow*, pp. 93–96, 2000.

[117] A. Cuevas and R.A. Sinton. Prediction of the open-circuit voltage of solar cells from the steady-state photoconductance. *Prog. Photovolt. Res. Appl.*, **5**(2):79–90, 1997.

[118] M. Bail, M. Schulz and R. Brendel. Space-charge region-dominated steady-state photoconductance in low-lifetime Si wafers. *Appl. Phys. Lett.*, **82**(5):757–759, 2003.

[119] C. Munakata and K. Watanabe. Charge storage effect in the microwave detected photoconductive decay method. *Jpn. J. Appl. Phys., Part 1*, **41**(5a):2796–2800, 2002.

[120] S. von Aichberger, O. Abdallah, F. Wünsch and M. Kunst. Influence of a space charge region on charge carrier kinetics in silicon wafers. *J. Appl. Phys.*, **91**(11):9147–9150, 2002.

[121] W. Kern and D.A. Puotinen. Cleaning solutions on hydrogen peroxide for use in silicon semiconductor technology. *RCA Review*, **31**(2):187, 1970.

[122] A.G. Aberle, T. Lauinger, S. Bowden, S. Wegener and G. Betz. Sunalyzer - a powerful and cost-effective solar cell *I-V* tester for the photovoltaic community. *Proc. 25th IEEE Photovoltaic Specialists Conf., Washington DC*, pp. 593–596, 1996.

[123] J. Metzdorf. Calibration of solar cells 1: The differential spectral responsivity method. *Applied Optics*, **26**(9):1701–08, 1987.

[124] J. Metzdorf, W. Möller, T. Wittchen and D. Hünerhoff. Principles and applications of differential spectroradiometrie. *Metrologia*, **28**:247–250, 1991.

[125] P. Basore. Extended spectral analysis of internal quantum efficiency. *Proc. 23rd IEEE Photovoltaic Specialists Conf., Louisville*, pp. 147–152, 1993.

[126] S. Keller, M. Spiegel, P. Fath, G. Willeke and E. Bucher. A critical evaluation of the effective diffusion length determination in crystalline silicon solar cells from an extended spectral analysis. *IEEE Trans. Electron Devices*, **45**(7):1569–74, 1998.

[127] E.Y. Wang, F.T.S. Yu, V.L. Simms, H.W. Brandhorst, Jr. and J.D. Broder. Optimum design of antireflection coating for silicon solar cells. *Proc. 10th IEEE Photovoltaic Specialists Conf., Palo Alto*, pp. 168–173, 1973.

[128] H.J. Hovel. *Solar Cells.* Semiconductors and Semimetals, Vol 11. Academic Press, New York, 1975.

[129] R. Hezel and R. Schörner. Plasma Si nitride - a promising dielectric to achieve high-quality silicion MIS/IL solar cells. *J. Appl. Phys.*, **52**(4):3076–79, 1981.

[130] R. Hezel and K. Jaeger. Low temperature surface passivation of silicon for solar cells. *J. Electrochem. Soc.*, **136**(2):518–523, 1989.

[131] A.K. Sinha, H.J. Levinstein, T.E. Smith, G. Quintana and S.E. Haszko. Reactive plasma deposited Si-N films for MOS-LSI passivation. *J. Electrochem. Soc.*, **125**:601–8, 1978.

[132] Z. Chen, P. Sana, J. Salami and A. Rohatgi. A novel and effective PECVD SiO_2/SiN antireflection coating for Si solar cells. *IEEE Trans. Electron Devices*, **40**(6):1161–65, 1993.

[133] J. Szlufcik, K. De Clercq, P. De Schepper, J. Poortmans, A. Buczkowski, J. Nijs and R. Mertens. Improvement in multicrystalline silicon solar cells after thermal treatment of PECVD silcion nitride AR coating. *Proc. 12th European Photovoltaic Solar Energy Conf., Amsterdam*, pp. 1018–21, 1994.

[134] D.S. Ruby, W.L. Wilbanks, C.B. Fleddermann and J.I. Hanoka. The effect of hydrogen-plasma and PECVD-nitride deposition on bulk and surface passivation in string ribbon silicon solar cells. *Proc. 13th European Photovoltaic Solar Energy Conf., Nice*, pp. 1412–14, 1995.

[135] J.-W. Jeong, M.D. Rosenblum, J.P. Kalejs and A. Rohatgi. Hydrogenation of defects in edge-defined film-fed grown aluminum-enhanced plasma enhanced chemical vapor deposited silicon nitride multicrystalline silicon. *J. Appl. Phys.*, **87**(10):7551–57, 2000.

[136] C. Leguijt, P. Lölgen, J.A. Eikelboom, A.W. Weeber, F.M. Schuurmans, W.C. Sinke, P.F.A. Alkemade, P.M. Sarro, C.H.M. Marée and L.A. Verhoef. Low temperature surface passivation for silicon solar cells. *Sol. Energy Mater. Sol. Cells*, **40**:297–345, 1996.

[137] L. Cai, A. Rohatgi, S. Han, G. May and M. Zou. Investigation of the properties of plasma-enhanced chemical vapor deposited silicon nitride and its effect on silicon surface passivation. *J. Appl. Phys.*, **83**(11):5885–89, 1998.

[138] M.J. Kerr and A. Cuevas. Recombination at the interface between silicon and stoichiometric plasma silicon nitride. *Semicond. Sci. Technol.*, **17**(2):166–172, 2002.

[139] H. Mäckel and R. Lüdemann. Detailed study of the composition of hydrogenated SiN_x layers for high-quality silicon surface passivation. *J. Appl. Phys.*, **92**(5):2602–2609, 2002.

[140] F. Schuurmans. *Surface passivation of silicon by PECVD silicon nitride*. Ph. D. thesis, Universiteit Utrecht, The Netherlands, 1998.

[141] H. Nagel, A.G. Aberle and R. Hezel. Optimised antireflection coatings for planar silicon solar cells using remote pecvd silicon nitride and porous silicon dioxide. *Prog. Photovolt. Res. Appl.*, **7**(4):245–260, 1999.

[142] T. Lauinger, A.G. Aberle and R. Hezel. Comparison of direct and remote PECVD silicon nitride films for low-temperature surface passivation of p-type crystalline silicon. *Proc. 14th European Photovoltaic Solar Energy Conf., Barcelona*, pp. 853–856, 1997.

[143] J. Robertson. Electronic structure of silicon nitride. *Philos. Magaz. B*, **63**:47–77, 1991.

[144] W.A.P. Claassen, W.G.J.N. Valkenburg, F.H.P.M. Habraken and Y. Tamminga. Characterization of plasma silicon nitride layers. *J. Electrochem. Soc.*, **130**(12):2419–23, 1983.

[145] B.E. Deal, P.J. Fleming and P.L. Castro. Electrical properties of vapor-deposited silicon nitride and silicon oxide films on silicon. *J. Electrochem. Soc.*, **115**(3):300–7, 1968.

[146] Y. Kamigaki and S. Minami. MNOS nonvolatile semiconductor memory technology: Present and future. *IEICE Trans. Electron.*, **E84-C**(6):713–723, 2001.

[147] A. Bierhals, A. Metz and R. Hezel. Surface recombination in oxide passivated silicon solar cells investigated by quasistatic capacitance voltage curves of $Al/SiO_2/p$-Si MOS capacitors under illumination. *Proc. 16th European Photovoltaic Solar Energy Conf., Glasgow*, pp. 142–145, 2000.

[148] J.R. Brews. An improved high-frequency MOS capacitance formula. *J. Appl. Phys.*, **45**(3):1276–9, 1974.

[149] B.E. Deal, M. Sklar, A.S. Grove and E.H. Snow. Characteristics of surface-state charge (QSS) of thermally oxidized silicon. *J. Electrochem. Soc.*, **114**(3):226, 1967.

[150] R. Hezel and K. Jäger. Properties of inversion layers for MIS/IL solar cells studied on low-temperture-processed MNOS transistors. *Solid State Electron.*, **26**(10):993–997, 1983.

[151] O. Leistiko, A.S. Grove and C.T. Sah. Electron and hole mobilities in inversion layers on thermally oxidized silicon surfaces. *IEEE Trans. Electron Devices*, p. 248, 1965.

[152] R. Hezel. High charge densities in Si-nitride and their effect on the inversion layer mobility of silicon MIS/IL solar cells. *Proc. 16th IEEE Photovoltaic Specialists Conf., San Diego*, pp. 1237–42, 1982.

[153] R. Hezel, K. Blumenstock and R. Schörner. Interface states and fixed charges in MNOS structures with APCVD and plasma silicon nitride. *J. Electrochem. Soc.*, **131**(7):1679–83, 1984.

[154] W. Bauch, K. Jäger and R. Hezel. Effect of Cs contamination on the interface state density of MNOS capacitors. *Appl. Surf. Sci.*, **39**(1-4):356–363, 1989.

[155] J.R. Elmiger and M. Kunst. Investigation of charge carrier injection in silicon nitride/silicon junctions. *Appl. Phys. Lett.*, **69**(4):517–519, 1996.

[156] J. Schmidt, F.M. Schuurmans, W.C. Sinke, S.W. Glunz and A.G. Aberle. Observation of multiple defect states at silicon-silicon nitride interfaces fabricated by low-frequency plasma-enhanced chemical vapor deposition. *Appl. Phys. Lett.*, **71**(2):252–254, 1997.

[157] K. Kawamoto, T. Nakai, T. Baba, M. Taguchi, H. Sakata, S. Tsuge, K. Uchihashi, M. Tanaka and S. Kiyama. A high-efficiency HIT solar cell (21% $\sim$100 cm^2) with excellent interface properties. *Technical Digest 12th International Photovoltaic Science and Engineering Conf., Cheju Island, Korea*, 2001.

[158] H. Sakata, T. Nakai, T. Baba, M. Taguchi, Sadaji Tsuge, Kenji Uchihashi and S. Kiyama. 20.7% highest efficiency large area (100.5 cm^2) HIT cell. *Proc. 28th IEEE Photovoltaic Specialists Conf., Anchorage*, pp. 7–12, 2000.

[159] N. Jensen, R. M. Hausner, R. B. Bergmann, J. H. Werner and U. Rau. Optimization and characterization of amorphous/crystalline silicon heterojunction solar cells. *Prog. Photovolt. Res. Appl.*, **10**(1):1–13, 2002.

[160] M.L.D. Scherff, A. Froitzheim, A. Ulyashin, M. Schmidt, W.R. Fahrner and W. Fuhs. 16.2% efficiency for amorphous/crystalline silicon heterojunction solar cells on flat *p*-type silicon wafer. *Proc. Photovoltaic in Europe Conf. and Exhibition, Rome, Italy*, 2002.

[161] R. Stangl, A. Froitzheim, L. Elstner and W. Fuhs. Amorphous/crystalline silicon heterojunction solar cells, a simulation study. *Proc. 17th European Photovoltaic Solar Energy Conf., Munich*, pp. 1387–90, 2001.

[162] S. Muramatsu, T. Uematsu, Y. Nagata, H. Ohtsuka and T. Warabisako. Control of μc-Si/c-Si interface layer structure for surface passivation of Si solar cells. *Sol. Energy Mater. Sol. Cells*, **48**:151–157, 1997.

[163] M.W.M. van Cleef, F.M. Schuurmans, A.S.H. van der Heide, A. Schönecker and R.E.I. Schropp. Passivation of c-Si solar cells by low temperature H-treatments and deposited a-Si:H layers. *Proc. 2nd World Conf. Photovoltaic Energy Conversion, Vienna*, pp. 1661–64, 1998.

[164] S.J. Pearton, J.W. Corbett and M. Stavola. *Hydrogen in Crystalline Semiconductors*. Springer Series in Materials Science 16. Springer Verlag, 1992.

[165] W. Beyer and H. Wagner. Determination of the hydrogen diffusion coefficient in hydrogenated amorphous silicon from hydrogen effusion experiments. *J. Appl. Phys.*, **53**(12):8745–50, 1982.

[166] M.J. Kerr. *Surface, Emitter and Bulk Recombination in Silicon and Development of Silicon Nitride Passivated Solar Cells*. Ph. D. thesis, The Austalian National University, 2002.

[167] D.L. Staebler and C.R. Wronski. Reservible conductivity changes in discharge-produced amorphous Si. *Appl. Phys. Lett.*, **31**(4):292–294, 1977.

[168] M.D. Archer and R. Hill, editors. *Clean electricity from photovoltaics*. Series on Photoconversion of Solar Energy, Vol 1. Imperial College Press, London, 2001.

[169] K. Tanaka, E. Maruyama, T. Shimada and H. Okamoto. *Amorphous silicon*. John Wiley & Sons, Chichester, 1999.

[170] A. Froitzheim, K. Brendel, L. Elstner, W. Fuhs, K. Kliefoth and M. Schmidt. Interface recombination in heterojunctions of amorphous and crystalline silicon. *J. Non-Cryst. Solids*, **299-302**(P1):663–667, 2002.

[171] J. Schmidt, A.G. Aberle and R. Hezel. Investigation of carrier lifetime instabilities in Cz-grown sillcon. *Proc. 26th IEEE Photovoltaic Specialists Conf., Anaheim*, pp. 13–18, 1997.

[172] A.G. Aberle, T. Lauinger and R. Hezel. *Remote* PECVD silicon nitride - a key technology for the crystalline silicon PV industry of the 21st century? *Proc. 14th European Photovoltaic Solar Energy Conf., Barcelona*, pp. 684–689, 1997.

[173] K. Jaeger and R. Hezel. Bifacial MIS inversion layer solar cells based on low temperature silicon surface passivation. *Proc. 19th IEEE Photovoltaic Specialists Conf., New Orleans*, pp. 388–391, 1987.

[174] A. Hübner, A.G. Aberle and R. Hezel. 20 % efficient bifacial silicon solar cells. *Proc. 14th European Photovoltaic Solar Energy Conf., Barcelona*, pp. 92–95, 1997.

[175] A. Hübner, C. Hampe and A.G. Aberle. A simple fabrication process for 20 % efficient silicon solar cells. *Sol. Energy Mater. Sol. Cells*, **46**(1):67–77, 1997.

[176] M. Kerr, J. Schmidt and A. Cuevas. Comparison of the open circuit voltage of simplified PERC cells passivated with PECVD silicon nitride and thermal silicon oxide. *Prog. Photovolt. Res. Appl.*, **8**(5):529–536, 2000.

[177] S.W. Glunz, R. Preu, S. Schaefer, E. Schneiderlöchner, W. Pfleging, R. Lüdemann and G. Willeke. New simplified methods for patterning the rear contact of RP-PERC high-efficiency solar cells. *Proc. 28th IEEE Photovoltaic Specialists Conf., Anchorage*, pp. 168–171, 2000.

[178] Jan Schmidt, Mark Kerr and Andrés Cuevas. Surface passivation of silicon solar cells using plasma-enhanced chemical-vapour-deposited SiN films and thin thermal SiO$_2$/plasma SiN stacks. *Semicond. Sci. Technol.*, **16**(3):164–170, 2001.

[179] A. Metz. *Neuartige höchsteffiziente Silicium-Solarzellen mit schräg im Hochvakuum aufgedampften Al/SiO$_x$/n-Si-Tunnelkontakten.* Ph. D. thesis (in German), University of Hannover, Germany. Published by Shaker Verlag, Aachen, 2000.

[180] S. Dauwe, A. Metz and R. Hezel. A novel mask-free low-temperature rear surface passivation scheme based on pecvd silicon nitride for high-efficiency silicon solar cells. *Proc. 16th European Photovoltaic Solar Energy Conf., Glasgow*, pp. 1747–50, 2000.

[181] S. Schaefer. *Plasmaätzen für die Photovoltaik - Plasmasysteme und -prozesse für die Herstellung von kristallinen Siliziumsolarzellen.* Ph. D. thesis (in German), University of Konstanz, Germany. Published by UFO Atelier für Gestaltung & Verlag, Konstanz, 2000.

[182] K.R. McIntosh and C.B. Honsberg. A new technique for characterizing floating-junction-passivated solar cells from their dark *I-V* curves. *Prog. Photovolt. Res. Appl.*, **7**(5):363–378, 1999.

[183] C.B. Honsberg, S.B. Ghozati, A.U. Ebong, Y.H. Tang and S.R. Wenham. Elimination of parasitic effects in floating junction rear surface passivation for solar cells. *Proc. 25th IEEE Photovoltaic Specialists Conf., Washington DC*, pp. 401–404, 1996.

[184] S.J. Robinson, S.R. Wenham, P.P. Altermatt, A.G. Aberle, G. Heiser and M.A. Green. Recombination rate saturation mechanisms at oxidized surfaces of high-efficiency silicon solar cells. *J. Appl. Phys.*, **78**(7):4740–4754, 1995.

[185] P.P. Altermatt, G. Heiser, X. Dai, J. Jürgens, A.G. Aberle, S.J. Robinson, T. Young, S.R. Wenham and M.A. Green. Rear surface passivation of high-efficiency silicon solar cells by a floating junction. *J. Appl. Phys.*, **80**(6):3574–3586, 1996.

[186] L. Mittelstädt, S. Dauwe, A. Metz and R. Hezel. Highly efficient all silicon nitride passivated multicrystalline silicon solar cells. *Proc. 17th European Photovoltaic Solar Energy Conf., Munich*, pp. 1311–14, 2001.

[187] Fraunhofer ISE CalLab, Freiburg, Germany.
www.ise.fhg.de/english/fields/callab/english/Welcome_english.html.

[188] L. Mittelstädt, S. Dauwe, A. Metz, R. Hezel and C. Häßler. Front and rear silicon-nitride-passivated multicrystalline silicon solar cells with an efficiency of 18.1 %. *Prog. Photovolt. Res. Appl.*, **10**(1):35–39, 2002.

[189] E. Schneiderlöchner, R. Preu, R. Lüdemann and S. W. Glunz. Laser-fired rear contacts for crystalline silicon solar cells. *Prog. Photovolt. Res. Appl.*, **10**(1):29, 2002.

Acknowledgements

List of Publications

1. S. Dauwe, A. Metz and R. Hezel. A novel mask-free low-temperature rear surface passivation scheme based on PECVD silicon nitride for high-efficiency silicon solar cells. *Proc. 16th European Photovoltaic Solar Energy Conf., Glasgow*, pp. 1747-50, 2000.

2. S. Dauwe, L. Mittelstädt, A. Metz and R. Hezel. Loss mechanisms in silicon nitride rear surface passivation for silicon solar cells. *Proc. 17th European Photovoltaic Solar Energy Conf., Munich*, pp. 338-341, 2001.

3. L. Mittelstädt, S. Dauwe, A. Metz and R. Hezel. Highly efficient all silicon nitride passivated multicrystalline silicon solar cells. *Proc. 17th European Photovoltaic Solar Energy Conf., Munich*, pp. 1311-14, 2001.

4. A. Metz, S. Dauwe, L. Mittelstädt, S. Steckemetz and R. Hezel. Industrially-feasible rear surface passivation schemes for crystalline silicon solar cells. *Proc. 17th European Photovoltaic Solar Energy Conf., Munich*, pp. 1913-16, 2001.

5. L. Mittelstädt, S. Dauwe, A. Metz, R. Hezel and C. Häßler. Front and rear silicon-nitride-passivated multicrystalline silicon solar cells with an efficiency of 18.1 %. *Prog. Photovolt. Res. Appl.*, **10**(1):35-39, 2002.

6. S. Dauwe, L. Mittelstädt, A. Metz and R. Hezel. Experimental evidence of parasitic shunting in silicon nitride rear surface passivated solar cells. *Prog. Photovolt. Res. Appl.*, **10**(4):271-278, 2002.

7. S. Dauwe, J. Schmidt, A. Metz and R. Hezel. Fixed charge density in silicon nitride films on crystalline silicon surfaces under illumination. *Proc. 29th IEEE Photovoltaic Specialists Conf., New Orleans*, pp. 162-165, 2002.

8. S. Dauwe, J. Schmidt and R. Hezel. Very low surface recombination velocities on p and n-type silicon wafers passivated with hydrogenated amorphous silicon films. *Proc. 29th IEEE Photovoltaic Specialists Conf., New Orleans*, pp. 1246-49, 2002.

9. S. Dauwe, L. Mittelstädt, A. Metz, J. Schmidt and R. Hezel. Low-temperature rear surface passivation schemes for > 20 % efficient silicon solar cells. *Proc. 3rd World Conf. Photovoltaic Energy Conversion, Osaka*, (in print), 2003.

Curriculum vitae

Name:	Stefan Dauwe
Date of birth:	07.07.1968
Place of birth:	Harderberg, Germany
Marital status:	married to Barbara Dauwe (née Vinke)
Parents:	Annemarie Dauwe (née Johannsmann) and Johannes Dauwe

Education:

1974-78	Grundschule Borgloh
1978-87	Gymnasium Ursulaschule, Osnabrück
1987-90	Trainee as Mathematisch-technischer Assistent at the Colonia Versicherung, Köln
1990-91	Community service

Studies:

10/91-10/97	Physics at the Universität Heidelberg
06/93	Vordiplom
09/94-06/95	Physics at the University of Edinburgh, Scotland
08/96-09/97	Diploma thesis at the Universität Heidelberg under the supervision of Prof. Dr. B. Jähne
	Infrarotuntersuchungen zur Bestimmung des Wasser- und Wärmehaushalts eines Blattes
01/98-02/98	Scientific assistant at the Botanisches Institut, Heidelberg
03/98-05/98	Scientific employee at the Philips Research Laboratories, Hamburg
08/98-04/03	Scientific assistant and PhD student under the supervision of Prof. Dr. R. Hezel at the Institut für Solarenergieforschung Hameln/Emmerthal
since 04/03	Scientific employee at ErSol Solar Energy AG, Erfurt

Index